Quasi-brittle failure of heterogeneous materials : damage statistics and localization

Estelle Berthier

THÈSE

PRÉSENTÉE À

L'UNIVERSITÉ PIERRE ET MARIE CURIE

École Doctorale de Sciences Mécaniques, Acoustique, Électronique et Robotique de Paris (ED391, SMAER)

Institut D'Alembert, Équipe Mécanique et Ingénierie des Solides et des Structures

Par **Estelle BERTHIER**

POUR OBTENIR LE GRADE DE

DOCTEUR

SPÉCIALITÉ : MÉCANIQUE

Quasi-brittle failure of heterogeneous materials : Damage statistics and localization

---

Directeur de thèse : Laurent PONSON

Soutenance le : *21 décembre 2015*

devant la commission d'examen formée de :

Elisabeth BOUCHAUD, Directrice de Recherche, ESPCI . . . . . *Rapporteur*

Vincent DÉMERY, Maître de Conférences, ESPCI . . . . . *Invité*

Alex HANSEN, Professeur, NTNU . . . . . *Examinateur*

Djimédo KONDO, Professeur, UPMC . . . . . *Examinateur*

Gilles PIJAUDIER-CABOT, Professeur, UPPA . . . . . *Examinateur*

Laurent PONSON, Chargé de Recherche CNRS, UPMC . . . . . *Directeur de thèse*

Jérôme WEISS, Directeur de Recherche CNRS, ISTerre . . . . . *Rapporteur*

Abstract

We propose a novel approach inspired from non-local damage continuum mechanics to describe damage evolution and quasi-brittle failure of disordered solids. Heterogeneities are introduced at a mesoscopic continuous scale through spatial variations of the material resistance to damage. The central role played by the load redistribution during damage growth is analyzed by varying the interaction function used in the non-local model formulation. The spatio-temporal evolution of the damage field is obtained from energy conservation arguments, so that the formulation is thermodynamically consistent. We analytically determine the onsets of localization and failure that appear controlled by the redistribution function. Damage spreading is characterized through a complete statistical analysis of the spatio-temporal organization of the precursors to failure. The power law increase of the rate of energy dissipated by damage and an extracted correlation length close to failure supports the interpretation of quasi-brittle failure as a critical phenomena. Indeed, we establish a connection between our damage model and the evolution law of an elastic interface driven in a disordered medium. It allows to identify the order and control parameters of the critical transition, and capture the scale-free statistical properties of the precursors within the mean field limit. Finally, we experimentally investigate the coaction of localized dissipative events and elastic redistributions in disordered media via compression experiments of two-dimensional arrays of hollow soft cylinders. Our experimental observations show a quantitative agreement with the predictions derived following our approach.

Keywords : damage mechanics, quasi-brittle failure, heterogeneous materials, intermittency, criticality

Résumé

Nous proposons une nouvelle approche inspirée des modèles d'endommagement non-locaux pour décrire la ruine des matériaux quasi-fragiles désordonnés. Les hétérogénéités matériaux sont introduites à une échelle continue mésoscopique via des variations spatiales de la résistance à l'endommagement alors que le mécanisme de redistribution des contraintes est décrit à travers une fonction d'interaction que l'on peut faire varier. L'évolution spatio-temporelle de l'endommagement est déterminée à partir du principe de conservation d'énergie et caractérisée via une étude statistique des précurseurs à la rupture. Cette approche nous permet de prédire la valeur des seuils de localisation et de rupture en fonction de la nature des redistributions. A l'approche de la rupture, nous mettons également en évidence une augmentation en loi de puissance du taux d'énergie dissipée ainsi qu'une longueur de corrélation, supportant l'interprétation de la rupture quasi-fragile comme un phénomène critique. En effet, nous démontrons que notre model d'endommagement s'apparente à la loi d'évolution d'une interface élastique évoluant dans un milieu désordonné. Cette analogie nous permet d'identifier les paramètres d'ordre et de contrôle de cette transition critique et d'expliquer les invariances d'échelle des fluctuations dans la limite champ moyen. Enfin, nous appliquons ces concepts théoriques à travers l'étude expérimentale de la compression d'un empilement bidimensionnel de cylindres élastiques. Notre approche permet de décrire de façon quantitative la réponse mécanique non-linéaire du matériau, et en particulier la statistique des précurseurs ainsi que la localisation des déformations.

Mots-clés : mécanique de l'endommagement, localisation, rupture quasi-fragile, matériaux hétérogènes, intermittence, criticalité

Remerciements

Je remercie Laurent Ponson d'avoir accepté de m'encadrer durant ces trois années et d'avoir su me faire découvrir avec enthousiasme un sujet qui m'était jusqu'alors inconnu. Laurent m'a permis de développer des compétences variées, tant théoriques avec des concepts allant de la physique statistique à la mécanique des milieux continus, des outils et approches mathématiques, qu'expérimentales avec cette riche et surprenante expérience de compression de pailles. Sa grande disponibilité et son investissement m'ont permis de mener à bien ce beau projet avec plaisir et curiosité.

Je tiens à remercier mes deux rapporteurs, Élisabeth Bouchaud et Jérôme Weiss, pour leur lecture minutieuse et rapports enrichissants qui m'ont permis de porter des questionnements nouveaux sur mon travail. Je remercie également Alex Hansen et Gilles Pijaudier-Cabot de m'avoir fait l'honneur de participer à mon jury de thèse, en particulier en cette toute fin d'année.

Doubles remerciements à Vincent Démery et Djimédo Kondo qui ont non seulement accepté de faire partie de ce jury mais m'ont également été d'une grande aide au cours de ma thèse. Djimédo a largement contribué à me familiariser avec la mécanique de l'endommagement et m'a permis un questionnement continu de mes approches. Merci aussi à lui d'avoir égayé mes longs vendredi soir et samedi en cette fin de thèse ! Chaque interaction avec Vincent aura permis de faire avancer ce projet, par la pertinence de ses questions et suggestions, mais aussi ce kernel calculé et formulé de manière si élégante, fil conducteur et inspirateur de ce travail.

Je remercie aussi Alberto Rosso et Harsha Bhat pour nos récents échanges. Ces réunions m'ont beaucoup apporté et ouvert de multiples et vastes orientations à ce projet de recherche.

Enfin, l'expérience présentée dans ce manuscrit a vu le jour grâce aux contributions de plusieurs personnes, entre autres Aurélie, initiatrice de cette expérience dans le cadre de sa thèse (et qui m'a fait découvrir les manips "cra-cra"), mais aussi Beth et Corentin, stagiaires coupeurs-empileurs de pailles et expérimentateurs autonomes d'un été, sans qui les presque 1400 pailles ne se seraient sûrement jamais mises en contact.

Je tiens aussi à remercier l'ensemble des membres de l'Institut Jean le Rond d'Alembert qui m'ont permis de réaliser ma thèse dans les meilleurs conditions. Je pense aux chercheurs mais aussi à Catherine, Olivier et Simona.

Si ces trois années ont été si belles c'est aussi et surtout grâce aux moments partagés avec les copains-(ex)thésards. Ceux du café en salle conviavialité, ceux des gourmets déjeuners au RA, mais aussi les thésards skieurs, les thésards amateurs de rugby, les thésards déménageurs, les thésards co-bureau et les thésards du soir (et ces interminables soirées au Local). Je citerai donc les actuels et les anciens, les thésards et les post-doc, les moitiés et leur moitié, sans aucune distinction et par répartition géographique, en espérant n'oublier personne : Bab et Mathieu, Claire, Lê, Marcello, Raph et Ben, Charles, Aurélie, Thomas, Claude, Ben, Joseph, JB, Hervé et Claudia, Paul, Etienne, Walid, Omar, David, Geoffroy, Mehdi, Adi, Thiago, Jan, Gounseti, Luca et Silvia, Valentina, Julieng, Jeff qui est presque du labo. Je n'oublie pas les copains récents, plus anciens, ou de toujours, qui m'ont malgré tout supportée et dont l'amitié m'est précieuse : Laure, Vincent, Julie et Simon, Marine, Nailée et

David, Anne-Lucie, Angélique, Maud, Aurélien, Greta, Maeva et Robin ; mais aussi les Rouennais, Claire, Pierre, Quentin et Mathilde, Félix (hum-hum), mon squatteur préféré Trugo, Seb et Maelle.
Enfin, je remercie ma famille et quasi-famille : mes parents, toujours présents, d'un soutien infaillible et dont les diners impromptus auront été salvateurs, mes frangins Rémi et Olivier et leurs multiples ressources pour me détendre et m'assouplir, mes grand-mères avec qui j'ai pu partager déjeuners à Jussieu et coups de fils affectueux, mes tatas folles-dingues, mes tatas et tontons plus raisonnables et mes cousins, ma deuxième maman Lucilia, sans oublier Valérie et Christophe, Aurélie et Charlie, Ben et Jess, Alexis et Régine. Merci à Bernard et Maman pour leur aide précieuse à la préparation de cette soutenance de thèse, leur oeil averti aura permis notamment ces couleurs flamboyantes. Merci aussi à Caroline, Claus, Thomas et Juliane pour leur amitié et multiples cartes postales.
J'ai une grande pensée pour mes grand-pères ; ils ont vu éclore mais pas s'achever ce projet . Ils auraient été de fins critiques mais de plus grands admirateurs encore, je pense fort à eux.
Merci au plus courageux de tous, Arthur, de m'avoir accompagnée, aidée et soutenue tout au long de ce projet. Tu as toujours trouvé le moyen de rendre heureuses et agréables ces trois années, la prochaine sera encore plus belle et plus riche, il me tarde d'entamer cette incroyable aventure à tes côtés.
And don't forget, *"Always look at the bright side of life"*.

Résumé détaillé de la thèse

Ce travail de thèse porte sur la rupture quasi-fragile des matériaux hétérogènes. La prédiction du comportement à rupture de tels matériaux, comme que le béton, le bois ou certaines roches, est un problème central pour l'amélioration et la conception de structures. Cette prédiction passe par une compréhension fine des mécanismes de dégradation mis en jeux au cours de la rupture quasi-fragile. Ceux-ci ont donné lieu à de nombreuses études théoriques et expérimentales qui ont permis de mettre en évidence que la rupture quasi-fragile découle de la nucléation et de la croissance stable d'un grand nombre de microfissures. Celles-ci évoluent de façon collective jusqu'à leur localisation selon une fissure macroscopique donnant lieu à la rupture catastrophique de la structure.

Dans le premier chapitre de ce manuscrit, consacré à l'état de l'art, nous proposons une description des principales caractéristiques de la rupture quasi-fragile. Les conséquences de l'endommagement sur les propriétés macroscopiques (dégradation des propriétés élastiques, adoucissement, effet de taille finie) sont discutées ainsi que l'organisation spatio-temporelle complexe de l'endommagement reportée dans différentes études expérimentales. On s'attache en particulier à la caractérisation des fluctuations mesurées lors de la croissance intermittente de l'endommagement. Leur statistique présente des propriétés remarquables caractérisées par des lois de puissance, et l'émergence d'une longueur de corrélation du champ spatial d'endommagement qui augmente à mesure que le matériau est proche de la rupture. Pour décrire l'endommagement de ces matériaux, de nombreux modèles ont été proposés. Nous décrivons ici succinctement deux classes principales, à partir desquelles nous construirons notre approche : les modèles d'endommagement continus, rigoureux mais dont la description, bornée à des matériaux homogènes, ne permet pas l'observation de l'organisation spatio-temporelle caractéristique des précurseurs, et les modèles statistiques, qui permettent de capturer cette complexité mais dont la simplicité fait obstacle à une description quantitative de l'évolution de l'endommagement.

Dans le second chapitre, nous présentons notre modèle d'endommagement mésoscopique de matériaux durcissants isotropes. Nous utilisons une formulation non-locale où la raideur microscopique dépend du paramètre d'endommagement non-local. Ce premier ingrédient nous permet de tenir compte des interactions entre évènements d'endommagement via une fonction d'interaction, choisie modulable, qui intervient dans la formulation non-locale. Nous ajoutons un second ingrédient : la présence d'hétérogénéités qui permettent de tenir compte de l'influence de la microstructure de ces matériaux sur leur comportement. Nous introduisons pour cela des variations spatiales de la résistance à l'endommagement à une échelle mésoscopique. Enfin, l'évolution de l'endommagement est obtenue en invoquant le principe de conservation de l'énergie, son évolution étant décrite comme un transfert d'énergie mécanique en énergie dissipée par rupture. L'analyse analytique des deux cas limites de systèmes hétérogènes sans interaction et homogènes avec interactions montre que la combinaison de ces deux propriétés est requise pour une description adéquate de la rupture quasi-fragile.

Dans le troisième chapitre, nous étudions l'influence de la fonction d'interaction sur la localisation de l'endommagement et la rupture du système. Cette fonction modulable est le produit d'un terme exponentiel, dont la vitesse de décroissance est fixée par l'introduction d'une longueur interne, et d'un terme sinusoïdal dont le contrôle est assuré via un paramètre κ. Lorsque celui-ci est nul, tous les points avoisinant un élément endommagé voient leur force motrice augmenter. Au contraire, lorsque ce paramètre est positif, certains points seront déchargés après un événement d'endommagement. L'étude des comportements prédits par la résolution numérique de notre modèle montre l'émergence de deux comportements distincts : pour de faibles valeurs de ce paramètre, la rupture catastrophique a lieu au point d'instabilité du système homogène. En revanche, au-delà d'une valeur seuil κ_c, une déviation à la réponse homogène est observée, rapidement suivie de la rupture catastrophique, à de plus faibles chargements. Nous rationalisons ces observations à l'aide d'une étude de stabilité linéaire. La valeur critique κ_c calculée consiste en un point de transition entre deux régimes : pour $\kappa \leq \kappa_c$, la rupture instable a lieu alors que le champ d'endommagement est homogène, sans localisation préalable. La réponse macroscopique correspond donc à celle d'un système homogène. Pour $\kappa > \kappa_c$, la rupture instable est précédée d'une transition d'un champ d'endommagement homogène à un champ hétérogène. Cette localisation de l'endommagement est caractérisée par une longueur d'onde finie qui dépend du paramètre κ et de la longueur interne. Dans ce second cas de figure, la prédiction de la rupture est seulement approximative. Les prédictions sont améliorées en considérant une seconde approche : la minimisation de l'énergie globale du système.

Dans le chapitre suivant, nous étudions l'organisation spatio-temporelle des précurseurs à la rupture. Comme observé expérimentalement, les avalanches d'évènements d'endommagement présentent une forte intermittence. En étudiant successivement les cas $\kappa = 0$ et $\kappa > \kappa_c$, nous montrons l'influence de la fonction d'interaction sur la réponse du système. Dans le premier cas, nous obtenons un comportement en loi de puissance de la taille caractéristique des avalanches, indépendamment de la longueur d'interaction. Celle-ci contrôle cependant l'organisation spatiale de l'endommagement. Une taille typique des zones endommagées au cours d'une avalanche émerge et augmente en loi de puissance. La signature de cette structuration des plus grandes avalanches est identifiable à partir de l'étude des corrélations spatiales du champ d'endommagement. Leur amplitude et extension spatiale croient à mesure que la rupture du système approche. Dans le second cas, la taille moyenne des avalanches ainsi que la longueur de corrélation sont bornées. La valeur limite, atteinte lorsque la localisation de l'endommagement débute, est fixée par la longueur d'onde critique identifié à partir de l'analyse de stabilité. Les divergences obtenues dans le premier cas de figure supporte l'interprétation de la rupture quasi-fragile comme un phénomène critique. Pour caractériser cette transition critique, nous montrons que notre modèle d'endommagement peut être exprimé comme un modèle de dépiégeage d'une interface élastique évoluant dans un milieu désordonné. La loi d'évolution de l'interface est gouvernée par un terme d'interaction élastique proportionnel à la fonction d'interaction introduite dans notre modèle. Nous montrons, à partir de cette analogie, que les exposants des lois de puissance suivies par les fluctuations du champ d'endommagement s'apparentent à un comportement champ

moyen de l'interface.

Dans le dernier chapitre, nous testons nos approches sur un système expérimental simple : la compression d'un empilement ordonné de cylindres creux élastiques (des pailles alimentaires) placés dans une boite rigide transparente. Ce système nous permet d'observer la localisation de la déformation mais aussi l'organisation temporelle caractéristique des évènements de dissipation. La transition vers la rupture est caractérisée par des évènements de dissipation locaux qui génèrent une dégradation progressive de la raideur du système. La dissipation provient de la friction entre pailles qui se déforment élastiquement au sein de l'empilement. A partir de la réponse macroscopique, nous définissons la dissipation d'énergie qui a lieu lors des avalanches. Nous montrons que, dans ce système aussi, la redistribution des contraintes élastiques générée par les évènements dissipatifs localisés permet d'expliquer le comportement spatio-temporel des précurseurs. L'étude des champs de déformation permet de déterminer l'initiation de la localisation. Ce comportement est expliqué à l'aide de notre approche, étendue au cas de solides 2D elasto-endommageables. Nous prédisons ainsi de manière adéquate les valeurs de la force au pic de la réponse macroscopique et les chargements critiques auxquels ont lieu la localisation.

Notations

D ..... Dimension of the system

N^D ..... Number of elements of the D-dimensional system

L^D ..... Size of the D-dimensional system

ξ_h ..... Heterogeneity size

F ..... Macroscopic force

Δ ..... Macroscopic displacement

k ..... Microscopic stiffness

d ..... Local damage parameter

$\overline{X}$ ..... Non-local variable

α ..... Interaction function

$\mathcal{F}$ ..... Total damage driving force

Y ..... Local rate of energy restitution

Y_c ..... Fracture energy threshold

Y_{c0} ..... Fracture energy threshold of the intact material

η ..... Hardening parameter

g ..... Random noise

σ_g ..... Random noise intensity

k_0 ..... Stiffness of the intact material

a ..... Stiffness stability parameter

γ ..... Stiffness polynomial degree

α_0 ..... Normalization constant of the interaction function

ℓ ..... Interaction length

ℓ_0 ..... Number of elements in the interaction length

κ ..... Shape parameter of the interaction function

d_{sb} ..... Damage level at the snap-back point of the homogeneous system

Δ_{c} ..... Macroscopic displacement at failure

Δ_{h} ..... Macroscopic displacement at localization

κ_c ..... Critical value of κ defining two regimes

d_{c} ..... Average damage at failure

d_{h} ..... Average damage at localization

d_{p} ..... Average damage at the peak of the homogeneous system response

δ ..... Distance to failure

Δ_{el} ..... Displacement at the first damage event

$\vec{q}$ ..... Fourier mode

$\vec{q}_c$ ..... Critical Fourier mode

λ ..... Wavenumber

λ_c ..... Critical wavenumber

d_0 ..... Homogeneous contribution of the damage field

δd ..... Heterogeneous (perturbation) contribution of the damage field

$\mathcal{F}^{(0)}$ ..... Homogeneous contribution of the total damage driving force

$\mathcal{F}^{(1)}$ ..... Heterogeneous (redistribution) contribution of the total damage driving force

δd_0 ..... Amplitude of the damage field perturbation

$\vec{q}_0$ ..... Mode of the damage field perturbation

$\delta(\vec{x})$ ..... Dirac function

$\tilde{X}$ ..... Fourier transform of a variable X

$\mathcal{G}$ ..... Effective redistribution function

S ..... Avalanche size

ℓ_x ..... Spatial extent of an avalanche

S_r ..... Fracture energy dissipated per avalanche

S_k ..... Kinetic energy dissipated per avalanche

S_d ..... Dissipated energy per avalanche

P_δ ..... Distribution density of avalanches taking at a given δ value

A_0 ..... Normalization constant of the distribution density

β_i ..... Power law exponent of the distribution $P_\delta(S_i)$

S_i^* ..... Cutoff of the distribution $P_\delta(S_i)$

μ_i ..... Power law exponent of S_i^* with δ

$\langle X \rangle$ ..... Average value of a variable X

τ_i ..... Power law exponent of $\langle S_i \rangle$ with δ

P ..... Distribution density of all avalanches

N_t ..... Total number of avalanches

N_a ..... Number of avalanches

ϵ ..... Power law exponent of N_a with δ

$(\beta_{tot})_i$ ..... Power law exponent of the distribution $P(S_i)$

d_f ..... Fractal dimension of avalanches

ℓ_x^* ..... Cutoff of the exponential distribution of avalanches spatial extent

ρ^* ..... Power law exponent of ℓ_x^* with δ

C ..... Correlation function

ξ ..... Correlation length

ρ ..... Power law exponent of ξ with δ

$\dot{X}$ ..... Rate of a variable X

v_ext ..... External driving velocity

v_{m} ..... Effective interface velocity

R ..... Radius of a straw

R_0 ..... Initial radius of a straw

u_y ..... Vertical displacement

E ..... Young's modulus

ν ..... Poisson's ratio

σ ..... Stress field

ε ..... Strain field

w ..... Free elastic density per unit volume

ψ ..... Calculated redistribution function

CONTENTS

INTRODUCTION

Concrete or wood structures, rocks or sandstone are surrounding us everyday. The prediction of the collapse of these materials and structures is a central practical issue and a deep knowledge on materials degradation is needed to design better structures and respond to attended features. For that reasons, the understanding of materials failure appears as a long-standing challenge that has attracted many researchers. Initially, the brittle failure of ideal homogeneous solids was studied by Griffith [40], whose work lead to the so-called linear elastic fracture mechanics theory that describes and predicts failure. However, material failure is due in many instances to the growth of multiple cracks, also called damage. Thus, for the above-mentioned materials, and under specific loading conditions, the failure process appears more complicated: it takes place through a progressive nucleation and stable growth of microcracks before *catastrophic* failure takes place. The description of such behavior requires not only to understand the effect of material heterogeneities, but also the complex interactions that arise as microcracks apprehend each others[8, 55, 88].

The existing continuum damage models [20, 60, 66] are currently not able to fully capture the failure of quasi-brittle materials. Firstly, their numerical implementation exhibits strong spurious mesh dependency with the localization taking place over a scale defined from the discretized element size [54, 87]. This leads to a non-physical description of failure, associated with zero dissipated energy. Such an issue prevents a realistic description of damage evolution from its localization to the catastrophic failure. Moreover, these models are limited to homogeneous media. It has now been well established that the complex development of precursory events results from the presence of heterogeneous distributions of material properties at the scale of the microstructure of the solids [1, 14]. Therefore, a description of the experimentally observed intermittency [42, 35] and spatial organization of damage [33, 71, 118] taking place before catastrophic failure is out of reach within that framework.

To overcome such deficiencies, two main solutions have been proposed. The former limitation has been resolved by introducing localization limiters in the constitutive equations. In particular, the insertion of non-local variables [87] has proved to be an efficient way to avoid mesh sensitivity.

However, this method relies on an arbitrary choice of the weighted averaging function. This key assumption controls the driving force redistribution after local damage events and should hence be physically motivated, which is not the case in the current models. Secondly, to capture the damage temporal and spatial organization resulting from the inherent material disorder and elastic interactions in the solids, statistical discrete failure models [1, 37, 48] were developed. Introducing distributions of failure strength and redistributions, this approach appears as an adequate way to capture the precursors behavior and failure. However, these models are restricted to qualitative predictions as they are not thermodynamically consistent and often based on non-realistic redistribution laws.

Throughout this study, we show that both problems can be overcome by taking into account the central role of heterogeneities, introduced at the continuous scale in a mesoscopic model. Indeed, disorder induces non-local effects, which allow describing the interactions arising as microcracking progresses. It also naturally regularizes the localization mesh dependency and thereby allows the description of damage from its initiation to its localization, and during its final stage leading to catastrophic failure. Combining both approaches we capture and describe properly the characteristic intermittency observed experimentally during quasi-brittle failure. In particular, the statistical study of the precursors features the characteristic power law behaviors of the bursts of dissipated energy, but also the complex spatial organization of damage with increased correlations as failure is approached.

The study of the precursors and observed behaviors have led to a long-standing debate on the critical nature of quasi-brittle failure. Our approach permits to clarify this controversial interpretation and answer to the following unresolved questions: what is the nature of such critical phenomena, *i.e.* to which class of universality is it related to? What is the critical point? What are the control and order parameters of this critical phenomenon? Finally, what are the time and length scale that diverge at the critical point? Using a simplified model, we address these issues and provide a better understanding on this critical transition interpretation.

This manuscript is divided in five chapters. In the first one, we give an overview of the main experimentally determined features of quasi-brittle failure and discuss the strengths and weaknesses of the actual models available for their description. We describe two main classes of models, namely continuum damage models and statistical models and highlight how they can be combined to build a consistent approach, has done in the following chapter.
The second chapter is devoted to the presentation of our model. We show how continuum damage and statistical models can be used to build a thermodynamically consistent non-local formulation of mesoscopically heterogeneous media. The determinant role of the coaction of both material disorder and interactions is emphasized through the analysis of two limit cases consisting in the study of alternatively a homogeneous material and disordered media without interactions.
In the third chapter, we perform an analytical prediction of both the localization of damage and failure of the material. In particular, we demonstrate the key role played by the shape of the redistributions of the damage driving force after local damage events, which fully controls the material response.

The precursory damage events are statistically studied in the fourth chapter. We show that our model captures their collective behavior and organization. In particular, our model predicts the power law behaviors of the damage burst sizes distribution and a diverging correlation length emerging form the spatial structure of the damage field. These predictions are qualitatively in good agreement with both experimental observations and recent studies numerical results. They also raise the question of the critical nature of the damage evolution towards failure. To go a step further in this interpretation, we connect our damage model to interface depinning models through the derivation of the damage evolution equation. In the mean field limit, this evolution equation permits an analytical prediction of the temporal behavior of the precursors, but also the determination of both the order and control parameters of the critical transition.

In the last chapter, we test our approaches on experiments performed on a model heterogeneous system consisting in a two-dimensional regular array of hollow soft cylinders. The local dissipation processes and elastic interactions allow observing the macroscopic stiffness degradation but also quantitatively determine and study the bursts of dissipated energy and strain localization. We show that this model experiment is well suited to a description as a two-dimensional elasto-damageable material via a realistic damage model formulation.

CHAPTER 1

CONTEXT AND MOTIVATION

In this first chapter, we give an overview of the failure behavior of quasi-brittle materials as observed in experiments and the theoretical models proposed to describe it. We also present the main questions that motivated this study. The first section, devoted to experimental observations, reviews the common features observed during quasi-brittle failure and highlights phenomena that are still poorly understood. We will focus both on observations of the material response at the local scale where damage actually takes place and at the macroscopic scale, through the mechanical response of the damaging solid. Numerous approaches have been proposed to describe quasi-brittle failure. In the second section, we briefly review the two main classes of models, namely continuum damage mechanics based models and discrete models of quasi-brittle failure, which very often come with a statistical description of damage growth. We emphasize their advantages and weaknesses, which motivated the elaboration of our own approach, based on a combination of ingredients issued from these two classes.

1.1 Experimental characterization of damage spreading and quasi-brittle failure

Quasi-brittle failure concerns a large variety of materials such as concrete, rocks, woods, fiberglass... It consists in a gradual deterioration of the material, which eventually leads to its abrupt failure. This degradation of the material properties is attributed to the progressive development of irreversible defects such as microcracks or voids, also called *damage*, while failure corresponds to the formation of a macroscopic crack that goes from one side of the sample to the other. The precursory microdefects can be defined as small flaws generally of similar dimensions as the characteristic microstructural feature of the material [61]. As they interact through the elastic field, their growth gives rise to complex collective behaviors that render the prediction of the material response a challenging task [8, 55, 88]. A collection of microscopic damage mechanisms such as crack face friction [64, 91],

crack kinking [52, 98], pore collapse [32, 7] and others can be involved in the deterioration process. Yet, a remarkable feature of quasi-brittle failure is that even though multiple scales and dissipative mechanisms are involved during the failure process, common behaviors emerge. In this section, we attempt to give an overview of the common features observed experimentally and discuss the associated challenges to understand them.

1.1.1 At the specimen scale: Average mechanical response of quasi-brittle materials

The irreversible defects formed during the loading result in a noticeable stiffness reduction of the altered material. The elastic moduli evolve as damage develops, which leads to a progressive decrease in load bearing capabilities of the structure. This has been observed for example upon the cycling loading of graphite/epoxy laminate [21], or triaxial testing of granite [58]. The decrease of the Young's modulus and increase of Poisson's ratio obtained by Heap et al. [46] on Etna basalt is shown in Fig.1.1a as a function of the number of applied cycles of an increasing-amplitude stress-cycling experiment. However, direct relationship between the moduli and damage itself is difficult to obtain. Indeed, experimental measures of damage remain a complicated task, as direct determination of the micro-defects is often associated with destructive techniques to study the material microstructure. As reported in [20, 67], different authors obtained indirect measures by considering the remaining life of a cycling loading, the stiffness reduction, density or resistivity variations. Thus, damage is usually quantified indirectly through its effect on the material properties.

Since elastic moduli set the relationship between stress and strain, progressive stiffness degradation leads to strongly non-linear macroscopic response of quasi-brittle materials. This has been largely explored experimentally. A characteristic force-displacement behavior obtained by Fortin *et al.* [33] for a triaxial test performed on a Bleurswiller sandstone is shown in Fig. 1.1b. It can be separated in three phases: The response is first linear, the loading being too small to nucleate new microcracks or activate the preexisting defaults. After some critical loading, a non-linear response is observed, associated with the nucleation and stable growth of micro-defects before the ultimate strength is reached (peak load). If the system is controlled in strain, this phase is often followed by a progressive strain softening prior to an abrupt failure. Finally, one might observe a plateau regime taking place after the formation of a macroscopic crack or fault that corresponds to the sliding of one part of the sample on the other.

However, noticeable variations in the behavior are worth mentioning. At the macroscopic scale, failure is associated with the separation of the sample in two pieces by a macrocrack and is very often preceded by the formation of a localized band where most of the damage activity accumulates. The orientation of this band depends on the type of loading considered. For example, for the triaxial test of Fortin *et al.*, an angle of about 45° was measured, whereas the macrocrack formed in

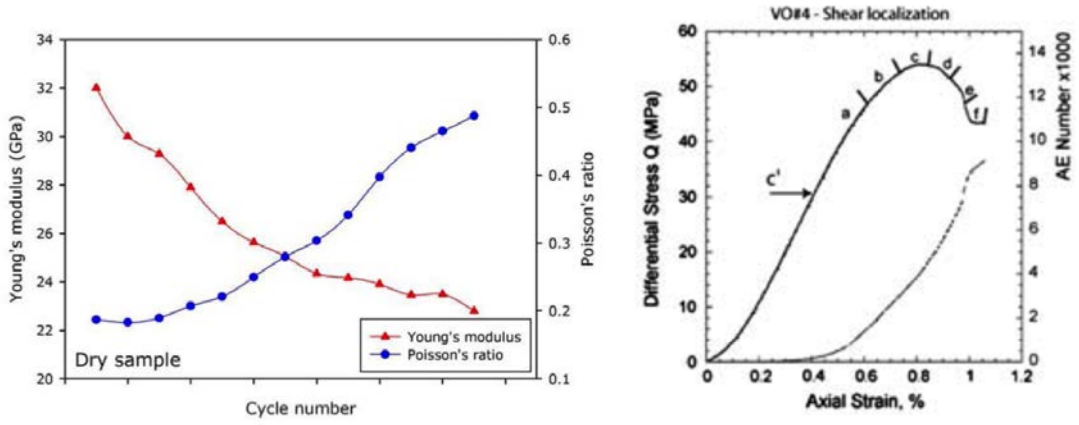

(a) (b)

Figure 1.1: (a) Evolution of the Young's modulus and Poisson's ratio obtained during an increasing-amplitude cyclic stressing experiment on a sample of Etna basalt obtained by [46] showing the gradual deterioration of the stiffness of the damaging material; (b) Differential stress (solid curve) and cumulative AE (doted line) versus axial strain for the triaxial test performed by [33]. Note that even if not exhibited here, rupture (taking place at a strain $\sim 1\%$) is associated with a surge in AE rate. The letters a-f indicate the loading frames over which the cartographies of damage event of Fig. 1.3 were obtained.

a prismatic spruce wood sample compressed in parallel to the fibers was perpendicular to the loading direction, as shown on Fig. 1.2 (image reproduced from [12]).

Failure and strength predictions are fundamental and long-standing [112] issue in material science and structural engineering. A general problem when performing laboratory experiments is the change of size of the tested specimens. For testing in the laboratory rock or concrete structures, size rescaling is very often unavoidable, but the sample size appears to greatly control its strength. Hence, a quantitative understanding of the effect of the specimen size on quasi-brittle strength is an important matter. Many systematic characterizations of this phenomenon were performed, as for example [10, 18, 39, 95, 110], but an extended range of length scales is generally difficult to achieve since large scale experiments are arduous to realize.

1.1.2 At the scale of damage and microstructure: Temporal and spatial organization of precursors to failure

If the macroscopic response and elastic moduli allow observing the effect of defects formation on the elastic properties of the material, they do not provide any hint on the local damage processes. A useful tool is the use of acoustic emission (AE) measurements during experiments. As early as 1942, Obert *et al.* [78] realized that during the loading of rocks, noises were emitted, which they assumed related to cracking events. Indeed, during microcracking, acoustic waves, associated with dissipation processes, radiate in the material. This non-destructive technique consists in using

Figure 1.2: Fracture due to deformation localization on a prismatic spruce wood sample compressed in parallel to the fibers. Image reproduced from [12].

piezoelectric sensors to record the acoustic waves emitted. Converted into an electric signal, the measurements are considered directly related to the local released elastic energy that takes place during microcracking [70, 29]. This technique allows characterizing both the temporal and spatial evolution of damage events, but also obtaining information on the microscopic mechanisms that take place. Considering some relation between the energy of the acoustic signal emitted and the energy dissipated into damage, one can study the evolution of the cumulated dissipated energy to characterize damage evolution, the distribution of the events intensity, their rate, duration and time separation or waiting time [22, 35, 42, 82]. Measurements performed with several receptors also allow to locate damage events and study damage spatial organization, in particular the phenomenon of localization, as discussed in the next paragraph. Finally, note that this approach can be made more quantitative since the different waveforms recorded can be used as indicators to characterize specific damage mechanisms, *e.g.* tensile, shear or implosive fracturing [65].

Spatial organization of the precursors during the transition from diffuse to localized damage

Fortin *et al.* obtained projections of the AE hypocenters at different stages of the response of the triaxial test. Each cartography of Fig.1.3 corresponds to damage events taking place during given loading windows, indicated by the letters a-f on Fig. 1.1b. For low loadings in the non-linear part of the force-displacement response, and neglecting the peculiar behavior in the load application regions, damage events are randomly distributed in the core of the material (frame a). As the loading proceeds, damage starts to concentrate in the upper region (frames b-c). In the post-peak regime, damage events are localized: Hypocenters form a localization band that develops progressively (frame d). Finally, the abrupt failure is associated with the growth or sliding of the macroscopic band, as exemplified on frames e and f where all damage events take place in the new formed fault. Therefore, it seems that damage is first diffuse with a spatial distribution that is mainly dependent on the disorder distribution: Microcracks nucleate or grow at the weakest points of the sample. As the density of defects increases, progressive clustering is observed, leading to a complex organization of damage and the presence of a localized zone where macroscopic failure initiates. This transition has been characterized for example

by the study of the change in entropy [35, 42] and diminution of fractal dimension of the damage clusters [71, 118], but a robust characterization of this localization process through the identification of a growing correlation length in the damage spatial distribution is still lacking.

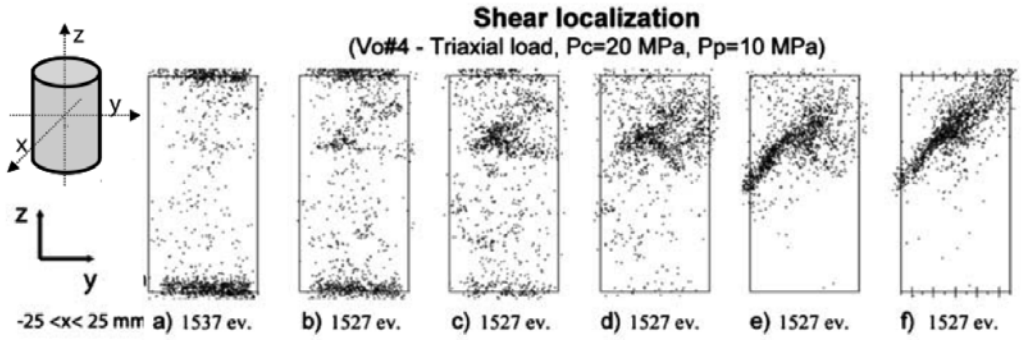

Figure 1.3: AE hypocenter distributions represented as a projection on the(z, y) plane and obtained during a triaxial test at 10MP on Bleurswiller stone by [33], the loading intervals considered are indicated on Fig. 1.1b. Overlooking the regions where the load is applied, damage spreads uniformly in the material at small loading (a). As loading is increased, damage starts to organize and one can foresee the localization band forming (b)-(c). In the post-peak regime, enhanced localization is obtained (d), followed by material failure through sliding of the new created fault where damage concentrates exclusively in the band formed during localization (e)-(f).

Temporal organization: Intermittency and scale-free fluctuations

As seen before, damage during quasi-brittle failure exhibits a complex spatial organization. Knowing the spatial distribution of the dissipative events, one can extract some information on how far the system is from failure by considering the diffuse to localized damage transition. Once damage starts to localize, one can also predict the location of the macrocrack that leads to failure. In addition to that, information relevant for failure prediction can be obtained from the temporal evolution of these precursors. The cumulated signal recorded on the Bleurswiller sandstone is shown on Fig. 1.1b. Very few or no events take place in the initial linear part of the stress-strain curve. If the cumulated AE signal gradually increases for low loadings, a sharp raise is observed close to failure. In particular, even through not exhibited here, rupture (taking place at a strain $\sim 1\%$) is associated with a surge in AE rate. The cumulated energy can be represented as a function of the distance to failure $(P_c - P)/P_c$, where P_c is the failure stress. This quantity ranges form one at the beginning of the experiment to zero at failure, and we could look at it as a control parameter within a critical phenomena description of quasi-brittle failure [1, 48]. Averaging over different experiments, the behavior obtained by Guarino *et al.* [42] when testing a planar sample of chipboard wood to which an effective tensile load is applied is shown in Fig. 1.4a. The power law behavior indicates a strong amplification of the average dissipated energy close to failure. In particular, the large increase close to failure that resembles a power law divergence argues for a critical transition interpretation. However, if there is a

common agreement on the increase of the damage activity as failure is approached, its nature remains unclear as exponential laws have also been reported [101].

The evolution of the cumulated energy suggests that either the size of the bursts or the event rate increases as damage progresses. To explore these two possibilities, the corresponding evolution of the bursts of dissipated energy obtained by Guarino *et al.* is represented as a function of the normalized applied pressure in Fig. 1.4b, where the cumulated measured energy is also indicated (dashed curve). Noticeably, damage events present a strong intermittency: the material exhibits phases were it deforms elastically, corresponding to silent periods were no AE is recorded, while short bursts of a broad range of amplitudes are observed in between. This behavior is often described as a crackling noise [105] and is observed for many physical systems, ranging from earthquakes faults dynamics [38] to the fracture of paper [101]. A strong amplification is observed close to failure with bursts of increasing amplitude. An acceleration of the damage process takes place with an increase of the event rate [26].

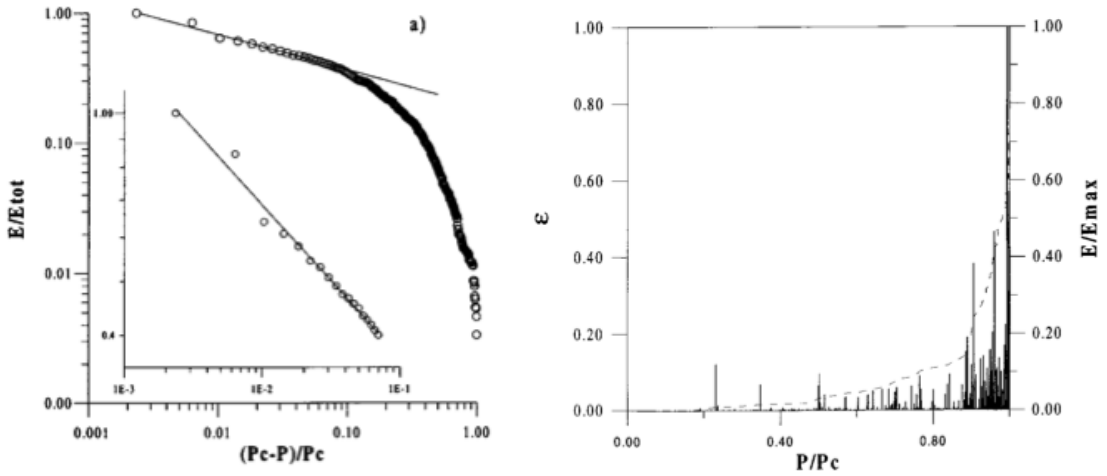

(a) (b)

Figure 1.4: Temporal behavior of AE events recorded by Guarino *et al.* [42] during the progressive damage of a chipboard wood up to failure at the pressure P_c: (a) Evolution of cumulated acoustic energy as a function of the distance to failure showing the diverging power law behavior obtained close to failure; (b) The corresponding rate of energy dissipated and cumulated energy (dashed curve) showing the intermittent crackling noise and acceleration of an amplified damage process as the sample is driven towards failure.

To characterize the amplitude of the energy bursts, we have to look at the statistics of avalanches in terms of probability density functions. The functions are usually obtained by considering all bursts taking place during the experiments. They exhibit power law behaviors, of the form $P(E) \sim E^{-\beta}$, arguing that fluctuations at all scales take place. However, the universality of the power law exponent remains to be discussed as values ranging from 1.2 to 2 have been re-

ported [27, 26, 35, 41, 42, 74, 82, 100]. Moreover, since the damage process amplifies as failure is approached, the acoustic signals might not have stationary statistical properties during the whole process of damage. As a result, computing the distributions at different distances to failure appears more appropriate. However, if some studies considered the lack of time invariance, the behavior obtained when considering different distances to failure remains under disagreement. Some studies report decreasing exponent of the power law behavior values as failure is approached [2, 72], while the recent work of Baró *et al.* [7] reports a constant exponent close to 1.4, independently of the distance to failure, as shown on Fig. 1.5 for a compression test on Vycor. A change of exponent is also reported as the loading condition is varied [2, 41]. Therefore, it seems that the general power law behavior, up to a cutoff, the origin of which is also unexplained, is common to all experiments whereas discrepancies remain on the actual value of exponents and their evolution as the material is driven towards failure. The lack of statistics may be responsible for the observed variations, as also the multitude of loading conditions and materials considered in the various studies. Finally, it should be mentioned that the linear relationship between the AE recorded signal and dissipated energy remains to be clarified as non-linear relations might actually relate them together.

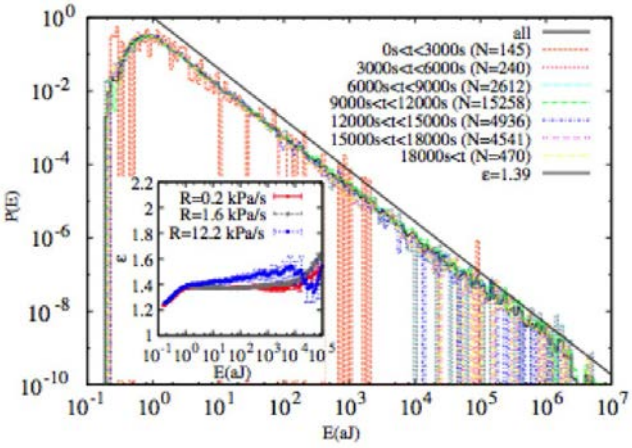

Figure 1.5: Time invariant power law distributions of exponent 1.4 of energy bursts obtained by Baró *et al.* [7] using AE during a compression test on Vycor. The lack of time dependency is in contradiction with the behaviors of the cumulated and rate of dissipated energy, which exhibit a strong acceleration as failure is approached.

1.1.3 Conclusions

It has been well shown that quasi-brittle failure is preceded by a complex evolution of precursory damage events. The use of AE allowed clarifying the heterogeneous materials response. Generally, it can be divided in four identified stages: The material first deforms elastically before microcracks nucleate and grow, leading to a nonlinear macroscopic response as the material stiffness deteriorates. During this phase, damage events are randomly distributed in space, microcracks forming in the weakest points of the material or extending the existing micro-defects. Their varying

amplitudes remain rather low in magnitude and the crackling noise is characterized by large time separation between events. As the system evolves towards failure, damage progressively organizes, forming clusters of non-trivial fractal dimension. This results from the increased density of microcracks in the system: As damage takes place somewhere in the system, the resulting stress variations in the neighborhood of the microcrack overlap with other microcracks, leading to complex interactions and cascade processes. This complex collective behavior of microcracks is well revealed by an increased AE activity, with a strong amplification of the damage burst size as the system gets close to failure. Finally, in the region where damage has localized, a macrocrack is formed. The system enters in another regime where the mechanics of the material is entirely governs by the behavior of the newly formed macrocrack or fault, similarly to crack propagation problems in brittle materials.

Moreover, the study of the temporal behavior of the precursors revealed interesting features such as a possible diverging dissipated energy at failure, and the presence of scale-free fluctuations, both indicated by power law behaviors. However, the lack of statistics does not allow for a clear assessment of the behaviors and power law exponent values. In particular, the change in behavior as failure is approached is not well established and calls for further experimental investigations. Finally, if the importance of the coaction of both the inherent disorder of the material and microcracks interactions is now well established, a better determination on the role of each component is still needed to understand the observed behavior. The common behaviors reported in quasi-brittle fracture experiments raise the following questions: Can we rationalize the temporal and spatial behavior of the precursors? How can we use their statistical properties to understand damage spreading and localization? What is the influence of the stress redistributions on damage evolution? More importantly, can we predict damage localization and failure? These questions led to numerous model descriptions that we classify in two main classes in the next section.

1.2 Damage models

The theoretical description of quasi-brittle failure is a long standing problem that has motivated a great number of researches, leading to the elaboration of various theoretical approaches. Yet, two main classes can be identified: Continuum damage mechanics and statistical models. The former consists in a continuous description of damage at a coarse scale through internal variables. Damage reflects the level of microcracking and affects the local mechanical behavior of the material through the degradation of the elastic moduli. At all time damage can be tracked and thermodynamical concepts allow for a rigorous description of the failure process. However, damage evolution remains described phenomenologically, the response is that of a statistically homogeneous material. A major problem in these approaches is the strong mesh dependency observed numerically, leading to a zero total dissipated energy at failure. The introduction of localization limiters, in particular through the use of non-local damage theory, has allowed overcoming this issue. However, non-locality is introduced heuristically, and physically motivated arguments to justify these models are still lacking.

On the other hand, the framework of statistical models relies on the central role played by microstructural heterogeneities. The solids are described by an array of discrete bonds with disordered properties interacting through an explicit law of force redistribution or implicitly through, *e.g.* elasticity laws. If these models allow capturing the main features of quasi-brittle failure in disordered materials, they still lack thermodynamics consistency and are hence limited to qualitative predictions of material failure behaviors. In this section, we briefly describe each approach, from which concepts are borrowed to build our model.

1.2.1 At the continuum scale: Damage mechanics

The concept of damage mechanics was first introduced in the context of creep rupture by Kachanov [56] who described the effect of gradual degradation of the material on its elastic properties through a continuous local damage variable. This concept was later generalized, as for example in [20, 60, 66] in particular through the theory of irreversible thermodynamics. Continuum damage mechanics (CDM) based models, consist in introducing one or more continuous internal damage variables in the equations predicting the mechanical fields. This local damage parameter is representative, at a coarse scale, of the damage density constituted by micro-defects on a representative volume element (RVE). The constitutive equations of damage evolution are formulated using the theory of irreversible thermodynamics combined with phenomenological or micromechanics considerations. It allows the description of the inelastic response of the damaged material as well as damage growth and localization.

In this section, to illustrate the main concepts of such models, we consider a simplified isotropic damage case. The analysis is restricted to a single internal variable, expressed as a scalar parameter d. Assuming that the observable variable is the elastic strain $\boldsymbol{\varepsilon}$ and that linear elasticity applies at a given damage level, the free energy density writes as

$$w(\boldsymbol{\varepsilon}, d) = \frac{1}{2}\boldsymbol{\varepsilon} : \mathbb{D}(d) : \boldsymbol{\varepsilon} \tag{1.1}$$

where $\mathbb{D}(d)$ denotes the damage dependent isotropic stiffness tensor. The Clausius-Duhem inequality gives the state law allowing to define the associated stress variable

$$\boldsymbol{\sigma} = \frac{\partial w}{\partial \boldsymbol{\varepsilon}}(\boldsymbol{\varepsilon}, d). \tag{1.2}$$

To describe damage evolution a damage criterion must be defined. To do so, a limit function, or loading surface, is introduced:

$$f(\boldsymbol{\varepsilon}, d) = \varepsilon_{eq}(\boldsymbol{\varepsilon}) - \kappa \tag{1.3}$$

where the equivalent strain ε_{eq} is a norm of the strain tensor $\boldsymbol{\varepsilon}$ and the function κ is representative of the damage resistance. This variable takes into account the material history through a function of the

damage variable

$$\kappa = g(d). \tag{1.4}$$

In Eq. (1.3), the expression of the norm fixes the shape of the elastic domain and should hence be formulated with care. A simple Euclidean norm, $\varepsilon_{eq}(\boldsymbol{\varepsilon}) = \sqrt{\boldsymbol{\varepsilon} : \boldsymbol{\varepsilon}}$ leads to an elliptical domain in the planes of principal stresses, symmetric with respect to the origin, leading to a non-representative material behavior as it implies similar responses in tension an compression. Hence, more elaborated expressions were introduced and motivated from experimental data. For example, different definitions (namely Rankine, Mazars [76] and modified von Mises based [24] definitions) are compared to experimental concrete data [63] in terms of strength envelopes in Fig. 1.6 (taken form [54]). Yet, experimental data provide thresholds for the strength of the material whereas damage initiation should correspond to the end of elastic response of the material. We see that the choice of the norm for the equivalent strain $\varepsilon_{eq}(\boldsymbol{\varepsilon})$ leads to very different elasticity domain shapes, which should be physically motivated.

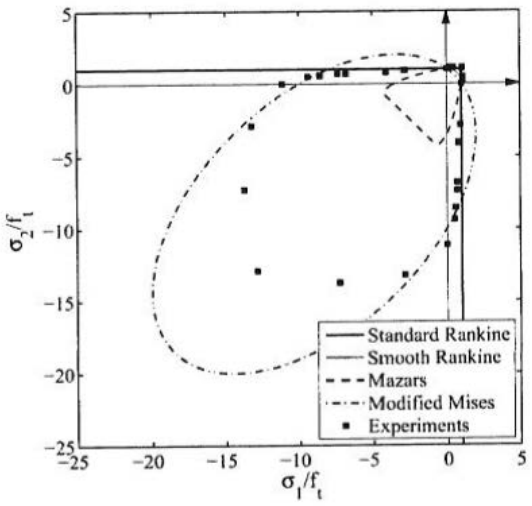

Figure 1.6: Biaxial strength envelopes for different damage models and experimental data for concrete [54] showing the importance of the norm definition for the determination of the equivalent strain.

Finally, the above equations are combined with the Kuhn-Trucker condition

$$f \leq 0; \dot{\kappa} \geq 0; \dot{\kappa} f = 0 \tag{1.5}$$

that translates in particular the irreversibility of the damage processes. The first condition imposes that $\kappa \leq \varepsilon_{eq}(\boldsymbol{\varepsilon})$, the second that κ cannot decrease and the last that damage increases only if $\varepsilon_{eq} = \kappa$. Hence, damage increases only if the condition $f(\boldsymbol{\varepsilon}, d) = 0$ is satisfied, and so the damage resistance κ increases too. If the function f is negative, in that case damage is stable and κ should not evolve. [1]

1. As an application, consider a damage resistance $\kappa = \kappa_0(1+\eta d)$ that increases with damage ($\kappa_0, \eta > 0$). Then

Due to the key role played by the equivalent strain definition, we prefer a thermodynamics-based description where the equivalent strain in Eq. (1.3) is rather expressed as a thermodynamical damage driving force:

$$\varepsilon_{eq} = Y(\boldsymbol{\varepsilon}, d) = -\frac{\partial w}{\partial d}(\boldsymbol{\varepsilon}, d) = -\frac{1}{2}\boldsymbol{\varepsilon} : \mathbb{D}'(d) : \boldsymbol{\varepsilon} \tag{1.6}$$

where $\mathbb{D}'(d) = \partial\mathbb{D}/\partial d$. In analogy with the elastic energy release rate G defined as the crack driving force in fracture mechanics [40], it corresponds to a rate of energy restitution. In that case, the damage resistance function κ can be seen here as an energetical threshold, *i.e.* the rate of dissipated energy for an infinitesimal increase of the damage level.

In summary, in the context of isotropic damage assumption, continuum damage mechanics relies on the definition of a scalar internal damage variable d, representative of the microcracks density at the scale of a RVE. Damage affects directly the elastic properties of the material through a progressive degradation of the isotropic stiffness tensor $\mathbb{D}(d)$. The dependency of the stiffness with damage is either arbitrarily fixed or derived from micromechanics concepts [19]. Considering the strain as the observable variable, one can calculate the elastic energy w of Eq. (5.13) and obtain the resulting stress field through the differentiation of w, Eq. (1.2). Damage evolution is obtained by fixing a damage threshold through a limit function f of Eq. (1.3), which consists in the difference between the damage driving force, the equivalent strain ε_{eq} or the energy release rate Y calculated using Eq. (5.14), and the damage resistance κ, increasing function of the damage level. For monotonic loading paths, damage evolution is fixed by solving, at a given strain level, the equation $f(\boldsymbol{\varepsilon}, d) = 0$.

Practically, following the thermodynamical approach, the following procedure can be used: At a given damage level d and having fixed the relations $\mathbb{D}(d)$ and $\kappa = g(d)$, (i) impose a strain $\boldsymbol{\varepsilon}$, (ii) calculate the stiffness $\mathbb{D}(d)$; (iii) calculate the free energy w; (iv) from this expression derive the rate of energy restitution Y; (iv) determine the sign of the function $f(\boldsymbol{\varepsilon}, d)$. If it is negative then damage is stable and does not evolve, if it is equal to zero then damage is solution of the equation $f = 0$; (v) calculate the corresponding stress at the considered damage level. An example of the obtained behavior will be shown in Sec. 2.2.1.

A main issue in such local models is the presence of spurious mesh sensitivity in their finite element implementation [54, 87]. During strain localization, damage processes and the associated energy dissipation concentrates over regions of finite size, fixed by the element size. Hence a strong mesh sensitivity arises: As the discretization is refined, the localization takes place over smaller and smaller volumes. As the damaged zone vanishes, the total energy dissipated through damage also tends to zeros, since the energy dissipation per unit volume is finite. Therefore, CDM models are un-

this set of conditions can be reformulated as $f \leq 0$; $\dot{d} \geq 0$; $\dot{d}f = 0$ which highlights that damage can solely remain stable when $f < 0$ or increase if $f = 0$, in which case κ also increases, as expected from the hardening law on $\kappa(d)$.

able to capture properly the transition from localized damage to failure. To address this problem and allow a continuum description of localization in quasi-brittle failure, approaches based on the introduction of localization limiters have been proposed. Such regularization techniques aim at avoiding localization over a zero volume. Several methods can be used, for example considering second or higher order gradients of some variables, *e.g.* deformation [81] or damage [83] or, as used in this study, non-local formulations in which a characteristic length is introduced [87].

Non-local integral formulations consist in replacing a certain variable by its non-local counterpart in the constitutive equations. This non-local variable corresponds to some weighted average over a spatial neighborhood. We denote by f the local variable and $\overline{f}$ its non-local counterpart that can be expressed as

$$\overline{f}(\vec{x}) = \int_V \alpha(\vec{x},\vec{\xi}) f(\vec{\xi}) d\vec{\xi} \tag{1.7}$$

where $\alpha(\vec{x},\vec{\xi})$ is a weighting function, which can be normalized such that the non-locality does not affect a uniform field. It is a decreasing function of the distance, and an internal length is introduced in its formulation to control the range, or spatial extent, of the effect of a damage events on the neighboring RVEs. This parameter is generally related to a characteristic microstructure length, *e.g.* the size of heterogeneities, even though there is actually no micromechanical justification for such a finite range non-local behavior. The determination of this length scale through experimental measurements is difficult. Some authors argue that it should be increasing as damage evolves so that the increase of the size of the fracture process zone, regions over which microcracking takes place, can be captured by the theory [89].

If the choice of the non-local variable remains arbitrary, it is shown to strongly affect the mechanical behavior of quasi-brittle materials [53], and should thus be chosen with care. Initially, Pijaudier-Cabot and Bažant used an energetical formulation of the CDM local model [87], where the limit function depends on the rate of energy restitution, and considered a function κ corresponding to the maximum non-local rate of energy restitution ever reached. In other approaches, the damage variable itself is considered non-local in the expression of the stiffness tensor, using a formulation of the type $\mathbb{D} = (1-\overline{d})\mathbb{D}_0$, where $\mathbb{D}_0$ is the stiffness tensor of the intact material [9], non-local equivalent fracturing strain has also been considered [87].

Integrating non-local variables in the constitutive equations of CDM has proved to be an efficient way to avoid non-physical localization. However, if these improved theory capture various aspects of quasi-brittle failure, it describes solids as homogeneous media. The effects of material microstructural features are neglected despite the central role that they play in failure problems (see *e.g.* [1, 14] for recent reviews). Therefore, a detailed understanding of the complex spatio-temporal structure of damage fields in quasi-brittle materials is out of reach from these models. In addition, the effect of material microstructure, however invoked to justify non-locality in the first step of the

derivation of the model, is then neglected in a second step by assuming that materials are homogeneous. It would seem more natural to consider material heterogeneities in the first place, and obtain non-local effects as a consequence of the model, but not as a postulate. To capture the effect of material heterogeneities on quasi-brittle failure behaviors, other approaches, that we categorize here as statistical models, were developed and are presented in the next section.

1.2.2 At the microstructure scale: Statistical models of quasi-brittle fracture

To capture the characteristic intermittency and spatial organization of damage, other approaches borrowing concepts issued from out-of-equilibrium statistical physics have been proposed. In these discrete models, the material is described by an array of discrete bonds or elements. Heterogeneities are introduced in the system via a statistical distribution of some properties, like failure threshold, or sometimes initial defects such as vacancies. During mechanical loading, the damage evolution is inferred from force balance in the network. The introduction of loads or energy redistributions, either explicitly or implicitly, allows to reproduce the complex interplay between disorder and microcracks interactions as the system is loaded up to failure.

The most widely known model is probably the fiber bundle model (FBM). In its simpler formulation, see [93] for a review, it consists in a 1D bundle of brittle fibers having randomly distributed failure strengths. As the external force is quasistatically increased, the weakest elements fail and the force carried by the broken fibers is redistributed among all intact fibers (global load sharing redistribution rule). The redistribution allows to trigger further breaking of fibers and the number of failures taking place between two equilibrium states allows defining an avalanche size. This simplified approach to quasi-brittle fracture allows to capture the temporal intermittency and power law distributions of avalanche sizes observed experimentally, as well as study of the evolution of the system up to its failure.

Moreover, the simplified framework allows for extensive analytical calculations. The critical force at failure has been determined [92] as also the temporal behavior of the precursors to failure. Indeed, a power law decrease of exponent $5/2$ [59] is established for the distribution of avalanches sizes when considering all damage events. If one considers a restricted loading frame, for example the last 10 percent of avalanches prior to failure, two power law behaviors emerge: For small avalanches, an exponent $3/2$ is determined while for larger ones, the exponent $5/2$ dominates [94]. The transition avalanche size can be considered as a cutoff parameter, which is shown to follow a power law increase with the distance to failure, clarifying the nature of the transition to failure. These results are essential as more complicated models usually do not allow for analytical determinations. Hence these behaviors serve as references for comparisons with that obtained numerically or from other theoretical descriptions.

The lack of realism of such description was however pointed out, in particular the lack of

spatial organization of damage due to the mean field nature of the redistributions. Many attemps to enrich these models have emerged (see [62] for a review), for example with the introduction of a gradual degradation of the fibers [49, 97] or more complex redistribution functions with the introduction of long-range interactions [50]. Finally, other models have emerged due to the rich behaviors that they predict. They are based on the description of solids as lattices or network of heterogeneous elastic beams, springs or electrical fuses. The main difference that arises with standard fiber bundle models is that the redistributions after damage events are implicitly taken into account.

Along this line, a widely used approach is the random fuse model [23, 120], which consists in a scalar electrical analogy of elasticity. The material is seen as an electric conductor consisting in a network of fuses. A voltage difference is applied to the network and each bond carries a current proportional to its conductance and the applied voltage. As the current density exceeds a certain threshold in a bond, the fuse burns and becomes an irreversible insulator. This leads to a redistribution of the current carried by each bond, the distribution of which is obtained by solving Kirchhoff equations (see [45] for a more detailed description). The analogy with elastic materials, even though it remains qualitative, is quite straightforward: The force applied to the material corresponds to the current, the displacement to the voltage, the stiffness to the conductance and the rupture strength is the threshold current. Hence, this model takes into account both the disorder, and the local stress (current) enhancements that result after failure events.

This and other discrete approaches like *e.g.* spring networks [77], in which as in the fiber bundle model the elements have brittle behaviors, have been extensively studied. The most interesting version of such models in the context of this thesis is its adaptation to continuously damaging bonds [121] and its elastic material counterpart [3, 37]. In both cases, when an element reaches its threshold, its conductivity, or stiffness, is decreased either by a factor $(1-D)$ where D is the bond damage parameter or a constant lower than one. Such an approach can be viewed as intermediary between continuous and discrete models, since damage is defined at the mesoscopic scale, that of the damaging elements, and represents a density of microcracks comprised within these elements.

These models predict power law distributed avalanches. The large statistics allowed by numerical experiments allowed in particular to characterize the temporal evolution of the distributions. It was identify that they display power law behavior up to an exponential cutoff [37, 120] or a crossover scale where a power law of larger exponent dominates [85]. The typical avalanche size extracted in both cases follows a power law increase with the distance to failure. This means that at failure, fluctuations at all scales take place and that at a given distance to failure, one can identify a typical avalanche size, which increases as failure is approached. The exponents have values close to $5/2$ (when taking into account all damage events) and $3/2$ (on a temporal frame). But significant deviations from the mean field analytical have been reported. This may arise from the non-trivial spatial structure of the redistributions. Note also that non-trivial finite-size scaling have been reported for the avalanche distributions [37]. Moreover, the use of two-dimensional lattices and the complex

shape of the redistributions allowed to evidence an interesting spatial organization of the damage or broken elements. In particular, a change in fractal dimension of the formed clusters [3, 4, 37] and a typical length over which damage is correlated have been evidenced, and the latter was shown to also follow a power law behavior with the distance to failure [37].

These observations, in qualitative agreement with the experimental results, support the interpretation of quasi-brittle failure as a critical phenomenon [106]. Critical phenomena are characterized by a sharp variation of some thermodynamic properties at a critical point. It is accompanied by the power law divergence of a length scale and time scale when the system is driven close to this point. It exists many different types of critical phenomena, which can be classified in universality classes. Inside a universality class, various physical systems that can look a priori very different share the same power law behaviors with the very same value of exponents and the same scaling functions. In a universality class, the details of the material properties and the local mechanisms generally no longer count. However, systems with different dimensionality or displaying interactions of different nature might not be in the same universality class. The interest in considering such interpretation is that if one knows the class of universality of the considered system, all exponents and scaling can be obtained and hence, the system response predicted. The interpretation of quasi-brittle failure as a critical phenomena is a long standing debate that we would like to clarify in this study. In that context, it was suggested in [113] that damage spreading and failure could be seen as a depinning transition of an elastic interface progressing in random media. However, only qualitative arguments were formulated and no direct calculations were performed to establish this link. We aim here at following this idea by bridging quantitatively depinning models and damage models.

1.2.3 Our approach: A mesoscopic description of damage spreading in heterogeneous media

We chose to benefit from both approaches by using some aspects of non-local continuum damage model together with other aspects used in statistical approaches. We consider a continuous non-local damage model formulated in a thermodynamical framework. The damage growth derives from the comparison of the damage driving force and the damage resistance. The former, the non-local rate of energy restitution is calculated from the free elastic energy. The latter can be viewed as its thermodynamic counterpart, the rate of dissipated energy. This last parameter is chosen as an increasing function of damage, representative of the material hardening. The non-locality is introduced via a non-local damage parameter in the stiffness expression. The expression of the interaction function is motivated by the recent study of Démery *et al.* [Démery et al.] who calculated the exact expression of the non-local redistribution function in the context of weakly disordered elasto-damageable solids. Moreover, to capture the characteristic fluctuations during damage spreading, we introduce material heterogeneities at a mesoscopic scale through a random distribution of damage resistance.

1.3 Conclusions

Experimental testing of a large variety of materials under diverse loading conditions allowed to extract the main features of quasi-brittle failure. The obtained macroscopic response, combined with acoustic emission measurements, revealed the general failure mechanism. It consists in the nucleation and stable growth of microdefects that affect the local stress and strain fields. They progressively deteriorate the material elastic properties, which leads to a non-linear macroscopic response. At some critical loading, a consequent density of microcracks is formed, and newly formed defects start to spatially organize. The localization of damage in some region of the material eventually leads to the formation of a macrocrack, at which point catastrophic failure takes place. If the damage progressive clustering has been well established, a unified description of the statistics of failure precursors is still lacking, in particular in terms of damage spatial structure. The same holds for the temporal behavior of the precursors. The intermittency and amplification of the fluctuations amplitude as failure is approached are well identified. However, there is no consensus on the actual evolution statistics of the bursts and the value of the exponents involved in that scale-free behavior.

We believe that a better understanding of the processes taking place during damage spreading in disordered materials would permit to clarify the observed behaviors and possibly predict the onset of failure. For that purpose, many models have been developed to describe quasi-brittle failure. The non-local extension of continuum damage mechanics based models capture well the macroscopic behavior of such materials. However, these models neglect the effect of microstructural heterogeneities and describe the solids as homogeneous media, which forbid the observation of the characteristic intermittency of the precursors to failure. To tackle this problem, statistical models of fracture appear very attractive. They allow the introduction of disordered material properties and redistributions after damage events. However, their lack of realism or thermodynamical consistency restricts them to qualitative predictions. In this study, we take advantage of both approaches by considering a non-local continuum damage model in which heterogeneities are introduced at the mesoscopic scale. We provide an extensive study of the role of the redistributions on both the macroscopic response, via the analytical determination of the localization and failure thresholds, and the precursors statistical behavior.

The strong increase of the dissipated energy as failure is approached, as well as the increase of the damage field correlation length obtained in some numerical studies, support the interpretation of quasi-brittle failure as a critical phenomena. The recent postulate that damage growth can be seen as a depinning transition of an elastic interface evolving in a random medium calls for further investigation. To clarify this long-standing debate, we perform a comprehensive statistical study of the precursors behavior obtained from our numerical approach and explicitly show how our damage evolution can be described through an elastic interface evolution law.

Finally, to characterize the statistical behaviors obtained in many complex experiments and

to test our approach, we also perform a compression experiment of a 2D array of hollow soft cylinders. We show that the bursts of dissipated energy can be fully characterized from the force-displacement response of the material. This suggests that many systems in which crackling noise is observed can be characterized rather simply from the measurement of this force-displacement response.

CHAPTER 2

MODEL FORMULATION AND LIMIT CASES ANALYSIS

As presented in the previous chapter, existing models for the description of the quasi-brittle failure of heterogeneous materials are not able to describe adequately all the features of such rupture phenomenon. We use advantages issued from the two main classes of models, non-local continuum damage and statistical models, to build our approach. We present our mesoscopic model in the first section. We detail the introduction of a non-local damage parameter dependency of the stiffness, the introduction of heterogeneities at the continuum scale and the thermodynamically consistent derived damage evolution law. The model is presented as a general formulation so that we also focus on the choice of the different material parameters (fracture energy heterogeneities, stiffness dependency with damage) used in this study, and discuss the formulation of the interaction function. Finally, numerical considerations (spatial discretization, extremal dynamics algorithm) are presented.

To understand the role played by each main ingredient, namely the interactions and heterogeneities in the system, we study in a second section two simple limit cases. We first discuss the behavior of a homogeneous system, which serves as a reference in the following, and highlight how the different material parameters affect its response, in particular how they control the existence of a snap-back instability. We then study a heterogeneous non-interacting system, and show how its response can be obtained as a statistical average. These two particular cases emphasize that these features taken separately do not allow to capture properly the main features of the quasi-brittle failure. Indeed, the coaction of both is required to obtain the complex damage organization and system response described previously.

2.1 Non-local damage model description of a heterogeneous material

Before detailing our model, we provide a brief general description of our approach. We build our model on classical concepts of continuum damage mechanics. Yet, instead of considering homogeneous material properties, we introduce spatial variations in the material resistance over a

typical scale ξ_h. To do so we consider media with heterogeneous fields of damage energy. Within this approach, material heterogeneities are introduced at a mesoscopic scale, intermediary between the microscale at which microfracturing processes take place and the macroscale at which the material can be seen as homogeneous. Moreover, the material is characterized by its damage field which represents in each material point the density of formed microcracks within an elementary volume δx^3. In principle, addressing numerically damage evolution within such a heterogeneous material would require to mesh the material at a fine scale $\delta x \ll \xi_h$ with respect to the heterogeneity size. However, we will see that using a coarser discretization $\delta x = \xi_h$ does not affect damage evolution, so that in the following, material heterogeneity and material representative element will be confounded.

Since our main focus is the effect of material heterogeneities on damage spreading within the material, we will consider simple loading conditions. In this first part of the thesis, materials will be loaded uniformly in tension, by the application of a displacement on the upper side of the specimen. During loading, damage will increase and affect the strength of an element via its stiffness, which decreases with damage. A central feature of our model is a non-local interaction function that allows to describe how stresses are redistributed after each damage event. In this study, a main objective is to understand how the nature of these interactions affects damage spreading and localization in heterogeneous solids.

2.1.1 Energy based damage criterion

We consider a system of N^D elements, where D is the dimension of the system Σ and is equal to 1 or 2, with periodic boundary conditions. Elements are distributed equidistantly in space and indexed by the position $\vec{x}$ of their center in the system of size L^D. As discussed the in introduction, these elements coincide with the typical heterogeneities of the material of size ξ_h. As a result, the total material size is effectively $N^D \xi_h^D$. The material is clamped between two rigid plates, as schematically represented in 1D in Fig. 2.1a where each element is represented by a spring: The bottom plate is maintained fixed whereas a uniform macroscopic displacement Δ, perpendicular to the x-axis in 1D and to the (x, y)-plane in 2D, is applied to the upper plate. Due to these clamping conditions, the microscopic displacement is homogeneous, equal to the macroscopic one, such that the macroscopic force writes as

$$F = \int_\Sigma \sigma(\vec{x}) d\vec{x} = \Delta \int_\Sigma k[d(\vec{x})] d\vec{x} \tag{2.1}$$

where σ is the stress field and $k[d(\vec{x})] = \sigma(\vec{x})/\Delta$ the local stiffness of an element which depends on its damage level $d(\vec{x})$. This scalar damage parameter ranges from zero when the element is intact to one when it is fully broken. For quasi-brittle fracture, it relates to the density of microcracks formed within the elementary volume represented by this element. On a broader perspective, it quantifies the degree of damage and the associated loss of stiffness of the elementary element. The variation of the elastic constant with damage is a central feature of continuum damage models [66]. However, as done in non-local damage models [9], we introduce here a dependency on the non-local parameter, $\overline{d}$,

defined as

$$\overline{d}(\vec{x}) = (\alpha * d)(\vec{x}) = \int_{\Sigma} \alpha(\vec{x} - \vec{x}')d(\vec{x}')d\vec{x}' \tag{2.2}$$

where α is a weight function that will be specified below satisfying to the normalization condition $\int_{\Sigma} \alpha(\vec{x})d\vec{x} = 1$ that ensures (i) energy conservation during damage growth (see Appendix A) and (ii) that a homogeneous field remains unaffected by the introduction of non-locality. This non-local damage parameter controls the stiffness through

$$k[d(\vec{x})] = k\left(\overline{d}(\vec{x})\right). \tag{2.3}$$

The introduction of a non-local variable allows to introduce interactions in the medium, as originally proposed by [87]. Though, contrary to this work and the several studies inspired from it [8, 73, 99], the interactions are introduced in our model at the level of the damage field, and not on the driving force. In other words, the stiffness in $\vec{x}$ depends on the damage level in an extended region defined by the range of the weight function α. This description was chosen to ensure a proper energy balance during the transfer of mechanical energy into fracture energy, as shown in Appendix A. The introduction of such a non-local failure behavior and heterogeneities results in a complex temporal and spatial organization of damage illustrated on the damage spatio-temporal evolution of Fig. 2.1b that resembles qualitatively the experimental observations and provides a rich macroscopic failure response.

To describe damage evolution, we start from the total energy of the system E^{tot} comprising the elasto-damageable material and the loading system. Hence, under some imposed loading Δ, the total energy is the sum of the elastic energy E^{el}, the fracture energy E^{d} and the work of the external force W:

$$\begin{aligned} E^{\text{tot}} &= E^{\text{el}} + E^{\text{d}} - W \\ &= \int_{\Sigma} \frac{1}{2}\Delta^2 k\left(\overline{d}(\vec{x})\right) d\vec{x} + \int_{\Sigma}\int_{0}^{d(\vec{x})} Y_{\text{c}}(\vec{x},\tilde{d})d\tilde{d}\,d\vec{x} - \int_{0}^{\Delta} F(\tilde{\Delta})d\tilde{\Delta} \end{aligned} \tag{2.4}$$

where $Y_{\text{c}}(\vec{x},d)$ refers to the damage energy of the element located in $\vec{x}$ and characterized by a damage level d. It is defined so that an increase δd of damage in a region $\delta\vec{x}$ of the material results in an energy dissipation $\delta E^{\text{d}} = Y_{\text{c}}(\vec{x},d)\,\delta d\,\delta\vec{x}$.

We introduce the thermodynamic driving force for damage as the change in total energy for a small increase $\delta d(\vec{x})$ of damage localized in $\vec{x}$

$$\mathcal{F}(\vec{x}) = -\frac{\delta E^{\text{tot}}}{\delta d} = \overline{Y}(\vec{x}) - Y_c(\vec{x}) \tag{2.5}$$

where $\overline{Y}$ corresponds to the elastic energy release rate, *i.e.* the thermodynamic driving force for damage, and Y_c corresponds to the rate of dissipation through damage, describing the resistance to

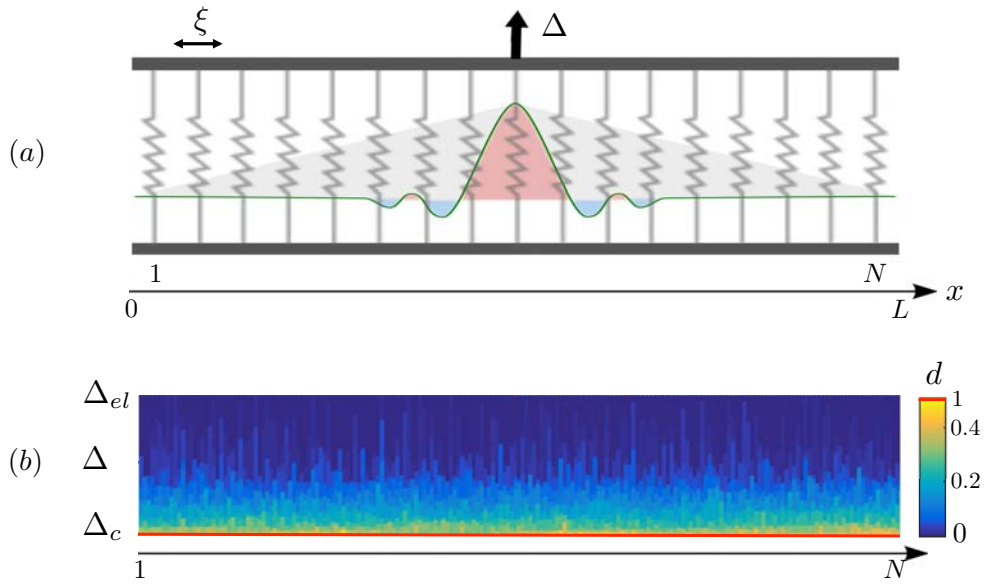

Figure 2.1: (a) Schematic representation of the loading system in 1D and the interaction function. The damage driving force that applies on the central fiber results from a spatial average of the driving force that applies on the other elements weighted by the interaction function α represented here. This interaction function also interprets as the spatial structure of the load redistribution that takes place in the material after the central element is damaged. (b) Spatio-temporal evolution of the damage field for a 1D system of $N = 2000$ elements. Initially, damage is zero everywhere ($d = 0$ for a driving $\Delta < \Delta_{\text{el}}$, upper blue line), until catastrophic failure of the system for $\Delta = \Delta_{\text{c}}$ ($d = 1$, lower red line).

damage.

We consider in this study quasi-static loading conditions where damage mechanisms take place at a much faster rate than the external driving. Thus, we assume that damage increases in the material under fixed applied displacement Δ. This implies that the work of the external force does not contribute to the energy release rate $\overline{Y}$ that hence writes as (see Appendix A for detailed calculations)

$$\overline{Y}(\vec{x}) = -\frac{\delta E^{el}}{\delta d} = (\alpha * Y)(\vec{x}) \tag{2.6}$$

Interestingly, with the introduction of the non-local damage parameter in the expression (2.4) of the elastic energy, the energy release rate $\overline{Y}$ takes a non-local form too and writes as the convolution of the weight function α with the *local* energy release rate defined as

$$Y(\vec{x}) = -\frac{\Delta^2}{2}\frac{dk}{d\overline{d}} = -\frac{\Delta^2}{2}k'\left(\overline{d}(\vec{x})\right) \tag{2.7}$$

Therefore, the damage driving force at one point of the system depends on the damage level of the other elements in a neighboring region. A typical example of redistribution function is shown schematically in Fig. 2.1(a). For elements close to the heterogeneity located at the center that has just damaged, the driving force will increase (red areas) while elements located further away might be unloaded (blue areas), depending on the actual shape and sign of the weight function.

The mechanical equilibrium that derives from the condition $\frac{\delta E^{\text{tot}}}{\delta d} = 0$ during damage growth is thus reached when

$$\overline{Y}(\vec{x}) = -\frac{\delta E^{\text{el}}}{\delta d} = \frac{\delta E^{\text{d}}}{\delta d} = Y_{\text{c}}(\vec{x}) \quad \text{if} \quad \delta d(\vec{x}) > 0 \tag{2.8}$$

Hence, damage increase require a balance between the elastic energy release rate and the damage dissipation rate, the same way crack propagation requires a balance between the energy release rate and the fracture energy [40]. In summary, we hence have the damage growth criterion

$$\begin{cases} \overline{Y}(\vec{x}) = Y_c(\vec{x}) & \Rightarrow \quad \text{Damage growth} \\ \overline{Y}(\vec{x}) < Y_c(\vec{x}) & \Rightarrow \quad \text{Stable damage.} \end{cases}$$

In Appendix A, we show that this damage evolution law can be derived equivalently from the variation of the total energy of the system with respect to the external driving Δ or with respect to damage.

2.1.2 Material parameters

Damage energy and material heterogeneity

To account for the heterogeneities of the material, we introduce a damage energy field dependent on the position $\vec{x}$ in the system through a random quenched noise g that accounts for the randomness of the fracture resistance to damage. The values of g are drawn from a uniform distribution of zero average value and variance σ_g. This distribution is classically used in statistical models of fracture [1], but other ones could be used without changing the general behavior of the disordered system. In addition, the material resistance is chosen to depend on the damage level in the elements as

$$Y_{\text{c}}(\vec{x}, d) = Y_{\text{c0}}[1 + g(\vec{x}, d) + \eta d(\vec{x})] \tag{2.9}$$

where $\eta > 0$ is a hardening parameter. Thus, at a given damage level d, the fracture energy field has a probability density function that writes as

$$p(Y_{\text{c}}) = \begin{cases} \dfrac{1}{Y_{\text{c}}^{\max} - Y_{\text{c}}^{\min}} & \text{for } Y_{\text{c}}^{\min} \leq Y_{\text{c}} \leq Y_{\text{c}}^{\max} \\ 0 & \text{for } Y_{\text{c}} < Y_{\text{c}}^{\min} \text{ or } Y_{\text{c}}^{\max} < Y_{\text{c}} \end{cases} \tag{2.10}$$

where $Y_{\text{c}}^{\min} = Y_{\text{c0}}(1 + \eta d) - \sqrt{3}\sigma_g$ and $Y_{\text{c}}^{\max} = Y_{\text{c0}}(1 + \eta d) + \sqrt{3}\sigma_g$. The function $p(Y_{\text{c}})$ is represented in Fig. 2.2a.

The increase of the average fracture energy $\langle Y_{\text{c}}(\vec{x})\rangle_{\vec{x}} = Y_{\text{c0}} + \eta\langle d(\vec{x})\rangle_{\vec{x}}$ with damage is assumed in several models, like *e.g.* [84]. It reflects qualitatively several microscopic toughening mechanisms taking place during material failure, as for example crack faces friction [64, 91], wing

cracks [5, 98] or crack bridging [16]. As justified later, it also allows to explore material behaviors with extended post-peak response and softening unlike when $\eta = 0$. Indeed, without hardening, the load redistribution described in Fig. 2.1(a) induces systematically an *increase* of the driving force of the damaging elements. In the limit of weak disorder intensity, it results in an unstable failure of the whole material as soon as the first element starts to damage. This is a strong indication that hardening is a relevant physical mechanism involved in quasi-brittle materials displaying an extended softening regime, as shown in the experimental part of this thesis.

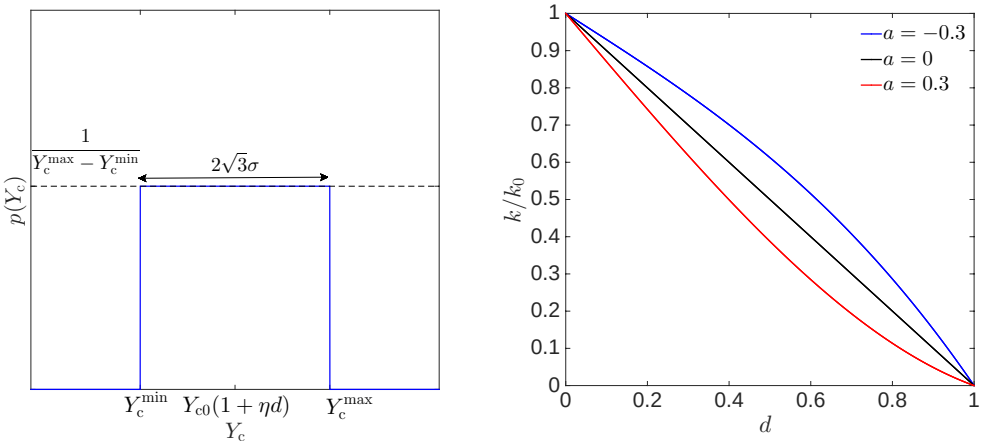

(a) (b)

Figure 2.2: (a) Probability density function of damage energy $Y_c(\vec{x}, d)$ at some fixed damage level d; (b) Effect of the stiffness parameter a introduced in Eq. (2.11) on the variations of the stiffness with the level of damage.

Material stiffness

To account for the degradation of the elastic properties of the material during damage, we describe the stiffness decay of a single element with the damage level through a polynomial law

$$k(d) = k_0[ad^\gamma - (a+1)d + 1] \tag{2.11}$$

where k_0 is the stiffness of the intact material, chosen homogeneous, and a is a constant verifying $-1 < a < 1/(\gamma - 1)$. The upper bound is obtained by considering that the derivative of the stiffness must be negative while d ranges from 0 to 1 and the lower one is defined such that the stiffness ranges from k_0 to 0. This law allows for the exploration of a large range of damage behaviors, as illustrated in Fig. 2.2b where the stiffness variations with d is shown for three values of a. The sign of a fixes the curvature of $k(d)$, and so the stability of the individual elements. Indeed, from Eq. (2.7) we obtain

$$\left.\frac{\partial Y}{\partial d}\right|_\Delta = -\frac{\Delta^2}{2}\frac{d^2k}{dd^2} = -\frac{\Delta^2}{2}k_0\gamma(\gamma-1)ad^{\gamma-2} \tag{2.12}$$

Thus, for negative values of a and no hardening, an element that starts to damage experiences a growing damage driving force Y at fixed displacement. Hence, damage evolves freely from

0 to 1, resulting in an abrupt failure at constant displacement. On the contrary, positive values of a lead to a stable damage process: As the heterogeneity gets damaged, Y decreases so that the external displacement has to be increased to further damage the heterogeneity.

The exponent γ drives the dynamics of the damage process. From the above equation of the damage driving force, one can see that for $\gamma = 0$, $\gamma = 1$, or equivalently the case $a = 0$ that corresponds to the largely used damage law $k(d) = k_0(1 - d)$ [66], we obtain a damage-independent driving force. Since interactions are mediated through the non-local damage variable $\bar{d}$ introduced in the model, this would amount to consider a *local* damage model: elements evolve independently from one another, and the material behavior would follow that of a single element, as discussed in Sec. 2.2. Since the effect of elastic interactions on the material failure behavior is the main purpose of this study, $\gamma = 3$ is chosen. Contrary to $\gamma = 2$, this value has the advantage to produce an acceleration of the damage growth close to final failure as largely reported in experiments [7, 32, 42]. However, any value of the exponent satisfying $\gamma > 2$ results in similar collective failure behaviors characterized by damage localization and catastrophic failure.

In any event, the choice of a polynomial variation of the stiffness with d does not limit the generality of our model. In the following, for all analytical calculations, we will keep its general form $k(d)$ as long as possible so that it can be specified to other behaviors. As evidenced here for a single element, the failure behavior of the material will be shown to depend on the *sign* of the second derivative $k''(d)$, *i.e.* the stability of individual elements, but not on the actual function $k(d)$ used to describe the stiffness degradation.

2.1.3 Interaction function

The shape of the interaction function will be shown to have a key role in controlling the material failure behavior. In general non-local models formulations, a Gauss distribution function form or a polynomial bell-shaped function is considered [53]. In both cases, an internal length is introduced that control the range of the interactions. In our case, to investigate the effect of complex damage driving force redistributions, in particular the reloading and unloading of elements with damage, we use the general form

$$\alpha(\vec{x}) = \alpha_0 \exp\left(-\frac{1}{2\ell}\|\vec{x}\|\right) \cos\left(\frac{\kappa}{2\ell}\|\vec{x}\|\right) \tag{2.13}$$

where $\|\vec{x}\|$ represents the distance between elements and α_0 is a the normalization constant defined such that $\int_\Sigma \alpha(\vec{x}) d\vec{x} = 1$. The parameters ℓ and κ can be tuned and control the spatial structure of the interactions. The internal length ℓ corresponds to a number $\ell_0 = \dfrac{\ell}{\xi_h}$ of elements. It controls the range of the interactions, *i.e.* the characteristic length over which an heterogeneity is affected by the occurrence of a damage event elsewhere. The parameter κ, defined as a positive constant, controls the shape of the redistribution function as illustrated in Fig. 2.3 where we have introduced the parameter value $\kappa_c = 0.58$. Note the change of sign of the interaction function if κ is non-zero. The sign of the

interaction function governs the sign of the redistribution during damage spreading: after a damage event takes place, elements located at a distance $\|\vec{x}\|$ from it for which $\alpha(\|\vec{x}\|) > 0$ experience a driving force increase whereas elements located so that $\alpha(\|\vec{x}\|) < 0$ are unloaded. In the two-dimensional version of our model, the interaction function solely depends on the distance between points, irrespective of the orientation within the plane perpendicular to the loading axis.

The choice of such an interaction function, and more broadly of non-local damage models for the study of damage spreading in heterogeneous materials, calls for a few comments. Nonlocal approaches in damage mechanics have be shown to address efficiently the problem of sensitivity to the element size observed in the softening regime during the progressive damage of quasi-brittle solids [54, 87, 88], as detailed more in the introduction. However, physical motivations for the introduction of non-local effects and justifications for the actual shape of the non-local function are still missing. Very recently, this approach was justified by the exact calculation of the redistribution function in elasto-damageable media [Démery et al.]. This interaction function was shown to be qualitatively similar to the Eshelby solution for the mechanical fields around a soft inclusion embedded in an infinite elastic medium [28] that displays a quadrupole symmetry $\alpha(\|\vec{x}\|, \theta) \sim \cos(4\theta\|\vec{x}\|)/\|\vec{x}\|^2$. Here in our damage model, we aim at keeping the main physical ingredients of these approaches, while simplifying the system studied so that the focus can be put on (i) the effect of material heterogeneities (ii) the actual shape of the redistribution function.

For that reason, we choose the redistribution function of Eq. (2.13) that shares the following similarities with the exact one: (i) The strength of the load redistribution is highly heterogeneous in space, since the closer the elements to the damage event, the larger the driving force redistribution; (ii) the sign of the load redistribution varies with the position in the damaged solid. As shown in the following, this property is a key feature of damage driving force redistribution after failure events that allow to describe the *unloading* of some regions while the rest of the material is actually further reloaded. Note however that there are significant differences between the interaction function used in our model and the one calculated for elasto-damageable solids: in our model, the interaction function changes of sign with the *distance* to the damage event, while the quadrupolar symmetry of the Eshelby redistribution function results in sign variations with the *direction* with respect to the loading axis. This difference results from our choice of loading configuration. Indeed, the macroscopic displacement is imposed uniformly to all the elements of the material that are arranged parallel to the loading plate so that the loading conditions do not define preferential direction in the material plane, while for $2D$ solids under uniaxial loading, the loading axis does define two orthogonal main directions. Another important difference is that our model considers interactions with finite-range given by the internal length ℓ. In the theory of elasto-damageable material, the function decays as a power-law of the distance. Despite this difference, we will see that our approach allows to explore the main features of damage spreading and localization in quasi-brittle solids, and understand the combined role of disorder and interaction functions on its evolution. The case of 2D elasto-damageable media using the interaction shape computed in [Démery et al.] is finally explored to interpret the experimen-

tal results of Chapter 5.

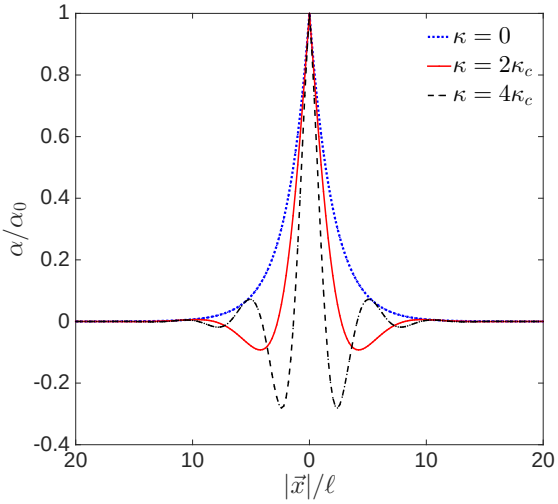

Figure 2.3: Interaction function α for three different values of the shape parameter κ (see Eq. (2.13)). For practical purposes, we have introduced $\kappa_c = 0.58$.

2.1.4 Numerical integration

Similarly to crack propagation problems, damage growth requires the equality $\overline{Y} = Y_c$ between the rate of energy released and the rate of energy dissipated. There are several ways to deal with this type of criterion in order to predict the system evolution. One of them is to regularize this criterion by assuming an over-damped dynamics $\frac{\partial d}{\partial t}(\vec{x},t) \sim \mathcal{F}(\vec{x})$ [15, 34]. Another possibility is to introduce a weakly rate-dependent critical energy release rate so that the damage evolution law takes the form of a kinetic relation $\overline{Y}(\vec{x}) = Y_c\left(\vec{x}, \frac{\partial d}{\partial t}\right)$ that can be solved assuming the irreversibility condition $\frac{\partial d}{\partial t} > 0$ [116, 117].

Here, we take advantage of the quasi-static loading conditions, and adopt a discrete dynamics inspired by [103] based on the following rules: The imposed displacement is increased until the failure criterion (2.8) is reached by one heterogeneity. The damage level of this heterogeneity is then increased by an increment $\delta d \ll 1$, and the spatial distribution of driving forces in the material is recalculated using Eqs. (2.6) and (2.7). The redistribution of driving force results in additional damage and subsequently additional driving force redistribution until this cascade process stops when the driving force is below its critical value everywhere in the system. Those three approaches result in the same avalanche-like dynamics of the damage growth illustrated in Fig. 2.1b. It corresponds to a damage process where damage increases by bursts that are localized both in space and time, characterized by power law statistics as observed for fracture processes in disordered media (see for example [1, 13, 48]). Despite the presence of strong fluctuations during the growth of damage, we will see in the next chapter that the main features of the macroscopic failure response of the system

can be captured without taking into account this intermittency.

In practice, we use the following numerical algorithm. Starting from an initially intact material (i) Δ is increased until one element satisfies to the condition $\overline{Y}(\vec{x}) = Y_c(\vec{x})$; (ii) the damage level of this element is increased by δd; (iii) the distributions of non-local damage driving force and fracture energy are recalculated using Eqs. (2.6) and (2.7) the discretized version of which is given in the following paragraph; (iv) step (ii) is repeated for all elements verifying $\mathcal{F}(\vec{x}, \Delta) \geq 0$; (v) steps (iii) and (iv) are repeated until no more points verify the damage criterion, *i.e.* equilibrium is reached; (v) we go back to step (i) and increase the external driving Δ again until new damage events take place. The simulation stops when all the elements are broken.

This discrete dynamics allows to explore large systems, typically $N = 10^4$ in 1D and $N \times N = 2.10^2 \times 2.10^2$ in 2D for a rather low computational time. An important gain of time was achieved by confounding the discrete elements with the individual heterogeneities, as justified below. As a result, we choose $L = N$ so that heterogeneities have a unit size $\xi_h = L/N = 1$ and the system size is $[0, L]^D$. As long as the spatial distribution $Y_c(x)$ of fracture energy is conserved, the number of elements (resp. the discretization step) can be increased (resp. decreased) without affecting the macroscopic failure response of the material, as will be shown in the following. Therefore, in the following the location $\vec{x} = (x, y)$ is actually a set of discrete values, ranging from 1 to N and separated by increments of $\xi_h = 1$. Finally, in order to limit finite size and spurious edge effects, we impose periodic boundary conditions.

To calculate the damage driving force defined with Eqs. (2.6) and (2.7), we use Fourier transforms since convolution products become simple products in Fourier's space. We calculate the non-local damage parameter through

$$\overline{d}(\vec{x}) = \mathrm{FT}^{-1}\left(\mathrm{FT}(\alpha(\vec{x})) \times \mathrm{FT}(d(\vec{x}))\right) \tag{2.14}$$

where FT denotes the Fourier transform and FT^{-1} the inverse Fourier transform, and We obtain the non-local rate of energy restitution using the same approach:

$$\overline{Y}(\vec{x}) = -\frac{1}{2}\Delta^2 \mathrm{FT}^{-1}\left(\mathrm{FT}(\alpha(\vec{x})) \times \mathrm{FT}(k'(\overline{d}(\vec{x}))\right) \tag{2.15}$$

where $\overline{d}$ was calculated using (2.14). The variation of the fracture energy with the damage level is discretized by introducing a small but finite damage increment δd that characterizes the amount of damage produced in an element when the condition $\overline{Y} = Y_c$ is reached. After each damage event, the fracture energy of the element is redrawn using

$$Y_c(\vec{x}, n_0) = Y_{c0}[1 + g(\vec{x}, n_0) + n_0\overline{\eta}] \tag{2.16}$$

where $n_0 = d/\delta d$ is the total number of damage events experienced by the element since the beginning of the test, $\overline{\eta} = \eta\delta d$ is the modified hardening parameter and $g(\vec{x}, n_0)$ is a random number drawn

in the interval $-\sqrt{3}\sigma_g < g < \sqrt{3}\sigma_g$. In the following, we use the value $\delta d = 0.005$ for the damage increment. Its value has a minor effect on the numerical results as long as taken much smaller than unity.

2.2 On the relevance of the combination of interactions and disorder

To emphasize the central role of the *coaction* of both heterogeneities and interactions between damaged elements, we investigate here two limit cases. We first study the behavior a homogeneous system of interacting elements for which we can track analytically the response. We then investigate the response of a non-interacting heterogeneous system. The two situations appear to be related and allow us to conclude that these ingredients used separately exclude the observation of the characteristic behavior of quasi-brittle failure.

2.2.1 Interacting homogeneous system response

A homogeneous system is obtained by imposing constant material properties through the medium. This amounts to eliminate the stochastic term $g(\vec{x}, d)$ introduced in the expression of the fracture energy field in Eq. (2.9), so that

$$Y_c(\vec{x}, d) = Y_{c0}[1 + \eta d(\vec{x})]. \tag{2.17}$$

As we start from an initially intact material with $d(\vec{x}) = 0$ everywhere, the damage resistance is homogeneous, so all points simultaneously verify the damage condition Eq. (2.8) for the same imposed displacement. This first failure event produces the same damage increment δd everywhere and hence the damage field remains uniform. Due to the normalization condition imposed to the interaction function α, it results that the total driving force $\mathcal{F}$ also remains homogeneous. Therefore, all points will again experience the same damage increment at the same loading, leading to a damage evolution that remains identical in each element all along the failure process.

This damage evolution has several important consequences: (i) Considering a homogeneous material amounts to consider a *local* and *interaction free* model of damage where the evolution of an element is independent of the response of the other ones. (ii) Each material point evolves identically. Therefore, the problem of damage evolution in the medium is reduced to a single element problem easily tractable analytically. (iii) Damage evolution is independent of the dimension D of the medium, so that the predicted force-displacement response is valid for any dimension. Note that this simple evolution of the damage field remains valid as long as the homogeneous state of damage remains *stable*. These stability conditions will be investigated in the following chapter.

Using the previous remarks, the damage evolution law (2.8) reduces to its local form which, for a

damage level d_0 in the system, writes as

$$Y(d_0) = Y_c(d_0). \tag{2.18}$$

Combining the above equation with the expressions (2.7) and (2.17) of the energy release rate and the fracture energy, the macroscopic displacement and force as a function of the level of damage follow

$$\left\{ \begin{array}{rcl} \Delta & = & \sqrt{\dfrac{-2Y_{c0}(1+\eta d_0)}{k'(d_0)}} \\ F & = & \Delta L^D k(d_0) \end{array} \right. \tag{2.19}$$

where the force evolution has been derived from its general expression given in Eq. (2.1).

The force-displacement response of the homogeneously damaged material is here a parametric curve where the damage variable plays the role of the parameter increasing from $d = 0$ when the first element starts to damage up to $d = 1$ at full failure when the material cannot sustain any loading. The normalized macroscopic mechanical response is represented in Fig. 2.4a for non-hardening ($\eta = 0$) materials for the three values of a also used in Fig. 2.2b. Normalization is here achieved by dividing the displacement by Δ_0^{br} and force by F_0^{br}. These quantities correspond, respectively, to the force and displacement at the end of the elastic regime for a brittle system ($a = 0$). Hence, $\Delta_0^{\text{br}} = \sqrt{2Y_{c0}/k_0}$ and $F_0^{\text{br}} = L^D\sqrt{2k_0Y_{c0}}$. As previously discussed, the parameter a controls the stability of individual elements. A positive value of a results in an extended softening regime characterized by a slowdown of the damage dynamics as complete fracture is approached. The case $a = 0$ corresponds to a driving force independent of the damage level. Hence, as soon as the threshold value $Y = Y_{c0}$ is reached, damage increases from 0 to 1 at constant displacement, which fits the behavior a brittle homogeneous system. Finally, negative values of a produce a snap-back instability in the force-displacement curve that would lead to an abrupt failure of the specimen as soon as the medium starts to damage. We focus in this study on this latter situation, which will reveal interesting features and appear to be the relevant case for the description of the quasi-brittle failure.

In the presence of hardening, the final failure can be delayed, as shown in Fig. 2.4b where we consider the negative value $a = -0.3$ and where the curves are normalized by the load and displacements at the end of the elastic regime, $\Delta_0 = \sqrt{\dfrac{2Y_{c0}}{k_0(a+1)}}$ and $F_0 = L^D\sqrt{\dfrac{2k_0Y_{c0}}{(a+1)}}$. The snap-back, which position is indicated by a dot, is observable for all the values of η explored here, even though less discernible as the hardening parameter is large. By tuning the value of η, its position can be shifted towards higher critical displacements and pushed away from the peak position.

For a homogeneous material, the snap-back position can be determined from the variations of the driving force with damage. If, at constant displacement, the difference $\mathcal{F} = Y - Y_c$ between the damage driving force and the damage resistance increases with d, the failure process is unstable since a constant loading would lead to abrupt failure. For the criterion (2.18) to be satisfied, the

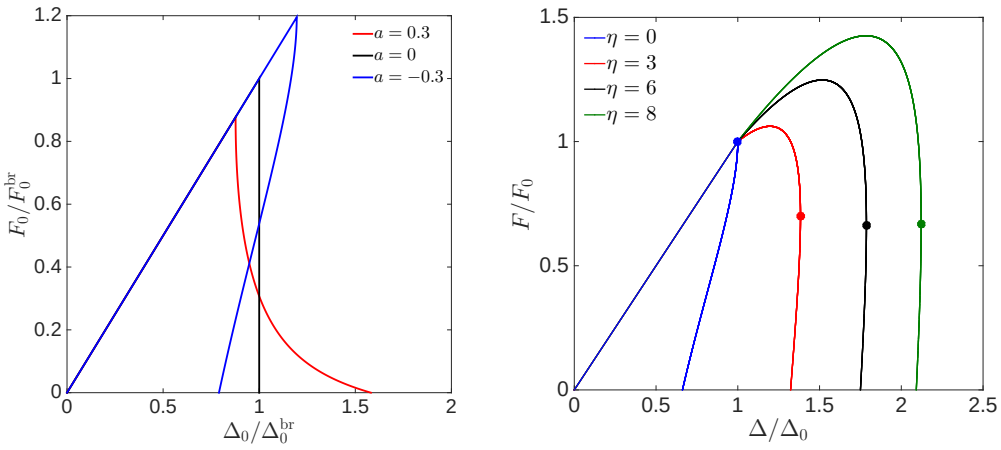

(a) (b)

Figure 2.4: (a) Effect of the stiffness parameter a introduced in Eq. (2.11) on the normalized Force-Displacement responses of the homogeneous non-hardening ($\eta = 0$) material. The normalization constants $\Delta_0^{\rm br}$ and $F_0^{\rm br}$ correspond, respectively, to the displacement and force at the end of the elastic regime when $a = 0$; (b) Effect of the hardening parameter η on the normalized mechanical response of the homogeneous material with $a = -0.3$. The normalization constants Δ_0 and F_0 correspond, respectively, to the displacement and force at the end of the elastic regime. The snap-back instability along the force-displacement curve is indicated by a dot.

macroscopic displacement must be decreased, leading to the characteristic snap-back behavior shown in Fig. 2.4b. Hence, the snap-back condition writes as

$$\left.\frac{\partial \mathcal{F}}{\partial d}\right|_{\Delta} = 0 \tag{2.20}$$

Assuming a driving force of the form

$$\mathcal{F}(d) = f(d)X^{\zeta} - h(d) \tag{2.21}$$

where $f(d)$ and $h(d)$ are functions of damage and X the control parameter, *i.e.* the displacement in our case, the criterion of Eq. (2.20) writes as

$$\frac{f'(d)}{f(d)} = \frac{h'(d)}{h(d)} \tag{2.22}$$

where we have used the equilibrium condition $\mathcal{F} = 0$ that gives $X = \left(\dfrac{h(d)}{f(d)}\right)^{1/\zeta}$.
Applying Eq. (2.22) to our specific case for which $f(d) = -1/2k'(d)$, $h(d) = Y_{c0}(1+\eta d)$, $X = \Delta$ and $\zeta = 2$, we obtain

$$\frac{k''(d_{\rm sb})}{k'(d_{\rm sb})} = \frac{\eta}{1+\eta d_{\rm sb}}. \tag{2.23}$$

This equality provides the critical level of damage at which snap-back occurs. Considering an exponent $\gamma = 3$ in the stiffness expression, one obtains

$$d_{\rm sb} = \frac{1}{\eta}\left(\sqrt{1-\eta^2\frac{1+a}{3a}}-1\right) \quad \text{for} \quad a<0 \tag{2.24}$$

from which one can obtain the snap-back displacement using Eq. (2.19). As expected, when $a > 0$, the condition (2.20) required for snap-back instability is never reached. From the condition $d_{\rm sb} \leq 1$, one can also discuss the existence of the snap-back instability for $a \leq 0$. For $-1 < a \leq -\frac{1}{4}$, the force-displacement response of the homogeneous medium always displays a snap-back, irrespective of the value of the hardening parameter η. On the contrary, when $-\frac{1}{4} < a \leq 0$, this instability takes place only for sufficiently low hardening parameter $\eta \leq \frac{-6a}{1+4a}$. Table 2.1 summarizes the damage level at snap-back for different values of γ . For $\gamma = 0$ or 1, no snap-back instability is obtained. For $\gamma = 2$, snap-back exists only for certain combinations of values of material parameters a and η and it takes place as soon as the material gets damaged. Expressions for higher γ values are complex and therefore not shown here. Note however that a positive value of a ensures the absence of instability, irrespective of the value of γ.

γ	a	η	d_{sb}
0	$\forall a$	$\forall \eta$	-
1	$\forall a$	$\forall \eta$	-
2	$-1 < a < -\eta/(2+\eta)$	$\forall \eta$	0
3	$-1 < a \leq -1/4$	$\forall \eta$	Eq. (2.24)
	$-1/4 < a \leq 0$	$\eta \leq -6a/(1+4a)$	Eq. (2.24)

Table 2.1: Conditions on the material parameters values a and η and corresponding damage level at the snap-back instability for different exponents γ of the stiffness polynomial expression. In the case of $\gamma = 0$ or 1, no snap-back instability is obtained.

Interestingly, even though the mechanical response of the medium depends on the value of a and in particular on its sign as illustrated in Fig. 2.4a, the total mechanical energy required for breaking the system, which can be inferred from the area under the force-displacement curve, is constant. Indeed, the total energy stored in the system before the application of the loading, and available for dissipation during damage growth is independent of a and follows $E^{\rm d}_{\rm tot} = (1+\eta/2)Y_{\rm c0}$ as derived from the expression (2.17) of the fracture energy. This is a remarkable property of the non-local damage model proposed here. As derived from thermodynamic principles, it allows to compare peak load and more generally macroscopic failure response of material systems with different microscopic failure behavior for a *constant* total fracture energy. For example, we see in Fig. 2.4a that under imposed displacement conditions, materials made of stable elements ($a > 0$) will sustain a larger loading, while under imposed force conditions, unstable elements ($a < 0$) will achieve a higher resistance.

2.2.2 Non-interacting heterogeneous system response

We now consider a heterogeneous system, *i.e.* the fracture energy field is given by Eq. (2.9), where elements are not interacting. The absence of interactions is obtained by considering a function α that takes the form of a Dirac function. This leads to a stiffness which depends only on the local value of damage so that $k(\overline{d}(\vec{x})) = k(d(\vec{x}))$ and a local damage driving force $\overline{Y}(\vec{x}) = Y(\vec{x})$. Hence the equilibrium condition takes a local form

$$Y(\vec{x}) = Y_c(\vec{x}, d) \tag{2.25}$$

As in the general case, the first damaged heterogeneity is the weakest one, corresponding to the element with the lowest damage energy. As damage increases in that element, the other regions of the material remain unaffected by the damage event. Thus, the next damage event will take place in the new weakest point of the system. If the disorder intensity σ_g is small with respect to the hardening η then it will, *a priori*, take place in another element and at an increased loading. This random damage process goes on until damage in an element reaches the snap-back instability value. In that case, the damage increases up to 1 at constant displacement in this element. We now discuss the effect of the noise g. After each failure event, the damage energy is redrawn. This results in a slightly varying snap back threshold with respect to the predicted value for an homogeneous system response. For that reason, the different elements abruptly break one by one, at different imposed displacements.

Due to these mechanisms, we can conclude that (i) since the elements behave independently, the response of the system is the same whatever its dimension D; (ii) the macroscopic response of the system is a statistical average of the response of each heterogeneity. Furthermore, apart from the abrupt failure of each element at different critical loadings, at each applied displacement only one damage event takes place. Hence, the fluctuations in terms of dissipated energy are of the same magnitude as the disorder intensity and the typical dissipated energy at a given loading is proportional to the average fracture energy of the system $\eta\langle d\rangle$. Since the disorder is spatially independent, the damage field in the system is completely random and uncorrelated. These two observations indicate that the response of such a system is far from the behaviors observed experimentally and described in the first chapter.

2.3 Conclusions

The proposed model takes into account the heterogeneities of the materials microstructure at the mesoscopic scale, at which a continuous damage parameter is defined. Following previous approaches, we adopt a non-local formulation via the introduction of a non-local damage parameter. The chosen redistribution function, in which an internal length is introduced, has a tunable shape through the introduction of shape parameter κ. Its expression was based on that calculated in a more realistic framework and allows for both reloading and unloading of neighboring elements after damage events. Finally, the damage evolution law is derived from energy conservation considerations and

permits a thermodynamically consistent description of damage evolution through bursts of dissipated energy taking place at fixed applied displacement.

If it may appear that many parameters are introduced in the formulation, the presented model and most calculations are expressed as general expressions, to which the specified properties, e.g. material stiffness, fracture energy field and interaction function, are considered and discussed. In this study, we focus principally on the role of the redistributions of the damage driving force, so that the main varied parameters are the internal length ℓ_0 and shape parameter κ, while the other properties remain invariant.

The application of this model in the case of either a homogeneous interacting or an interaction-free disordered system showed that the quasi-brittle failure features cannot be properly captured if heterogeneities and interactions are taken separately. If the system behavior becomes trivial, it allowed to investigate the role of the stiffness expression and the introduction of hardening in the damage resistance field. The homogeneous media response will serve as a reference in the course of this study, in particular to compare with the complex behavior of systems with both disorder and interactions, as considered in the next chapter.

CHAPTER 3

DAMAGE LOCALIZATION AND FAILURE PREDICTIONS OF THE QUASI-BRITTLE MATERIAL

In this chapter, we apply our model and explore the resulting behavior when both heterogeneities and interactions between damaged elements are taken into account. As discussed in the previous chapter, these ingredients taken separately render the system behavior trivial and unable to describe quasi-brittle failure. We show here that taking into account both ingredients lead to a complex response where damage evolves from a diffuse spatial distribution to a localized state. The failure of the system takes place at or shortly after this localization. Through an analytical determination of the critical loadings at localization and failure via both a linear stability analysis and a global energy minimization, we determine that it is the shape of the interaction function α, fixed by the parameter κ that controls the system response.

In the first section we investigate the one-dimensional system response. Varying the shape parameter value, the system force-displacement response is shown to either follow that of the homogeneous system up to the snap-back point at which catastrophic failure takes place, or up to a critical loading at which a deviation is observed, shortly followed by an abrupt failure of the system that occurs at lower loadings than the instability of the homogeneous system. The determination of the critical loadings and damage level at which these transitions take place show that (i) there is a continuous evolution of these thresholds with the parameter κ and (ii) the internal length value does not affect the critical loadings. The damage field organization is shown to organize with a particular critical mode that also scales with κ. In the second section, we rationalize these observations by predicting both the localization, at which deviation from the homogeneous behavior is observed, and failure loadings through a linear stability analysis. The study is performed on both one and two-dimensional systems, the dimensionality affecting only the values but not the behaviors. This approach showing limitations if the damage field localizes before failure takes place, we complement this study by performing a global energy minimization in a third section. This allows recovering the localization threshold and

improve the failure prediction.

3.1 Failure behavior of the heterogeneous system: numerical observations

In this section we focus first on 1D systems while 2D systems, that display similar behaviors, are left for Sec. 3.2.3. We study the response of a material made of heterogeneities with unstable failure properties using a negative stiffness parameter $a = -0.3$. The results are here shown for a hardening parameter value $\eta = 8$ but the system behavior is the same as long as a and η are verifying the conditions described in Table 2.1. We consider several realization of the disorder, the intensity of which (σ_g) ranges from 0.001 to 0.2. The influence of the internal length parameter, with $\ell_0 = 5$ or 10, and shape parameter κ is investigated.

3.1.1 Macroscopic response

The normalized macroscopic response of weakly heterogeneous materials ($\sigma_g = 0.001$) is presented in Fig. 3.1a for different values of the shape parameter κ and compared with the response of the homogeneous material. The force and displacement are normalized by their values at the end of the elastic regime. In order to smooth out the fluctuations observed from one material to another, the response of the heterogeneous material is shown after averaging over twenty different realizations of the disorder.

For small imposed displacements $\Delta \ll \Delta_c$, where Δ_c is the applied displacement at failure, the response of the heterogeneous system is identical to that of the homogeneous system. As Δ gets close to Δ_c, for the non zero κ values shown here, its behavior deviates slightly from the homogeneous response, as illustrated in the inset of Fig. 3.1a for $\kappa = 2\kappa_c$. Finally, we observe at Δ_c a sudden drop of the force that reveals the catastrophic failure of all the surviving material elements. The force and displacement at failure are indicated by dots in Fig. 3.1a. For $\kappa = 0$, no deviation is observed until the catastrophic failure takes place at the snap-back instability of the homogeneous system.

Thus, varying the value of κ shifts the failure instability that lies (i) at the snap-back point for $\kappa = 0$, (ii) between the peak force and the snap-back point for $\kappa = 2\kappa_c$, and (iii) in the pre-peak region for $\kappa = 4\kappa_c$. Lastly, at low disorder level, it appears that the shape of the interaction function controls the occurrence of the failure instability while maintaining a global behavior close to the one of a homogeneous material.

Before determining the critical damage and loading levels at which deviation and catastrophic failure take place, we show the negligible influence of the spatial discretization on the system response. To do so, we compare the critical loading at failure when varying (i) the number N of heterogeneities in the system, and (ii) the number of discretization points N_ξ of the heterogeneities.

In the latter case, the fracture energy thresholds are correlated so that they vary continuously from one heterogeneity to another. In both cases, convergence is obtained. For $\kappa = 0$, $\ell_0 = 2$ and $\sigma_g = 0.001$, on Fig. 3.1b, top, we show the deviation of the obtained displacements at failure from that for which the results are independent of the discretization, as a function of N. The deviation can be considered negligible for the system size $N = 10000$ used in this study which is much larger than the transition point at which increased deviations are observed. Secondly, the discretization of the heterogeneities is performed for a system of $N = 1000$ elements so that the actual value of N does not affect the results while the system size is not too large and allows for a fine discretization. The behavior presented in Fig. 3.1b, bottom, shows that if a stronger deviation is obtained when heterogeneities are not discretized ($N_\xi = 1$), the amplitude can be considered negligible.

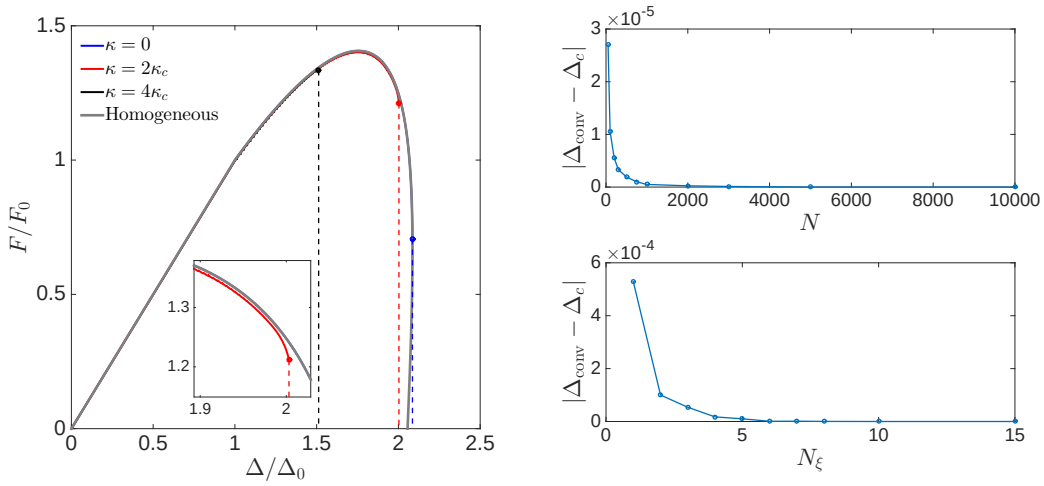

(a) (b)

Figure 3.1: (a) Normalized Force-Displacement response of a weakly heterogeneous material ($\sigma_g = 0.001$) for $\ell_0 = 5$ and $\eta = 8$ and three different values of κ after averaging over twenty realizations of the disorder, and comparison with the response of the homogeneous material with local failure behavior. Catastrophic failure is indicated by dots. The inset is a zoom of the response with $\kappa = 2\kappa_c$ that shows the deviation from the local behavior close to failure; (b) Effect of the numerical discretization of the system on the critical loading at failure. The influence of (top) the number of heterogeneities N in the system and (bottom) number of points in an heterogeneity, N_ξ, for $N = 1000$ are studied. In both cases an internal length $\ell = 2\xi_h$ is used. The finer mesh loading at failure Δ_{conv} serve as a reference and is compared to Δ_c for the different discretizations.

3.1.2 Deviation from the homogeneous system response and failure damage thresholds

We now aim to determine the critical damage levels d_h and d_c, respectively loadings Δ_h and Δ_c, at which deviation and catastrophic failure take place. To do so, we introduce the intensity

of the damage spatial fluctuations

$$\sigma_{\rm d} = \sqrt{(\langle d(x)^2\rangle - \langle d(x)\rangle^2)} \tag{3.1}$$

that we represent as a function of the average damage level $\langle d\rangle = \frac{1}{L}\int_\Sigma d(x)dx$ in Fig. 3.2 for $\kappa = 3\kappa_{\rm c}$. After a short transient regime, the level of the fluctuations in the damage field remains rather constant and then shows a rapid increase from which the onset $d_{\rm h}$ is defined: we fit this increase by a linear behavior (green dashed line) and define $d_{\rm h}$ from the intersection with the average damage fluctuations (red thick line) far away from failure $d \ll d_{\rm c}$. The onset $d_{\rm c}$ of failure is more obvious and is defined as the average damage level in the material prior to the final catastrophic failure event. Note that the failure of one single element is systematically accompanied by the failure of the whole material. Hence, full failure is achieved when at least one of its elements is fully broken. Moreover, the same procedure can be used to determine the corresponding critical loadings Δ_h and Δ_c from the numerical data and produce similar figures in terms of Δ.

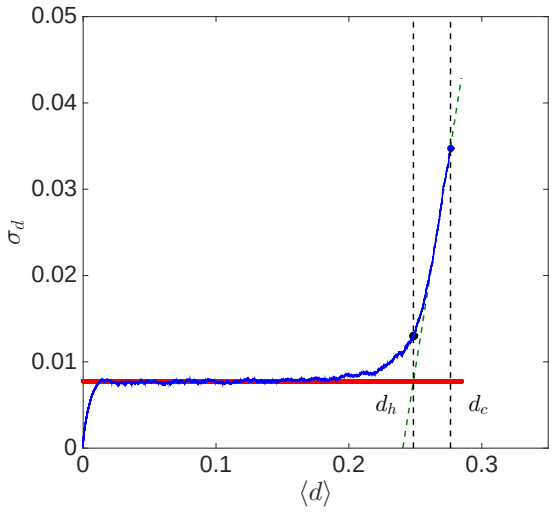

Figure 3.2: Methodology used to determine the onset $d_{\rm h}$ of the deviation to the homogeneous response: The typical fluctuations of the damage field, characterized by its standard deviation $\sigma_{\rm d}$ shows a sudden increase indicated by the black dot at the damage level $d_{\rm h}$. The catastrophic failure is indicated here by the blue dot and correspond to $d_{\rm c}$.

In Fig. 3.3 are shown the thresholds in terms of damage as a function of the normalized κ values, for two internal lengths $\ell_0 = 5$ and 10 and various disorder intensities σ_g. A first observation is that the values of the thresholds depend weakly on the material disorder: low variations of $d_{\rm h}$ and $d_{\rm c}$ are observed while the fluctuation amplitude σ_g of fracture energy is varied from 0.1 % to 20 % of its average value. Another interesting observation is that the critical damage levels are rather independent of the internal length scale ℓ_0. The material response is essentially governed by the value of κ and two distinct regimes emerge:

– (i) for $\kappa \leq \kappa_{\rm c}$, catastrophic failure takes place at the snack-back instability ($d_{\rm c} \simeq d_{\rm sb}$),

and is not preceded by a phase where the response of the material deviates from the homogeneous material behavior.

– (ii) for $\kappa > \kappa_c$, the thresholds strongly depend on the shape of the redistribution function. A careful comparison between Fig. 3.3(a) and (b) reveals that the deviation to the homogeneous response takes place close, but prior to complete failure ($d_h \lesssim d_c < d_{sb}$). In this regime, failure occurs earlier when the value of κ is increased, taking place even before peak load for $\kappa \gtrsim 3\kappa_c$.

As will be shown, the same behaviors are obtained in terms of critical displacement.

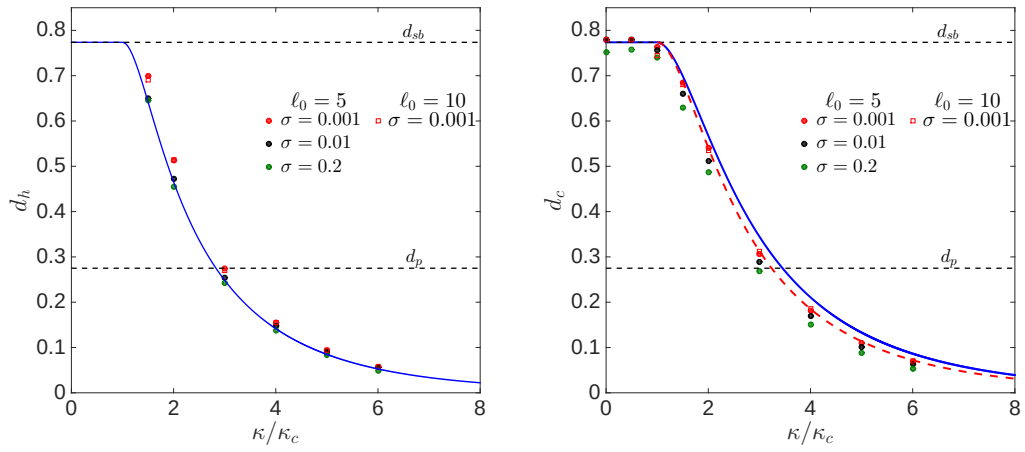

(a) (b)

Figure 3.3: Effect of the interaction function on localization and failure: (a) Variations of the localization threshold d_h as a deviation from the homogeneous material response with the interaction parameter κ; (b) Variations of the failure threshold d_c with κ. Dots and squares correspond to internal lengths $\ell_0 = 5$ and $\ell_0 = 10$, respectively, for different disorder levels σ_g. The position of the snap-back d_{sb} and peak force d_p for the interaction-free system are indicated by horizontal dashed lines. The solid and dotted lines correspond to the analytical predictions made from the stability analysis of Sec. 3.2.1 and the energy minimization of Sec. 3.3, respectively.

3.1.3 Damage field spatial organization

To further characterize the behavior of the heterogeneous system, we now explore the spatial structure of the damage field as the loading brings the material towards complete failure. We define the distance to failure as:

$$\delta = \frac{\Delta_c - \Delta}{\Delta_c - \Delta_{el}} \tag{3.2}$$

where Δ_{el} is the loading at the end of the elastic regime, where the first damage event takes place. This parameter δ ranges from unity at the end of the elastic regime to zero at catastrophic failure.

The power spectrum

$$P_\delta(q) = \frac{|\tilde{d}_\delta(q)|^2}{N} \tag{3.3}$$

is computed at different distance δ from failure. Here, $\tilde{d}_\delta(q)$ is the Fourier transform of the damage field and q is the Fourier mode corresponding to the wavenumber $\lambda = 2\pi/q$. The power spectrum is used to characterize the spatial structure of the damage field and its evolution. If the damage fluctuations are random, all wavenumbers contribute equally and the power spectrum is flat. Instead, if damage develops favoring a certain mode, the spectrum exhibits a peak. A typical power spectrum evolution is shown in Fig. 3.4a for $\kappa = 2\kappa_c$ and $\ell_0 = 5$. As highlighted in the inset, far from failure ($\delta \gtrsim 0.3$), the power spectrum is fairly flat which indicates random fluctuations of the damage field. On the contrary, as the system gets closer to failure ($\delta \lesssim 0.05$), a peak emerges in the Fourier spectrum, indicating that damage spatially organizes and develops over the corresponding mode. This peak reveals the characteristic mode q_c that is defined from the peak of the power spectrum at $d = d_c$. Its amplification as $\delta \to 0$ suggests that a characteristic length scale $\frac{2\pi}{q_c}$ emerges from the damage spatial structure. This observation is consistent with the deviation from the homogeneous system response brought out in Fig. 3.1a close to failure.

Figure 3.4b shows the effect of κ on q_c for two values of the internal length, $\ell_0 = 5$ and $\ell_0 = 10$, and for a large range of disorder intensities, $0.001 \leq \sigma_g \leq 0.2$. The two regimes identified from the variations of the thresholds d_h and d_c with κ are also revealed by the value of the characteristic mode: for $\kappa \leq \kappa_c$, the power spectrum does not reveal any characteristic length scale whereas for $\kappa > \kappa_c$, the peak emerges and its position q_c increases with κ. Furthermore, the characteristic wavelength $\frac{2\pi}{q_c}$ increases linearly with the internal length ℓ_0.

3.1.4 Conclusions

In summary, the numerical investigation of the damage evolution in heterogeneous materials with interacting elements shows that their response can be captured by the homogeneous interaction-free material behavior up to some critical loading where the two responses deviate from each other, quickly followed by an abrupt failure. Both onsets can take a broad range of values, from the snap-back position to the pre-peak regime, depending on the value of the shape parameter κ of the interaction function. Two distinct regimes can be evidenced:

- For $\kappa \leq \kappa_c$, the damage field does not display a characteristic mode until unstable failure takes place close to the snap-back instability and without any deviation from the homogeneous system response.
- For $\kappa > \kappa_c$, we evidence a deviation to the homogeneous response, quickly followed by an abrupt failure. Evolution towards failure is characterized in this regime by the rapid growth of a characteristic mode in the damage field.

These observations call for the following questions: Can we explain the deviation and instability points and predict their onset? Where does the characteristic length scale of the damage field

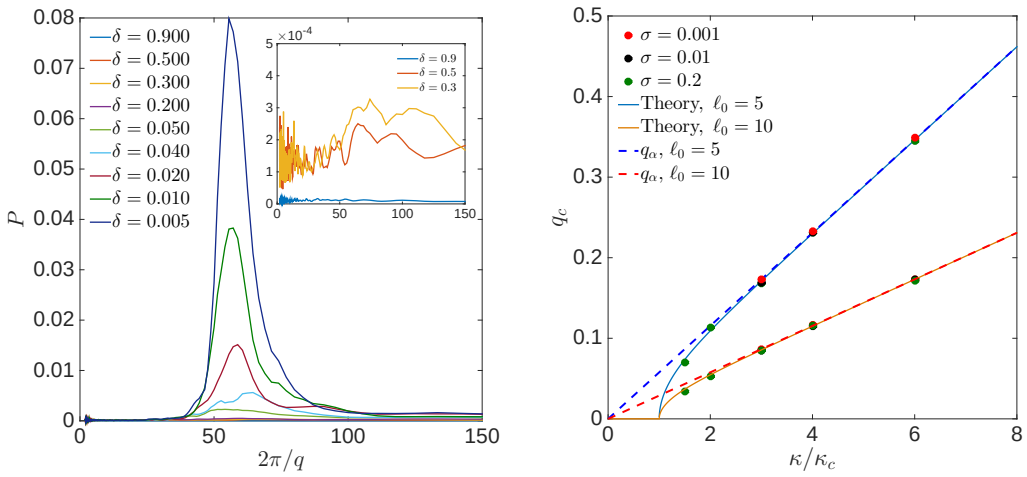

(a) (b)

Figure 3.4: (a) Evolution of the power spectrum of the damage field with the distance δ to failure showing the emergence of a peak of mode q_c as the system evolves towards fracture. The inset shows a zoom highlighting the far from failure regime $\delta \gtrsim 0.3$, for which all modes contribute equally; (b) Variations of the peak mode q_c with κ for different disorder levels σ and comparison with the analytical predictions (see Sec. 3.2.1). The corresponding mode $q_\alpha = \kappa/2\ell_0$ introduced in the interaction function expression is also shown in dashed lines, in blue for $\ell_0 = 5$ and red for $\ell_0 = 10$.

close to failure emerge from? What is the origin of the two regimes with distinct failure behaviors as the interaction function is varied?

3.2 Critical loadings prediction: linear stability analysis

3.2.1 Stability analysis of the homogeneous damage states

To address the questions raised by the numerical study, we carry out a stability analysis of the states reached by the *homogeneous* medium during its evolution. Here, we do not restrict our analysis to 1D media, and explore the stability of the homogeneous behaviors obtained in Sec. 2.2.1 for any dimension. At a given displacement Δ, we assume small variations of the damage field around a homogeneous value. We decompose it into two contributions: a uniform contribution d_0 close to the average damage level in the material and a heterogeneous contribution $\delta d(\vec{x})$

$$d(\vec{x}) = d_0 + \delta d(\vec{x}) \tag{3.4}$$

where δd is assumed very small with respect to d_0. To determine the evolution of the perturbation δd, the total damage driving force $\mathcal{F} = \bar{Y} - Y_c$ is also decomposed into two contributions

$$\mathcal{F}[d(\vec{x})] = \mathcal{F}^{(0)}(d_0) + \mathcal{F}^{(1)}[\delta d(\vec{x})] \tag{3.5}$$

where the constant term $\mathcal{F}^{(0)}$ is the contribution of the homogeneous part of the damage field while

the heterogeneous part of the driving force $\mathcal{F}^{(1)}$ results from the perturbation δd. The expression of each of these terms is determined by linearizing the expressions (2.6) and (2.17) of the non-local energy release rate and the fracture energy, respectively. The first step is to decompose the non-local damage parameter into two terms

$$\overline{d}(\vec{x}) = d_0 + (\alpha * \delta d)(\vec{x}) \tag{3.6}$$

which leads to the following expansion of the stiffness derivative

$$k'(d(\vec{x})) = k'(d_0) + k''(d_0)\overline{\delta d}(\vec{x}). \tag{3.7}$$

In this expression where only first order terms in δd have been kept, we have introduced the non-local perturbation parameter $\overline{\delta d}(\vec{x}) = (\alpha * \delta d)(\vec{x})$. Using Eq. (3.7) into Eq. (2.6), one obtains the first order expansion of the non-local energy release rate

$$\overline{Y}(\vec{x}) = Y(d_0) - \frac{\Delta^2}{2} k''(d_0)(\alpha * \overline{\delta d})(\vec{x}). \tag{3.8}$$

Since the fracture energy also decomposes into two contributions

$$Y_c(\vec{x}, d) = Y_c(d_0) + Y_{c0}\eta\delta d(\vec{x}), \tag{3.9}$$

one gets the zero and first order contributions of the total driving force

$$\begin{cases} \mathcal{F}^{(0)}(d_0) & = & Y(d_0) - Y_c(d_0) \\ \mathcal{F}^{(1)}[\delta d(\vec{x})] & = & -\dfrac{\Delta^2}{2} k''(d_0)(\alpha * \overline{\delta d})(\vec{x}) - Y_{c0}\eta\delta d(\vec{x}). \end{cases} \tag{3.10}$$

The zero order provides the equilibrium condition

$$\mathcal{F}^{(0)} = 0 \quad \Rightarrow \quad Y(d_0) = Y_c(d_0). \tag{3.11}$$

It corresponds to the evolution equation of the homogeneous medium obtained in Sec. 2.2.1. It gives the typical damage level $d_0(\Delta)$ in the material as a function of the external loading as given in Eq. (2.19).

We now focus on the perturbative term $\mathcal{F}^{(1)}$ of the driving force. Its expression provides physical insights on the weight function α introduced in the model definition. Assume that we have a perturbation of the damage field $\delta d(\vec{x}) \sim \delta(\vec{x} - \vec{x}_0)$, where $\delta(\vec{x})$ is the Dirac function, resulting from a damage event localized in $\vec{x}_0$. The perturbation on the driving force produced by this damage event can be deduced from Eq. (5.31) and follows $\mathcal{F}^{(1)}(r) \sim (\alpha * \alpha)(r)$ where $r = \|\vec{x} - \vec{x}_0\| > 0$ is the distance from the damaged element. For $\kappa = 0$, this term is positive. This means that a damage event in the medium is followed by an increase of the driving force everywhere else. On the contrary, for $\kappa > 0$, α and so $\mathcal{F}^{(1)}$ change of sign with r, indicating that some elements will be unloaded while some others will be loaded further. The detailed spatial structure of the load redistribution is actually set by the convolution of α with itself, which behaves qualitatively as the function α represented in

Fig. 2.3.

Therefore, the weight function α involved in the definition of the non-local quantities like the damage parameter $\overline{d}$ plays a central role in our model by describing how the driving force is redistributed in the medium after any failure event. If the non-local formulation of our damage model results in a load redistribution the sign of which may vary with the distance to the damaged element, the damaging element itself is always unloaded. Indeed, the sign of the load redistribution in $\vec{x}_0$ is provided by $\Delta^2|k''(\langle\Delta\rangle)|/2 - Y_{c0}\eta$ which is negative before the snap-back instability as shown by the instability criterion (2.21). This illustrates the key role played by the hardening behavior of the material that prevents unstable failure of individual elements before the snap-back point.

Localization prediction

We now use the expression of the driving force perturbation $\mathcal{F}^{(1)}[\delta d(\vec{x})]$ to determine the material stability. We consider perturbations with some periodicity of mode $\vec{q}_0$ and of positive amplitude δd_0. It takes the form

$$\delta d(\vec{x}) = \delta d_0 \cos(\vec{q}_0 \cdot \vec{x}) \tag{3.12}$$

Inserting this expression in Eq. (5.31) provides the driving force redistribution

$$\mathcal{F}^{(1)}[\delta d(\vec{x})] \quad = \quad \delta d_0 \cos(\vec{q}_0 \cdot \vec{x}) * \left(-\frac{\Delta^2}{2} k''(d_0)\alpha(\vec{x}) * \alpha(\vec{x}) - Y_{c0}\eta\delta(\vec{x}) \right) \tag{3.13}$$

as the homogeneous damage is increased by $\delta d(\vec{x})$. Since this expression comprises convolution products, it is more convenient to express it in Fourier space

$$\tilde{\mathcal{F}}^{(1)}[\tilde{\delta d}(\vec{q})] = \delta d_0 \delta(\vec{q} - \vec{q}_0) \times \left(-\frac{\Delta^2}{2} k''(d_0)\tilde{\alpha}^2(\vec{q}) - Y_{c0}\eta \right) \tag{3.14}$$

Introducing the function

$$\tilde{\mathcal{G}}(\vec{q}, d_0) = -\frac{1}{2}\Delta^2 k''(d_0)\tilde{\alpha}^2(\vec{q}) - Y_{c0}\eta, \tag{3.15}$$

where Δ is related to d_0 via Eq. (2.19), the driving force perturbation takes the simple form

$$\tilde{\mathcal{F}}^{(1)}[\tilde{\delta d}(\vec{q})] = \tilde{\mathcal{G}}(\vec{q}, d_0)\delta d_0 \delta(\vec{q} - \vec{q}_0) \tag{3.16}$$

Taking the inverse Fourier transform of this equation provides the driving force perturbation

$$\mathcal{F}^{(1)}[\delta d(\vec{x})] = \tilde{\mathcal{G}}(\vec{q}_0, d_0)\delta d_0 \cos(\vec{q}_0 \cdot \vec{x}) \tag{3.17}$$

It provides the condition for a homogeneous damage growth: if $\mathcal{F}^{(1)}(\vec{x})$ is higher at the most damaged zones, *i.e.* for $\vec{x}\cdot\vec{q}_0 = 0, \pm 2\pi, \pm 4\pi...$, the perturbation will grow and hence deviation from the homogeneous response will occur. At the opposite, if the driving force is higher on the elements with smaller damage levels, *i.e.* for $\vec{x}\cdot\vec{q}_0 = \pm\pi, \pm 3\pi...$, these elements will damage first and perturbations to the homogeneous damage field will be smoothed out. Using the above considerations, we conclude that

$$\tilde{\mathcal{G}}(\vec{q}_0, d_0) > 0 \quad \Rightarrow \quad \text{Damage localization.} \tag{3.18}$$

In the following, we refer to this process as *damage localization*, since it results into a concentration of the failure processes in some regions of the material. This condition is satisfied above a critical value of the imposed displacement, or equivalently above some critical level of damage, for the most unstable mode $\vec{q}_c$ that maximizes $\tilde{\alpha}$. Indeed, according to Eq. (3.15), the position $\vec{q}_c$ of the maximum of $\tilde{\mathcal{G}}(\vec{q}_0, d_0)$ is also the one of $\tilde{\alpha}$, irrespective of the typical damage level d_0. At some critical damage level d_h (resp. some critical loading Δ_h), the function $\tilde{\mathcal{G}}$, which increases with d_0 (resp. Δ), hits zero at $\vec{q}_0 = \vec{q}_c$. The perturbation then grows and leads to an heterogeneous damage field with a characteristic mode $\vec{q}_\mathrm{c}$. On the force-displacement response, one expects this damage localization to produce a departure from the homogeneous material behavior of Eq. (2.19).

Failure prediction

If the condition (3.18) predicts the emergence of growing heterogeneous modes in the damage field, it does not predict the abrupt failure observed in the simulations. To determine the critical loading at which it takes place, one must consider a slightly modified expression of $\delta d(\vec{x})$

$$\delta d(\vec{x}) = \delta d_0 \left(1 + \cos(q_0 \cdot \vec{x})\right) \tag{3.19}$$

While the expression of Eq. (3.12) allowed for damage decrease, describing healing processes of the material, this expression ensures the irreversibility condition $\delta d \geq 0$ imposed to the damage evolution. This expression leads to the heterogeneous damage driving force contribution written as

$$\mathcal{F}^{(1)}[\delta d(\vec{x})] = \delta d_0 \left(\tilde{\mathcal{G}}(\vec{q}_0, d_0)\cos(\vec{q}_0 \cdot \vec{x}) + \tilde{\mathcal{G}}(\vec{0}, d_0)\right). \tag{3.20}$$

where the normalization condition on the interaction function which leads to $\tilde{\alpha}(\vec{0}) = 1$ was used.

As we now consider that the perturbation of mode $\vec{q}_c$ grows, so that in the following $\vec{q}_0$ is replaced by $\vec{q}_c$, we determine its stability in the following way: unstable failure requires an increase of the damage somewhere in the medium to be accompanied by an increase of the driving force at the same location. In other words, for a damage increment $\delta d(\vec{x}) = \delta d_0(1 + \cos(\vec{q}_c \cdot \vec{x}))$ positive in $\vec{x}\cdot\vec{q}_c = 0, \pm 2\pi...$, catastrophic failure takes place if $\mathcal{F}^{(1)}(\vec{x})$ is also positive at these points. It leads to

the instability condition written as

$$\tilde{\mathcal{G}}(\vec{q}_c, d_0) + \tilde{\mathcal{G}}(\vec{0}, d_0) > 0 \quad \Rightarrow \quad \text{Unstable failure.} \tag{3.21}$$

Similarly to the localization criterion, the condition for unstable failure is satisfied at some critical damage level d_c (resp. some critical loading Δ_c) for the most unstable mode $\vec{q}_c$ at which the perturbation started to develop at $d = d_\mathrm{h}$.

Note that if the unstable mode is not the homogeneous mode ($\vec{q}_c = \vec{0}$) then it means that when the localization criterion is reached ($\tilde{\mathcal{G}}(\vec{q}_c, d_\mathrm{h}) = 0$) the function $\tilde{\mathcal{G}}(\vec{0}, d_\mathrm{h})$ is still negative. This ensures that localization takes place *prior* to abrupt failure. Moreover, as for all loadings and damage levels the function is higher at $\vec{q}_c$ than at mode $\vec{q} = \vec{0}$, it means that the failure criterion of Eq. (3.21) will necessarily be verified at a damage level d_c lower than the critical level at which the homogeneous system snap-back instability takes place. Hence, if $\vec{q}_c \neq \vec{0}$, the system behaviors verifies $d_\mathrm{h} < d_\mathrm{c} < d_\mathrm{sb}$, or respectively $\Delta_\mathrm{h} < \Delta_\mathrm{c} < \Delta_\mathrm{sb}$.

An important point is that, contrary to the localization prediction, the onset of failure determined from Eq. (3.21) predicts only approximately the actual failure threshold, even in the limit of weakly heterogeneous media. Indeed, this criterion is derived from a perturbation of the *homogeneous* material response, hence assuming a homogeneous distribution of damage in the medium. Since localization might take place prior to final failure, damage might be distributed heterogeneously when unstable failure takes place. We will see that the predictions derived from Eq. (3.21) are rather good as long as κ is not too large with respect to κ_c, *i.e.* that localization does not occur much earlier than failure, so that the assumption of a relatively homogeneous damage field is not strongly violated.

Therefore, the investigation of the material behavior close to the homogeneous systems response allows for predictions of the onset of localization and failure that will be compared with the simulation results in the following section. As a summary, from criteria (3.18) and (3.21), two cases were identified for the system behavior:

- The most unstable mode corresponds to a homogeneous perturbation $\vec{q}_\mathrm{c} = \vec{0}$. Both criteria are then equivalent, and damage localization is simultaneously accompanied by unstable failure. In that case, catastrophic failure takes place without any prior deviation from the homogeneous material response. In addition, the onset of failure is similar to the one of the homogeneous system given in Eq. (2.24) and corresponds to the snap-back instability evidenced on Fig. 2.4. This behavior is thus characterized by $d_\mathrm{h} = d_\mathrm{c} = d_\mathrm{sb}$.
- The most unstable mode $\vec{q}_\mathrm{c}$ that maximizes the function $\tilde{\alpha}$ is different from the homogeneous mode $\vec{q} = \vec{0}$. This translates into $\tilde{\alpha}(q_\mathrm{c}) > \tilde{\alpha}(0)$ from which one deduces, using the expression (3.15) of $\tilde{\mathcal{G}}(\vec{q}_0, \Delta)$, that localization is strictly anterior to abrupt failure and that both occur before the snap-back instability of the homogeneous system. Therefore, this regime is characterized by the growth of heterogeneous modes of damage followed by an abrupt failure, leading to $d_\mathrm{h} < d_\mathrm{c} < d_\mathrm{sb}$.

3.2.2 Application to 1D media

We now test the relevancy of the analysis performed in the previous section by comparing its predictions with the numerical results of Sec. 3.1. We focus first on 1D media for which all calculations can be performed analytically. The first step is the determination of the critical mode that maximizes $\tilde{\mathcal{G}}(q, d_0)$. According to Eq. (3.15), this amounts to determine the maximum of $\tilde{\alpha}(q)$. Taking the Fourier transform

$$\tilde{\alpha}(q) = \int_{-\infty}^{+\infty} \exp(-iqr)\alpha(x)dx \tag{3.22}$$

of the weight function α given in Eq. (2.13), one obtains

$$\tilde{\alpha}(q) = \frac{(1+\kappa^2)(1+\kappa^2+(2\ell_0 q)^2)}{(\kappa^2+1)^2+2(2\ell_0 q)^2(1-\kappa^2)+(2\ell_0 q)^4}. \tag{3.23}$$

The function $\tilde{\mathcal{G}}(q, d_0)$ is shown on Fig. 3.5 as a function of q/q_c at different damage levels for the parameter values $\kappa = 2\kappa_c$, $\ell_0 = 5$ and $\eta = 8$ for which $q_c \simeq \dfrac{0.55}{\ell_0}$. As expected, one sees that the location q_c of the maximum does not change as the average damage increases. On the contrary, the maximum value $\tilde{\mathcal{G}}(q_c, d_0)$ of the function increases and eventually hits zero at the critical damage level $d_h \simeq 0.466$.

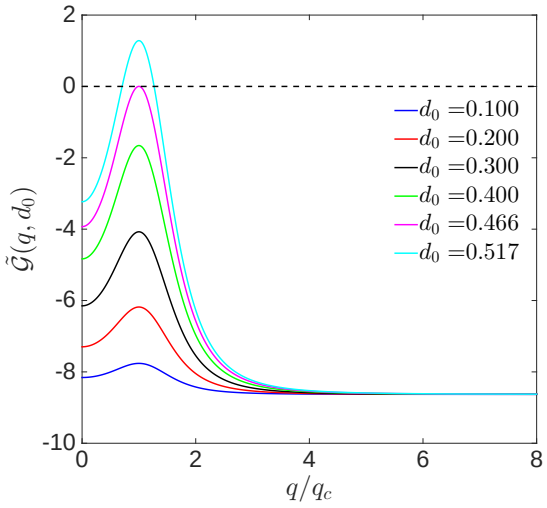

Figure 3.5: Prediction of the localization for a 1D medium with $\kappa = 2\kappa_c$, $\ell_0 = 5$ and $\eta = 8$. This graph shows the amplitude of the driving force perturbation for a sinusoidal perturbation of mode q of the damage field (Eq. (3.15)). Growing modes correspond to positive amplitude, so localization takes place at the damage level $d_0 \simeq 0.466$ for the mode q_c given in Eq. (3.24).

From the analysis of the function $\tilde{\alpha}$, one extracts the critical value $\kappa_c = 1/\sqrt{3}$ that distinguishes two different behaviors:

– For $\kappa \leq \kappa_c$, the Fourier transform of the weight function is maximum for $q_c = 0$ and hence $\tilde{\alpha}(q_c) = 1$.

– For $\kappa > \kappa_c$, the maximum is reached for $q_c > 0$ which follows

$$q_c = \frac{1}{2\ell_0}\sqrt{2\kappa\sqrt{1+\kappa^2} - (1+\kappa^2)}. \tag{3.24}$$

The criterion $\tilde{\mathcal{G}}(q_c, d_h) = 0$ of Eq. (3.18) provides the critical damage level at localization (or equivalently the loading Δ_h at localization using Eq. (2.19)). Inserting the expression of the stiffness Eq. (2.11) with exponent $\gamma = 3$ into the expression of $\tilde{\mathcal{G}}(q,d)$ given in Eq. (3.15) we obtain

$$d_h = \frac{1}{\eta}\frac{\tilde{\alpha}^2(q_c)}{2\tilde{\alpha}^2(q_c)-1}\left(\sqrt{1-\eta^2\frac{2\tilde{\alpha}^2(q_c)-1}{\tilde{\alpha}^4(q_c)}\frac{1+a}{3a}}-1\right) \tag{3.25}$$

$$\text{with}\begin{cases} \tilde{\alpha}(q_c) &= \dfrac{(1+\kappa^2)^{3/2}}{4\kappa(1+\kappa^2-\kappa\sqrt{1+\kappa^2})} \quad \text{for} \quad \kappa > \kappa_c \\ \tilde{\alpha}(q_c) &= \tilde{\alpha}(0) = 1 \qquad\qquad\qquad\quad \text{for} \quad \kappa \leq \kappa_c. \end{cases} \tag{3.26}$$

For $\kappa \leq \kappa_c$, the onset d_h becomes independent of the shape of the redistribution function and the parameters ℓ_0 and κ. This is in agreement with the conclusions drawn in Sec. 3.2.1 where the condition $q_c = 0$ ensures that localization takes place at the snap-back position $d_h = d_{sb}$ that is independent of α (Eq. (2.24)). On the contrary, for $\kappa > \kappa_c$ the most unstable mode $q_c > 0$ is not homogeneous, and the shape of the redistribution function affects the onset d_h of heterogeneous damage growth through the parameter κ. The internal length ℓ introduced in the interaction function sets the wavelength of the unstable mode $\dfrac{1}{q_c} \sim \ell_0$, but does not affect the localization threshold. The introduction of an internal length in the redistribution function reflects on the characteristic wavevector of the instability and hence sets the width of the 'localization bands' emerging close to failure. This result is rather natural since all the other length scales introduced in the model, the heterogeneity size ξ_h and the sample size L, do not play any role on the stability of the homogeneous material response.

Note that from the expression of $\tilde{\mathcal{G}}$ given in Eq. (3.15), if the stiffness parameter γ equals to 0 or 1 the second derivative is null. Hence, $\tilde{\mathcal{G}}(\vec{q_0}, d_0) = -Y_{c0}\eta$ is negative. The same is true for all γ exponents values if the stiffness parameter a is positive: in that case, the second derivative of the stiffness is always positive and therefore the function $\tilde{\mathcal{G}}$ is also negative for all loadings and damage level. Therefore, no localization can be obtained in these cases and the response of the system follows that of the homogeneous material system up to its failure threshold, which is in that case $d_0 = 1$ as no snap-back instability take place in that case (see Sec. 2.2.1).

The analytical predictions can be compared to the numerical results. Figure 3.3(a) shows the variations of the localization threshold d_h with κ (solid line). The theory captures nicely its decay in the regime $\kappa > \kappa_c$, irrespective of the disorder amplitude. [1].

In Fig. 3.4(b), the comparison made between the wavenumber q_c of the growing mode for two values of the internal length ℓ_0 and several disorder levels is also successful, confirming especially

1. For $\kappa \leq \kappa_c$, we could not identify the localization threshold in the simulations using the definition given in Fig. 3.2 since catastrophic failure occurs without prior deviation to the homogeneous material response

the scaling $q_c \sim \frac{1}{\ell_0}$. The predictions are also compared to the periodicity introduced in the interaction function expression (dashed lines). Indeed, we have

$$\alpha(x) = \exp\left(-\frac{|x|}{2\ell_0}\right)\cos\left(q_\alpha|x|\right) \tag{3.27}$$

where $q_\alpha = \kappa/2\ell_0$. Interestingly, the characteristic mode q_c of the unstable mode *is not* equal to the mode of the redistribution kernel: q_c is much larger than q_α for shape parameter $\kappa \preceq \kappa_c$, while it tends asymptotically towards q_α as $\kappa >> \kappa_c$. This behavior is a signature of a transition from a load redistribution dominated by the exponential term of the interaction function α at low κ values, to a redistribution dominated by its sinusoidal variations at large κ values. The value of κ_c can therefore be interpreted as the transition point between both behaviors.

We now focus on the prediction of the catastrophic failure. To determine d_c, the failure criterion $\tilde{\mathcal{G}}(q_c, d_c) + \tilde{\mathcal{G}}(0, d_c) = 0$ of Eq. (3.21) is applied using the critical mode q_c determined in Eq. (3.24). This gives

$$d_c = \frac{1+\tilde{\alpha}^2(q_c)}{2\eta\tilde{\alpha}^2(q_c)}\left(\sqrt{1-\frac{1+a}{3a}\left(\frac{2\eta\tilde{\alpha}(q_c)}{1+\tilde{\alpha}^2(q_c)}\right)^2}-1\right) \tag{3.28}$$

where the expression of $\tilde{\alpha}(q_c)$ is given in Eq. (3.26). If $\kappa \leq \kappa_c$, we verify that $d_c = d_h = d_{sb}$ ($\Delta_c = \Delta_h = \Delta_{sb}$) as expected from Sec. 3.2.1. In that case, perturbation growth and unstable failure occur simultaneously at the instability point of the interaction-free material. In the other regime, when $\kappa > \kappa_c$, we obtain $d_h < d_c < d_{sb}$ ($\Delta_h < \Delta_c < \Delta_{sb}$), in agreement with the analysis performed for any dimension in Sec. 3.2.1. Here, the damage field becomes heterogeneous with a characteristic mode q_c when the damage level reaches d_h and grows in a stable manner up to d_c.

The predicted failure threshold is shown in solid line in Fig. 3.3(b) and compared with the simulations results. The equation (3.28) slightly overestimates the onset of failure, in particular for $\kappa \gg \kappa_c$. This was expected since the theory relies on a perturbation analysis close to a *homogeneous* damage state, while localization already took place when the failure threshold is reached. Nevertheless, we note that this approach captures qualitatively well the behavior observed in the simulations, and in particular the decrease of d_c with the interaction parameter κ. An improved criterion for failure relying on a global energy minimization will be provided in Sec. 3.3.

3.2.3 Application to 2D media

We now apply the theoretical developments of Sec. 3.2.1 to the prediction of the failure behavior of 2D systems. We shall use the criteria derived in Eqs. (3.18) and (3.21) for localization and failure, which involve the Fourier transform of the interaction function. Since $\alpha(\vec{x}) = \alpha(r)$ is a function of the distance $r = \|\vec{x}\|$, $\tilde{\alpha}(\vec{q}) = \tilde{\alpha}(q)$ is a function of the norm $q = \|\vec{q}\|$ of the wavenumber. Hence, the stability analysis of a 2D medium reduces to a 1D problem where all the perturbation

modes with the same norm q_0 have the same effect on the system stability. The localization and failure thresholds are determined following a two steps procedure:

(i) The norm q_c of the most unstable modes is determined from the maximum of $\tilde{\mathcal{G}}(q_0, d_0)$. According to Eq. (3.15), this amounts to determine the maximum of the Fourier transform of the interaction function $\tilde{\alpha}(\vec{q}) = \iint_{-\infty}^{+\infty} \alpha(\vec{x}) e^{-i\vec{q}.\vec{x}} d\vec{x}$. Using the isotropy $\alpha(\vec{x}) = \alpha(r)$ of the interaction function, the Ankel transform gives $\tilde{\alpha}(q) = 2\pi \int_0^{+\infty} \alpha(r) J_0(qr) r dr$ where J_0 is the Bessel function of the first kind of order zero. This integral is computed numerically to determine its maximum $\tilde{\alpha}(q_c)$ and the norm q_c of the unstable modes.

(ii) From the values of q_c and $\tilde{\alpha}(q_c)$ calculated numerically, the critical damage levels for localization and failure are determined from the criteria $\tilde{\mathcal{G}}(q_c, d_h) = 0$ and $\tilde{\mathcal{G}}(q_c, d_c) + \tilde{\mathcal{G}}(0, d_c) = 0$, respectively. Since the function $\tilde{\mathcal{G}}$ introduced in Eq. (3.15) depends on the dimension of the system only through $\tilde{\alpha}(q)$, the expressions (3.25) and (3.28) of both thresholds remain unchanged.

This procedure is applied for different values of κ and $a = -0.3$. Note that in 2D media, the normalization constant α_0 of Eq. (2.6) is non-negative only for $\kappa < 1$. Above this upper bound the redistributions become non-physical and hence we limit our analysis to the range $[0, 1[$. The obtained variations of the critical wavenumber q_c with the shape parameter κ of the redistribution function are represented in Fig. 3.6a. [2] As for 1D media, one obtains two regimes: For $\kappa \leq \kappa_c^{2D}$ where $\kappa_c^{2D} \simeq 0.42$, the critical mode is the homogeneous perturbation $q_c = 0$ while for $\kappa > \kappa_c^{2D}$, the norm q_c of the critical wavevectors increases continuously with the parameter κ.

The critical damage values for localization (solid line) and failure (dashed line) derived from these critical perturbation modes are represented as a function of κ in Fig. 3.6b for a toughening parameter $\eta = 8$. Similarly to 1D systems, we observe a transition from a response similar to the one of a homogeneous interaction free material for low values of κ, to another regime where the deviation to the homogeneous material response is observed prior to catastrophic failure. The later intervenes prior to the snap-back instability observed in the homogeneous system response, resulting in $d_h < d_c < d_{sb} \simeq 0.78$.

These theoretical predictions are now compared with direct numerical simulations of the damage spreading in 2D systems with $\eta = 8$ following the procedure described in Sec. 3.1. Irrespective of the value of the disorder level σ_g, the theory captures well the decrease of the localization threshold d_h with κ shown by dot symbols on Fig. 3.6b. The decrease of the failure threshold d_c (cross symbols) is also described, but only qualitatively for the same reasons invoked in the former section in the context of 1D media.

2. Since the interaction function writes as $\alpha(\frac{r}{\ell_0})$, its Fourier transform writes as $\tilde{\alpha}(\ell_0 q)$, so the normalized quantity $\ell_0 q_c$ is naturally used on Fig. 3.6(a).

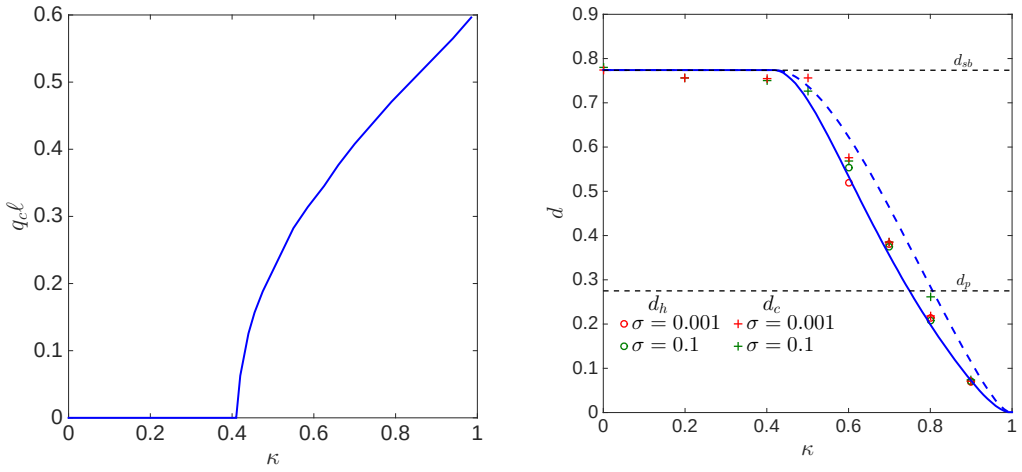

(a) (b)

Figure 3.6: Failure behavior of 2D media: (a) Evolution of the norm q_c of the critical wavevector as a function of the shape parameter κ of the interaction function; (b) Variations of the thresholds for heterogeneous damage growth d_h (circle) and failure d_c (cross) as a function of κ for $\eta = 8$ and different disorder levels σ_g.

If failure behaviors are qualitatively similar in 1D and 2D systems, we would like however to emphasize some quantitative differences. First, the threshold value $\kappa_c^{2D} \simeq 0.43$ in 2D is significantly smaller than its value in 1D for which $\kappa_c^{1D} = \dfrac{1}{\sqrt{3}} \simeq 0.58$. Second, the critical damage values for both localization and failure go to zero for $\kappa = 1$, whereas in 1D these quantities would tend to zero only as κ goes to infinity. This corresponds to a rapid failure $d_h = d_c \simeq 0$ after the elastic regime that is also obtained for other material parameter, namely non-hardening $\eta = 0$ materials, regardless of the shape of the interaction function.

The decrease of the failure threshold with κ is a general feature of the elasto-damageable medium considered here, irrespective of its dimension D (see Figs. 3.3 and 3.6b). This behavior might be counter-intuitive since large κ values result in unloading over an extended region of the material after failure events, while $\kappa = 0$ produces only reloading (see Fig. 2.3). However, this unloading is also accompanied by a larger load redistribution over some localized regions, which favors the build up of an unstable failure mode. Indeed, it is the redistribution function of periodicity q_α that structures the damage field over some material zones where damage can rapidly accumulate.

The variations of the failure threshold with the interaction parameter κ also reflect this transition: at low κ values, the load redistribution is essentially exponential. As a result, the most unstable mode corresponds to $q = 0$ that maximizes $\tilde{\alpha}(q)$ and failure takes place at the snap-back instability. The snap back point corresponds to an upper limit of the failure onset and reflects the failure resistance of an individual element or the one of an interaction free material. However, failure can be accelerated because of collective effects allowed by interactions within the material. Indeed, large κ values,

for which the load redistribution is essentially sinusoidal, favors a damage accumulation over some elements only. This might control the integrity of the whole material instead of sharing the applied load over all the elements. In the case of a localized damage, the failure of elements over which the load redistribution is more intense results in an earlier catastrophic failure of the material. Hence, in our model the interactions have a clear *detrimental* incidence on the resistance of the material, since it allows failure to take place much earlier than the snap-back point. We believe that this observation reflects a general feature of the failure behavior of materials as the actual failure threshold of solids is systematically *lower* than the one of the individual elements like atomic bonds due to emergence of cracks, localization bands, etc.

3.3 Critical damage at failure: global energy minimization

We now explore an alternative approach to predict the localization and failure thresholds of the elasto-damageable materials studied here. In the previous section, we performed a stability analysis of the damaged medium based on the distribution of *local* damage driving force. This allowed us to determine the unstable mode q_c over which damage field heterogeneities develop and the critical damage level at which this mode starts to grow. Assuming that the damage distribution remains close to the homogeneous state, solution of the equation $Y(d_0) = Y_c(d_0)$, even after damage localization, we have also determined the critical damage level at which the full system fails. Despite this rather rough approximation, our predictions provided a correct estimate of the failure threshold.

However, in an attempt to provide a better assessment of the failure threshold, we propose here a complementary approach based on the minimization of the total energy of the damaged media. Here, we take advantage of our damage model formulation based on energy consideration. The approach consists in assuming that, at a given applied displacement Δ, the damage field takes a certain shape, either given by Eq. (3.12) or Eq. (3.19), and determine the set of solutions $(d_0, \delta d_0)$ for which the energy is minimum. Only the *admissible* solutions are considered: both d_0 and δd_0 must be positive, increasing functions of Δ, otherwise the solution is not taken into account. Unlike for the linear stability analysis where the homogeneous solution (2.19) is used, no relationship is here assumed between the applied loading and the homogeneous contribution of the damage field. As will be shown in this section, the same localization criterion is obtained, whereas the failure prediction shows a better agreement with the numerical results. For the sake of simplicity, to perform this minimization we limit our study to the case of $1D$ systems.

3.3.1 Before localization: Prediction of the homogeneous material evolution and its loss of stability

The energy of the system corresponds to the total energy of Eq. (2.4) where we neglect the term of external work. This amounts to seek for the damage distribution $d(x)$ that minimizes the

energy stored in the material in elastic and damage energy at some fixed loading condition. Using

$$\overline{d}(x) = d_0 + \delta d_0 \tilde{\alpha}(q_0)\cos(q_0 x), \tag{3.29}$$

and again assuming a weakly heterogeneous damage field, expressed as $d(x) = d_0 + \delta d_0 \cos(q_0 x)$ corresponding to the homogeneous damage perturbation given by Eq. (3.12), the energy of the system can be expressed as

$$\frac{E_\Delta(d_0, \delta d_0)}{L} = \frac{1}{2}\Delta^2 k(d_0) + Y_{c0}\left(d_0 + \frac{1}{2}\eta d_0^2\right) + \delta d_0^2\left(\frac{1}{8}\Delta^2 k''(d_0)\tilde{\alpha}^2(q_0) + \frac{1}{4}Y_{c0}\eta\right) \tag{3.30}$$

If the values $(d_0, \delta d_0)$ are minimizing the total energy, they must satisfy the system of equations

$$\left.\frac{\partial E_\Delta}{\partial d_0}\right|_{\delta d_0} = 0 \tag{3.31a}$$

$$\left.\frac{\partial E_\Delta}{\partial \delta d_0}\right|_{d_0} = 0 \tag{3.31b}$$

which leads to the system of equations

$$\frac{1}{2}\Delta^2 k'(d_0) + Y_{c0}(1+\eta d_0) + \delta d_0 \frac{1}{8}\Delta^2 k'''(d_0)\tilde{\alpha}^2(q_0) = 0 \tag{3.32a}$$

$$\delta d_0\left(\frac{1}{4}\Delta^2 k''(d_0)\tilde{\alpha}^2(q_0) + \frac{1}{2}Y_{c0}\eta\right) = 0 \tag{3.32b}$$

from which one identifies the only admissible solution as long as $\Delta < \Delta_h$: the homogeneous behavior where $\delta d_0 = 0$ and $d_0 = d^h$. d^h denotes the homogeneous solution and is set by $\frac{1}{2}\Delta^2 k'(d_0) + Y_{c0}(1+\eta d_0) = 0$, corresponding to the relationship Eq. (2.19). An example of energy field is shown on Fig. 3.7a for an applied displacement above Δ_{el} and lower than Δ_h. The energy is normalized by its minimum value and shown as a function of both d_0 and δd_0. We see that in that case, the location of the energy minimum indicated by a red dot indeed correspond to the homogeneous solution with $\delta d_0 = 0$.

The signs of the second partial derivatives of the energy with respect to d_0 and δd_0 give the localization criterion. Indeed, they must both be positive for the homogeneous solution to minimize the energy of the system

$$\left.\frac{\partial^2 E_\Delta}{\partial d_0^2}\right|_{\delta d_0 = 0}(d^h, 0) = \frac{1}{2}\Delta^2 k''(d^h) + Y_{c0}\eta = -\tilde{\mathcal{G}}(0,\Delta) > 0 \tag{3.33a}$$

$$\left.\frac{\partial^2 E_\Delta}{\partial \delta d_0^2}\right|_{d_0}(d^h, 0) = \frac{1}{4}\Delta^2 k''(d^h)\tilde{\alpha}^2(q_0) + \frac{1}{2}Y_{c0}\eta = -\frac{1}{2}\tilde{\mathcal{G}}(q_0,\Delta) > 0 \tag{3.33b}$$

where $\tilde{\mathcal{G}}$ is given by Eq. (3.15). Therefore, from the homogeneous solution arises a local minimum of the energy as long as these two conditions are verified. As from the linear stability analysis, we see that

- if $\kappa \leq \kappa_c$, the function $\tilde{\mathcal{G}}(q_0, \Delta)$ is maximized for the homogeneous mode $q_c = 0$. Hence, both inequalities will stop being verified for $\tilde{\mathcal{G}}(0, \Delta) = 0$. As described in the previous section, it corresponds to the snap-back instability condition of the homogeneous system. Hence, we predict damage localization at a critical damage level $d_h = d_{sb}$, corresponding to a loading $\Delta_h = \Delta_{sb}$.
- if $\kappa > \kappa_c$, the critical mode $q_c \neq 0$ that minimizes the total energy is given by Eq. (3.24). As a result, the inequalities are verified up to the critical damage level $d_h < d_{sb}$, given by Eq. (3.25) that corresponds to the loading $\Delta_h < \Delta_{sb}$.

Figure 3.7b shows the change of curvature sign of the total energy as the loading Δ increases for $\kappa \leq \kappa_c$. The energy is represented for $d_0 = d^h$ as a function of δd_0 and is normalized by its value in $(d^h, 0)$. For loadings smaller than Δ_h, the energy field displays a sink for $\delta d_0 = 0$: The homogeneous solution minimizes the energy and hence the damage field remains homogeneous as any perturbation will be smoothed out since not energically favorable. As $\Delta \geq \Delta_h$, the curvature is inverted: The homogeneous solution becomes unstable, and hence damage will grow dramatically. Hence, for $\kappa \leq \kappa_c$, failure can actually be interpreted as an instability resulting from the loss of any equilibrium stable position.

Therefore, both the stability analysis and global energy minimization lead to the same localization criterion given by Eq. (3.18) or (3.33b). Note that from the expression of the energy given by Eq. (3.30) one could easily foresee the localization criterion: The prefactor of δd_0 becomes negative when $\tilde{\mathcal{G}}(q_0, \Delta)$ is positive where it hence becomes energetically favorable to increase δd_0.

3.3.2 After localization: Failure prediction

To determine the critical loading at failure, we now consider an applied loading $\Delta > \Delta_h$ and the growth of the perturbation of mode $q_c > 0$. Thus we replace q_0 by q_c in the following expressions. We consider here only the case $\kappa > \kappa_c$ that display a stable post-localization regime, the case $\kappa \leq \kappa_c$ leading to catastrophic failure at $\Delta = \Delta_h$ as illustrated in Fig. 3.7. We must again consider a damage expression that satisfies the condition $\dot{\delta d} \geq 0$, so that in the following we consider a damage field of the form $d(x) = d_0 + \delta d_0(1 + \cos(q_c x))$ as given by Eq. (3.19). In that case, the energy of the system is of the form

$$E_\Delta(d_0, \delta d_0) = A(d_0) - B(d_0)\delta d_0 + C(d_0)\delta d_0^2 - D(d_0)\delta d_0^3 \tag{3.34}$$

where, using the stiffness expression (2.11) with $\gamma = 3$:

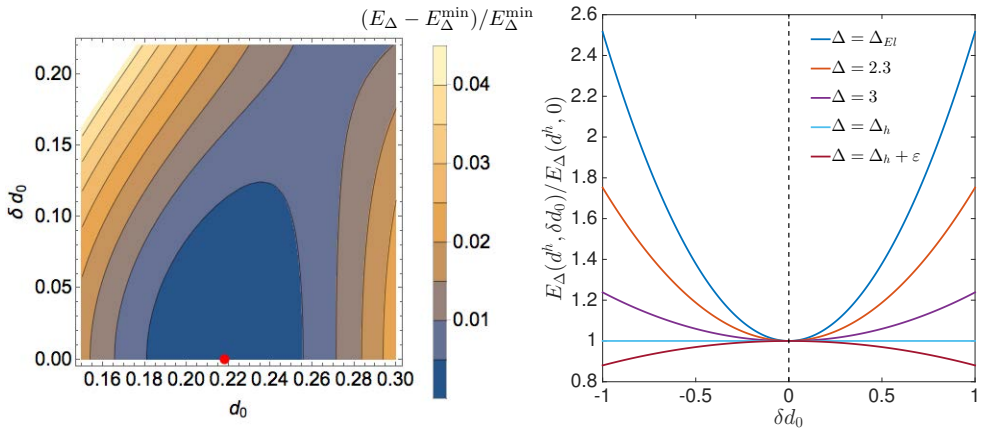

(a) (b)

Figure 3.7: (a) Energy landscape $E_\Delta(d_0, \delta d_0)$ of the damaged material as given by Eq. (3.30) before localization. The minimum, indicated by a red dot, is obtained for $(d_0, \delta d_0) = (d^h, 0)$. The corresponding energy value $E_\Delta^{\min}$ has been used to normalize E_Δ; (b) Variations of the total energy of the material as a function of δd_0 at different applied loadings for $\kappa \leq \kappa_{\mathbf{c}}$.The average damage level is set to $d_0 = d^h$ that is solution of $Y(d_0) = Y_c(d_0)$. The total energy is normalized by its minimum value. Before localization, for $\Delta < \Delta_h$, the energy displays a minimum at the point $(d^h, 0)$, corresponding to the homogeneous solution. For $\Delta > \Delta_h$, the curvature changes of sign, indicating that the homogeneous solution is no longer a minimum and becomes unstable. This leads to unstable growth of the damage and catastrophic failure of the sample at $\Delta = \Delta_h = \Delta_{sb}$.

$$A(d_0) = \frac{1}{2}\Delta^2 k(d_0) + Y_{c0}(d_0 + \frac{1}{2}\eta d_0^2) \tag{3.35a}$$

$$B(d_0) = -\frac{1}{2}\Delta^2 k'(d_0) - Y_{c0}(1 + \eta d_0) \tag{3.35b}$$

$$C(d_0) = \frac{1}{4}\Delta^2 k''(d_0)\left(1 + \frac{\tilde{\alpha}^2(q_c)}{2}\right) + \frac{3}{4}Y_{c0}\eta \tag{3.35c}$$

$$D(d_0) = -\frac{1}{4}\Delta^2 k'''(d_0)\left(\frac{1}{3} + \frac{\tilde{\alpha}^2(q_c)}{2}\right) \tag{3.35d}$$

The equilibrium positions are again determined at fixed displacement by solving the system of equation (3.31). The homogeneous solution satisfies this set of equations, however, as shown in the previous section for $\Delta \geq \Delta_h$ the energy does not have a minimum at that point. Hence, we shall now study the heterogeneous solution of the system. Note that the difficulty in this post-localization regime is that the damage level $d_0^{\min}$ that minimizes the total energy is different from the solution d_0^h of the homogeneous problem. As a result, it must be deduced from the energy minimization procedure, together with the value of $\delta d_0^{\min}$. This last quantity is determined first as a function of Δ and d_0^{min} by solving Eq. (3.31b)

$$\delta d_0^{\min} = \frac{C(d_0^{\min})}{3D(d_0^{\min})}\left(1 - \sqrt{1 - \frac{3D(d_0^{\min})B(d_0^{\min})}{C^2(d_0^{\min})}}\right). \tag{3.36}$$

As no simple expression can be obtained for $d_0^{\min}$, we use the following method. We approximate $\delta d_0^{\min}$ by

$$\delta d_0^{\min} \simeq \frac{B(d_0^{\min})}{2C(d_0^{\min})} \tag{3.37}$$

where we have used $3DB/C^2 << 1$ when Δ is close to Δ_h. Indeed, we consider now loadings Δ close to Δ_h. Hence, $d_0^{\min}$ is also close to d_h

$$\Delta = \Delta_h + \delta\Delta \tag{3.38a}$$

$$d_0^{\min} = d_h + \delta d. \tag{3.38b}$$

One can then derived the linearized expressions of Eqs. (3.35a)-(3.35d) and their first and second derivatives up to the first order in $\delta d_0^{\min}$ and $\delta\Delta$. Using these expressions and the approximation of $\delta d_0^{\min}$ given by Eq. (3.37), the resolution of Eq. (3.31a) gives the relationship between the loading increment $\delta\Delta$ from the critical loading Δ_h and the resulting damage increment:

$$\begin{aligned} &\delta d = T \times \delta\Delta \\ &T = -\frac{\Delta_h^2 k'(d_h)k'''(d_h)\left(1+\frac{\tilde{\alpha}^2(q_c)}{2}\right) + 2Y_{c0}\eta k''(d_h)(\tilde{\alpha}^2(q_c)-1)}{Y_{c0}\eta\Delta_h k'''(d_h)\left(1-\frac{1}{\tilde{\alpha}^2(q_c)}\right)\left(1+\frac{3\tilde{\alpha}^2(q_c)}{2}\right)}. \end{aligned} \tag{3.39}$$

From this expression, one determines the critical loading $\delta\Delta_c$ at which a stable solution $\{d_0^{\min}, \delta d_0^{\min}\}$ that minimizes the total energy stops to exist. From Eq. (3.36), we obtain that this critical loading $\delta\Delta_c$ satisfies to the equation $C(d_0^{\min})^2 > 3D(d_0^{\min})B(d_0^{\min})$, leading to

$$\begin{aligned} \delta\Delta_c = &-Y_{c0}^2\eta^2\left(1-\frac{1}{\tilde{\alpha}^2(q_c)}\right)^2 / \\ &\left[2Y_{c0}\eta\Delta_h\left(1-\frac{1}{\tilde{\alpha}^2(q_c)}\right)\left(1+\frac{\tilde{\alpha}^2(q_c)}{2}\right)\left(\frac{1}{2}T\Delta_h k'''(d_h)+k''(d_h)\right)\right. \\ &\left.-3\Delta_h^2 k'''(d_h)\left(\frac{1}{3}+\frac{\tilde{\alpha}^2(q_c)}{2}\right)\left(TY_{c0}\eta\left(1-\frac{1}{\tilde{\alpha}^2(q_c)}\right)+\Delta_h k'(d_h)\right)\right]. \end{aligned} \tag{3.40}$$

From $\delta\Delta_c$ we obtain the critical loading at failure Δ_c and the critical average damage in the system d_c:

$$\Delta_c = \Delta_h + \delta\Delta_c \tag{3.41}$$

$$d_c = d_h + T\delta\Delta_c + \delta d_0(\Delta_c). \tag{3.42}$$

Before comparing the analytical predictions to numerical results, it should be emphasized that as for the linear stability analysis these critical values also remain approximations. Indeed, they

are obtained by linearizing the energy coefficients with the assumptions of small deviations from the homogeneous state at Δ_h (see Eqs. (3.38a) and (3.38b)). Similarly, assuming a system close to the localization threshold state we have used an approximate expression of $\delta d_0^{\min}$ given by Eq. (3.37). Therefore, we expect some small deviations in the critical value predictions between the exact numerical value and our theoretical prediction.

Fig. 3.8a shows the evolution of the energy for $d_0 = d_0^{\min}$ as a function of δd_0 at different loading increment $\delta\Delta$ ranging from zero at localization threshold to $\delta\Delta_c = 0.088$ with the set of parameters considered here ($\eta = 8$, $a = -0.3$, $\kappa = 2\kappa_c$). The analytical minima are indicated by dots. From this representation, one can observe that the critical loading increment is slightly overestimated from our analysis as the energy has actually no local minima for $\delta\Delta > 0.08$. However, we note that overall the agreement with the numerical determination of the heterogeneous equilibrium position is excellent. Figure 3.8b compares the analytical predictions of the failure threshold with the numerical results for other κ values. For comparison, we also show the results of the linear stability analysis already shown on Fig. 3.3b. Failure prediction is significantly improved. This can be explained by the difference between both methods: The energy minimization procedure allows the determination of both $d_0^{\min}$ and $\delta d_0^{\min}$ in the post-localization regime while the homogeneous solution $d_0^h = d_0^{\min}$ is assumed in the stability analysis.

The energy minimization procedure sheds light on the nature of the localization for $\kappa > \kappa_c$ when a stable post-localization regime does exist. At the localization onset, the equilibrium position of the system shifts from a homogeneous to a heterogeneous damage configuration. When the loading is further increases, the equilibrium heterogeneous solution evolves with an increasing localized mode amplitude $\delta_0^{\min}$. Finally, at the failure threshold Δ_c, the system becomes unstable as no local minima exists anymore along the energy landscape.

3.4 Conclusions

We have defined a simple mesoscopic model able to describe rigorously the transfer of mechanical into fracture energy during progressive damage of materials and based on a few, well identified and tunable sets of physical ingredients (disorder, interaction...). The coaction of both material disorder and damage driving force redistributions after damage events seem the adequate ingredients for the description of the complex macroscopic response and damage localization of quasi-brittle failure of heterogeneous materials.

The linear stability analysis employed has shed light on the nature of the transitions observed during damage spreading:

– for the interaction parameter $\kappa > \kappa_c$, we evidenced a continuous transition from a homogeneous to a heterogeneous damage distribution. This damage localization is characterized by a characteristic finite wavelength proportional to the internal length introduced

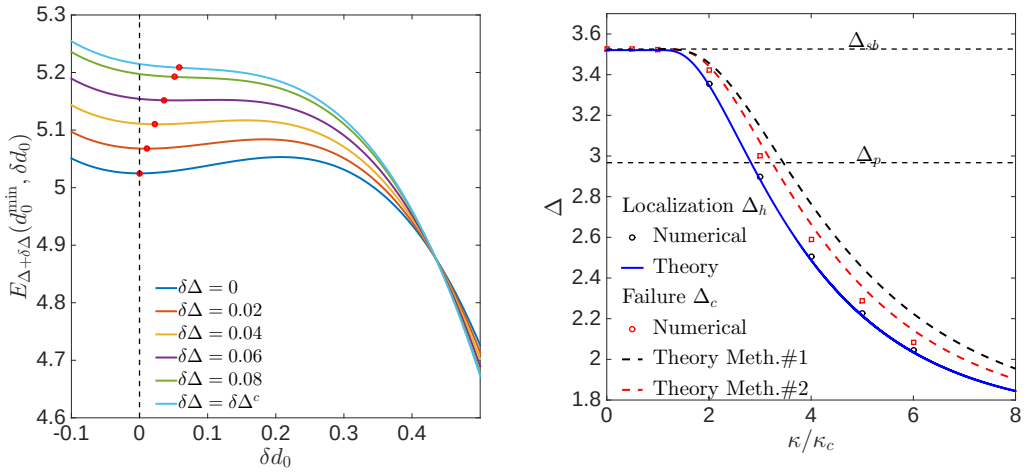

(a) (b)

Figure 3.8: Energetical interpretation of localization and failure for the case $\kappa > \kappa_c$ in presence of a post-localization regime: (a) Total energy of the system for $d_0 = d_0^{\min}$ as a function of the perturbation amplitude δd_0 for different loading increments $\delta\Delta$. The position of the minima determined theoretically are indicated by dots; (b) Evolution of the critical displacements Δ_h at localization and Δ_c at failure for $\eta = 8$, $\ell_0 = 5$, $\kappa = 2\kappa_c$ and $\sigma_g = 0.001$. The theoretical values at localization are shown by the solid blue line, at failure in black dashed for the predictions from the linear stability analysis (referred to as Meth. #1) and red dashed for the predictions from the global energy minimization (referred to as Meth. #2). The horizontal dotted lines indicate the loading at peak force and at the snap-back instability.

in the redistribution function and depends on its actual shape through the parameter κ. Before localization takes place, the system response is that of a homogeneous material. Once localization takes place, a deviation is obtained and it is shortly after followed by the catastrophic failure, triggered by the breakage of one heterogeneity.

– for $\kappa < \kappa_c$, unstable failure takes place directly from a homogeneous damage configuration, without prior localized damage state. Therefore, the macroscopic response can be fully predicted form that of a homogeneous material.

The conditions for the existence of these transitions during the progressive damage of the material can be inferred from the shape of the kernel $\mathcal{G}$ that describes the damage driving force redistribution $\delta\mathcal{F}(x) = (\mathcal{G} * \delta d)(x)$ resulting from a damage increment $\delta d(x)$: If its Fourier transform $\tilde{\mathcal{G}}(\vec{q_0}, \Delta) = -\dfrac{\Delta^2}{2} k''[d_0(\Delta)]\tilde{\alpha}^2(\vec{q_0}) - Y_{c0}\eta$ changes of sign to become positive, damage localizes while catastrophic failure is controlled by the sign of $\tilde{\mathcal{G}}(\vec{q_0}, \Delta) + \tilde{\mathcal{G}}(0, \Delta) = -\dfrac{\Delta^2}{2} k''[d_0(\Delta)](\tilde{\alpha}^2(\vec{q_0}) + 1) - 2Y_{c0}\eta$. These expressions reveal that $k''(d) < 0$ is required to observe localization and then abrupt failure. In other words, the constitutive elements of the solids the stability of which is controlled by the sign of k'' must themselves display an unstable failure behavior to generate instabilities at the large scale.

An alternative approach was also proposed to complement the linear stability analysis and in particular determine more accurately the failure threshold. The determination of the global energy minimum allowed recovering the same analytical behaviors for the damage localization. Therefore, localization is associated to the heterogeneous growth of the damage field, which permits to minimize the energy of the system. It is associated to the progressive growth of a perturbation from an initially homogeneous field. Our system naturally regularizes localization that consists in regions with enhanced damage either over a finite wavelength or spread throughout the system. The critical loading and damage level at which it takes place were also refined using this approach as no assumption on a relationship between the homogeneous damage level and applied displacement was considered.

These techniques were here applied to our simplified model to predict localization and failure of an isotropic continuously damaging material. It revealed the drastic effect of the choice of the redistribution function that was here set as tunable. It should be emphasized that these approaches are not restricted to this particular model and can be used in a general framework, in particular when more complex and realistic anisotropic redistribution functions are used. Finally, the study of damage temporal and spatial organizations as the material is progressively damaged is necessary to complete this study . The characterization of damage spreading during quasi-brittle failure is the focus of the next chapter.

CHAPTER 4

DAMAGE SPREADING TOWARD FAILURE: STATISTICS OF FLUCTUATIONS

We have so far studied the system behavior in terms of damage localization and failure predictions. However, temporal and spatial organization of damage as it spreads in the system was left aside. In this chapter, we focus on the precursors to *catastrophic* failure and investigate how the redistribution function, namely the internal length ℓ_0 and the shape parameter κ, influences their evolution. The quasi-brittle failure of heterogeneous materials is characterized by a complex damage organization both in space and time. Experimentally, it was observed using acoustic emission during the compression of wood [42, 35] that the intermittent fluctuations follow power law behaviors and spatially localize as failure is approached. Similar behaviors were obtained when studying many other quasi-brittle disordered materials, for example paper [101], cellular glass [42, 35] rocks [33] or synthetic plaster [82]. Hence, it seems that these features are characteristic of such failure phenomena.

These puzzling aspects of damage spreading in quasi-brittle materials have motivated a large number of numerical studies focusing on the characterization of the fluctuations and the elaboration of more realistic models to capture them (see [1] for a review). These statistical models generally combine disorder and elastic interactions – or very often their scalar counterpart, using the analogy between elasticity and electricity problem, see for example [121]. They evidence the *critical* nature of fractured media as they are driven towards failure, through the observation of scaling behaviors in the fluctuation statistics characterized by universal exponents. However, the origin of this universality and the nature of the critical point involved in driven damaged media are very often missing. The quantitative link with the experimental observations of damage spreading in heterogeneous media is also generally not established. Here, we seek to determine if our approach proposed in Chapter 2 captures the critical behavior of micro-fractured systems. If so, we must address the question of the nature of the critical point involved in this type of failure phenomena. Hence, we provide in the following an extensive characterization of the temporal and spatial structure of damage and its fluctuations.

This chapter is divided in three parts. In the first section, after defining quantitatively avalanches or bursts of damage activity, we focus on the characterization of the avalanche statistics, their spatial structure, and the resulting damage field correlations when the interaction function is solely positive with $\kappa = 0$. This corresponds to systems where damage events result in a *reloading* of the other parts of the material. We will show that the temporal structure of the damage evolution is mostly independent of the internal length ℓ_0 while its spatial organization, on the contrary, varies with ℓ_0 and shows non-trivial scaling behaviors when the internal length is much smaller than the system size. The second section is devoted to sign changing redistribution functions with $\kappa > \kappa_c$. We will see that the introduction of an unstable mode of finite wavelength λ_c drastically modifies the spatial structure of the avalanches and the resulting damage field, as well as the critical behavior of the system. In the last section, we reformulate our model as an equivalent, simpler formulation, which helps us interpreting our observations in terms of classical models of elastic interfaces driven in random media [6]. In particular, when considering the mean field limit for the elastic interactions, we quantitatively explain the scaling behaviors observed in our simulations and provide the physical origin of the critical nature of the behaviors emerging from our damage model.

4.1 Statistics of fluctuations in damage models with positive load redistributions ($\kappa = 0$)

We first focus on the case of an exponential interaction function where the parameter κ of Eq. (2.13) is set to zero. We consider the behavior of a system with unstable elements, *i.e.* for which the stiffness parameter a of Eq. (2.11) is negative, and a hardening behavior. A one-dimensional system of size $N = 10000$ elements is used with a disorder strength $\sigma_g = 0.2$ and the internal length is varied from 1 to ∞. The infinite interaction length actually corresponds to the mean field limit where all elements are subjected to the same damage driving force, proportional to the average damage in the system. This limit is also similar to the case of a global load sharing fiber bundle model where force is equally redistributed among all surviving elements after a fiber is broken [93], even though we consider here progressively damaging elements.

4.1.1 Avalanche definition

A zoom on the force-displacement response of the material as predicted from our model reveals the intermittent behavior of the failure process (see the top inset of Fig. 4.1a). Rather than a smooth response, as for homogeneous materials, the curve exhibits sudden drops of force at constant displacement (red plain curves). They result from damage events that induce a decrease of the elastic stiffness of the material. During these damage phases, since the externally applied displacement does not vary, elastic energy stored in the material is transferred into dissipated damage energy. These

micro-instabilities are separated by phases where the system deforms elastically (see the blue dashed curves in the inset) and hence where no damage takes place. This complex dynamics results in a crackling behavior [105] that reflects these localized bursts of damage events.

The evolution of the amplitude of the damage bursts, also called *avalanches*, is shown in the lower inset of Fig. 4.1a as a function of the applied displacement. It displays the characteristic intermittency and acceleration close to failure observed in several experimental studies, as depicted in the first chapter. There are different ways to define avalanche size. One possibility is to compute the total increase of damage between two successive equilibrium positions. Figure 4.1b shows damage profiles before and after an avalanche for an internal length scale $\ell_0 = 5$. The area between both curves defines the avalanche size S, which can be computed from

$$S(\Delta) = \sum_{x=1}^{N} \delta d(x, \Delta) \tag{4.1}$$

where $\delta d(x, \Delta)$ is the increase of the damage field in x at some imposed loading Δ.

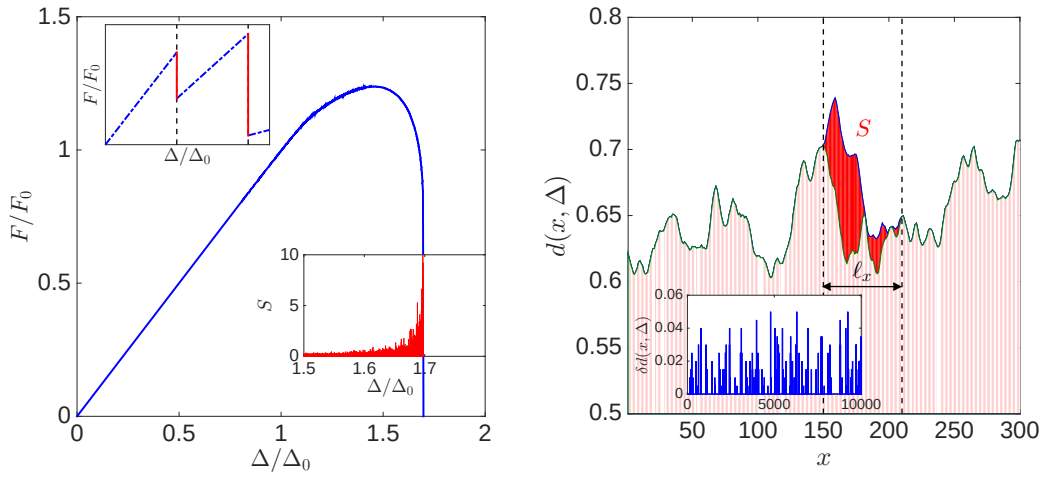

(a) (b)

Figure 4.1: (a) Normalized macroscopic response of one disorder realization for $\ell_0 = 5$. The top inset shows a zoom of the crackling behavior resulting from bursts of damage events while the bottom inset shows the evolution of the burst size S with the prescribed displacement, highlighing the strong intermittence of the damage process; (b) Definition of the avalanche size S and its spatial extent ℓ_x from the damage field: The damage field is shown before and after an avalanche for $\ell_0 = 5$. The avalanche size is defined by the area S between both curves while the spatial extent ℓ_x corresponds to the distance between the two most distant points damaged during the avalanche. The inset shows the spatial structure $\delta d(x)$ of a single avalanche for ℓ_0 very large. In this limit, damage spreads randomly within the material.

Taking advantage of the energetical formulation of our model, we can also describe the avalanches in terms of energy variation. As mentioned, avalanches correspond to a transfer of elastic

energy ΔE_{el} into dissipated energy ΔE_{d} so that

$$|\Delta E_{\mathrm{el}}| = \Delta E_{\mathrm{d}} = \frac{1}{2}\Delta^2 |\delta K|. \tag{4.2}$$

where $\delta K < 0$ is the variation of the macroscopic stiffness due to the damage burst. The dissipated energy can actually be divided into two contributions: the damage energy ΔE_{r}, expressed in its discretized form as

$$\Delta E_{\mathrm{r}} = \sum_{x=1}^{N} Y_c(x,d)\delta d(x,\Delta), \tag{4.3}$$

and the kinetic energy ΔE_{k} obtained using energy conservation through the relation

$$|\Delta E_{\mathrm{el}}| = \Delta E_{\mathrm{d}} = \Delta E_{\mathrm{r}} + \Delta E_{\mathrm{k}} \tag{4.4}$$

where we use the expression of ΔE_{r} (4.3) and ΔE_{el} (4.2). In our model, it corresponds to the mismatch between the elastic energy actually released during the avalanche and the energy dissipated by damage as calculated from the fracture energy field of the material defined in Eq. 2.9. Since these micro-instabilities are dynamic processes, we interpret this mismatch in terms of kinetic energy of the material elements that can be ultimately dissipated through acoustic emissions or other dissipative mechanisms.

Interestingly, if these definitions are *a priori* different, they can be used equivalently to study the statistics of damage fluctuations. Indeed, all the quantities introduced previously scale linearly with each other, as shown on Fig. 4.2a and 4.2b where the energy dissipated by damage $S_{\mathrm{r}} = \Delta E_{\mathrm{r}}$ is represented as a function of S and of the kinetic energy $S_{\mathrm{k}} = \Delta E_{\mathrm{k}}$, respectively. Note that the kinetic energy contribution remains at least one order of magnitude lower than that of the other ones and can therefore be considered negligible. Nevertheless, its scaling with S_r indicates that this quantity follows the same behavior as S or S_r and hence provides an interesting insight on the relation between acoustic emission and avalanche size in the frame of our model. Since all these quantities are linearly related, we use in the following only the avalanche size S defined from the number of damage increments to characterize the fluctuation statistics and its evolution as the system is driven closer to failure, the behavior of $S_{\mathrm{d}} \simeq S_{\mathrm{r}}$ and S_{k} being deduced from their linear relationship with S.

4.1.2 Temporal behavior: avalanche size evolution

A classical way to characterize the temporal evolution of avalanche sizes is to study their probability density functions at different distances δ to catastrophic failure. It provides information on how likely it is to obtain an avalanche of size S at some distance δ. The type of probability density function, *e.g.* Gaussian, power law... and its evolution as the material is driven towards full failure provide relevant insights on the damage spreading mechanisms. To determine the probability densities as the damage grows, we divide the lifetime of the system, characterized by the distance to failure

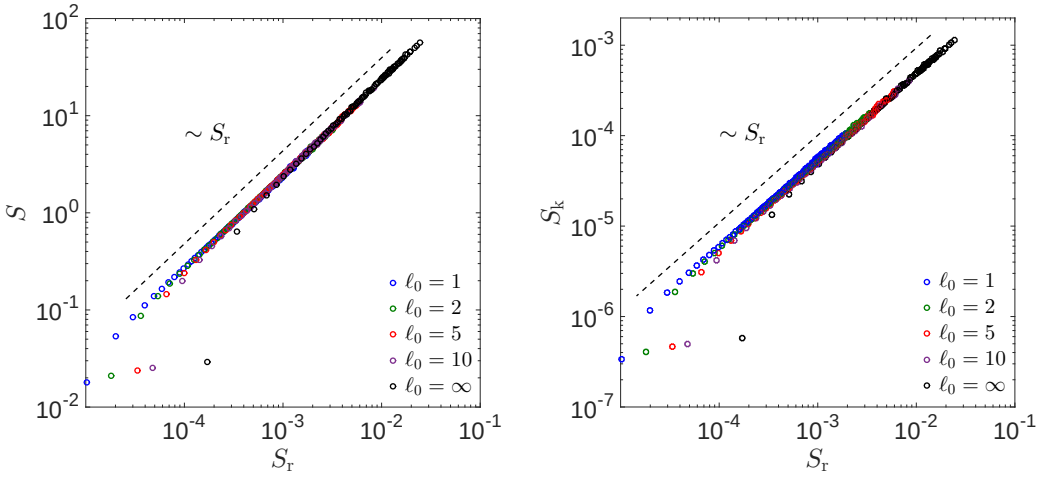

(a) (b)

Figure 4.2: Relationship between the fracture energy $S_{\rm r}$ of an avalanche with (a) its size S as defined in Fig. 4.1 and (b) its kinetic energy $S_{\rm k}$. The linear behaviors show that we can use indifferently any of these quantities to characterize the avalanche statistics.

δ (defined by Eq. (3.2)), into bins. Considering several realizations of the disorder, we then compute the distribution in each bin. The final avalanche during which catastrophic failure takes place is however left aside since it is not representative of the spreading of damage in the material, but instead, of the critical level of damage at catastrophic failure. Actually, it was shown to follow a Gaussian distribution [120] while avalanches taking place before this final event follow generally power law distributions, as also observed here.

The distributions $P_\delta(S)$ of avalanche sizes are shown in Fig. 4.3a and 4.3b for $\ell_0 = 5$ and $\ell_0 = \infty$, respectively. For both internal lengths power law behaviors with an exponent β are observed, up to an exponential cutoff of characteristic size S^* that increases with the distance to failure, so that

$$P_\delta(S) = A_0 S^{-\beta} \exp\left(-\frac{S}{S^*(\delta)}\right) \tag{4.5}$$

where A_0 is a normalization constant and $\beta = 1.5 \pm 0.1$.

The evolution of the cutoff with the distance to failure can be obtained by fitting the distributions using Eq. (4.5) with $\beta = 3/2$. The growth of S^* as a function of δ is shown for both internal length $\ell_0 = 5$ and $\ell_0 = \infty$ in the inset in Fig.4.4a. For both values a power-law behavior

$$S^* \sim \delta^{-\mu} \tag{4.6}$$

is obtained where $\mu = 1.0 \pm 0.1$ with a weak deviation close to failure for the lowest internal length. The variations of S^* with δ can also be inferred from the evolution of the average avalanche size $\langle S \rangle$. Indeed, as we shall now determine, both quantities are related. We first calculate the constant A_0 of

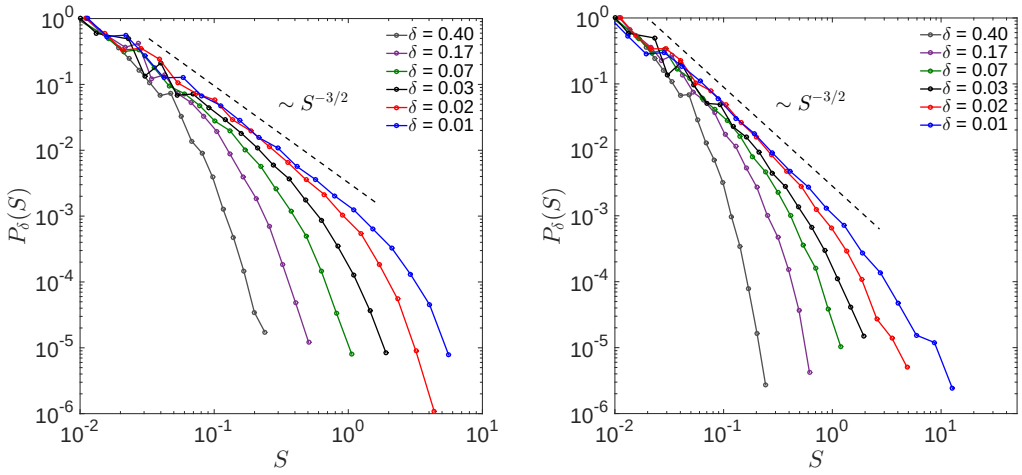

(a) (b)

Figure 4.3: Probability density functions of avalanche sizes S for different distances to failure δ for (a) $\ell_0 = 5$ and (b) $\ell_0 = \infty$. In both cases the distributions exhibit a power law behavior of exponent $\beta = 1.5 \pm 0.1$ up to an exponential cutoff S^* that evolves with δ.

the avalanche size distributions using the normalization condition

$$\int_{S_m}^{+\infty} P_\delta(\tilde{S}) d\tilde{S} = 1 \tag{4.7}$$

where S_m is the minimum value of S. Replacing $P_\delta(S)$ by its expression in Eq. (4.5) and using the change of variable $u = S/S^*$, ones obtains

$$1 = A_0 (S^*)^{1-\beta} \int_{S_m/S^*}^{+\infty} \tilde{u}^{-\beta} \exp(-\tilde{u}) d\tilde{u}. \tag{4.8}$$

Neglecting the exponential tail, *i.e.* the area for $S/S^* > 1$, ones gets

$$1 = A_0 (S^*)^{1-\beta} \int_{S_m/S^*}^{1} \tilde{u}^{-\beta} d\tilde{u} = -A_0 (S^*)^{1-\beta} \left[1 - \left(\frac{S_m}{S^*} \right)^{1-\beta} \right] \simeq A_0 S_m^{1-\beta} \tag{4.9}$$

where we have used that close to failure the cut-off value S^* is much larger than the minimum avalanche size S_m and that the exponent β is larger than 1. We obtain finally the normalization constant $A_0 \simeq S_m^{\beta-1}$. Therefore, at a given δ, the average avalanche size follows

$$\langle S \rangle = \int_0^{+\infty} S P_\delta(S) dS = S_m^{\beta-1} \int_{S_m}^{+\infty} \tilde{S}^{1-\beta} \exp\left(-\frac{\tilde{S}}{S^*(\delta)} \right) d\tilde{S} \tag{4.10}$$

Using the same change of variable as for the normalization constant determination and again neglecting the exponential contribution, we obtain

$$\langle S \rangle \sim S_m^{\beta-1} (S^*)^{2-\beta} \left[1 - \left(\frac{S_m}{S^*} \right)^{2-\beta} \right] \tag{4.11}$$

which leads, close to failure where $S^* >> S_m$, to the relationship

$$\langle S \rangle \sim (S^*)^{2-\beta} \tag{4.12}$$

where both quantities are functions of the distance to failure δ.

The evolution of the average avalanche size is shown as a function of the distance to failure for different internal lengths in Fig. 4.4b. It follows a power law behavior

$$\langle S \rangle \sim \delta^{-\tau} \tag{4.13}$$

where $\tau = 0.50 \pm 0.05$, which is consistent with the exponent $\mu = 1.0 \pm 0.1$ of Eq. (4.6) when using the relationship

$$\tau = \mu(2 - \beta) \tag{4.14}$$

derived from Eqs. (4.6), (4.12) and (4.13) and the value $\beta = 1.5$. Note however that for small internal lengths, we observe a deviation to the scaling law $\langle S \rangle \sim \delta^{-\tau}$ over the last decade of δ, typically for $\delta \in [10^{-4}, 10^{-3}]$, as also observed for S^*. This may indicate some saturation effect that bounds avalanche sizes very close to failure when redistribution takes place over small distances ℓ_0 close to the heterogeneity size. Nonetheless, this effect is limited to damage events taking place very close to failure where the statistics is rather scarce, and so it might reflect more some numerical limitations than physically relevant observations.

To summarize, it turns out that at a given distance to failure, we can identify a characteristic size S^* (or equivalently $\langle S \rangle$) of damage burst that increases as a power law with δ. It reflects the intensification of damage processes as catastrophic failure is approached, and indicates that avalanches take place at all scales very close to failure, as shown further in the following.

We now investigate the avalanche size distribution when recorded over the *entire* failure process, from the first avalanche to the last one before catastrophic failure. Interestingly, we can actually determine it from the distributions obtained at different distances to failure: Let us note $P(S)$ the distribution of avalanche sizes over $\delta \in [0, 1]$. It follows

$$P(S) = \frac{1}{N_t} \int_0^1 \dot{N}_\mathrm{a}(\delta) P_\delta(S) d\delta \tag{4.15}$$

where $\dot{N}_\mathrm{a}(\delta)d\delta$ is the number of avalanches during the interval $[\delta, \delta + d\delta]$ and N_t their total number. The evolution of $\dot{N}_\mathrm{a}$ with δ is shown in the inset of Fig. 4.4b for $\ell_0 = \infty$ and $\ell_0 = 5$. In both cases, it does not vary much. In fact, after a transient regime, it reaches a constant value so that we can write

$$\dot{N}_\mathrm{a} \sim \delta^\epsilon \tag{4.16}$$

with $\epsilon \simeq 0$. Introducing this expression into Eq. (4.15) together with the distribution $P_\delta(S)$ of Eq. (4.5) and the relationship between the cutoff with the distance to failure (Eq. (4.6)), one obtains

$$P(S) = \frac{A_0}{N_t} \int_0^1 \tilde{\delta}^\epsilon S^{-\beta} e^{-S\tilde{\delta}^\mu} d\tilde{\delta} \tag{4.17}$$

where A_0 is the normalization constant of Eq. (4.9). Using the substitution $u = S\delta^\mu$, one gets

$$P(S) = \frac{A_0}{\mu N_t} S^{-\beta-(\epsilon+1)/\mu} \int_0^S \tilde{u}^{(1+\epsilon)/\mu-1} e^{-\tilde{u}} d\tilde{u} \tag{4.18}$$

The integral term being negligible with respect to the prefactor, the distribution follows

$$P(S) \sim S^{-\beta-(\epsilon+1)/\mu} \tag{4.19}$$

so that finally one gets the following scaling relation

$$P(S) \sim S^{-\beta_{\text{tot}}} \quad \text{with} \quad \beta_{\text{tot}} = \beta + \frac{\epsilon+1}{\mu}. \tag{4.20}$$

Using the numerical values obtained previously, *i.e.* $\beta \simeq 3/2$, $\mu \simeq 1.0$ and $\epsilon \simeq 0$, one finds $\beta_{\text{tot}} \simeq 5/2$. This prediction is tested on Fig. 4.4b that shows the distribution of avalanche sizes recorded over the full failure process for $\ell_0 = 5$ and $\ell_0 = \infty$. The probability density functions follow power laws with exponent $\beta_{tot} = 2.5 \pm 0.2$ that agrees well with the predicted value.

To summarize, we have seen that irrespective of the internal length scale ℓ_0, the probability density of avalanche sizes, or equivalently, of bursts of dissipated energy, follows a power law with an exponential cutoff. The cutoff size, related to the average avalanche size, increases as a power law with the distance to failure. Table 4.1 summarizes the different scaling and the exponents measured in the simulations. These are compared in the third column with the calculated values obtained from the scaling relations derived in this section.

These findings call for a few comments. First, power law behaviors of the avalanche sizes distribution with exponents $\beta = 3/2$ and $\beta_{\text{tot}} = 5/2$ were observed numerically and predicted analytically in simplified damage models referred to as fiber bundle model with global load sharing (see [93] for a review). In these models, when an element breaks, the load that it carried is redistributed equally on the other elements of the system, similarly to our own damage model in the limit $\ell_0 \to \infty$. Note however that in the global load sharing fiber bundle model, elements are either intact ($d = 0$) or broken ($d = 1$), contrary to our approach where element can progressively damage through the introduction of the continuous damage parameter $0 \leq d \leq 1$.

Interestingly, the transition from a *global* redistribution of damage driving force ($\ell_0 \to \infty$) to a *localized* redistribution ($\ell_0 \ll N$) does not affect the statistics of avalanches that remain power law distributed. This is quite different from the behavior of traditional fiber bundles where elements break abruptly. Indeed, for *local* load sharing fiber bundles, damage fluctuations follow exponential

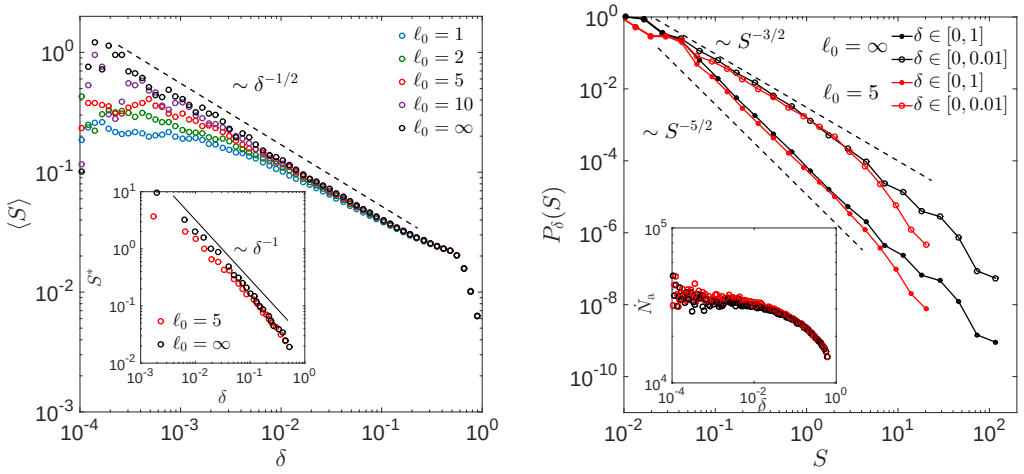

(a) (b)

Figure 4.4: (a) Evolution of the average avalanche size as a function of the distance to failure for different internal length scales. The curves show a power law behavior of exponent $\tau = 0.50 \pm 0.05$, independently of ℓ_0. The inset shows the evolution of the cutoff S^* of the avalanche size distribution that also exhibits a power law behavior with δ, but with exponent $\mu = 1.0 \pm 0.1$, in agreement with the scaling relation of Eq. (4.14); (b) Probability density functions of avalanche sizes when taking into account all damage events (closed symbols) or only those taking place for $\delta \in [0, 0.01]$ (open symbols) for the two internal lengths $\ell_0 = 5$ and $\ell_0 = \infty$. They both follow power laws with exponents $\beta_{\text{tot}} \simeq 5/2$ and $\beta \simeq 3/2$, respectively, in agreement with the scaling relation of Eq. (4.20). The inset shows the rate of avalanche $\dot{N}_a$ as a function of the distance δ to catastrophic failure.

statistics [59] so that the largest avalanches do not span over the whole system, even when driven close to catastrophic failure. Actually, Hidalgo *et al.* considered redistribution functions of the form $1/r^\gamma$ where r denotes the distance to the broken element [50] in a 2D system. They showed that in traditional fiber bundles, there is a change of behavior for local redistributions, *i.e.* large γ values, and models with longer range redistribution functions with γ below a critical value γ_c that fall into the global loading sharing universality class with power law statistics. The existence of two distinct statistical signatures for local and global load redistribution mechanism contrasts with the results of our simulations. We believe that this difference arises from the abrupt failure of elements in the traditional fiber bundle models. In our model, the introduction of a positive hardening parameter $\eta > 0$ results in a progressive damage of the elements, while for $\eta = 0$ elements recover a brittle behavior as in traditional fiber bundles. In that second case, it is interesting to note that we also recover an exponential statistical behavior, similar to traditional fiber bundle models with local load sharing mechanisms, as shown in Appendix B. Therefore, we believe that material hardening is a key ingredient for a proper description of progressive damage spreading in quasi-brittle media.

Interestingly, our findings indicate that both the onsets of localization and failure (Chapter 3) and the statistics of fluctuations (this chapter) are independent of the internal length ℓ_0 introduced in

the redistribution function. We will now see that ℓ_0 actually does play a role on the damage spreading, by controlling the spatial organization of damage events during avalanches. Indeed, as exemplified on Fig. 4.1b, a small internal length results in spatially localized damage events, whereas large internal length values produce avalanches rather uniformly distributed through the material. The following section is devoted to the spatial structure of avalanches.

Definitions	Measured values	Predicted values	Scaling relations
$S \sim S_{\mathrm{r}}^{\gamma}$	$\gamma = 1.00 \pm 0.05$		
$S_k \sim S_{\mathrm{r}}^{\gamma_{\mathrm{k}}}$	$\gamma_{\mathrm{k}} = 1.00 \pm 0.05$		
$P(S) \sim S^{-\beta} \exp(-S/S^*)$	$\beta = 1.5 \pm 0.1$		
$P(S) \sim S^{-\beta_{\mathrm{tot}}}$	$\beta_{\mathrm{tot}} = 2.5 \pm 0.2$	$\beta_{\mathrm{tot}} = 2.45 \pm 0.17$	$\beta_{\mathrm{tot}} = \beta + (\epsilon+1)/\mu$
$S^* \sim \delta^{-\mu}$	$\mu = 1.0 \pm 0.1$		
$\langle S \rangle \sim \delta^{-\tau}$	$\tau = 0.50 \pm 0.05$	$\tau = 0.52 \pm 0.10$	$\tau = \mu(2-\beta)$
$\dot{N}_{\mathrm{a}} \sim \delta^{\epsilon}$	$\epsilon = 0.0 \pm 0.1$		
$S \sim \ell_x^{d_{\mathrm{f}}}$	$d_{\mathrm{f}} = 1.8 \pm 0.1$		
$\ell_x^* \sim \delta^{-\rho^*}$	$\rho^* = 0.6 \pm 0.1$	$\rho^* = 0.58 \pm 0.07$	$\rho^* = \mu/d_{\mathrm{f}}$
$\xi \sim \delta^{-\rho}$	$\rho = 0.6 \pm 0.1$	$\rho = 0.58 \pm 0.07$	$\rho = \mu/d_{\mathrm{f}}$

Table 4.1: Definition of the scaling exponents measured from the statistics of fluctuations during damage spreading and their values measured from the simulations. When possible, these values are compared to each others in the third column using the scaling relations of Eqs. (4.14), (4.20) and (4.22) derived in this chapter.

4.1.3 Spatial structure of the avalanches

The study of the clusters formed during avalanches can provide several indications on the damage process of the system. The way damage at one point affects its neighbors can be more or less localized depending on the formulation of the redistribution function. It directly affects the shape of the avalanches that can either be structured with a particular scaling between their deepness (along d) and width (along x), or randomly spread in space. To characterize this property, a relevant quantity to extract from the clusters formed during avalanches is the spatial extent ℓ_x of bursts of damage events. As defined on Fig. 4.1b, it corresponds to the distance between the two most distant damaged points during an avalanche. Its scaling with the avalanche size S is a useful tool to characterize the structure of the avalanches.

On Fig. 4.5 we show for each ℓ_x value the corresponding avalanche size, for different internal length scales. For each ℓ_0 value shown here, a plateau, the height of which is controlled by the hardening parameter η, is obtained before a power law behavior dominates. The extent of the plateau is controlled by ℓ_0, as indicated by the rescaled curves S vs ℓ_x/ℓ_0 shown in the inset. The constant part of the curves extend to a length of about $2\ell_0$, at which scale a transition towards a power law

behavior dominating for ℓ_x values larger than about $10\ell_0$ is obtained. Hence, at large ℓ_x values, we describe this behavior as

$$S \sim \ell_x^{d_f} \quad \text{for} \quad \ell_0 << \ell_x \tag{4.21}$$

where $d_f = 1.8 \pm 0.1$. Note that the average avalanche size $\langle S \rangle$ computed at some distance to failure δ follows the very same scaling with the average cluster width $\langle \ell_x \rangle$ computed at the same value of δ.

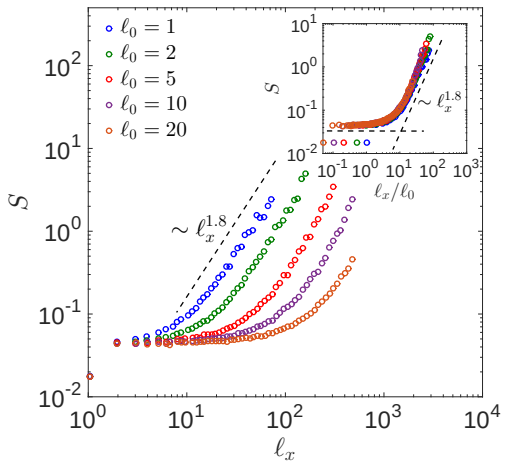

Figure 4.5: Avalanche size S as a function of the spatial extent of the avalanche ℓ_x for different internal length scales, showing a plateau regime at small scale and a power law behavior at large scale with exponent $d_f = 1.8 \pm 0.1$. The inset shows the collapse of the data when ℓ_x is normalized by ℓ_0.

The transition between the plateau and the power lower behavior indicates that for each length ℓ_0, a range of avalanche sizes exist over which they do not have a particular shape: for small sizes, typically of the order of the plateau level, avalanches can have a spatial extent ranging from a few element sizes to ℓ_0. This effect emerges from the rather flat redistribution function in a region of length scale fixed by ℓ_0 since $\alpha(|\vec{x}|) \simeq 1$ for $|\vec{x}| \ll \ell_0$. Since fracture energy thresholds are random, damage events comprised in small avalanches are randomly distributed within a region of size $\ell_x < \ell_0$. For large internal lengths, comparable to the system size, the same mechanism takes place: the redistribution is uniform within the whole system so that damage events take place at random location. While the spatial structure of damage bursts is random for avalanches of extension smaller than ℓ_0, they are spatially organized with a fractal dimension $d_f \simeq 1.8$ for the largest ones. Hence, for internal lengths close to the system size, this second regime disappears and a mean field approach is expected to describe accurately the damage evolution.

We now bridge these observations on the spatial structure of avalanches with the size distribution investigated in the previous section. It was shown that avalanche size distributions follow a power law behavior up to a cutoff size S^*. For the values of $\ell_0 \ll N$ studied here, the cutoff S^* is much larger than the plateau evidenced on Fig. 4.5, especially close to failure when δ is close to

zero. As a result, the scaling relation of Eq. (4.21) valid for large avalanches also holds for the cutoff size $S^* \sim (\ell_x^*)^{d_f}$ where ℓ_x^* denote the characteristic spatial extent of the largest avalanches. Since otherwise, S^* diverges as $\delta^{-\mu}$ as failure is approached (see Eq. (4.6)), one predicts that the spatial extent ℓ_x^* of the largest avalanches also diverges as

$$\ell_x^* \sim \delta^{-\rho^*} \quad \text{with} \quad \rho^* = \mu/d_f. \tag{4.22}$$

Using the measured values of μ and d_f (see Table 4.1), we expect a divergence of the spatial extent of the largest avalanches with an exponent $\rho^* = 0.58 \pm 0.07$. Hence, the clusters of damaged events formed close to failure might span over the full system. To verify this scaling, we investigate the probability density $P(\ell_x)$ of cluster sizes at different distances to failure for small internal lengths with respect to the system size. An example is shown on Fig. 4.6a for $\ell_0 = 5$. We observe exponential tails in the range of values $\ell_x >> \ell_0$. Figure 4.6b shows the variation of the exponential decay constant, denoted by ℓ_x^* and normalized by the internal length ℓ_0 as a function of the distance to failure. The expected power law behavior is well verified as ℓ_x^* increases as a power law with exponent $\rho^* = 0.6 \pm 0.1$ as the system approaches failure. Moreover, we verify that the lowest values of the cutoffs measured far from failure are of the order of $2 - 3\ell_0$, *i.e.* comparable with the cluster size at the transition between the plateau regime and power law evolution on Fig. 4.5. Finally, to go a step further in the analysis one can wish to relate the power law behaviors of the distribution of avalanche sizes and exponential one of that of the spatial extent. However, this is no simple task as close to failure the avalanches are mostly constituted of clusters of size of a few ℓ_0 distributed over a scale ℓ_x^*. Hence a deep study of each cluster is required and this is beyond the scope of this study.

To conclude this section, we see that as long as scale separation is ensured between the internal length and the system size, the largest avalanches, of size S^* do not only localize in time but also in space, with a characteristic size noted ℓ_x^*. Both quantities grow as failure is approached, following power laws. They are related via the fractal dimension of the damage clusters $d_f \simeq 1.8$ that indicates a non-trivial structure of the clusters formed during each avalanche. We now investigate how the spatial organization of damage clusters affects the resulting cumulated damage field.

4.1.4 Spatial organization of the cumulated damage field

To investigate the effect of the spatial organization of the avalanches on the cumulated damage field in the material, we study its correlations through the following function C. To define it, we first consider the field $d(x)$ at some given distance to failure δ. Dividing the system into boxes of size δx, we compute the average damage $\langle d(x) \rangle_{\delta x}$ at the scale δx and determine its standard deviation over the $N/\delta x$ boxes that constitute the system. This defines the correlation function

$$C(\delta x) = \sqrt{\langle \langle d(x) \rangle_{\delta x}^2 \rangle_x - \langle \langle d(x) \rangle_{\delta x} \rangle_x^2}. \tag{4.23}$$

This function is then averaged over different disorder realizations, for different distances to failure δ, as performed previously for the determination the probability density $P(S)$. If the spa-

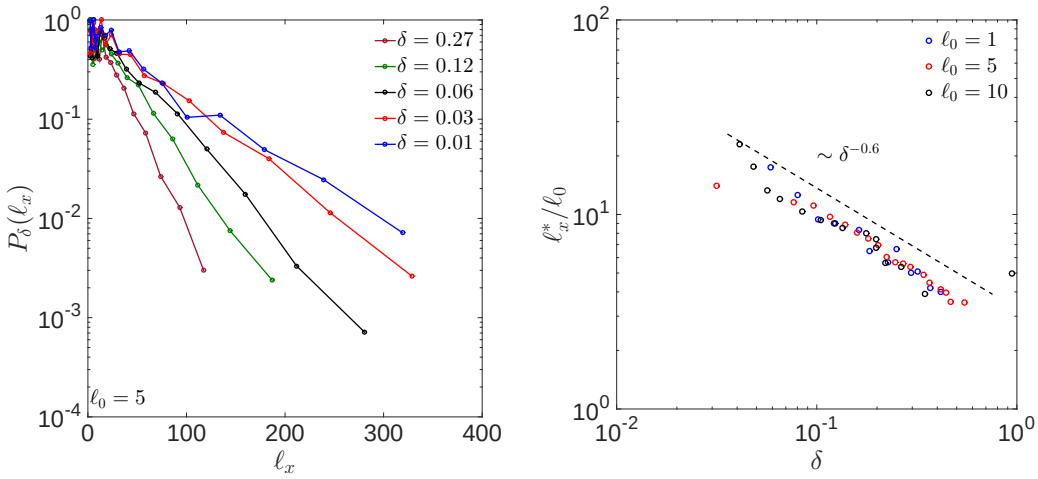

(a) (b)

Figure 4.6: (a) Probability density functions of the damage cluster spatial extent ℓ_x for $\ell_0 = 5$ at different distances to failure. The distributions exhibit an exponential tail for $\ell_x >> \ell_0$ with characteristic size ℓ_x^* that grows as δ goes to zero; (b) evolution of ℓ_x^* with the distance to failure for different internal length scales. We observe a power law with exponent $\rho^* = 0.6 \pm 0.1$ in good agreement with the increase of the avalanche size S^* with δ and the relation between the spatial extent ℓ_x^* and the size S^* of the largest avalanches (Eqs. (4.6) and (4.5)).

tial distribution of the damage field is purely random, *i.e.* resulting from randomly located damage events, the correlation function should decay as $1/\sqrt{\delta x}$. This results from the central limit theorem: Assuming that we have m randomly distributed points in a box of size δx, then the standard deviation of their sum is proportional to $\sqrt{m}$. Therefore, since $m = \delta x$ due to our spatial discretization, the standard deviation of the average values is proportional to $\sqrt{m}/m = 1/\sqrt{\delta x}$. On the other hand, if the damage field is correlated over a given length scale, then a deviation from this behavior should be observed over the corresponding range.

Figure 4.7a shows, for $\ell_0 = 5$ and varying distances to failure, the evolution as a function of the box size δx of the correlation function C normalized by $\sqrt{\delta x}$. As can be observed far from failure, for example for $\delta = 0.98$, the curve is constant. This means that $C \sim 1/\sqrt{\delta x}$ that indicates an uncorrelated damage field. As failure is approached, a deviation from this plateau behavior can be identified. The transition point, denoted by ξ, defines the correlation length of the damage field, or the characteristic length scale over which the damage field is spatially correlated. This spatial extent of the damage field organization increases as failure is approached together with the amplitude of the deviation to the behavior of the random field. Hence, the damage field seems to become increasingly correlated over length scales that increase with δ. As for the spatial organization of the avalanches (see Section 4.1.3), no correlations of the damage field could be evidenced for large internal length scales, typically $\ell_0 > 20$. On the contrary, as shown on Fig. 4.7b, short internal length results in an increase of the correlation length ξ as failure is approached. Once again, we obtain a power law

behavior

$$\xi \sim \delta^{-\rho} \tag{4.24}$$

where $\rho = 0.6 \pm 0.1$. This value is compatible with the scaling of the spatial extent of the avalanches ℓ_x^* with δ, suggesting that both quantities are directly related. Moreover, the lowest values of ξ that could be observed are of the order of $10\ell_0$, compatible with the smallest size of the spatially organized avalanches evidenced on Fig. 4.5. Hence, we conclude that the spatial structure of the large bursts of damage events dictates the shape of the damage field and controls its correlation length. For small internal lengths, the correlation length that builds up in the system as $\delta \to 0$ could be extracted both from the spatial extent of damage clusters and from the correlation length of the damage field. On the contrary, for interaction lengths of the order of the system size, damage clusters have no spatial organization and the resulting damage field is random at all scales.

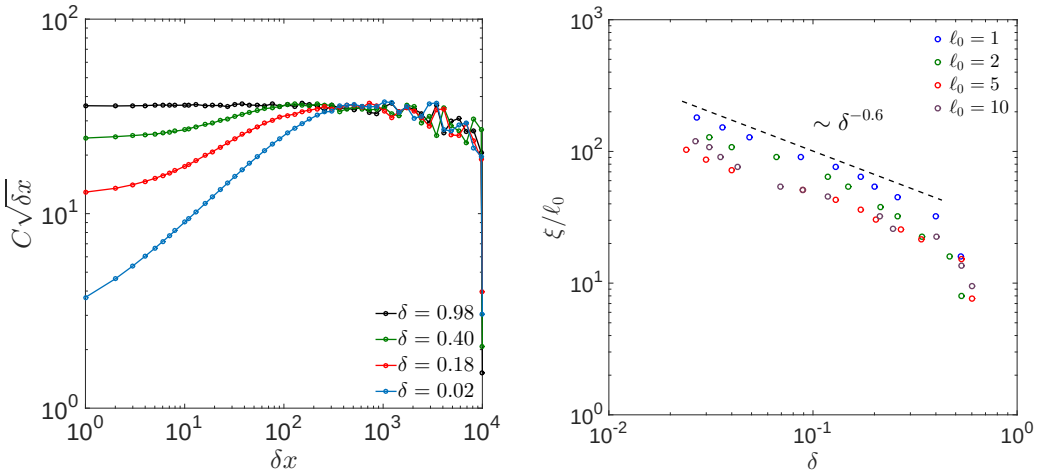

(a) (b)

Figure 4.7: (a) Correlation function $C(\delta x)$ of the cumulated damage field normalized by the inverse of the square-root of the box size $1/\sqrt{\delta x}$ that corresponds to a random spatial distribution of damage. The correlation function is computed here for $\ell_0 = 5$ at different distances δ to failure. The deviation from the constant behavior observed for $\delta x < \xi$ indicates the range of length scales over which the damage field is spatially correlated; (b) evolution of the correlation length ξ normalized by the internal length as a function of the distance to failure δ showing power law behaviors with an exponent $\rho = 0.6 \pm 0.1$.

To conclude the section 4.1 devoted to positive redistribution functions, we have seen that the avalanche size statistics studied at the *global* scale remains independent of the internal length involved in the damage driving force redistribution. The probability density of avalanche sizes S exhibits a power law behavior up to a the cutoff that increases as a power law of the distance to the onset of failure and localization. [1] On the contrary, the study of the avalanche statistics at the *local*

1. We recall that for positive redistribution functions, localization and failure takes place at the same loading that

scale reveals two different behaviors:

- For $\ell_0 \ll N$, two distinct types of avalanches could be identified: The smallest ones with a lateral extension $\ell < \ell_0$ have no particular spatial structure. They correspond to a burst of randomly located damage events that spread over a length scale smaller than the internal length. On the contrary, the largest damage bursts do not distribute randomly in the material. Instead, their spatial structure is characterized by a non-trivial fractal exponent $d_\mathrm{f} \simeq 1.8$. This complex structure reflects on the damage field, which becomes correlated close to failure up to a length ξ given by the lateral size ℓ^* of the largest clusters. As ℓ^* diverges as a power law as fracture approaches, the correlation length of the damage field also diverges next to failure.
- Without a clear scale separation between the internal length and the system size, for example for $\ell_0 \simeq N$, the large non-trivial avalanches disappear. This regime corresponds to a percolation process where damage events take place randomly within the material. Note however that by considering sufficiently large system sizes, large avalanches with complex spatial structure will take place again. As a result, in the limit of infinitely large systems, the damage field will always exhibit a correlated structure above the internal length scale ℓ_0 and below a correlation length ξ that will increase and finally diverge at the failure threshold.

Remarkably, varying the internal length does affect the spatial organization of the avalanches at the local scale, but does not change their size distribution at the global scale that follows $P(S) \sim S^{-3/2}$, irrespective of the presence of one or two distinct types of avalanches for $\ell_0 \sim N$ and $\ell_0 \ll N$, respectively. This puzzling observation can be explained by noticing that the largest avalanches that display a non-trivial spatial structure actually contributes to the exponential tail of the global avalanches distribution.

In the next section we shall evidence that the emergence of a diverging correlation length as the system is driven towards failure holds for some specific types of redistribution functions only. So far, we have considered a function α with a shape parameter $\kappa = 0$. This implies that the load redistribution is always positive, and that the wavelength λ_c of the localization mode at $\delta \to 0$ is infinite. In the next section, we consider sign-changing redistribution functions using larger shape parameter values $\kappa > \kappa_\mathrm{c}$ that result in a finite critical wavelength at the localization threshold. We will see that it drastically alters the spatio-temporal evolution of damage.

4.2 Statistics of fluctuations in damage models with finite wavelength at localization ($\kappa > \kappa_\mathrm{c}$)

We now investigate the statistics of damage growth for a redistribution function with a shape parameter $\kappa > \kappa_c$. This introduces an additional length scale, the wavelength $\lambda_\mathrm{c} = 2\pi/q_\mathrm{c}$, on top of

corresponds to the snap-back observed on the response of the homogeneous system.

the internal length ℓ_0. It characterizes the damage growth mode at the *onset of failure* (see Chapter 3) that will be shown to play also a central role in the spreading of damage *prior* failure. We remind that this characteristic wavelength follows $\lambda_c = \frac{4\pi\ell_0}{\sqrt{2\kappa\sqrt{1+\kappa^2}-(1+\kappa^2)}}$ (see Eq. (3.24)). The power spectrum of the damage field studied in Chapter 3 and shown in Fig. 3.4a has allowed to evidence the central role played by this mode as the system approaches failure. Here, we aim at determining its effect on the avalanche statistics during the whole process of damage spreading.

We first investigate on Fig. 4.8a the avalanche sizes distributions when considering either the entire phase of damage spreading before localization ($\delta \in [\delta_h, 1]$), damage events taking place just before localization ($\delta \in [\delta_h, \delta_h + 0.01]$) or between localization and failure ($\delta \in [0, \delta_h]$). Two shape parameter values are considered: $\kappa = 2\kappa_c$ and $\kappa = 4\kappa_c$, for which the distance to failure at localization are respectively $\delta_h \simeq 0.04$ and $\delta_h \simeq 0.2$. For $\delta \in [\delta_h, 1]$, we obtain a power law behavior of exponent 2.5 ± 0.3 up to a cutoff. The exponential dominates at lower avalanche sizes as κ is increased. For $\delta \in [\delta_h, \delta_h + 0.01]$, we recover the exponent $\beta = 1.5 \pm 0.2$ measured for the positive redistribution function case ($\kappa = 0$). Here also, the value of κ does not affect the value of the exponent, but instead controls the position of the cutoff. The effect is emphasized as the value of the distance to failure at localization is considerably higher in the case of $\kappa = 4\kappa_c$: the exponential dominates at much lower value. Finally, close to failure, the power law behavior of exponent β is extended to higher values but an exponential tail remains: the avalanche sizes are bounded, even close to failure, and their amplitude varies with the parameter κ.

Since the size of the largest avalanches that relates to the average avalanche size through the relation $\langle S \rangle \sim (S^*)^{2-\beta}$ (see Eq (4.12)) changes with the value of κ, we study it in more details in the inset of Fig. 4.8b where the variations of $\langle S \rangle$ are represented as a function of the distance $\delta - \delta_h$ to localization. We first observe an increase of the average avalanche size as the system evolves towards localization, followed by a saturation. The normalization of the ordinates $\langle S \rangle$ by $\lambda_c^{(2-\beta).d_f}$ allows to collapse the saturation regime corresponding to different κ, indicating that the plateau level, *i.e.* the average avalanche size close to localization, saturates at $\langle S \rangle \sim \lambda_c^{(2-\beta).d_f}$. This indicates that the cuttoff $S^* \sim \langle S \rangle^{1/(2-\beta)}$ of the distribution also saturates when the largest avalanches reach the lateral extension $\ell_x^* \sim (S^*)^{1/d_f} \sim \lambda_c$ following the scaling relations of Eqs. (4.12) and (4.21) observed in section 4.1 for the case $\kappa = 0$. [2]

2. In addition to the avalanche size exponent $\beta \simeq 1.5$ measured in Fig. 4.8a, we have also verified that the fractal dimension of the largest avalanches is equal to $d_f \simeq 1.8$ both for $\kappa = 0$ and for $\kappa = 2\kappa_c$. In other words, the largest avalanches during the spreading of damage are controlled by the value of the critical wavelength λ_c for localization. In particular, it sets the lateral extension of the largest avalanches, evidenced by the cutoff of the distribution. Interestingly, for the largest value of λ_c considered, *i.e.* $\lambda_c \simeq 12\ell_0$ corresponding to the case $\kappa = 2\kappa_c$, the growth regime of the average avalanche size before saturation can be described by a power law with exponent $\simeq 0.4 \pm 0.1$, rather compatible with the scaling $\langle S \rangle \sim \delta^{-\tau}$ with $\tau \simeq 0.52$ measured in the previous section for the case $\kappa = 0$ (see Eq. 4.13). The discrepancy may arise from the rather limited range of length scales between the lateral extension of a few ℓ_0 of the smallest avalanches with a non-trivial spatial structure taking place at the beginning of the damage growth process, and $\lambda_c \simeq 12\ell_0$, the lateral size of the largest avalanches taking place close to localization.

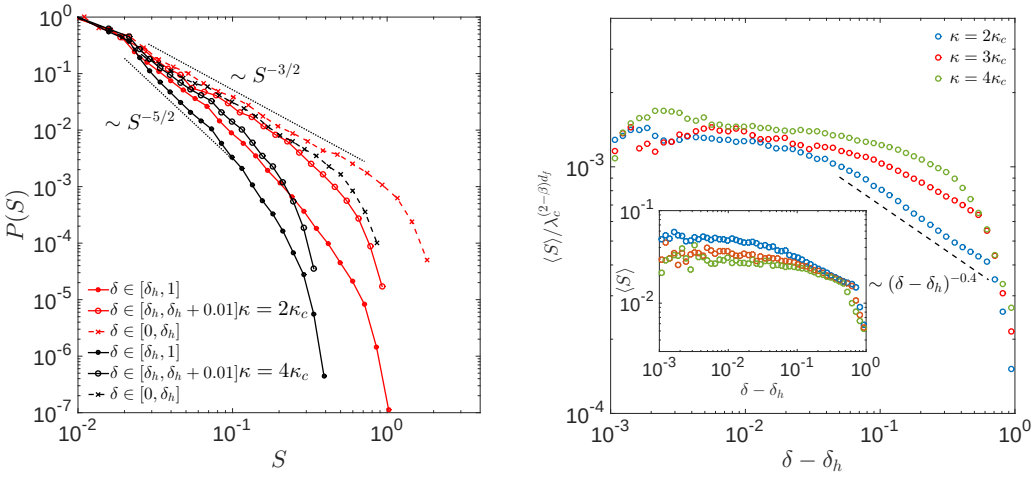

(a) (b)

Figure 4.8: (a) For shape parameters $\kappa = 2\kappa_c$ and $\kappa = 4\kappa_c$, normalized distribution densities when considering all damage events, $\delta \in [0, 1]$, or those taking place close to failure $\delta \in [0, 0.01]$. We retrieve the exponent values $3/2$ and $5/2$, however the cutoff of the distributions evolve with the parameter κ; (b) Average avalanche size normalized by the critical wavelength λ_c of each κ value considered as a function of the distance to failure. A power law behavior of exponent $\simeq 1/4$ is obtained, up to an upper cutoff that scales with λ_c and hence κ.

We can now extend the scenario proposed in Section 4.1 for $\kappa < \kappa_c$ that corresponds to an *infinite* critical wavelength at localization to the case $\kappa > \kappa_c$ with a finite value. In both cases, the damage spreads in the material through power law distributed avalanches up to a cutoff size that increases as the material is closer to localization. In addition, the exponents $\beta \simeq 1.5$ and $\tau \simeq 0.5$ that characterize the size distribution of avalanches and the growth of their average size with the distance to localization does not change significantly from one case to another. However, for a finite value of λ_c, this growth saturates and the largest avalanches measured at the localization onset are set by λ_c.

We now investigate the material behavior after localization. We characterize first the spatial organization of cumulated damage field using the same tool than in the previous section: Its correlation function defined in Eq. 4.23 is plotted on Fig. 4.9a as a function of $\delta x / \lambda_c$ for different distance to failure δ for $\kappa = 4\kappa_c$. The deviation to the uncorrelated behavior $C \sim 1/\sqrt{\delta x}$ shows that correlations build up in the damage field up to a scale $\delta x < \lambda_c$ as soon as localization starts, at $\delta = \delta_h \simeq 0.2$. Note that after localization, and prior to catastrophic failure, the correlation length does not evolve anymore, but only the strength of the correlations increases. This behavior is evidenced for other values of κ in the inset of Fig. 4.9a where the damage field structure functions next to the failure threshold all collapses on the same master curve. This observation confirms that the critical mode determined in Chapter 3 at the onset of localization is dominating the process of damage growth in the post-localization regime. Note also the secondary peak in the correlation function for $\delta x \simeq 2\lambda_c$

indicating the presence of other growing modes in this regime prior to catastrophic failure. The actual damage field and its evolution with δ is shown on Fig.4.9b for $\kappa = 4\kappa_c$. Far from localization, for $\delta \gg \delta_h \simeq 0.2$, the damage field remains rather similar to the one observed in the case $\kappa = 0$, without particular periodicity. As $\delta \simeq \delta_h$, some periodicity of wavelength $\simeq \lambda_c$ builds up in the damage field. As the system is driven even closer to failure, the localization mode becomes obvious and its amplitude increases drastically, reflecting the stable heterogeneous damage growth evidenced by the stability analysis of Chapter 3.

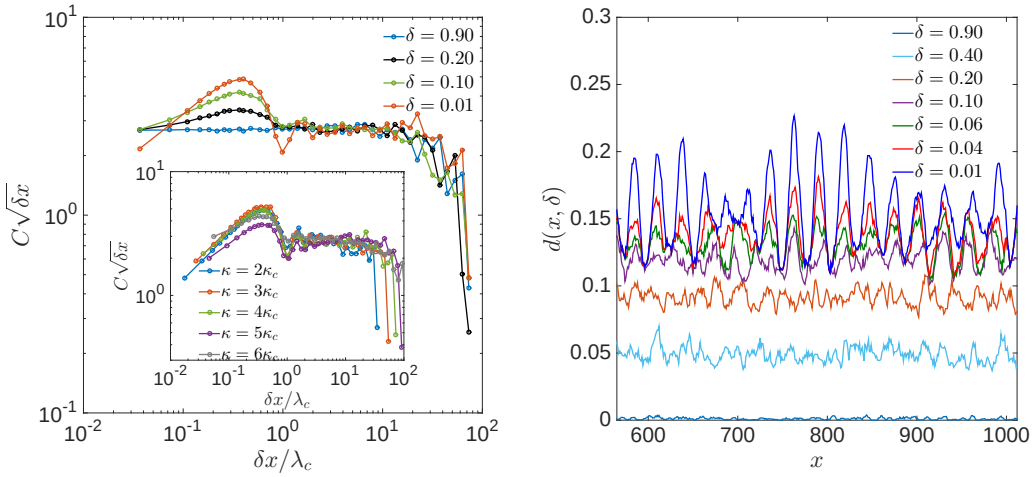

(a) (b)

Figure 4.9: (a) Evolution of the structure function C of the cumulated damage field as defined in Eq. (4.23) represented as a function of the box size δx normalized by λ_c for $\kappa = 4\kappa_c$. It shows the emergence of correlations over the length scales $\delta x < \lambda_c$ in the post-localization regime ($\delta > \delta_h \simeq 0.2$). The inset shows the correlation function close to failure ($\delta \simeq 0.01$) for different values of κ. (b) Evolution of the actual damage field for $\kappa = 4\kappa_c$: For $\delta < \delta_h \simeq 0.2$, we see the obvious emergence of the localization mode of wavelength λ_c the amplitude of which increases until abrupt failure ($\delta = 0$).

To conclude, we note that the introduction of a localization mode of finite wavelength bounds the fluctuations taking place during the spreading of damage: both the largest avalanches and the largest correlation length of the damage field observed when the material is close to localization are set by λ_c. This signifies that no divergence of a characteristic length scale, signature of a critical point, can be observed for these systems. To make sense to these observations, we now move to the analytical investigation of the statistical features of damage growth through the derivation of a simple damage evolution equation from our model formulation. In particular, this will allow us to provide exact predictions for the damage evolution statistical features in the mean field limit of the model.

4.3 Theoretical analysis of the damage growth fluctuations: A disordered elastic interface analogy

The fluctuations in damage growth, despite their apparent complexity, have been shown to follow some simple evolution laws, described by power laws with universal exponents. Interestingly, such a picture seems also to emerge from the different experimental and numerical studies devoted to damage spreading in quasi-brittle materials with in particular the clear demonstration of power law behaviors for the statistics of avalanches [37], even though a consensus on the value of the measured exponents and their universality is far from being reached. As a result, we believe that our model, although very simplified, contains the key ingredients necessary to describe the statistics of avalanches in disordered quasi-brittle solids. In the following, we seek to determine why power law and universality emerge from the statistics of damage growth in our model. And whether or not these behaviors can be interpreted in terms of critical phenomena. At the end, we hope that our understanding of the emergence of such behaviors in our simplified model will provide relevant information regarding the apparition of such laws in experiments and simulations of quasi-brittle failure.

In our approach described in Chapter 2, the power law behaviors result from the coaction of randomness in the material fracture properties and the mechanism of driving force redistribution that takes place after damage events. Indeed, the process of force redistribution in presence of disorder is known to give rise to unstable *cascades* of individual events that are generally power law distributed [1, 6, 14]. To go a step further in the analysis of our model and determine the actual nature of the critical behavior evidenced in the simulation results, we now explore analytically the growth of damage as predicted by our model.

The resolution of damage models in disordered materials has been already proposed in [59, 94] for simpler redistribution laws, like *e.g.* in the global load sharing fiber bundle. In that case, the successive redistributions can be tracked and the resulting power laws predicted analytically. However, these types of models remain rather far from a realistic description of the failure process in actual quasi-brittle materials characterized by inhomogeneous redistribution functions. In addition, the abrupt failure of individual elements assumed in these approaches does not seem appropriate to describe the progressive damage evolution and the transition to failure as observed in quasi-brittle solids (see Appendix B for a more extended discussion). As a result, we seek for an alternative theoretical framework. A natural class of model for describing quasi-brittle failure is the one describing the evolution of elastic manifolds driven in random media [6, 36, 68]. Indeed, the corner stone of these approaches is also the interplay between the disorder and the redistribution of driving force along the interface when a part of it moves forward after depinning from the surrounding disorder. For that reason, depinning models of elastic interfaces have already been proposed for explaining some specific failure properties of quasi-brittle materials, in the context of the study of failure strength size effects [113]. Here, we show that there is indeed an intimate connection between damage spreading in disordered materials and disordered elastic interface problems.

This section is organized as follows. First, the damage evolution law proposed in Chapter 2 is linearized around the homogeneous problem solution. This allows to show that the damage evolution law is actually similar to the problem of driven elastic interface where the properties are evolving with the distance to localization. Then, we consider the mean field limit of our model and obtain the value of the exponents involved in the damage growth statistics for an infinite internal length $\ell_0 \to +\infty$. In particular, the exponents β and μ obtained analytically are compared with those obtained numerically in the previous sections of this chapter. We also show that the stability analysis performed in Chapter 3 for predicting the onset of localization can be performed easily in this new formulation of the model.

4.3.1 Analogy between damage growth and driven disordered elastic interface

We provide first a basic description of the problem of elastic interfaces driven in disordered media, first proposed in Ref. [30], and schematically represented on Fig. 4.10. Consider heterogeneities randomly distributed in a medium of dimension D that exert pinning forces on an elastic interface of dimension $D-1$. The interface is initially in a flat configuration and we study the evolution of its position and geometry as we apply an external driving f on it. In fact, we consider that the external driving is applied through the slow motion of a rigid bar connected to the interface through springs of fixed stiffness, as represented schematically on Fig. 4.10. We denote $d(\vec{x})$ the position of the interface with respect to this reference initial position. If f is too small (or equivalently, if the rigid bar is too close to the interface), the local driving force applied to the interface is not sufficient to overcome the pinning forces applied by the external medium. As a result, it remains pinned to its initial configuration. However, if the external force is gradually increased (or equivalently, if the rigid bar is gradually moved forward), the local driving forces along the interface will increase, allowing ultimately one point to move a little. Since the interface is elastic, this local displacement results in a force redistributions along the interface. This redistribution can trigger the movement of other parts of the interface, until the system eventually reaches a metastable equilibrium position at which it stays at rest. Moving the rigid driving bar very slowly will result in an intermittent evolution of the interface as it moves from one pinned position to another. In fact, the detailed study of such a model shows that interface motion displays micro-instabilities (or avalanches) that are both localized in time and space. In addition, this intermittent dynamics can be characterized by scaling laws and scaling exponents, the value of which depends only on the dimension D of the medium and the type of elasticity (in other words, on the type of redistribution). If the function redistribution is maintained constant and the rigid bar is moved at constant velocity, the interface reaches a stationary state characterized by power law distribution fluctuations that can go on indefinitely.

With that description, the analogy with our damage model is rather straightforward. The heterogeneities reflects the fracture energy thresholds $Y_c(\vec{x})$ and the interface position represents the

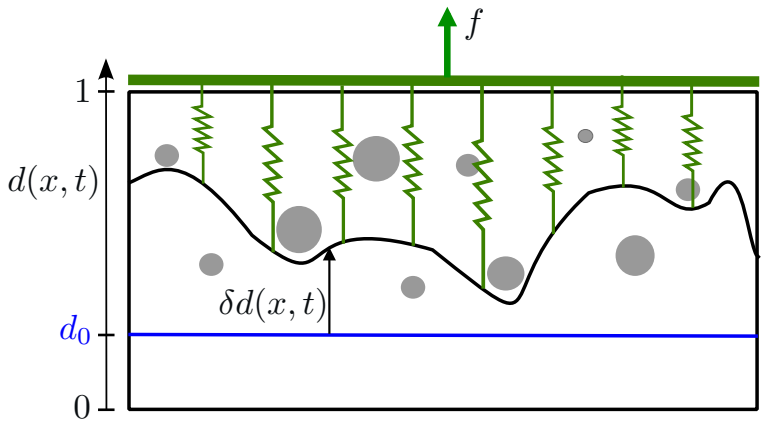

Figure 4.10: Schematic representation of an elastic interface evolving in a disordered medium. The interface is initially flat ($d(x) = d_0$) at $t = 0$, corresponding to a loading Δ_0. As an external loading f is applied, the interplay between elasticity and heterogeneities in the medium leads to a distorted interface.

damage field: It is initially a homogeneous field with $d(\vec{x}) = 0$ since the material is initially intact. As the driving Δ increases above a critical value Δ_{el}, the interface moves forward by jumping from one metastable state to another, each configuration being characterized by the position of the interface, or equivalently, by the damage field $d(\vec{x})$. The elasticity of the interface that describes how forces are redistributed when a zone of the interface moves forward (or when the material damages locally) are defined through the interaction function α introduced in our model. Interestingly, traditional models of pinning/depinning of elastic interfaces under displacement imposed conditions do not predict neither localization of the interface motion, nor unstable growth of the whole interface, as observed in our damage model. The origin of localization and failure within the frame of disordered elastic interface models for damage growth will be the central point of the following section.

4.3.2 Linearized evolution equation for the damage growth

To derive an analytical expression of evolution equation of the damage field, we limit our analysis to weakly heterogeneous damage field d that amounts to consider weakly heterogeneous materials prior their localization threshold. As a result, we note δd the perturbation of the damage field with respect to its average value $\langle d \rangle$, so that

$$d(\vec{x}) = \langle d \rangle + \delta d(\vec{x}). \tag{4.25}$$

Following the same calculation performed for investigating the stability of the damaged material (see Eqs. (3.6)-(3.8) where d_0 is replaced here by $\langle d \rangle$), one obtains

$$\dot{d}(\vec{x}, \Delta) \propto -\frac{1}{2}\Delta^2 k'[\langle d \rangle] - Y_{c0}(1 + \eta d(\vec{x})) + \frac{1}{2}\Delta^2 k''[\langle d \rangle]\langle d \rangle - \frac{1}{2}\Delta^2 k''[\langle d \rangle](\alpha_2 * d)(\vec{x}) - g(\vec{x}, d) \tag{4.26}$$

where $\alpha_2(\vec{x})$ denotes the convolution of the interaction function α with itself. To close the governing equation of the damage field, we have assumed that the rate of damage is proportional to the damage driving force, $\dot{d}(\vec{x},\Delta) \propto \mathcal{F}$. This assumption is largely used for deriving kinetic law from thermodynamic driving force, like *e.g.* in brittle fracture or plasticity problems to relate the crack speed [15, 34] or the plastic flow [96] to their driving force. Note that this particular kinetic law actually does not modify the model predictions regarding the onset of localization and failure, but also regarding the statistics of fluctuations.

We now introduce the time $t_0 = 0$ that corresponds to a loading Δ_0 at which the damage field is at equilibrium and constant in space, $d(x) = \langle d \rangle = d_0$. This allows for the determination of the homogeneous system equation that links the homogeneous damage d_0 and the loading Δ_0 at $t = 0$

$$t = 0 \Rightarrow -\frac{1}{2}\Delta_0^2 k'[d_0] - Y_{c0}(1 + \eta d_0) = 0. \tag{4.27}$$

As time evolves ($t > 0$), we consider a loading that evolves continuously with time via an external loading velocity v_{ext}. Consequently, the damage field deviates from its initial position d_0

$$t > 0 \Rightarrow \Delta = \Delta_0 + v_{\text{ext}} t,\ d(\vec{x}) = d_0 + \delta d(\vec{x}). \tag{4.28}$$

Using $\langle d \rangle = d_0 + \langle \delta d(\vec{x}) \rangle$ and $\dot{d} = \dot{\delta d}$, we obtain

$$\dot{\delta d}(\vec{x},t) \propto \delta\left[\Omega v_{\text{ext}} t - \delta d(\vec{x})\right] + (s - \delta)\int_\Sigma \alpha_2(\vec{x} - \vec{x}')\left[\delta d(\vec{x}') - \delta d(\vec{x})\right] d\vec{x}' - g(\vec{x}, d) \tag{4.29}$$

where we assume quasistatic loading conditions ($v_{\text{ext}} \to 0$). Note that the damage evolution law is valid up to the first order in the damage field perturbation δd since it has been linearized around a constant value d_0. Note also that since our damage model does not allow healing of the material ($\dot{\delta d} \geq 0$), a more accurate formulation of the damage evolution law is $\dot{\delta d}(\vec{x},t) \propto \max(0, \mathcal{F})$, where the total driving force $\mathcal{F}$ is the right term of the above equation. The different parameters of this equation correspond to

$$\begin{cases} s &= Y_{c0}\eta \\ \Omega &= \dfrac{\Delta_0 k'(d_0)}{Y_{c0}\eta(Y_{c0}\eta + \frac{1}{2}\Delta_0^2 k''(d_0))} \\ \delta &= Y_{c0}\eta + \dfrac{1}{2}\Delta^2 k''(d_0) \end{cases} \tag{4.30}$$

The interpretation of such equation can be done by considering again the scheme of Fig. 4.10 where the interface is represented in 1D by the damage field $d(x,t)$. The reference configuration is the flat interface located in d_0. It corresponds, at equilibrium, to a loading Δ_0. The interface is driven though the displacement of the rigid bar represented by the thick green line that moves at the velocity Ωv_{ext}. It pulls on the interface via springs of stiffness δ. The interface evolves in the disordered medium where heterogeneities are described by the function $g(x,d)$ and represented by the grey circles on the scheme. The interface gets distorted from its initial flat shape due to the interplay between

the heterogeneities and its elastic properties, expressed via the integral expression in Eq. (4.29). This term describes the driving force distribution along the interface as a function of its geometry $\delta d(\vec{x})$. Note that for a flat interface, this contribution is zero, so the driving force is constant along the interface. On the contrary, if a point located in $\vec{x}$ is in advance with respect to the rest of the interface ($\delta d(\vec{x}) > \delta d(\vec{x}')$ for all $\vec{x}'$), the driving force in $\vec{x}$ is then smaller than in other points (this is true as along as the interaction function is positive, *i.e.* for $\kappa = 0$). In other words, the interaction term contributes to maintain the interface as flat as possible, that is why it is referred to as the interface elasticity.

To emphasize the main difference between the evolution equation involved in traditional pinning/depinning models of interfaces driven in random media and that of our damage model, the evolution equation Eq. (4.29) is rewritten under the following form

$$\dot{\delta d}(\vec{x},t) \propto s\left[v_{\mathrm{m}}t - \delta d\right] + f(d_0)\left(\alpha_2 * \delta d\right)(\vec{x}) - g(\vec{x},d) \tag{4.31}$$

where the velocity $v_{\mathrm{m}} = -\Delta_0 k'(d_0) v_{\mathrm{ext}}/(Y_{c0}\eta)$ corresponds to the speed of the driving rigid bar and where the notation $f(d_0) = -\frac{1}{2}\Delta_0^2 k''(d_0)$ has been introduced. In standard depinning models, the prefactor of the elastic interaction term, $f(d_0)$, is generally a constant that do not vary during the interface evolution. However, in that case, $f(d_0)$ does vary with the interface position. Indeed, the reference position must be regularly updated so that the development $d(x) = d_0 + \delta d(x)$ performed around the reference position d_0 remains valid. The evolution of the prefactor in front of the interaction term in the evolution equation has important consequences. In particular, it leads to sharper redistributions of the damage driving force, even though the actual shape of the interaction function remains fixed by the expression of the function α. The evolution equation in this simple form will allow to perform some theoretical calculations in the mean field limit to predict the statistics of avalanches, as shown in the following.

The linearized expression of the total damage driving force given by the right hand term of Eq. (4.31) gives the opportunity to determine again the stability of the interface. Indeed, assuming a homogeneous material by setting the term $g(x,d)$ to zero and a perturbation of the form $\delta d(\vec{x}) = \delta d_0(1+\cos(\vec{q_0}\cdot\vec{x}))$, $\mathcal{F}$, the total driving forces, writes as

$$\mathcal{F}(\vec{x},\Delta_0) = sv_m t + (f(\Delta_0)\tilde{\alpha}^2(\vec{q_0}) - s)\delta d_0 \cos(\vec{q_0}\cdot\vec{x}) - \delta\delta d_0 \tag{4.32}$$

where we have used $\alpha_2(\vec{x}) * \cos(\vec{q_0}\cdot\vec{x}) = \tilde{\alpha}^2(\vec{q_0})\cos(\vec{q_0}\cdot\vec{x})$. From the expressions of k and $f(d_0)$ given in Eq. (4.30), and using the definition of the function $\tilde{\mathcal{G}}(\vec{q},\Delta)$ of Eq. (3.15), we can express the variations of the total damage driving force as a function of the damage perturbation

$$\frac{\delta\mathcal{F}}{\delta\delta d_0}(\vec{x},\Delta_0) = \tilde{\mathcal{G}}(\vec{q_0},\Delta_0)\cos(\vec{q_0}\cdot\vec{x}) + \tilde{\mathcal{G}}(0,\Delta_0). \tag{4.33}$$

Using the same arguments as in Chapter 3, we obtain again the critical initial interface position d_h and d_c and their corresponding loading Δ_h and Δ_c at localization and failure, respectively. The

positiveness of the prefactor of the cosine, $\tilde{\mathcal{G}}(\vec{q}_0, \Delta_0)$, provides the former, while the sign of the entire expression, at the critical mode, sets the stability and hence gives the failure criterion. We find the very same criteria for localization and failure, confirming the consistency between the stability analysis performed in Chapter 3 and the evolution equation of the damage field derived here.

4.3.3 Exponents prediction

To predict the scaling properties characterizing the statistics of damage fluctuations, we use the work of Zapperi *et al.* [119] who analyzed an equation similar to the damage evolution law of Eq. 4.31. They analyzed the dynamics of an interacting ferromagnetic domain wall evolving in a random uncorrelated medium when an external field $H(t)$ is applied. The position of the domain wall is noted $h(\vec{x},t)$ and the interactions between points of the wall are described through a function $J(\vec{x})$. They obtained an evolution equation by differentiating the total energy of the system:

$$\frac{\partial h(\vec{x},t)}{\partial t} = H(t) - kh + J(\vec{x}) * (h - h(\vec{x},t)) - \eta(\vec{x},h) \tag{4.34}$$

where $\eta(\vec{x},h)$ is a random field, h the average of the field $h(\vec{x})$ and the term $-kh$ is a demagnetizing field of intensity k. By considering the mean-field limit, where the function J becomes a constant in space, they determined that the avalanche exponent β of Eq. (4.5) scales as $\beta = 3/2 - c/2$ where c is a constant proportional to the driving rate. Moreover, they also demonstrated that the cutoff of the distribution scales as k^{-2}.

To use these results in the case of our damage model, we write Eq.(4.31) in the mean field limit:

$$\dot{\delta d}(x,t) \propto s v_{\mathrm{m}} t - \delta \langle \delta d \rangle + s\left(\langle \delta d \rangle - \delta d(x,t)\right) - g(x,d) \tag{4.35}$$

where we have used that in the mean field limit $(\alpha_2 * \delta d)(x) = \langle \delta d \rangle$. The identification with Eq. (4.34) is rather clear: The demagnetizing field $H(t) \sim s v_{\mathrm{m}} t$ corresponds to the driving, the location $h(\vec{x},t)$ of the domain wall corresponds to the deviation of damage from the initial configuration, $\delta d(\vec{x},t)$, while the intensity of the demagnetizing field k is the parameter δ introduced in the damage evolution equation (4.29) and expressed in Eq. (4.30). Finally, the constant kernel in the mean field limit gives $J = s$.

Considering quasistatic loading conditions, the parameter c in their exponent prediction is set to zero. Hence, in the mean field limit, the avalanche size distribution exponent is $\beta = 3/2$. Moreover, to determine the dependency of the cutoff of the distributions with the control parameter, we shall relate the previously defined parameter given by Eq. (3.2), denoted here by δ_Δ, to the parameter δ (analogous to k in their case) of Eq. (4.35). Using that initially the loading and damage d_0 are

related through Eq. (4.27) and using a series expansion when δ_Δ tends to 0 leads to

$$\delta = Y_{c0}\eta + \frac{1}{2}\Delta_0^2 k''(d_0) \sim \sqrt{\delta_\Delta} = \sqrt{\frac{\Delta_c - \Delta_0}{\Delta_c - \Delta_{el}}} \tag{4.36}$$

Consequently, from the result of Zapperi *et al.*, the cutoff of the avalanche S^* is expected to scale as

$$S^* \sim \delta_\Delta^{-1} \tag{4.37}$$

and since $\beta = 3/2$ in the mean-field limit, using the relation between the average avalanche size and the cutoff given by Eq. (4.12), we also expect

$$\langle S \rangle \sim \delta_\Delta^{-1/2}. \tag{4.38}$$

Considering the case where the interaction function parameter κ is set below its critical threshold, the exponents measured in Sec. 4.1.2 are in good agreement with these predicted values (see Tab. 4.1 for a review of the values). Surprisingly, whatever the internal length value, damage temporal organization is hence equivalent to that of a system in a mean field limit. If a small deviation close to failure was observed for internal lengths tending to the heterogeneities size, the general statistical behavior remains very similar to that obtained for an infinite internal length scale.

4.4 Conclusions

Damage evolution takes place through sudden bursts of dissipated energy. Due to the very small loading rate, it here takes place at constant applied displacement and hence corresponds to macroscopically observable drops of force. These avalanches of damage events present a strong intermittency and the signal can be seen as a crackling noise, as observed in experiments. The thermodynamic consistency of our model allows to equivalently consider avalanches in terms of number of damage event, dissipated energy but also kinetic energy, as measured in experiments. The linear scalings obtained between these quantities allow to restrict the analysis to only one observable.

As for the localization, critical mode and failure predictions, the interaction function appears to greatly control the system response via its influence on the precursors to failure organization. For an interaction function where elements are only reloaded after a damage event ($\kappa = 0$) we have shown the existence of a power law behavior of the typical avalanche size independently of the range of the interactions. We remind that the latter is controlled via the internal length ℓ_0 introduced in the interaction function. A remarkable feature of our model is that the intermittency in the damage growth observed at a global scale is independent of ℓ_0, the avalanche statistics being similar for local ($\ell_0 \to \xi$) and mean field ($\ell_0 \to \infty$) limits. Instead, the characteristic extent of the load redistribution is shown to control the spatial organization of the damage clusters formed during avalanches and the resulting cumulated damage field. If a large scale separation between ℓ_0 and the system size is chosen,

the largest avalanches are shown to have an increasing spatial extent. Indeed, the smallest avalanches are localized over a length fixed by the internal length, while the largest can extend in space via the formation of a cascade of small clusters. It directly affects the damage field, as it becomes more and more correlated over an increasing correlation length that display the same power law behavior with the distance to failure than the spatial extent of the clusters. Therefore, for small internal lengths, non-trivial scalings are obtained between the typical avalanche size, its spatial extent, and the correlation length of the damage field that we can characterize through the fractal dimension of the clusters. All these quantities follow power law behaviors and diverge close to failure which corresponds also to the onset of localization for $\kappa \leq \kappa_c$.

At the opposite, when strong unloading is made possible through a sign changing interaction function ($\kappa > \kappa_c$) the precursors behavior drastically changes. In that case, the localization of damage takes place prior to complete failure. We have shown that the average avalanche size and their spatial correlation length increases first as the system is driven close to localization, this quantity reaches a plateau value in the post-localization regime. This upper bound is shown to be related to the finite wavelength λ_c of the critical mode identified previously from the stability analysis in the previous chapter. Once localization takes place, the damage field builds up over this characteristic length, increasing the strength of the correlations within the damage field but not its spatial extent.

Therefore, even though $\kappa > \kappa_c$ is excluded from this interpretation, the divergence of the correlation length of the damage field and the average avalanche size at failure for $\kappa = 0$ argues for a critical interpretation of failure. To characterize this transition, we show that our damage model can be viewed as a depinning model of an elastic interface driven in a random medium. The damage evolution law is governed by the elastic term that describes the interactions between the different regions of the interface. In our case, it corresponds to the convolution with itself of the introduced interaction function. Hence, the damage level in the material can be seen as the position of an elastic interface driven in a disordered media and where elastic redistributions are given by the interaction function of our non-local damage model. Within this framework, using the work of Zapperi *et al.* [119] who addressed the mean field limit of elastic interface problems, we acheive a relevant prediction of the statistics of avalanches as obtained in the simulations. In particular, we capture quantitatively the power law increase of the average avalanche size close to failure. It also allows to identify the control parameter that can be defined either as the distance to failure in terms of displacement or in terms of average damage level.

As a consequence, we believe our model contains the relevant ingredients required to capture properly the precursor behavior, namely temporal intermittency and spatial clustering. In particular, it can be used to predict the scaling behavior of precursors beyond the mean field limit. It amounts to investigate the pinning/depinning dynamics of an interface with a non-local elasticity provided by the interaction function involved in the non-local formulation of the damage model. We now move to the practical application of these concepts trough the experimental study of the compression up to

localization of arrays of soft hollow cylinders.

CHAPTER 5

COMPARISON WITH EXPERIMENTS: COMPRESSION OF A 2D ARRAY OF HOLLOW SOFT CYLINDERS

Acoustic emissions have been a preferred mean to study damage spreading during quasi-brittle failure [26, 33, 35, 42]. It allows analyzing the dynamics of damage growth and extracting the location of damage events. However, a major difficulty to overcome with this approach is the relation between the acoustic energy of the damage events and the actual energy dissipated into failure at the microstructure level in the material. Even though this relation can be explored theoretically [114], or experimentally [107], acoustic emission provides indirect information on the energy of the damage events that might be complex to interpret. Another obstacle in the experimental study of damage spreading is the limited statistics of damage events, especially because the transition to failure in quasi-brittle materials is unstationary, which imposes to perform statistical analyses of the experimental data at some fixed distance to failure. Many studies actually do not address this problem and compute statistical distributions over the full fracture experiments. This gives rise to major problems to interpret the measured behaviors. To obtain a proper dialogue between models and experiments, we aim at performing a fracture experiment from which damage events can be investigated both at the local scale, trough the damage field, and the macroscopic scale, through the mechanical response of the specimen.

The complex features observed both experimentally and numerically result from local dissipative events. At the local scale, they lead to complex strain and stress redistributions and interactions as defects are progressively formed, allowing for both a spatial organization of the damage events and crackling noise. At the sample scale, they induce a gradual degradation of the elastic properties of the specimen and result in a non-linear characteristic behavior. As argued in this chapter, such a system can be actually obtained using a two-dimensional granular material under compressive loading conditions. It will be shown to mimic many aspects of the failure behavior of disordered elasto-damageable solids, with which a clear analogy can be established. We will also show how to take advantage of the

lower dimension of this system to characterize its mechanical behavior both at the local and global scales as it is driven towards localization and failure.

Two-dimensional packings of rigid cylinders placed in a transparent box and under compressive loadings have been largely used to explore force chains in granular systems [43]. This setup, inspired by the Schneebeli model [104], offers the advantage to be observed from the lateral side through a camera. It also allows controlling to some extent the level of disorder in the material: A weak disorder resulting from variations in the contact conditions between cylinders is inherent to such a system, even for ordered packings[108]. Yet, it can be enhanced by the introduction of hard and soft elements [109] or even large variations in the elements diameters [11]. Photoelasticity techniques reveal that even for weak disorder, such a 2D array lead to inhomogeneous distributions of stress and chain forces, as it is generally observed in granular media. Inspired by these previous studies, Poirier *et al.* [90] replaced the rigid cylinders by hollow soft elements consisting in drinking straws. In this configuration, the experiment resembles to the ones performed by Papka and Kyriakides who study the crushing of honeycomb materials with circular cells [79, 80]. Both setups give rise to localization of the deformation at some critical compression level. Poirier's experiment is shown on Fig. 5.1. The loading is applied through a piston and photographs are taken during the experiment. Under strain-controlled compression, the weakly disordered regular array shows a strong non-linear behavior and softening, as shown on the macroscopic response of Fig. 5.2. Moreover, the pictures allow observing and characterizing the gradual local deformation of the straws, eventually localizing in the system as illustrated in Fig. 5.1.

Such an experimental setup is appealing to investigate the transition to localization and precursors in disordered media. Indeed, two-dimensional arrays of soft cylinders naturally display disordered properties. Moreover, under compression they give rise to localized dissipative events that result from the friction between cylinders in contact. These events induce a degradation of the macroscopic stiffness that reflects on the non-linear behavior of the force-displacement response of the array. Finally, this setup is interesting as it gives access not only to the macroscopic properties with the measured force-displacement response, but also to the local deformation field by tracing the motion of the individual elements and their deformation. Controlling the system in strain allows to observe the drops of force associated with dissipative events and define quantitatively avalanches, which result from long-range elastic redistributions in the medium. This will allow us to fully characterize the temporal clustering of local dissipative events.

In the following, we first present the experimental setup, which is similar to Poirier *et al.*'s experiment. Then, the study of the macroscopic response combined with the local observations made with the camera allow us to characterize the macroscopic mechanical response and the onset of localization. We use an analogy between our experimental device and 2D elasto-damageable solids to predict theoretically the onset of localization and failure, following the work of Démery *et al.* [Démery et al.]. In the last part, we investigate the statistics of fluctuations and the avalanches

dynamics of damage growth process.

Figure 5.1: Experiment performed by Poirier *et al.* [90] (image taken from [12]) on a 2D regular array of hollow soft cylinders confined in a rectangular box. The compressive loading is applied via the piston. Note the localization of the deformations on the last image.

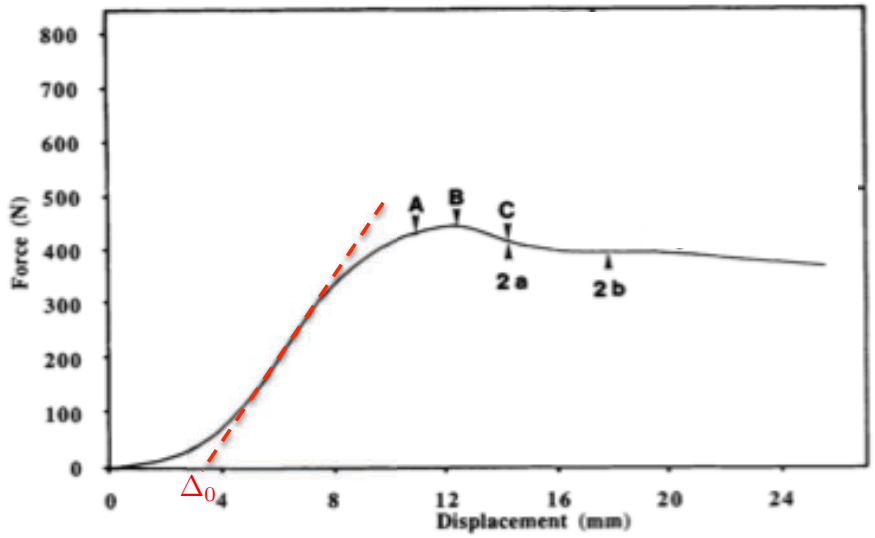

Figure 5.2: Macroscopic response of the array of hollow soft cylinders as measured by Poirier *et al.* [90] using the setup described in Fig. 5.1. The system displays a nonlinear behavior before softening that is followed by a plateau. We indicate the method used to remove the initial non-linear behavior: The red dashed curve corresponds to the extrapolated linear elastic response. Its intersection with the displacement axis fixes the corrected initial displacement Δ_0. The first part of the curve which is located above the red line is finally removed.

5.1 Experimental setup

We follow the experimental setup designed by Poirier *et al.* [90]: Our system consists in a regular assembly of 41 rows and alternatively 36 or 35 columns of straws, as schematically repre-

sented in Fig. 5.3. The straws are of 3 cm length and 5 mm diameter. The straws are placed in a transparent box of dimension $20.5 \times 18 \times 3$ cm. As a results, pictures of the array can be taken during the test from the lateral side of the box using a D800 Nikon camera with a resolution of 6000×6000 pixels. A constant displacement rate is applied via an AG-X Schimadzu test machine through a beam placed on the upper layer of the straw packing. During the test, the force imposed to the material is measured using a 10 kN load cell with an acquisition rate of 1000 Hz. The load cell provides force values with a precision better than 0.5 % from forces as low as 20 N.

Four experiments were realized. Note that all the straws were replaced after each experiment. Tests labeled $\#1$, $\#2$ and $\#3$ were performed at a strain rate of 2 mm/min. Before the test, we realized three cycles of 6 mm amplitude that is comprised in the linear elastic range of the system. These preliminary cycles are used to organize the packing and avoid subsequent strong reorganizations during the test with monotonic increasing displacement. For these three experiments, pictures were taken with an acquisition rate of one image every two seconds. For the test $\#4$, no cycle was performed and a higher displacement rate of 5 mm/min was investigated. Pictures were taken here every five seconds.

In addition to the small variations in contacts between straws, for some experiments some other sources of heterogeneities played an important role. For experiment $\#1$, a few straws were missing, creating vacancies in the array. For experiment $\#2$, we realized that a layer of black straws that was mixed with the other colored straws were actually softer. They resulted in an anticipated localization of deformation, hence this experiment will not be considered in the following analyses. For the third and fourth experiments, only local misarrangements were noticed.

5.2 Mechanical behavior

5.2.1 Macroscopic Force-Displacement response

The macroscopic force-displacement response of the packing is shown on Fig. 5.4 for each of the four experiments. On this representation, the first part of the curve was corrected to remove the initial non-linearity observed at small loading, as explained in Fig. 5.2. We think that this behavior results from strong local rearrangements of the straws that are not perfectly ordered before the test starts and from some misalignment of the top straws, which come in contact progressively with the beam as the loading initially increases. The initial part of the curve for $\Delta < \Delta_0$ with $\Delta_0 \simeq 2-3$mm is replaced by a linear elastic response. Hence, the packing is considered to first deform elastically before non-linear events that softens the material take place.

We observe variations in the mechanical response from one experiment to another. However, the general behavior remains the same: Above some critical loading, the response deviates from

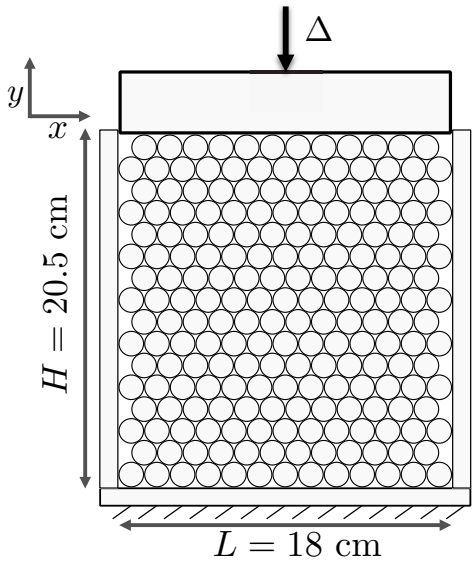

Figure 5.3: Schematic representation of the experimental setup. 41 rows and alternatively 36 or 35 columns of soft hollow cylinders (drinking straws) are placed in a transparent box of size $H \times L \times b = 20.5 \times 18 \times 3$ cm. The edges are fixed, and a macroscopic displacement is applied with a constant rate on a beam placed on the top of the array.

the linear elastic response. Until peak force, the straws, as observed with naked eyes, deform rather homogeneously, even thought some straws in direct contact with the walls are more compressed due to frictional effects taking place at the edges (Fig. 5.5a). At the peak, the deformation field is still rather homogeneous, as shown on Fig. 5.5b. However, soon after, we observe a progressive crushing of the straws in some localized region of the array, as shown in Figs.5.5c and 5.5d. This localization is accompanied by a slight decay of the applied force. Generally, the region where deformation concentrates initiates from the top corners of the system, which we believe results from the enhanced friction at the walls of the box. This effect is also observed in Poirier's experiments (see Fig. 5.1). The region of localized deformations progressively develops until spanning from one side of the box to the other. For the experiments $\#2$ and $\#4$, the force finally increases again. For experiments $\#1$ and $\#3$, this increase is also observed, but later, next to $\Delta = 30$ mm. At this point, the straws located just above the region of localized deformations also crush and contribute to further increase the width of the localization band. At the opposite, straws below the band remain unaffected by the subsequent increase of the loading.

A zoom on the macroscopic response observed for experiment $\#3$ is shown in the inset of Fig. 5.4. The force drops reveal sudden events that take place during the test and soften the material. Similarly to our numerical investigation of damage growth in disordered media, the force-displacement curve displays short softening phases characterized by force drop that alternate with longer periods during which the force increases rather linearly with the displacement. These force drops are interpreted as the signature of dissipative processes associated with local rearrangements within the array of cylinders. If the actual nature of the dissipative processes into play remains diffi-

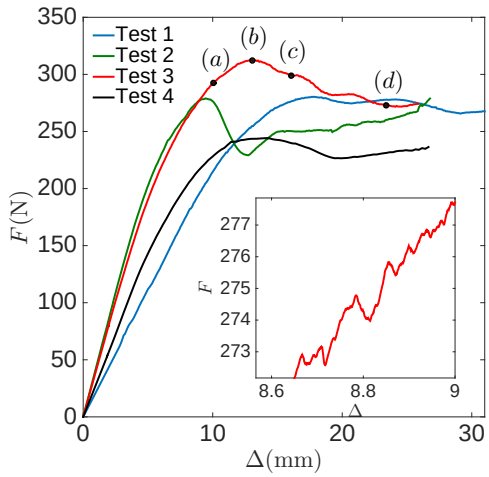

Figure 5.4: Macroscopic force - displacement response obtained for each experiment. A zoom for the experiment #3 is shown in inset. It highlights the intermittent behavior of the systems resulting from local sliding events in the system. The dots and letters indicate the loadings to which the pictures shown on Fig. 5.5 corresponds to.

cult to verify experimentally, we think that frictions between straws as they rearrange to fill the space between them as they deform is the central mechanism. In the following section, we will see how these fluctuations in the macroscopic response can be used to define avalanches of dissipated energy.

5.2.2 Intermittent dynamics of the compaction process: Avalanches definitions

We now focus on the fluctuations in the mechanical response of the array of hollow cylinders. The signature on the macroscopic force-displacement curve of the dissipative events taking place at the local scale in the system is schematized on Fig. 5.6. At some critical loading Δ_i, the behavior deviates from the linear response, and the force progressively decreases. The force evolution can then be rather complex until it increases again significantly to recover a linear behavior. This behavior is different from the signature of the damage events obtained from our unidimensional model of elasto-damageable disordered material. Indeed, this model predicts a sudden drop of the force at constant applied loading followed immediately by another linear regime, as shown on Fig. 4.1a. This difference may arise from the mechanical response of individual elements that differ from one system to another: While the elements considered in our model are unstable under fixed imposed displacement (see Fig. 2.4), they are actually stable in the experiments, as shown in [57]. As a result, the displacement must be increased further, up to Δ_e to fully complete the damage event and recover a linear elastic behavior.

Hence, to define avalanches, we use another method than that proposed in the context of our model. We consider the response of the system that one would obtain if the compression test was realized under imposed force, and not under imposed displacement as actually done according to our experimental procedure. In that case, the elastic response between avalanches, *i. e.* for $\Delta \leq \Delta_i$ and

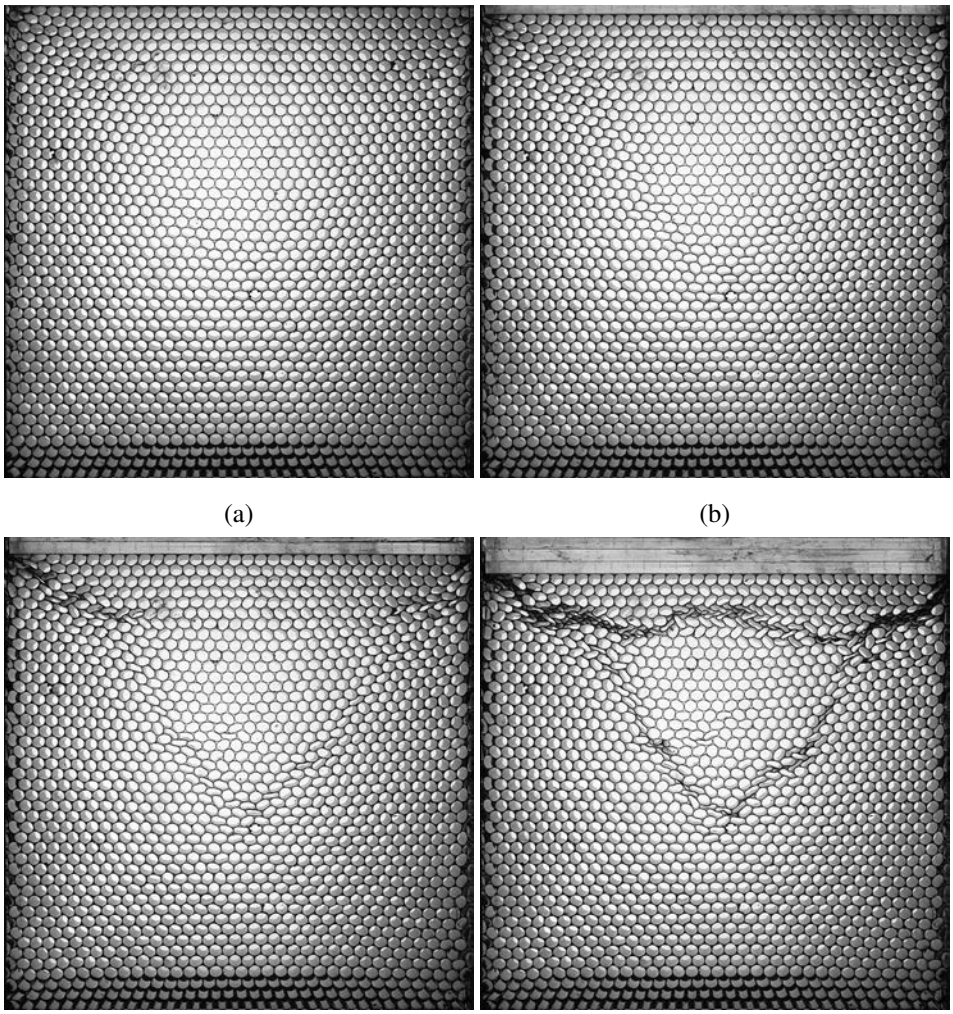

(a) (b)

(c) (d)

Figure 5.5: Pictures of the array of cylinders for the experiment $\#3$ taken respectively (a) before, (b) at, (c) after and (d) far away from the peak. The corresponding loadings are indicated on Fig. 5.4. In (a) and (b), the cylinders first deform rather homogeneously, before a region of higher deformation nucleates shortly after the peak (c) and extends to eventually span the whole system (d).

$\Delta_e \leq \Delta$ would be the same. But the behavior for $\Delta_i \leq \Delta \leq \Delta_e$ during the avalanche would change since it would give rise to a micro-instability characterized by a plateau behavior at constant force F_i, as illustrated in Fig. 5.6. On this schematic representation, the upper curve is the response that would be obtained if controlling the system in force and the curve bellow, between the yellow and red areas, is the actual material response when driven in displacement.

Using this definition, we can determine the transfer of mechanical energy into dissipated energy during the avalanche at constant force. The variation of mechanical energy ΔE_m corresponds to the work of the external force during the avalanche minus the variation of elastic energy. Considering the $k-$th avalanche taking place at the displacement $\Delta_i \leq \Delta \leq \Delta_e$ at the constant force F_i, the

variation of mechanical energy follows

$$\Delta E_{\mathrm{m}} = \Delta W - \Delta E_{\mathrm{el}} = F_{\mathrm{i}}(\Delta_{\mathrm{e}} - \Delta_{\mathrm{i}}) - \frac{1}{2}F_{\mathrm{i}}(\Delta_{\mathrm{e}} - \Delta_{\mathrm{i}}) = \frac{\Delta W}{2} = \Delta E_{\mathrm{el}}. \tag{5.1}$$

From the scheme of Fig. 5.6, we see that half of the area under the curve at constant force corresponds to the mechanical energy, while the other half is the dissipated energy ΔE_{d}. This last term is actually the sum of two contributions: (i) The largest part in red is called rupture energy ΔE_{r} by analogy with our theoretical approach, even though it corresponds to energy dissipated by friction during to local rearrangements in the network; (ii) the smallest part in yellow corresponds to the excess of mechanical energy released that is not consumed into fracture, and that we assume to be transferred into kinetic energy, and eventually dissipated in the material by heat and acoustic emission. Its contribution remains, as will be shown, of meager amplitude. Hence, we can write the transfer of energy during avalanches as

$$\Delta E_{\mathrm{m}} = \Delta E_{\mathrm{d}} = \Delta E_{\mathrm{r}} + \Delta E_{\mathrm{k}} \simeq \Delta E_{\mathrm{r}} \tag{5.2}$$

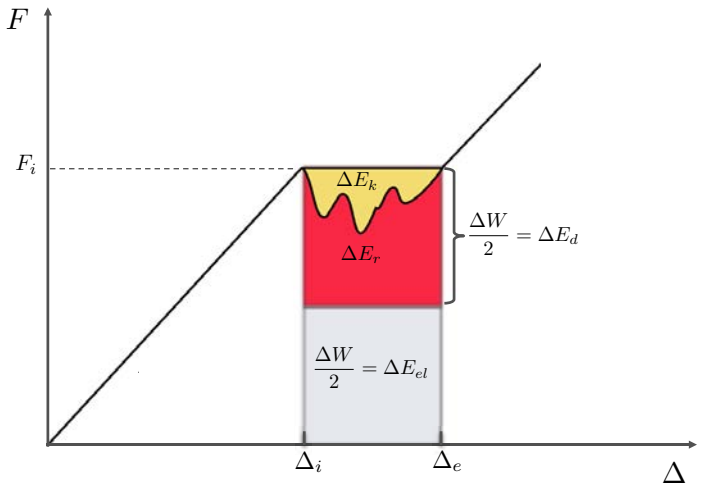

Figure 5.6: Avalanches definition: Schematic representation of the response of the system at imposed strain and imposed stress. During elastic deformation phases the responses are identical, while during avalanches the former exhibits drops of force and in the latter case the force remains constant. The corresponding variations of work of external force ΔW, elastic energy ΔE_{el},dissipated energy ΔE_{d}, kinetic energy ΔE_{k} and fracture energy ΔE_{r} during the avalanche are indicated as well as their relationships. During the avalanche for $\Delta_{\mathrm{i}} \leq \Delta \leq \Delta_{\mathrm{e}}$, the mechanical energy $\Delta E_{\mathrm{m}} = \Delta W - \Delta E_{el} = \Delta W/2$ is dissipated into fracture and kinetic energy $\Delta E_{\mathrm{d}} = \Delta E_{\mathrm{r}} + \Delta E_{\mathrm{k}}$.

Using the experimental force-displacement curve $F(\Delta)$, the evolution of the work of the external force W, the elastic energy E_{el} and the dissipated energy E_{d} can be computed as a function of the loading. To do so, we first use the force drop to define the displacements Δ_{i} at the onset of individual avalanches, and deduce the displacement Δ_{e} at the end assuming a constant force. Then, variations of energy are calculated using $\Delta E_{\mathrm{el}} = \Delta W$ between two avalanches, and $\Delta E_{\mathrm{el}} = \Delta E_{\mathrm{d}} =$

$\Delta W/2$ during the dissipative events. To study their evolution, we can plot them as a function of our control parameter, defined here as the distance to the peak δ

$$\delta = \frac{\Delta_\mathrm{p} - \Delta}{\Delta_\mathrm{p} - \Delta_\mathrm{el}} \tag{5.3}$$

where Δ_p is the displacement at the peak load and Δ_el is that at which the first dissipation event takes place. Hence, δ ranges from 1 (first avalanche) to 0 at the peak, and becomes increasingly negative after the peak. Figure 5.7a shows the cumulated energy variations as a function of δ for the experiment $\#3$. As expected, the three contributions W, E_el and E_el increase as one gets closer to the peak at $\delta = 0$. We also verify that the energy W injected in the system through the work of the external force equals to the sum $E_\mathrm{el} + E_\mathrm{d}$ of the elastic energy stored in the material and the dissipated energy at any time δ. A zoom on the dissipated energy, as shown in the inset, emphasizes the intermittent nature of the dissipation: The plateau regions correspond to elastic phases and are separated by avalanches of duration $\Delta\delta$ during which an energy ΔE_d is dissipated. Note that the same pattern is observed when looking at the evolution of the cumulated kinetic or rupture energy.

We now test the consistency of our description: We have assumed that between dissipative events, the material is elastic and characterized by the macroscopic stiffness K_m. This macroscopic stiffness decays during compaction as more dissipative events take place in the material. For our approach to be consistent, K_m should represents the instantaneous material stiffness

$$K_\mathrm{m} = \frac{F}{\Delta}. \tag{5.4}$$

But it should also be consistent with the total elastic energy stored in the material through the relation $E_\mathrm{el}(\delta) = \frac{1}{2}\Delta^2 K_\mathrm{E}(\delta)$. To test this correspondence, we compute the stiffness K_E from energy conservation arguments using

$$K_\mathrm{E} = \frac{E_\mathrm{el}}{\frac{1}{2}\Delta^2} \tag{5.5}$$

where the cumulated elastic energy E_el is obtained from the work of the external force computed from the experimental $F(\delta)$ curve: During the elastic phases, the elastic energy increases of $\Delta E_\mathrm{el} = \Delta W$, while during avalanches it increases of $\Delta E_\mathrm{el} = \Delta W/2$. To account for the noise in the force measurement that results in non-physical force drops, we remove the smallest avalanches. An avalanche is removed if the difference between the plateau level F_i (see Fig. 5.6) and the minimum force during the avalanche is less than 0.2 N, which is of the order of the actual load cell accuracy. The instantaneous stiffness K_m defined in Eq. (5.4) is calculated before and after each avalanche. The two stiffnesses thereby obtained are compared on Fig. 5.7b where their evolution is shown as a function of δ for each experiments. For sake of clarity, we normalize them by the stiffness value K_0 measured at the end of the elastic regime for $\delta = 1$. For all experiments, the two procedures give similar values of macroscopic stiffness within 3 %. In the following, we preferentially use K_m so that it can also be

defined in the post-peak region.

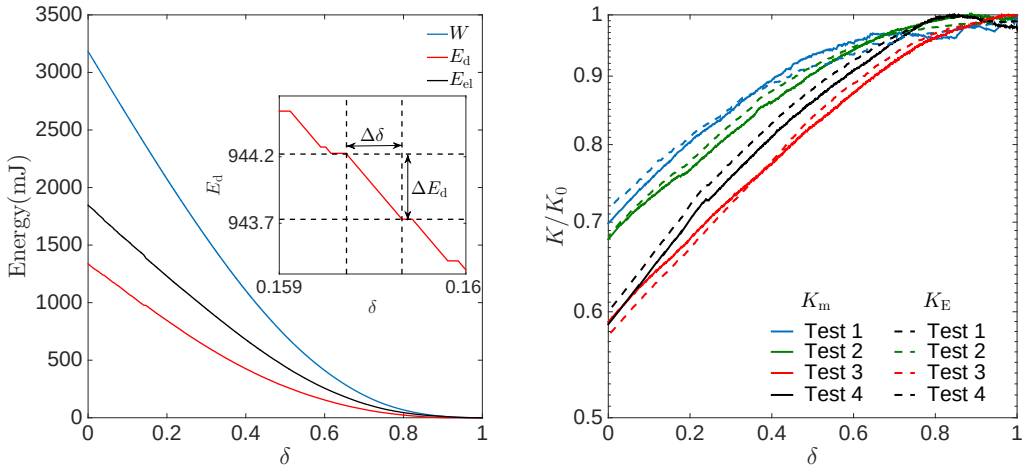

(a) (b)

Figure 5.7: (a) Evolution of the different energetical contributions during the experiment #3 as a function of the distance δ to peak load: W, E_{el} and E_{d} are the work of the external force, the elastic energy and the dissipated energy, respectively. The inset shows a zoom of the latter one and highlights the intermittent nature of the dissipation process. It also allows for the definition of the avalanche duration $\Delta\delta$ and dissipated energy ΔE_{d}; (b) Evolution of the stiffness $K_{\mathrm{m}} = F/\Delta$ as derived from the macroscopic force-displacement curve (solid lines) and from the elastic energy $K_{\mathrm{E}} = E_{\mathrm{el}}/(1/2\Delta^2)$ (dashed lines), for each experiment. Deviation of K_{E} with respect to K_{m} is less than 3%, supporting the consistency of our approach.

In summary, from the study of both the macroscopic response and a qualitative observation of the pictures taken during the experiments, the compaction experiments can be divided in four stages. First, we observe a linear elastic domain, before dissipative events localized in time generate a non-linear macroscopic response. At the peak load, the system appears still homogeneously deformed when observed with naked eyes. After the peak, during the softening stage, the deformation progressively localizes into a narrow band that grows until spanning the whole system. At this point, the force might increase again, associated with the further crushing of the upper straws and the broadening of the compaction band. These four steps are very similar to the four phases observed during failure of elasto-damageable solids. The non-linearities observed at the sample scale result from dissipative events taking place at the cylinder scale in the materials. In particular, these events deteriorate the overall material stiffness that decreases from its initial value. In the following, we show how the concepts derived previously to predict localization and failure in elasto-damageable materials apply to the array of soft cylinders. The investigation of the statistics of avalanches is left for the last part of this chapter.

5.3 Characterization and prediction of localization

The localization of deformation is a central feature of the mechanics of elasto-damageable solids. Our two-dimensional packing of hollow cylinders allows for its direct observation. To infer the localization onset, we look at the scale of the cylinders and investigate the deformation field during compaction. Describing our material as an elasto-damageable solid, localization is investigated theoretically following the approach developed in Chapter 3. Approximating our material as an isotropic elastic solid, we use the work of Démery *et al.* [Démery et al.] that provides the actual stress and strain redistributions after damage events take place. This allows predicting the critical loading at localization and the geometry of the compaction bands that are compared with the experimental observations.

5.3.1 Determination of the localization threshold from the deformation field

To analyze further the localization observed on the pictures of Fig. 5.5, we explore the deformation and displacement fields at the scale of the cylinders. In particular, we derive an indicator of the localization from the temporal and spatial variations of the deformation field $d(\vec{x})$. From the pictures taking during the test, we track each individual straw and define their deformation as

$$d(\vec{x}) = 1 - \frac{R(\vec{x},\delta)}{R_0(\vec{x},1)} \tag{5.6}$$

where R_0 is their initial radius and R is the radius of the largest circle that can fit into the compressed elliptical straw at a given peak distance δ. To study its evolution, we divide the loading into small intervals of δ and compute the variations $\delta d(\vec{x})$ of the deformation field over each interval. Maps thereby obtained are shown on Fig. 5.8. Before peak load, for $\delta \simeq 0.2$, the field δd exhibit fluctuations that are rather homogeneously distributed in the material. Indeed, the small clusters with a large deformation rate visible on Fig. 5.8a appear randomly located. As we reach peak load for $\delta \simeq 0$ (Fig. 5.8b), the deformation starts to localize into a $V-$shape like region while some other regions show intense activity elsewhere in the material. After the peak $\delta \simeq -0.2$, the activity progressively decays in the other part of the system (Fig. 5.8c), to finally concentrate essentially on the straws in and above the localization band. At this loading level, straws below the compaction band do not feel anymore the monotonic increase of the displacement (see the lower region of the material on Fig. 5.8d for $\delta \simeq -0.4$ that do not show any activity).

From the qualitative investigation of the pictures and the deformation rates computed at the scale of the straws, one can conclude that localization takes place at or shortly after peak load. However, we would like to derive a more quantitative estimate of the localization onset. To do so, we notice that once localization takes place the straws that are located below the localization band do not feel anymore the external driving. This suggests that the average value of the displacement field in the lowest part of the material and its evolution with time could be used to determine it [90]. Indeed, before localization, this quantity follows the deformation imposed to the sample, while at localization

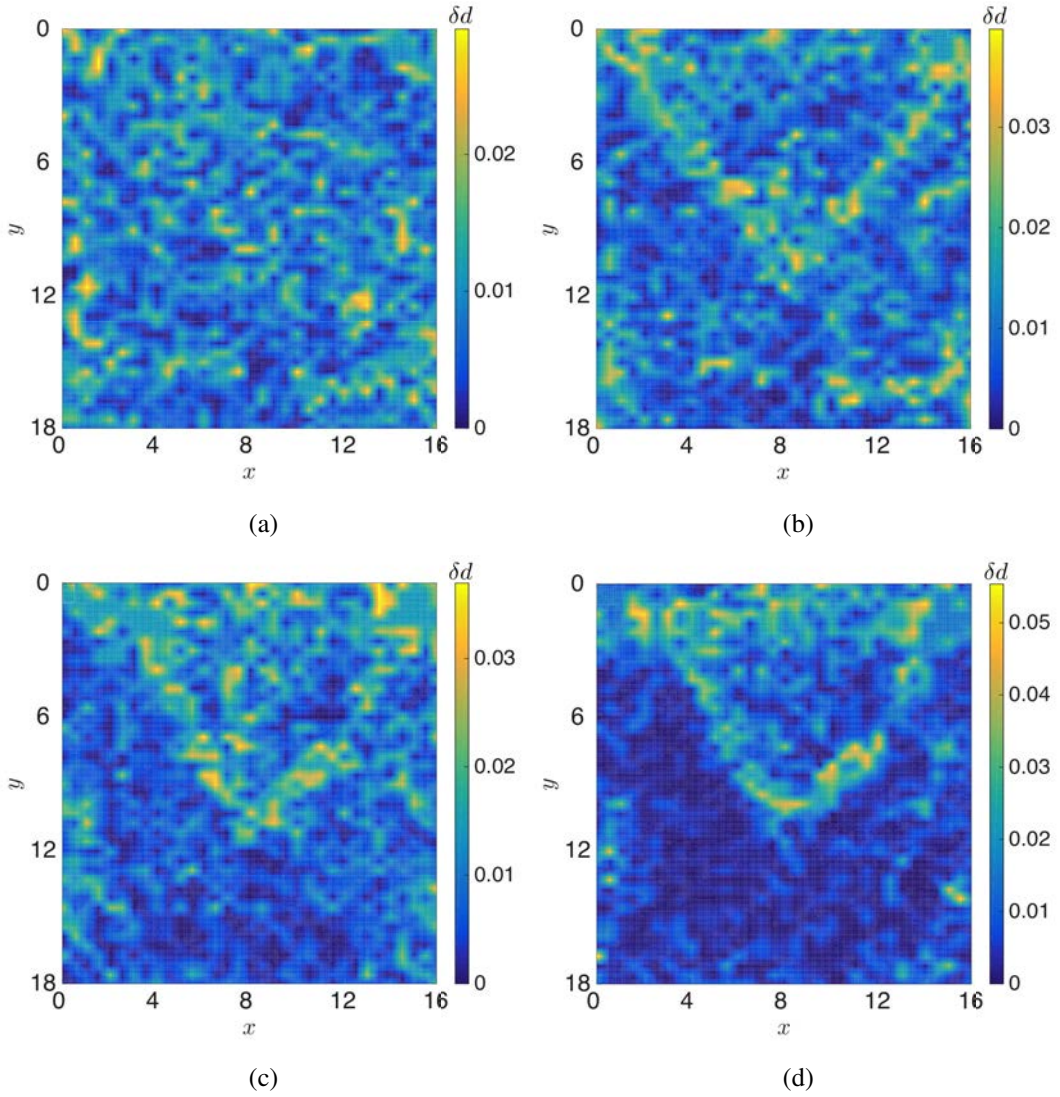

Figure 5.8: Maps of the deformation rate $\delta d(\vec{x}) = d(\vec{x}, \delta + \varepsilon) - d(\vec{x}, \delta)$ for the experiment $\#3$: (a) Before peak load for $\delta = 0.2$, the system displays a rather uniform distribution of deformation rates; (b) At peak load $\delta = 0$, one can identify a V-shape like localization band; (c) after peak load for $\delta = -0.2$, the deformation increases progessively in the compation band and vanishes in the other region of the material (d) while for $\delta = -0.4$, we can observe that straws below the band do no longer deform.

it saturates and remains then roughly constant. To use this method, we determine on each picture the centroids of the straws from which we calculate their vertical displacement $u_y(\vec{x})$. Considering only the straws located in the very bottom of the box, within $10\ \%$, we compute their average displacement $\langle u_y(\vec{x}) \rangle$ that is represented in Fig. 5.9 for each experiment as a function of δ. The curves are normalized by the maximum average displacement $\langle u_y(\vec{x}) \rangle_{max}$ obtained at peak load.

Whatever the experiment considered, we observe the same characteristic behavior: Before the peak ($\delta \geq 0$), the response is close to linear, while for $\delta < 0$ the displacement of the straws re-

mains fairly constant, *i.e.* the straws below the localization band no longer see the deformation that is imposed at the top of the sample. On the contrary, straws above the localization band follow the displacement that is imposed to the packing during the whole experiment, as shown in the inset.

Therefore, we conclude that localization takes place at peak load. Can we predict such a behavior, and the value of the critical loading at which it takes place? Can we understand the shape of the localization band and the loading at which it spans the whole system? We now address these questions by investigating theoretically the stability of the compressed array of hollow cylinders.

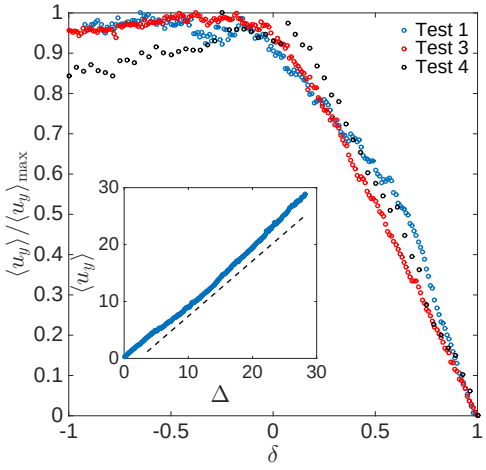

Figure 5.9: Average vertical displacement of the $10\ \%$ lowest straws as a function of the distance to peak δ, allowing for the determination of the localization threshold that corresponds to the crossover between the linear and the plateau behavior. The same procedure is applied in inset for the $10\ \%$ highest straws which deform linearly with the applied displacement, since located above the localization band.

5.3.2 Analytical investigation of localization

From our experimental study, we have shown that the compression of an array of soft cylinders is characterized by the progressive deterioration of its macroscopic stiffness. This softening relates to dissipative events taking place at the scale of the material microstructure and that are localized both in time and space. We have also showed that ultimately, this progressive decrease of the elastic modulus gives rise to localization of the deformation into a narrow band that appears close to the peak load.

From these observations, damage mechanics seems like a natural framework for describing the mechanical behavior of this material. However, several questions remain to be addressed. First, we need to introduce a damage parameter that describes the state of the material at the local scale. We choose the cylinder deformation d defined in Eq. (5.6) that describes the compression state of individual elements. Then, we need to derive the redistribution function that was shown in chapter

3 to play a central role in the stability of elasto-damageable materials. Here, we make the choice to describe the system through linear isotropic elasticity, despite the complex chain force network observed in granular media [43] and the symmetry of the ordered array used in our experiments. This choice is motivated by the following observations. First, we have observed that the material behaves rather linearly and reversibly at small imposed loading. Second, for larger loading, we have shown that the material could be characterized by a macroscopic stiffness from which one could infer the total linear elastic energy $E_{\text{el}} = \frac{1}{2} K_{\text{E}} \Delta^2$ stored in the material under the compressive displacement Δ, even though this stiffness could decay with the maximum applied loading as a result of dissipative local mechanisms. This effective stiffness was also shown to be consistent with the instantaneous stiffness F/Δ measured from the value of the force F sustained by the material under some prescribed displacement Δ. Finally, our observations of the different fields at the cylinder scale did not evidence any effect of the symmetry of the array on its deformation mechanisms. We believe that the disorder resulting from imperfections in the arrangement between cylinders dominates over the anisotropy induced by the cylinder spatial order.

We admit that the use of linear elasticity for describing this material might primary look abusive, in particular due to the presence of long range chain forces that dominate the mechanics of hard sphere packings. However, we think that cylinders are here soft enough to allow elasticity to dominate over other types of interactions. In addition, we seek here to capture the main features of the observations made in the experiments and so we let further investigations based on more complex, but more precise, constitutive laws for future studies.

We now move to the derivation of the interaction function involved in the redistribution mechanisms following damage events. Recently, Démery *et al.* [Démery et al.] have calculated this function for a general 2D elasto-damageable material under general loading conditions. We apply here this calculation for the specific loading used in the experiments and material properties adapted to the description of an array of soft hollow cylinders.

Damage model of a 2D elasto-damageable solid

We consider a homogeneous 2D elasto-damageable solid following Hooke's law under plane strain conditions

$$\boldsymbol{\varepsilon} = a\boldsymbol{\sigma} - \nu a \mathrm{tr}(\boldsymbol{\sigma}).\mathbf{1} \tag{5.7}$$

where a is an elastic modulus related to the Young modulus E through

$$a(d) = \frac{1+\nu}{E(d)}. \tag{5.8}$$

The Poisson's ratio ν is assumed to be constant, independent of the damage level d. Taking into

account the lateral confinement of the material, the stress and strain tensors write as

$$\boldsymbol{\sigma} = \sigma_{\text{ext}} \begin{pmatrix} \dfrac{\nu}{1-\nu} & 0 \\ 0 & 1 \end{pmatrix}, \tag{5.9}$$

$$\boldsymbol{\varepsilon} = \varepsilon_{\text{ext}} \begin{pmatrix} 0 & 0 \\ 0 & 1 \end{pmatrix}, \tag{5.10}$$

where $\sigma_{\text{ext}} < 0$ and $\varepsilon_{\text{ext}} < 0$ are the external stress and strain along the y-axis, respectively. We have here taken advantage of the plane strain conditions to write mechanical fields as 2×2 components tensors. The z components can be recovered from the relations $\sigma_{zz} = \sigma_{xx}$ and $\epsilon_{zz} = 0$ while the non-diagonal terms are all equal to zero. Note that this simplification explains the modified Hooke's law used in Eq. (5.7). In addition to Hooke's law, the external stress and strain along the vertical y axis are related by

$$\sigma_{\text{ext}} = cK(d)\varepsilon_{\text{ext}} \tag{5.11}$$

where $K(d)$ is the macroscopic stiffness and $c = H/A$ a constant, where H is the height of the box, as defined on Fig. 5.3 and A is area corresponding to $L \times b$ where L and b are, respectively, the length and width of the box. We deduce from it the relationship between the Young modulus $E(d)$ and the measured stiffness $K(d)$:

$$E(d) = \frac{cK(d)(1+\nu)(1-2\nu)}{1-\nu}. \tag{5.12}$$

To derive our damage model we should express both the damage driving force and damage resistance. In the general case, the free elastic density per unit volume is expressed as

$$w = \frac{1}{2}\boldsymbol{\varepsilon} : \boldsymbol{\sigma} \tag{5.13}$$

from which one obtains the damage driving force expressed as

$$Y = -\left.\frac{\partial w}{\partial d}\right|_{\varepsilon} = \left.\frac{\partial w}{\partial d}\right|_{\sigma}. \tag{5.14}$$

The term in the middle corresponds to the damage driving force at imposed strain whereas the last one to the driving force at imposed stress. Even though we control our system in strain, we will use the latter formulation. Indeed, both types of loading result in the same localization threshold. However, the calculations appear more complex under strain imposed conditions, so for the sake of simplicity, we consider stress imposed conditions. Nevertheless, one can easily translate the results obtained on the critical stress at localization into a critical strain at localization by using Hooke's law, as it will be used later in this analysis. Coming back to the calculation of the damage driving force under imposed stress, Eqs. (5.7), (5.13) and (5.14) lead to

$$Y = \frac{a'(d)}{2}\left(tr\left(\boldsymbol{\sigma}^2\right) - \nu tr(\boldsymbol{\sigma})^2\right). \tag{5.15}$$

The damage resistance is written as $Y_c(d)$ that we assume a known function of damage. The damage criterion thus writes as

$$Y(d) = Y_c(d) \Rightarrow \text{Damage increases} \tag{5.16}$$

To study the stability of the homogeneous solution and derive conditions for localization, we consider some small spatial variations of the damage field around a value $d = d_0$. We decompose it into two contribution: $d(\vec{x}) = d_0 + \delta d(\vec{x})$. Note also that the consideration of a spatially varying damage field can be justified by the presence of material heterogeneities, and the model derived will be also able to assist us for understanding the effect of material disorder on damage spreading. Assuming here weak spatial variations make sense for describing our experiments where a rather weak disorder was introduced in the regular array of cylinder. This heterogeneous contribution results in a weakly heterogeneous elastic modulus a with linearized expression

$$a(\vec{x}) = a(d_0) + \delta a(\vec{x}) = a(d_0) + a'(d_0)\delta d(\vec{x}), \tag{5.17}$$

and in heterogeneities in the stress and strain fields, leading to:

$$\boldsymbol{\sigma} = \boldsymbol{\sigma_0} + \boldsymbol{\delta\sigma} \tag{5.18a}$$

$$\boldsymbol{\varepsilon} = \boldsymbol{\varepsilon_0} + \boldsymbol{\delta\varepsilon} \tag{5.18b}$$

where $\boldsymbol{\sigma_0}$ and $\boldsymbol{\varepsilon_0}$ are the homogeneous applied stress and strain tensors given, respectively, by Eq. (5.9) and (5.10). Using linearized expressions, and considering the loading conditions used in the experiments, the damage driving force can be expressed up to the first order in the mechanical field perturbations as

$$Y(\vec{x}) = \frac{1}{2}\sigma_{\text{ext}}^2 a'(d_0)\frac{1-2\nu}{1-\nu} + \frac{1}{2}\sigma_{\text{ext}}^2 a''(d_0)\delta d(\vec{x})\frac{1-2\nu}{1-\nu} + \delta\sigma_{yy}\sigma_{\text{ext}}a'(d_0)\frac{1-2\nu}{1-\nu}. \tag{5.19}$$

It now remains to calculate the stress redistribution component $\delta\sigma_{yy}$ that arises from the heterogeneous damage contribution. To do so we use the compatibility equations under plane strain conditions

$$\partial_x\sigma_{xx} + \partial_y\sigma_{xy} = 0, \tag{5.20a}$$

$$\partial_x\sigma_{xy} + \partial_y\sigma_{xy} = 0, \tag{5.20b}$$

$$2\partial_x\partial_y\varepsilon_{xy} - \partial_y^2\varepsilon_{xx} - \partial_x^2\varepsilon_{yy} = 0. \tag{5.20c}$$

In Fourier's space, the first two equations give

$$\widetilde{\delta\sigma}_{xx}(\vec{q}) = -\frac{q_y}{q_x}\widetilde{\delta\sigma}_{xy}(\vec{q}), \tag{5.21a}$$

$$\widetilde{\delta\sigma}_{yy}(\vec{q}) = -\frac{q_x}{q_y}\widetilde{\delta\sigma}_{xy}(\vec{q}). \tag{5.21b}$$

To solve the compatibility equation (5.20c), we use the linearized strain fluctuations, which are related to the stress fluctuations tensor via

$$\boldsymbol{\delta\varepsilon} = \delta a(d_0)(\boldsymbol{\sigma_0} - \nu tr(\boldsymbol{\sigma_0}).\mathbf{1}) + a(d_0)(\boldsymbol{\delta\sigma} - \nu tr(\boldsymbol{\delta\sigma}).\mathbf{1}), \tag{5.22}$$

that we express in Fourier's space. Also using the expression (5.9) of the stress tensor for the homogeneous solution and Eqs. (5.21a) and (5.21b), one obtains

$$\widetilde{\delta\sigma}_{xy}(\vec{q}) = \sigma_{\text{ext}} \frac{a'(d_0)\widetilde{\delta d}(\vec{q})(1-2\nu)}{a(d_0)(1-\nu)^2} \frac{q_x^3 q_y}{(q_x^2+q_y^2)^2}. \tag{5.23}$$

Hence, the damage driving force of Eq. (5.19) can be expressed as

$$Y(\vec{x}) = Y_0(d_0) + \delta Y(\delta d) = Y_0 + \psi(\vec{x}) * \delta d(\vec{x}) \tag{5.24}$$

where the homogeneous contribution writes as

$$Y_0(d_0) = \sigma_{\text{ext}}^2 \frac{a'(d_0)}{2} \frac{(1-2\nu)}{(1-\nu)} \tag{5.25}$$

whereas the kernel ψ is expressed, respectively in real and Fourier space as

$$\psi(\vec{x}) = \left.\frac{\partial Y_0}{\partial d_0}\right|_\sigma \delta(\vec{x}) - \sigma_{\text{ext}}^2 \frac{a'^2(d_0)}{a(d_0)} \frac{(1-2\nu)^2}{(1-\nu)^3} \frac{\pi(3y^4 - x^4 - 6x^2y^2)}{(x^2+y^2)^3} \tag{5.26}$$

$$\tilde{\psi}(\vec{q}) = \left.\frac{\partial Y_0}{\partial d_0}\right|_\sigma - \sigma_{\text{ext}}^2 \frac{a'^2(d_0)}{a(d_0)} \frac{(1-2\nu)^2}{(1-\nu)^3} \cos^4(w) \tag{5.27}$$

where $\cos^4(\omega) = q_x^4/\boldsymbol{q}^4$ is the polar angle of the mode $\boldsymbol{q} = \vec{q}$. Since both expressions have indeterminate forms in $\vec{0}$, the kernel is regularized at this point by setting $\psi(\vec{0}) = \tilde{\psi}(\vec{0}) = \partial Y_0/\partial d_0$. The shape of the kernel is shown in real space in Fig.5.10. In polar coordinate it is of the form $g(\theta)/r^2$, where g is a function of the polar angle θ and r is the distance. Thus, contrary to the isotropic 2D redistribution function presented in Chapter 2, the kernel here varies with directionality and allows for long-range interactions. The explicit calculation of the redistribution kernel ψ calls for a few comments. First, it resembles, but is different, from the variation in stress field induced by the introduction of a soft inclusion in a more rigid matrix also referred to as the Eshelby's solution [28]. Indeed, we have calculated here the effect of a local drop of the elastic properties on the mechanical fields in the rest of the material. However, we focused here on the variations on the *driving force for damage* induced by a local damage event, that we also called driving force redistribution. As a result, and contrary to the study of Eshelby, our solution involves the relative variations $a'(d_0)/a(d_0)$ of the elastic properties of the material with damage that is not involved in Eshelby's work. Secondly, we have calculated the redistribution kernel for the specific loading conditions considered in our experiments that consists of a compressive loading with lateral confinement that is analogous to bi-axial loading conditions. Démery *et al.* [Démery et al.] have calculated the redistribution kernel in the general case, for any uniform loading conditions. It is worth noting that the kernel does depend

on the type of loading. Indeed, following our analogy with Eshelby's problem, the stress field variations resulting from the local drop in the elastic properties of the medium does depend on the loading conditions applied far away from the perturbation. For example, under shearing loading conditions, stress field perturbations follow the characteristic quadrupolar symmetry analogous to the one considered in amorphous plasticity problems [69, 86, 102, 111] where regions of the material located in the diagonal are reloaded. For the loading conditions studied here, the reloading takes also place on the horizontal axis, as shown on Fig. 5.10. Finally, the explicit calculation of the long-range redistribution kernel for an elasto-damageable medium provides a physical ground to the non-locality in damage models proposed 30 years ago [9, 87]. As shown in the following, the actual shape of the redistribution kernel does control the onset of localization, the localization band orientation and more generally, the damage evolution up to failure. Its explicit calculation hence provides new perspectives for the quantitative prediction of damage processes in quasi-brittle media.

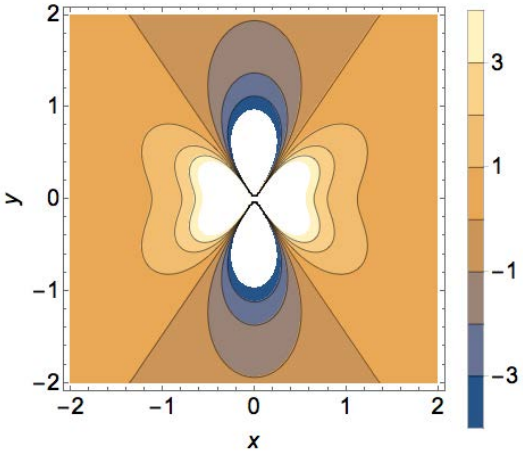

Figure 5.10: Elastic kernel shape in real space showing the change of sign with directionality and the long-range decay of the amplitude of the redistribution.

Finally, we must also express the damage resistance that results from the introduction of heterogeneities in the damage field. It simply writes as

$$Y_c(\vec{x}) = Y_c(d_0) + Y_c'(d_0)\delta d(\vec{x}). \tag{5.28}$$

The total damage driving force follows

$$\mathcal{F}(d) = \mathcal{F}^{(0)}(d_0) + \mathcal{F}^{(1)}(\delta d) \tag{5.29}$$

where the zero order provides the equilibrium equation which allows to relate the loading to the homogeneous damage contribution

$$\mathcal{F}^{(0)}(d_0) = 0 \Rightarrow Y_0(d_0) = Y_c(d_0) \tag{5.30}$$

and the first order represents the driving force redistributions

$$\mathcal{F}^{(1)}(\delta d) = \left(\psi(d_0,\vec{x}) - Y_c'(d_0)\delta(\vec{x})\right) * \delta d(\vec{x}) \tag{5.31}$$

after the damage increase of $\delta d(\vec{x})$.

From this damage model formulation, following the same approach as in Chapter 3, one derives the stability of the material that provides both localization and failure thresholds. Since both criteria will involve the expression of the force peak derived from the homogeneous solution, we first perform its determination so that its expression can be identified and interpreted when dealing with questions related to system stability.

Peak load of the homogeneous material

In the case of a homogeneous material, only the homogeneous part of the total damage driving force $\mathcal{F}^{(0)}$ has to been taken into account. Following the approach described in Chapter 2, the system reaches peak load when the criterion of Eq. (2.22) is verified. The control parameter X is here the external stress while the exponent $\zeta = 2$. From Eq. (5.25) we define the function $f(d_0) = a'(d_0)(1-2\nu)/(2(1-\nu))$ and the function h is given by $h(d_0) = Y_c(d_0)$. After calculations, using Eqs. (5.8) and (5.12) for the expression of the elastic modulus as a function of the measured macroscopic stiffness, we obtain that peak load takes place at an homogeneous damage level d_0 verifying

$$\left.\frac{\partial Y_0}{\partial d_0}\right|_\sigma = Y_c'(d_0) \Leftrightarrow \frac{K''(d_0)K(d_0) - 2K'^2(d_0)}{K(d_0)K'(d_0)} = \frac{Y_c'(d_0)}{Y_c(d_0)} \tag{5.32}$$

It should be mentioned that the same criterion would have been obtained if the lateral confinement had not be taken into account. Indeed, the elastic energy of the homogeneous system takes the simple form $w = 1/2\varepsilon_{\text{ext}}\sigma_{\text{ext}}$ irrespective of the presence of confinement.

Localization threshold

To determine the localization threshold, we consider periodic damage perturbations of mode $\vec{q}_0$ and positive perturbation $\delta d(\vec{x}) = \delta d_0(1+\cos(q_0\cdot\vec{x}))$ as in Eq. (3.19). The heterogeneous part of the damage driving force thus writes as

$$\mathcal{F}^{(1)}(\vec{x}) = \left(\left.\frac{\partial Y_0}{\partial d_0}\right|_\sigma - Y_c'(d_0)\right)\delta d_0 + \left(\widetilde{\psi}(d_0,\vec{q}_0) - Y_c'(d_0)\right)\delta d_0 \cos(\vec{q}_0\cdot\vec{x}) \tag{5.33}$$

where we have used that $\psi(\vec{x}) * \cos(\vec{q}_0\cdot\vec{x}) = \widetilde{\psi}(\vec{q}_0)\cos(\vec{q}_0\cdot\vec{x})$ and the regularization condition on ψ at $\vec{0}$. Following the same argumentation as for the stability analysis performed in Chapter 3, damage localization will take place if the prefactor of the cosine function becomes positive. From Eq. (5.27), we see that $\widetilde{\psi}$ is maximum for modes of polar angle $w_c = \pi/2 + n\pi$, regardless of the norm of the

mode $\vec{q}_c$. This leads to an angle $\theta_{\text{loc}} = \pi/2 - w_c = 0$ in real space, and hence localization is expected to take place perpendicularly to the applied loading. The critical homogeneous damage level at which it takes place is obtained by solving

$$\widetilde{\psi}(d_0, \vec{q}_c) = Y_c'(d_0) \Leftrightarrow \left.\frac{\partial Y_0}{\partial d_0}\right|_{\sigma} = Y_c'(d_0) \tag{5.34}$$

that corresponds to Eq. (5.32) derived for determining the position of the peak. It means that localization takes place at the peak load of the homogeneous system provided by the expression (5.32).

Failure prediction

To determine the failure threshold, we must look at the sign of $\mathcal{F}^{(1)}$ for the growing modes $\vec{q}_c$. Using $\widetilde{\psi}(d_0, \vec{q}_c) = \partial Y_0/\partial d_0$, the stability criterion once again writes as the right term of Eq. (5.34) that provides the peak load position. As a consequence, for stress imposed conditions, both localization and failure takes place at peak load. The redistributions of the damage driving force are independent of the loading parameter, yet, if ones to investigate the post-peak behavior of the system, strain control must be considered. To do so, we replace σ_{ext} by its strain counterpart using Hooke's law given by Eq. (5.7) and differentiating the damage driving rate Y_0 with respect to d_0 at fixed applied strain. Then considering the growing perturbation of mode $\vec{q}_c$, $\mathcal{F}^{(1)}$ becomes positive for $\left.\dfrac{\partial Y_0}{\partial d_0}\right|_{\varepsilon} = Y_c'(d_0)$. This leads to

$$\frac{2K'^2(d_0) - K''(d_0)K^3(d_0) + 2K'^2(d_0)K^2(d_0)}{K'(d_0)K^3(d_0)} = \frac{Y_c'(d_0)}{Y_c(d_0)} \tag{5.35}$$

which corresponds to the failure instability of the homogeneous system controlled in strain as the spatial dependency of the kernel was set to zero since $\cos(w_c) = 0$. Note however that the relevancy of this prediction can be questioned. As previously explained, the assumption of weak variations of the damage field might be violated, since localization takes place prior to failure. Moreover, one can question the meaning of a failure instability in a confined system. For a set up with free edge boundary conditions, failure can be observed from the separation of the system in two pieces through the propagation of a crack spanning over the whole material. In the case of a confined body, the concept of unstable failure remains to be clarified and characterized.

As a summary, we have first determined the position of the peak load. The criterion (5.32) provides the damage level at which it occurs. From the linear stability analysis, we have established that localization, whatever the control parameter, takes place at a damage level that corresponds to peak load. It was shown that localization should consist in a concentration of the deformation perpendicularly to the external loading axis. Considering a control in strain, we have characterized the stability of the growing heterogeneous damage field, and obtained an approximation of the failure threshold, given by the criterion (5.35). In that case, failure occurs in the post-peak response, after localization. For the peak, localization and failure prediction, the stresses and strains corresponding to the critical damage values are obtained using the equilibrium equation $Y_0(d_0) = Y_c(d_0)$ and Hooke's

law.

Comparison between theoretical predictions and experimental observations

To compare the analytical predictions to our experimental results, we define the homogeneous damage level d_0 or homogeneous deformation as the spatial average of the local deformation

$$d_0 = \frac{1}{N_s} \sum_i d_i \tag{5.36}$$

where N_s is the number of straws identified on the pictures and d_i is the deformation defined in Eq. (5.6) of the $i-th$ cylinder which is located at a position $\vec{x}$. For each d_0 value obtained (one per frame), we calculate the corresponding macroscopic stiffness K_{m}, from Eq. (5.4). We obtain the evolution of K with d_0 by fitting the curve with a polynomial expression of order four. The same procedure is performed for the rupture energy $E_r \simeq E_d$ which is fitted as a function of d_0 by a polynomial form of degree five and then differentiated to obtain Y_c as a function of the homogeneous deformation. Note that lower degree polynomials would give an acceptable behavior of both quantities. However, since the criteria for localization and failure involve first and second derivatives, we favor more accurate expressions.

The thresholds values calculated using the theoretical expressions are summarized in Tab. 5.1 where the damage, force and displacement at localization and failure are shown. For the former critical values, the deviation from the experimentally measured position of the peak is indicated in percent. From the study of the relative height evolution of the straws with the distance to failure, shown on Fig. 5.9, and from the qualitative study of the local deformation rate, we have determined that localization of deformation takes place at the peak of the macroscopic response. This corresponds to the analytical prediction performed above. The predictions are in good agreement with experimental values calculated, as indicated by the low deviations. However, we predicted that localization should take place perpendicularly to the applied loading. This is not very well verified, as shown in Fig. 5.11 where the post-localization pattern is shown for $\delta \simeq -0.4$. We think that the presence of some friction on the side on the specimen does influence the inclination of the localization band.

The failure predictions seem to coincide with the point at which the macroscopic force starts increasing again after its decay in the post-peak region. Qualitatively, from the study of the pictures taken during the experiments, it may coincide with the loading at which a fully developed localization band goes through the whole system. This corresponds to the situation where a complete layer of straws going from one side of the sample to the other are fully compacted, with a parameter value $d = 1$. As a consequence, the system can be seen as separated in two pieces, and further loading increments will lead to the crushing of straws located above the discontinuity in the active fault, whereas the other regions of the material remain essentially inactive.

Experiment	Peak load and localization	Failure
#1	$d = 0.11 (3.8\%)$ $F = 279\ \mathrm{N}\,(0.4\%)$ $\Delta = 18.8\ \mathrm{mm}\,(6.8\%)$	$d = 0.16$ $F = 266.1\ \mathrm{N}$ $\Delta = 29.5\ \mathrm{mm}$
#3	$d = 0.09 (5.4\%)$ $F = 308.4\ \mathrm{N}\,(1.4\%)$ $\Delta = 13.4\ \mathrm{mm}\,(2.8\%)$	$d = 0.13$ $F = 273.8\ \mathrm{N}$ $\Delta = 22.6\ \mathrm{mm}$
#4	$d = 0.10 (2.5\%)$ $F = 243.2\ \mathrm{N}\,(0.4\%)$ $\Delta = 13.6\ \mathrm{mm}\,(3.7\%)$	$d = 0.13$ $F = 227.7\ \mathrm{N}$ $\Delta = 21.4\ \mathrm{mm}$

Table 5.1: For each experiment, analytical prediction of damage, force and displacement at the peak, which corresponds to the onset of localization of deformation, deviation from the experimental results are indicated in percent. The quantities are also determined at failure of the system.

To conclude this section, it seems that the modeling of 2D arrays of soft hollow cylinders under compression as 2D elasto-damageable solids provides a meaningful description of the localization process. However, taking a closer look at the macroscopic response, we have evidenced strong fluctuations that are not captured by the current model. We shall now characterize them as the system evolves towards localization.

5.4 Temporal fluctuations study

To compare the behavior of the packings with that of our numerical study, we study in this section the evolution of the intermittent bursts of dissipated energy. We extract the avalanche size in terms of dissipated and kinetic energies, as well as avalanche duration, from the macroscopic response of the system. If the study of their distributions close and far from failure, average evolution with distance to peak and scaling with each other show a qualitative agreement with the power law behaviors obtained numerically, the exponent values differ. To complete the study, we also define the avalanche size from the local field that is studied by considering the average local deformation variation, and determine its scaling with energetical bursts definition.

The progression of bursts of dissipated energy $S_d = \Delta E_\mathrm{d}$ and kinetic energy $S_k = \Delta E_\mathrm{k}$ per avalanche is shown as a function of the distance to peak load δ on Fig. 5.12a. The plots are realized here for experiment $\#3$ but the behavior would be the same for the other tests. Both quantities exhibit strong fluctuations and an amplification close to $\delta = 0$. The increased width of the avalanches when δ is close to zero indicates that the duration of the dissipation processes grows as the system approaches localization. Moreover, we once again observe that the kinetic energy contribution to the dissipated energy is very small, roughly three orders of magnitude lower than S_d.

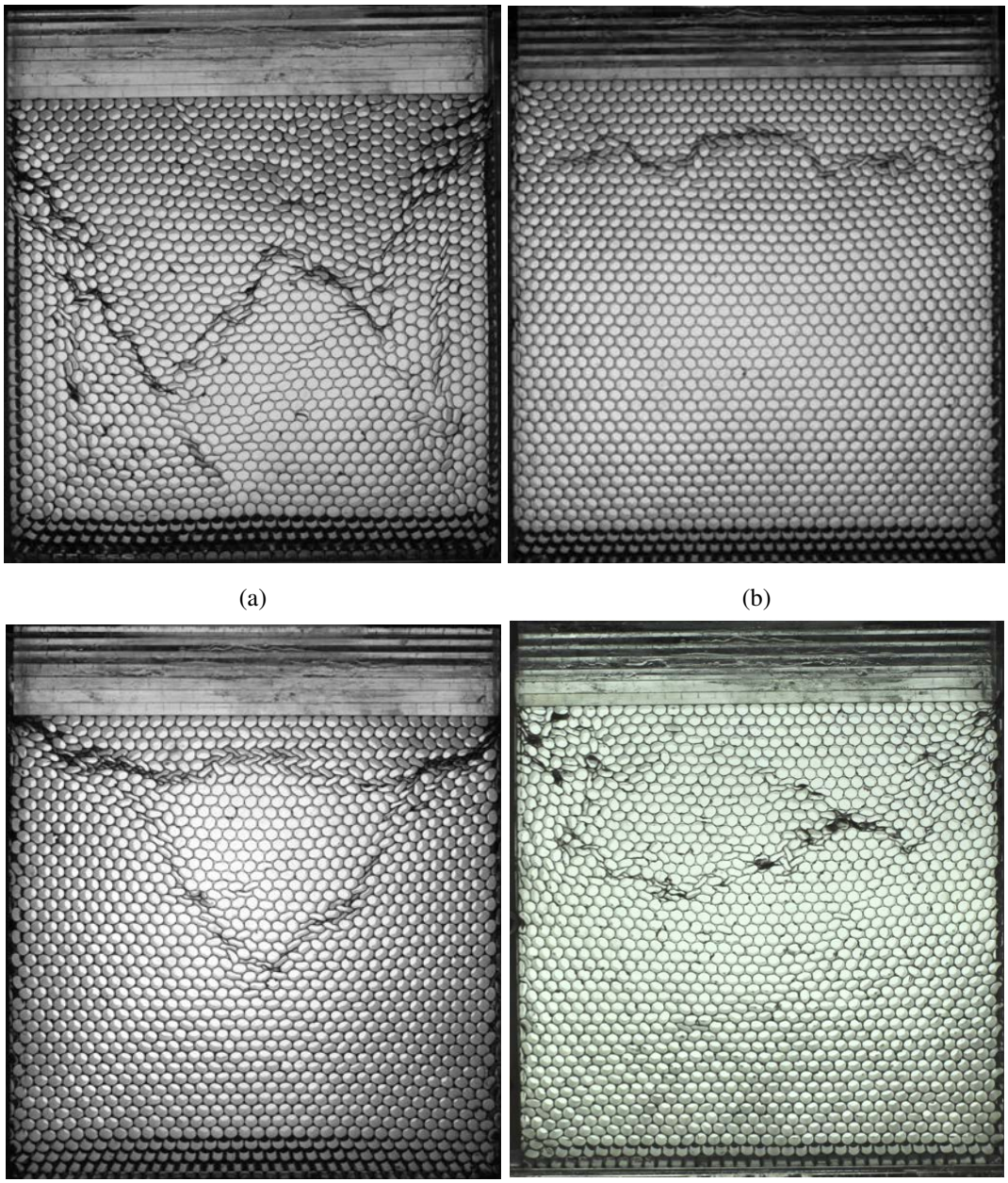

(a) (b)

(c) (d)

Figure 5.11: For each experiment, (a) test 1, (b) test 2, (c) test 3, (d) test4, photo of the packing at the predicted failure threashold which seems to correspond to the onset of the crushing of the straws above the already formed localization band. The angle formed by the macroscopic band is more or less perpendicular to the loading axis; the strongest deviation is oberserved for experiment 1 (a) where it took place following the strong defects that were introduced in the system.

The increase of both the average dissipated energy and kinetic energy as a function of the distance to peak, shown on Fig. 5.12b, testify for the global increase of the avalanches amplitude. S_d and S_k both follow power law behavior with δ, of respective exponent τ_d and τ_k. With i standing for

d or k we have

$$\langle S_i \rangle \sim \delta^{-\tau_i}, \tag{5.37}$$

where $\tau_d = 1.2 \pm 0.2$ and $\tau_k = 1.6 \pm 0.2$.

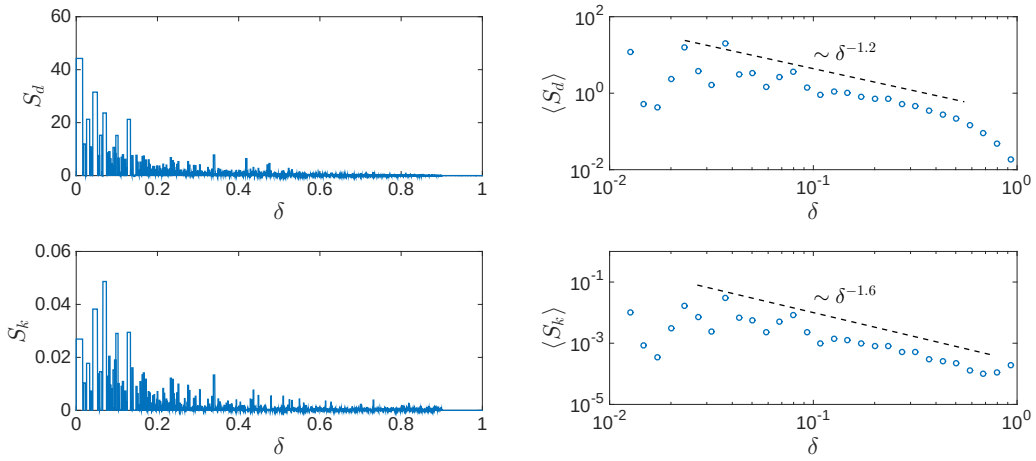

(a) (b)

Figure 5.12: Evolution as a function of the distance to the peak load δ of (a) the avalanches in term of dissipated energy S_d and kinetic energy S_k, both exhibiting strong fluctuations with an amplification of amplitude and duration close to the peak; (b) the average dissipated energy $\langle S_d \rangle$ and average kinetic energy $\langle S_k \rangle$ per avalanche, both show power law scalings of respective exponent $\tau_d = 1.2 \pm 0.2$ and $\tau_k = 1.6 \pm 0.2$.

To further characterize the dissipation process as the system evolves towards failure, we study on Fig. 5.13 the probability density functions of each quantity. We consider either all the avalanches taking place before the peak (blue curves), or we restrict the study to avalanches taking place close localization, for $\delta \in [0, 0.1]$ (orange curves). Whatever the avalanche definition, i.e. the dissipated energy S_d, the kinetic energy S_k or the avalanche duration S_T (expressed here in seconds) , two behaviors emerge. When considering all the dissipation events, we observe a power law dependency of exponent $(\beta_{\text{tot}})_i$, with i standing for d, k or T:

$$P(S_i) \sim S_i^{-(\beta_{\text{tot}})_i} \tag{5.38}$$

where $(\beta_{\text{tot}})_d = 2.15 \pm 0.1$, $(\beta_{\text{tot}})_k = 2 \pm 0.1$ and $(\beta_{\text{tot}})_T = 2.35 \pm 0.1$. When limiting the study to avalanches close to localization, power law scalings with a smaller exponent β_i ($\beta_d = 1.55 \pm 0.2$, $\beta_k = 1.4 \pm 0.2$ and $\beta_T = 1.6 \pm 0.2$) are obtained up to a critical value S_{ic}:

$$P_{\delta \to 0}(S_i) \sim S_i^{-\beta_i}, S_i << S_{ic} \tag{5.39}$$

Moreover, using the same approach as in the numerical model fluctuation study, we can verify the agreement between the exponents β_i and $(\beta_{\text{tot}})_i$. To do so, we use the power law behavior

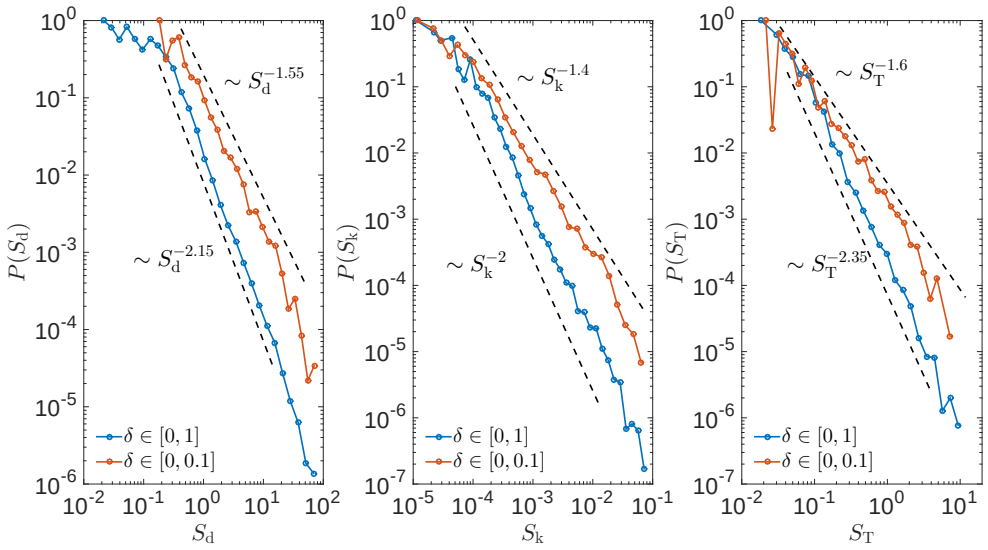

Figure 5.13: Probability densities obtained by considering all damage events, $\delta \in [0,1]$ (blue curve), or damage events close to the peak load, $\delta \in [0,0.1]$ (orange curve), of (a) the dissipated energy per avalanche S_d; (b) the bursts of kinetic energy S_k; and (c) the avalanche duration S_T.

of exponent ϵ ($\epsilon = 0.6 \pm 0.2$) with δ of the number of avalanches, which is shown on Fig. 5.14a. We rewrite Eq. (4.19) as

$$(\beta_{\mathrm{tot}})_i = \beta_i + \frac{(\epsilon+1)(2-\beta_i)}{\tau_i} \tag{5.40}$$

The predicted $(\beta_{\mathrm{tot}})_i$ values obtained using this scaling are compared to the fits of the distributions in Tab. 5.2 where are also summarized the different power law behaviors and show fair agreement with the measured values. Another way to verify the consistency of the exponents measured is to consider the power law scalings of exponents γ_i ($\gamma_T = 0.9 \pm 0.05$ and $\gamma_k = 1.35 \pm 0.1$) of S_T and S_k with the avalanche dissipated energy S_d, shown on Fig. 5.14b. Using that close to failure

$$\begin{cases} P(S_i) \sim S_i^{-\beta_i} \\ P(S_d) \sim S_d^{-\beta_d} \\ S_i \sim S_d^{\gamma_i} \\ P(S_i)dS_i = P(S_d)dS_d \end{cases} \tag{5.41}$$

we obtain the relationship

$$\beta_i = 1 - \frac{1-\beta_d}{\gamma_i} \tag{5.42}$$

Note that the same is true when considering all the damage events and therefore replacing β_i and β_d by $(\beta_{\mathrm{tot}})_i$ and $(\beta_{\mathrm{tot}})_d$, respectively. The values obtained using the scaling are shown in Tab. 5.2.

The temporal statistical behavior was so far determined from the macroscopic fluctuations extracted from the force-displacement response of the system. These avalanches directly result from

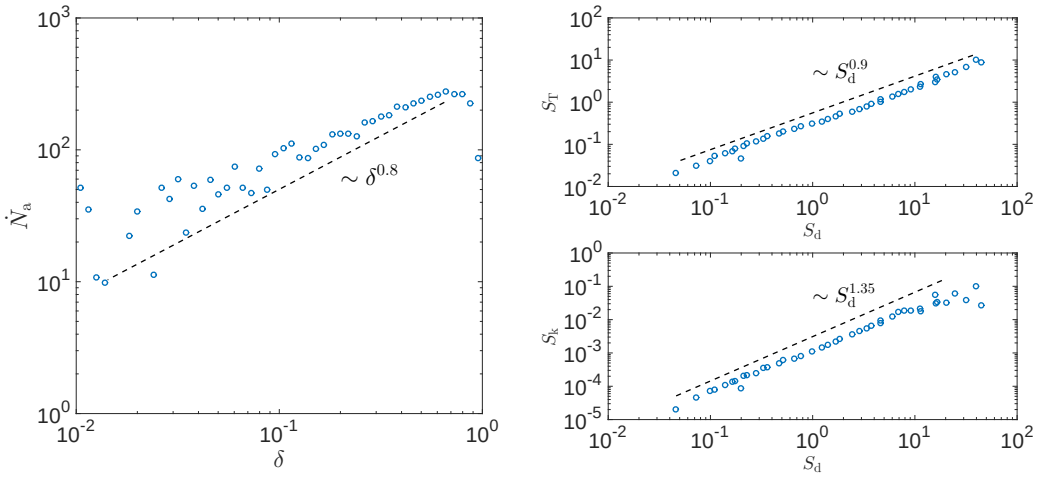

(a) (b)

Figure 5.14: (a) Evolution of the number of avalanches as a function of the distance to peak showing a power law behavior of exponent $\epsilon = 0.8 \pm 0.2$; (b) power law behaviors of the dissipated energy S_{d} (top) and kinetic energy S_{k} (bottom) with the avalanche duration S_T, of respective exponents $\gamma_{\mathrm{T}} = 0.9 \pm 0.05$ and $\gamma_{\mathrm{k}} = 1.35 \pm 0.1$.

the local behavior of the system as the energy variations are directly related to the local deformation variations. Indeed, we can define an avalanche size S from the study of the local deformation field: $S = \sum_k d_k(\Delta_e) - d_k(\Delta_i)$. This quantity corresponds to the total local deformation variation of the system taking place during in avalanche that starts at Δ_{i} and ends at Δ_{e}. It is related to the dissipated energy per avalanche through a power law behavior for sufficiently large avalanches ($S_{\mathrm{d}} > 0.1$): $S \sim S_{\mathrm{d}}^{\gamma}$ with $\gamma = 0.9 \pm 0.1$, as shown on the top frame of Fig.5.15a. As the energetically defined avalanche sizes, it is also growing as peak load is approached. This is well shown by the power law behavior of the average value $\langle S \rangle$ with δ of exponent $\tau = 1.2 \pm 0.3$. Moreover, as for the bursts defined in terms of energy, we obtained two different power law behaviors when considering the avalanche sizes distributions close to localization or considering all damage events. This is shown on Fig. 5.15b where exponents $\beta = 1.65 \pm 0.3$ and $(\beta_{\mathrm{tot}}) = 2.4 \pm 0.1$ are respectively identified. Using the scaling between S and S_{d}, the exponents obtained from the distribution densities of S are compatible with that measured, as reported in Tab. 5.2.

In summary, from both the energetical definition of the bursts obtained from the macroscopic response and the evolution of the local deformation field, the avalanches statistics is qualitatively similar to that observed during quasi-brittle materials fracture tests or from our one-dimensional model. The different quantities are related through power law scalings that are summarized in Tab. 5.2. As observed in our numerical study, the progression of the average quantities with δ, in particular the rate of dissipated energy and avalanche duration, follow power law behaviors. The distributions of avalanche sizes reveal that the bursts sizes follow power law behaviors, either when taking into account all damage events or, taking into account the non-stationnarity of the avalanches,

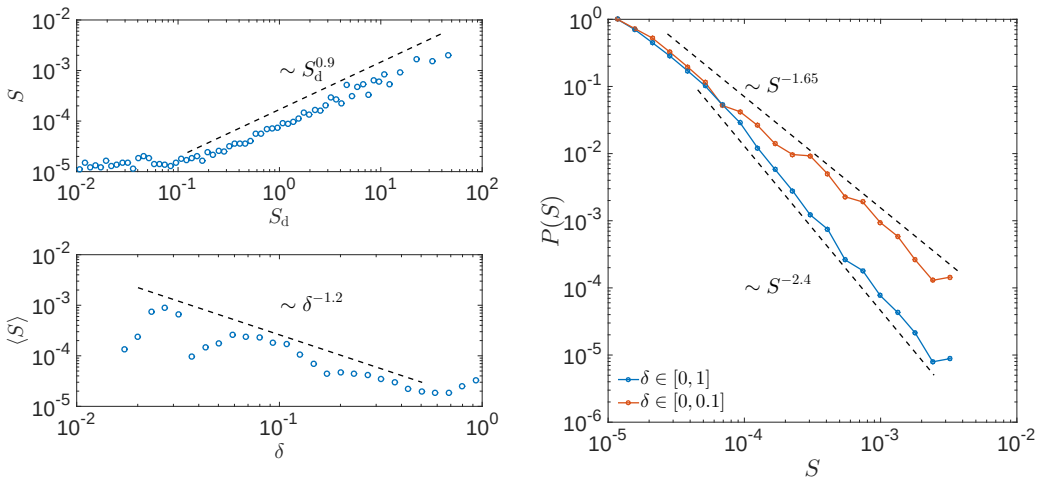

(a) (b)

Figure 5.15: Statistics of avalanches S defined from the deformation field of the material. (a) Top figure : scaling between S and the dissipated energy per avalanche $S_{\rm d}$ showing a power law behavior at large $S_{\rm d}$ values of exponent $\gamma = 0.9 \pm 0.1$, Lower figure: power law behavior of exponent $\tau = 1.2 \pm 0.3$ of the average avalanche size with distance to peak δ; (b) Distribution densities obtained when considering all damage events ($\delta \in [0,1]$) or that taking place close to failure ($\delta \in [0,0.1]$). Power law behaviors of exponents $(\beta_{\rm tot}) = 2.4 \pm 0.1$ and $\beta = 1.65 \pm 0.3$ are respectively determined.

when considering events taking place close to the peak load. The amplification of the intermittency close to $\delta = 0$ is revealed by a smaller exponent, indicating that bursts of larger amplitude take place, but also longer if one considers the duration of the dissipation events.

5.5 Conclusions

The compression of a two-dimensional array of hollow soft cylinders appears as an interesting setup to test our numerical approach and obtain the characteristic features associated with the quasi-brittle failure. In this system, where disorder is inherent due to variations in contacts, the local dissipative events can be well defined from both the macroscopic response and the study of the local field. They result in a gradual degradation in the system stiffness, leading to a non-linear macroscopic response and a softening behavior. In coaction with elastic interactions, they give rise to a rich bursts statistics and permit the observation of the transition to localization. Hence, this setup is particularly interesting as it captures both the intermittent behavior and localization observed experimentally and numerically in our model.

From the study of the macroscopic response of the system and the observation of the progressive local deformation of the cylinders, we have identified the general macroscopic mechanical response. At some critical loading, the system deviates from its initial linear elastic response, as

Definitions	Measured values	Predicted values	Scaling relations
$S_k \sim S_d^{\gamma_k}$	$\gamma_k = 1.35 \pm 0.1$		
$S_T \sim S_d^{\gamma_T}$	$\gamma_T = 0.9 \pm 0.05$		
$S \sim S_d^{\gamma}$	$\gamma = 0.9 \pm 0.1$		
$P_{\delta \to 0}(S_d) \sim S_d^{-\beta_d}$	$\beta_d = 1.55 \pm 0.2$		
$P_{\delta \to 0}(S_k) \sim S_k^{-\beta_k}$	$\beta_k = 1.4 \pm 0.2$	$\beta_k = 1.41 \pm 0.15$	$\beta_k = 1 - (1 - \beta_d)/\gamma_k$
$P_{\delta \to 0}(S_T) \sim S_T^{-\beta_T}$	$\beta_T = 1.6 \pm 0.2$	$\beta_T = 1.61 \pm 0.22$	$\beta_T = 1 - (1 - \beta_d)/\gamma_T$
$P_{\delta \to 0}(S) \sim S^{-\beta}$	$\beta = 1.65 \pm 0.3$	$\beta = 1.61 \pm 0.23$	$\beta = 1 - (1 - \beta_d)/\gamma$
$P(S_d) \sim S_d^{-(\beta_{\mathrm{tot}})_d}$	$(\beta_{\mathrm{tot}})_d = 2.15 \pm 0.1$	$(\beta_{\mathrm{tot}})_d = 2.22 \pm 0.14$	$(\beta_{\mathrm{tot}})_d = \beta_d + (\epsilon + 1)(2 - \beta_d)/\tau_d$
$P(S_k) \sim S_k^{-(\beta_{\mathrm{tot}})_k}$	$(\beta_{\mathrm{tot}})_k = 2 \pm 0.1$	$(\beta_{\mathrm{tot}})_k = 1.85 \pm 0.1$ $(\beta_{\mathrm{tot}})_k = 2.08 \pm 0.11$	$(\beta_{\mathrm{tot}})_k = 1 - (1 - (\beta_{\mathrm{tot}})_d)/\gamma_k$ $(\beta_{\mathrm{tot}})_k = \beta_k + (\epsilon + 1)(2 - \beta_k)/\tau_k$
$P(S_T) \sim S_T^{-(\beta_{\mathrm{tot}})_T}$	$(\beta_{\mathrm{tot}})_T = 2.35 \pm 0.1$	$(\beta_{\mathrm{tot}})_T = 2.28 \pm 0.13$ $(\beta_{\mathrm{tot}})_T = 2.4 \pm 0.24$	$(\beta_{\mathrm{tot}})_T = 1 - (1 - (\beta_{\mathrm{tot}})_d)/\gamma_T$ $(\beta_{\mathrm{tot}})_T = \beta_T + (\epsilon + 1)(2 - \beta_T)/\tau_T$
$P(S) \sim S^{-(\beta_{\mathrm{tot}})}$	$(\beta_{\mathrm{tot}}) = 2.4 \pm 0.1$	$(\beta_{\mathrm{tot}}) = 2.28 \pm 0.18$ $(\beta_{\mathrm{tot}}) = 2.18 \pm 0.15$	$(\beta_{\mathrm{tot}}) = 1 - (1 - (\beta_{\mathrm{tot}})_d)/\gamma$ $(\beta_{\mathrm{tot}}) = \beta + (\epsilon + 1)(2 - \beta)/\tau$
$\langle S_d \rangle \sim \delta^{-\tau_d}$	$\tau_d = 1.2 \pm 0.2$		
$\langle S_k \rangle \sim \delta^{-\tau_k}$	$\tau_k = 1.6 \pm 0.2$		
$\langle S_T \rangle \sim \delta^{-\tau_T}$	$\tau_T = 0.9 \pm 0.2$		
$\langle S \rangle \sim \delta^{-\tau}$	$\tau = 1.2 \pm 0.3$		
$\dot{N}_{\mathrm{a}} \sim \delta^{\epsilon}$	$\epsilon = 0.8 \pm 0.2$		

Table 5.2: Definition of the scaling exponents measured form the statistics of fluctuations during loading and their values measured from the experiments. These values are compared to each other in the third column using the equations indicated in the fourth. S_{d}, S_{k} and S_{T} correspond to, respectively, the dissipated energy, kinetic energy and duration of the avalanches, while S corresponds to the total variation of local deformation.

local dissipative events take place. Before the peak of the force-displacement response, they appear randomly distributed in space. At peak load, localization of the deformation of the cylinders takes place. As it progresses, cylinders below the forming band no longer see the applied loading. Using this observation, we quantitatively determined that the onset of localization takes place at the peak of the macroscopic response through the study of the evolution of the relative height of the lowest cylinders. As loading proceeds, the localized region eventually spans the system, going from one side to the other. At this point, further loading increments lead to the crushing of cylinders above the discontinuity.

Taking the advantage of the similarities observed in the system behavior and failure of quasi-brittle solids, we used the damage mechanics framework applied to two-dimensional elasto-damageable solids to describe the mechanical evolution of the system. Using this approach, we analytically determined the onset of localization as the peak load, and obtained the critical loading

at failure, identified as the separation of the system with a band of fully crushed cylinders. The predictions are in good agreement with the experimental observations, even though this description predicts a localization of the deformation perpendicularly to the applied loading, which is not well observed, probably due to strong friction at the edges. To go a step further, it would be interesting to characterize the spatial organization of the deformation as the system evolves towards localization. In particular, extract a correlation length and study its evolution, and compare the spatial distribution with the redistribution function obtained from the model derived in this chapter.

The coaction of local dissipative events and elastic interactions taking place in the system results in a strong intermittency of bursts. From the macroscopic response, we quantitatively defined the energy associated with these bursts, but also their duration. All these quantities appear to increase as localization is approached. In particular, the average values follow power law behaviors with the distance to peak. The study of the distributions of bursts sizes and duration also revealed power law statistics. As expected from the non-stationnarity of the system response, a smaller exponent is obtained when considering events taking place close to localization rather than throughout the whole loading process. Similar behaviors were obtained when considering bursts defined from the local deformation field. Indeed, the dissipated and kinetic energy, the duration of the dissipative events and deformation variations exhibit power law scaling. To understand these scaling behaviors more quantitatively, one may derive the evolution equation of the heterogeneous contribution of the damage field, assuming weakly perturbed field with respect to the homogeneous damage state, as detailed in chapter 4. This equation of evolution can be shown to be similar to the one of an elastic interface driven in a random medium. The interface behavior is characterized by the elastic redistribution kernel given in Eq. (5.26) calculated for predicting the onset of localization. A key feature of this kernel is that it changes of sign with the considered direction. This relates to the fact that some regions of the material get reloaded while others get unloaded after a damage event takes place in the solid. In that case, Lin *et al.* [69] showed the scaling exponents do vary from traditional depinning models that considers positive redistribution kernel. Indeed, instead of two independent exponents for traditional models, the interface behavior is now characterized by three independent exponents. The value of this additional exponent, noted θ by Lin *et al.* that is equal to zero for traditional depinning models, does depend on the actual shape of the kernel. As a result, the prediction of the exponents would require the determination of the depinning exponents for the specific kernel of Eq. (5.26), following for example the numerical methodology proposed by Lin *et al.*. This determination and the comparison with the value of the exponents measured in our experiments is let for future works. Interestingly, beyond the loading condition used in this study, different loading conditions like shearing or uniaxial loading that result in different redistribution kernels, may result in variations in the value of the scaling exponents characterizing the statistics of damage bursts. The study of the precursors statistics for different loading conditions might also be an interesting research direction for future works.

CONCLUSIONS

In this study, we investigated the quasi-brittle failure of heterogeneous materials, from the initiation of damage to the catastrophic failure associated with the precursors localization. To do so, we build a continuous model describing damage, viewed as a microcracks density, at the mesoscopic scale. It is at this microstructure scale that heterogeneities of the materials are taken into account through a disordered fracture energy field. The introduction of a non-local damage variable into the stiffness expression permits to take into account the damage driving force redistributions after damage events. The derivation of energy conservation allowed to obtain a thermodynamically consistent damage evolution law. A strength of this model is the possibility of tuning all the material properties, namely the fracture energy field, the stiffness expression and the interaction function α that controls the interactions between damaged heterogeneities. In this study we focused on the role of the latter one, the expression of which was chosen to both be able to perform analytical calculations and be physically relevant by being inspired from that calculated from the stresses redistributions taking place during the progressive damaging of 2D elasto-damageable solids.

This model was detailed in the second chapter were we have also shown that it is the coaction of interactions and heterogeneities that render the materials behavior interesting, whereas these ingredients taken separately makes the response of the system trivial. Nonetheless, the homogeneous material response is particularly interesting as a large part of the macroscopic response of interacting heterogeneous system can be predicted from it. This was shown in the third chapter were we performed analytical predictions of both the localization and failure thresholds. Both critical loadings (or equivalently damage levels in the system) appear to be fully controlled by the way the damage driving force is redistributed after a damage event, *i.e.* the expression of the interaction function used in the non-local formulation. If the critical thresholds appear independent of the internal length introduced in the interaction function, they continuously evolve with the shape parameter κ that controls the periodicity and amplitude with which the redistributions change of sign with the distance to the local damage event.

For κ below a critical value κ_c, the amplitude of the unloading regions is low or null. In that

case, we have shown that damage localizes over a homogeneous critical mode $q_c = 0$, associated with an infinite wavelength λ_c, so that both localization and failure take place at the same critical loading, corresponding to that of the homogeneous system snap-back instability. On the other hand, when strong unloading is allowed by fixing $\kappa > \kappa_c$ it allows damage to develop over a finite critical wavelength as localization proceeds and takes place prior to complete failure. Thus, the onset of damage localization and failure can take a broad range of value: in between the peak load and snap-back, at peak load, or even before peak load. Hence, from this analysis we conclude that the interaction function is the key ingredient controlling the material failure behavior. From a complementary energetical approach, we obtained physical insights on the localization process which was shown to correspond to a bifurcation of the solution of minimum energy from a homogeneous to a heterogeneous damage distribution. Both the linear stability analysis and this approach lead to the same localization criterion. Note also that our model naturally regularizes problems related to mesh sensitivity close to localization. Indeed, the zone of localized damage is either over a finite wavelength ($\kappa > \kappa_c$) or spread throughout the system ($\kappa \leq \kappa_c$).

In chapter four we have seen that the redistributions also control the damage evolution before localization. The complex spatio-temporal organization of damage observed experimentally in quasi-brittle materials is captured qualitatively well by our model. We show that a condition to observe the characteristic power law divergence of the rate of dissipated energy and damage field correlation length is an infinite critical wavelength over which damage develops ($\kappa \leq \kappa_c$). If it is finite ($\kappa > \kappa_c$), our statistical study of the precursors showed that both the avalanche size and spatial organization are bounded by the scale λ_c that characterizes the localization pattern. On the contrary, for $\kappa = 0$, the typical power law behavior of the dissipated energy with distance to failure is obtained, independently of the internal length ℓ_0. Yet, a net scale separation between the interaction length and the system size is required to observe the emergence of correlations in the damage field and the divergence of the extracted length scale. In that case, we were able to evidence robust scaling behaviors that relate the average avalanche size, its spatial extent and the correlation length of the cumulated damage field.

These observations argue for a critical interpretation of quasi-brittle failure. To explore this idea and determine the nature of the critical point, we show that the damage field follows an evolution law analogous to the one of an elastic interface driven in a random medium. The depinning dynamics of such an elastic manifold has been extensively used as a paradigm to understand the intermittency in disordered systems. In our case, the elasticity of the interface is set by the interaction function introduced in the non-local formulation of the damage model. In particular, when we consider the mean field limit, the power law statistics of the fluctuations observed in the numerical resolution of the model can be fully captured by this approach. The homogeneous damage represents the order parameter of the transition while the control parameter is shown to be the distance to catastrophic failure (for $\kappa \leq \kappa_c$), which can be related to a critical displacement or damage level at failure through the homogeneous equilibrium equations.

In the final chapter, we illustrate the versatility of our approach by applying it to the compression of a two dimensional array of soft hollow cylinders. We show that the transition to failure is characterized by local dissipative events that results in a progressive stiffness degradation. Disorder is naturally present in the system through variations in the contacts of the cylinders. The local dissipation events take place through friction between the elastically deforming elements forming the lattice. From the macroscopic response, we defined the resulting bursts of dissipative events in terms of dissipated and kinetic energy. We showed that in this system too, the interplay between elastic redistributions and heterogeneities results in the characteristic avalanche dynamic observed in quasi-brittle materials. The study of the deformation field permitted to define precisely the onset of localization. We also demonstrate how this behavior can be studied through our approach extended to 2D elasto-damageable solids. We predict the peak force and localization thresholds that are found in good agreement with the experimental measurements. Hence, for these types of system, if one manages to measure the elastic degradation and fracture energy evolution, the response, in particular localization and failure loadings, can be predicted.

If we have identified the relevant ingredients required to describe quasi-brittle failure of disordered materials, several material dependent properties remain to be evaluated and better understood. First, can the elastic moduli degradation with damage, which was experimentally measured in our experiment, be theoretically determined? Different expressions have been proposed so far [19, 37], but their relevance in the context of experimental fracture test remains to be shown. Moreover, we have introduced hardening in the material fracture energy field. We believe that it is an important feature for properly describing damage evolution. However, its origin remains unclear: does is associate with specific microscopic mechanism (friction, crack pinning and bridging) and how can it be measured in materials?

The understanding of the emergence of this hardening behavior, and in particular the associated micro mechanisms could allow a better design of materials. If one can increase the hardening by tuning, for example, the microstructure of the material, then the dissipated energy at failure could be increased so that more robust materials can be designed. Following the recent strong booming of metamaterials [31], from the observed control of localization and failure by the redistribution function, one could envisage the design of structures by taking advantage of its critical influence. Indeed, as the redistributions of the driving force depend on the elasticity of the material but also its loading conditions [Démery et al.], novel structures could be elaborated so that to postpone localization and failure through a taylored interaction function.

Finally, the statistical description of precursors to failure proposed here opens various perspectives for the monitoring hazarding structures and failure prediction. The recent development of powerful techniques of full field characterization such as in-situ tomography [17, 75], laminography [47], infrared radiations [115], combined with digital volume correlation [51] allows for accurate

monitoring of damage events. From the statistical study, we have seen that during the course of progressive damage, microdefects progressively cluster and spatially organize, while the dissipated energy, measured by AE, increases as failure is approached. Coupled with the type of models developed here, these features could be used as warnings to assess the lifetime of structures.

BIBLIOGRAPHY

[1] Alava, M. J., Nukala, P. K., and Zapperi, S. (2006). Statistical models of fracture. *Advances in Physics*, 55(3-4):349–476

[2] Amitrano, D. (2003). Brittle-ductile transition and associated seismicity: Experimental and numerical studies and relationship with the b value. *Journal of Geophysical Research: Solid Earth (1978–2012)*, 108(B1

[3] Amitrano, D. (2006). Rupture by damage accumulation in rocks. *International Journal of Fracture*, 139(3-4):369–381 0376–9429.

[4] Amitrano, D., Grasso, J., and Hantz, D. (1999). From diffuse to localised damage through elastic interaction. *Geophysical research letters*, 26(14):2109–2112

[5] Ashby, M. and Sammis, C. (1990). The damage mechanics of brittle solids in compression. *Pure and Applied Geophysics*, 133(3):489–521

[6] Barabási, A.-L. and Stanley, H. E. . . (1995). *Fractal concepts in surface growth*. Cambridge university press.

[7] Baró, J., Corral, Á., Illa, X., Planes, A., Salje, E. K., Schranz, W., Soto-Parra, D. E., and Vives, E. (2013). Statistical similarity between the compression of a porous material and earthquakes. *Physical review letters*, 110(8):088702.

[8] Bažant, Z. P. (1994). Nonlocal damage theory based on micromechanics of crack interactions. *Journal of engineering mechanics*, 120(3):593–617 0733–9399.

[9] Bažant, Z. P. and Pijaudier-Cabot, G. (1988). Nonlocal continuum damage, localization instability and convergence. *Journal of applied mechanics*, 55(2):287–293

[10] Bažant, Z. P., Şener, S., and Prat, P. C. (1988). Size effect tests of torsional failure of plain and reinforced concrete beams. *Materials and Structures*, 21(6):425–430

[11] Bideau, D., Gervois, A., Oger, L., and Troadec, J. (1986). Geometrical properties of disordered packings of hard disks. *Journal de Physique*, 47(10):1697–1707

[12] Bigoni, D. (2012). *Nonlinear solid mechanics: bifurcation theory and material instability*. Cambridge University Press.

[13] Bonamy, D. (2009). Intermittency and roughening in the failure of brittle heterogeneous materials. *Journal of Physics D: Applied Physics*, 42(21):214014 0022–3727.

[14] Bonamy, D. and Bouchaud, E. (2011). Failure of heterogeneous materials: A dynamic phase transition? *Physics Reports*, 498(1):1–44

[15] Bonamy, D., Santucci, S., and Ponson, L. (2008). Crackling dynamics in material failure as the signature of a self-organized dynamic phase transition. *Physical review letters*, 101(4):045501.

[16] Bower, A. and Ortiz, M. (1991). A three-dimensional analysis of crack trapping and bridging by tough particles. *Journal of the Mechanics and Physics of Solids*, 39(6):815–858

[17] Buffiere, J.-Y., Maire, E., Adrien, J., Masse, J.-P., and Boller, E. (2010). In situ experiments with x ray tomography: an attractive tool for experimental mechanics. *Experimental mechanics*, 50(3):289–305

[18] Carpinteri, A. and Ferro, G. (1994). Size effects on tensile fracture properties: a unified explanation based on disorder and fractality of concrete microstructure. *Materials and Structures*, 27(10):563–571

[19] Castañeda, P. P. and Willis, J. R. (1995). The effect of spatial distribution on the effective behavior of composite materials and cracked media. *Journal of the Mechanics and Physics of Solids*, 43(12):1919–1951

[20] Chaboche, J. (1987). Continuum damage mechanics: present state and future trends. *Nuclear Engineering and Design*, 105(1):19–33

[21] Daniel, I. and Charewicz, A. (1986). Fatigue damage mechanisms and residual properties of graphite/epoxy laminates. *Engineering Fracture Mechanics*, 25(5):793–808

[22] Davidsen, J., Stanchits, S., and Dresen, G. (2007). Scaling and universality in rock fracture. *Physical Review Letters*, 98:125502.

[23] De Arcangelis, L., Redner, S., and Herrmann, H. (1985). A random fuse model for breaking processes. *Journal de Physique Lettres*, 46(13):585–590

[24] De Vree, J., Brekelmans, W., and Van Gils, M. (1995). Comparison of nonlocal approaches in continuum damage mechanics. *Computers & Structures*, 55(4):581–588

[Démery et al.] Démery, V., Berthier, E., Kondo, D., and Ponson, L. Stability analysis of a heterogeneously damaged solid. *(submitted for publication)*.

[26] Deschanel, S., Vanel, L., Godin, N., Vigier, G., and Ciliberto, S. (2009). Experimental study of crackling noise: conditions on power law scaling correlated with fracture precursors. *Journal of Statistical Mechanics: Theory and Experiment*, 2009(01):P01018

[27] Diodati, P., Marchesoni, F., and Piazza, S. (1991). Acoustic emission from volcanic rocks: an example of self-organized criticality. *Physical review letters*, 67(17):2239.

[28] Eshelby, J. D. (1957). *The determination of the elastic field of an ellipsoidal inclusion, and related problems*, volume 241. The Royal Society.

[29] Evans, A. (2011). Acoustic emission sources in brittle solids. *Lawrence Berkeley National Laboratory*.

[30] Fisher, D. S. (1998). Collective transport in random media: from superconductors to earthquakes. *Physics reports*, 301(1):113–150

[31] Florijn, B., Coulais, C., and van Hecke, M. (2014). Programmable mechanical metamaterials. *Physical review letters*, 113(17):175503.

[32] Fortin, J., Stanchits, S., Dresen, G., and Guéguen, Y. (2006). Acoustic emission and velocities associated with the formation of compaction bands in sandstone. *Journal of Geophysical Research: Solid Earth (1978–2012)*, 111(B10

[33] Fortin, J., Stanchits, S., Dresen, G., and Gueguen, Y. (2009). *Acoustic emissions monitoring during inelastic deformation of porous sandstone: comparison of three modes of deformation*, pages 823–841 Springer.

[34] Gao, H. and Rice, J. R. (1989). A first-order perturbation analysis of crack trapping by arrays of obstacles. *Journal of applied mechanics*, 56(4):828–836

[35] Garcimartín, A. Á., Guarino, A., Lebon, L., and Ciliberto, S. . .-. (1997). Statistical properties of fracture precursors.

[36] Giamarchi, T., Kolton, A., and Rosso, A. (2006). *Dynamics of disordered elastic systems*, pages 91–108 3540300287. Springer.

[37] Girard, L., Amitrano, D., and Weiss, J. (2010). Failure as a critical phenomenon in a progressive damage model. *Journal of Statistical Mechanics: Theory and Experiment*, 2010(01):P01013

[38] Grasso, J. and Sornette, D. (1998). Testing selforganized criticality by induced seismicity. *Journal of Geophysical Research: Solid Earth (1978–2012)*, 103(B12):29965–29987

[39] Grégoire, D., Rojas-Solano, L., and Pijaudier-Cabot, G. (2013). Failure and size effect for notched and unnotched concrete beams. *International Journal for Numerical and Analytical Methods in Geomechanics*, 37(10):1434–1452

[40] Griffith, A. A. (1921). The phenomena of rupture and flow in solids. *Philosophical transactions of the royal society of london. Series A, containing papers of a mathematical or physical character*, pages 163–198

[41] Guarino, A., Ciliberto, S., Garcimartín, A., Zei, M., and Scorretti, R. (2002). Failure time and critical behaviour of fracture precursors in heterogeneous materials. *The European Physical Journal B-Condensed Matter and Complex Systems*, 26(2):141–151

[42] Guarino, A., Garcimartín, A., and Ciliberto, S. (1998). An experimental test of the critical behaviour of fracture precursors. *The European Physical Journal B-Condensed Matter and Complex Systems*, 6(1):13–24

[43] Guyon, E., Roux, S., Hansen, A., Bideau, D., Troadec, J.-P., and Crapo, H. (1990). Non-local and non-linear problems in the mechanics of disordered systems: application to granular media and rigidity problems. *Reports on Progress in Physics*, 53(4):373

[44] Hansen, A. and Hemmer, P. (1994). Burst avalanches in bundles of fibers: Local versus global load-sharing. *Physics Letters A*, 184(6):394–396

[45] Hansen, A. and Roux, S. (2000). *Statistics toolbox for damage and fracture*. Springer.

[46] Heap, M. J., Vinciguerra, S., and Meredith, P. (2009). The evolution of elastic moduli with increasing crack damage during cyclic stressing of a basalt from mt. etna volcano. *Tectonophysics*, 471(1):153–160

[47] Helfen, L., Myagotin, A., Mikulík, P., Pernot, P., Voropaev, A., Elyyan, M., Di Michiel, M., Baruchel, J., and Baumbach, T. (2011). On the implementation of computed laminography using synchrotron radiation. *Review of Scientific Instruments*, 82(6):063702

[48] Herrmann, H. J. and Roux, S. (2014). *Statistical models for the fracture of disordered media*. Elsevier.

[49] Hidalgo, R. C., Kun, F., and Herrmann, H. J. (2001). Bursts in a fiber bundle model with continuous damage. *Physical Review E*, 64(6):066122.

[50] Hidalgo, R. C., Moreno, Y., Kun, F., and Herrmann, H. J. (2002). Fracture model with variable range of interaction. *Physical review E*, 65(4):046148.

[51] Hild, F., Bouterf, A., and Roux, S. (2015). Damage measurements via dic. *International Journal of Fracture*, 191(1-2):77–105 0376–9429.

[52] Horii, H. and Nemat-Nasser, S. (1985). Compressioninduced microcrack growth in brittle solids: Axial splitting and shear failure. *Journal of Geophysical Research: Solid Earth (1978–2012)*, 90(B4):3105–3125

[53] Jirásek, M. (1998). Nonlocal models for damage and fracture: comparison of approaches. *International Journal of Solids and Structures*, 35(31):4133–4145

[54] Jirásek, M. (2015). Modeling of localized inelastic deformation, lecture notes. *Czech Technical University, Prague*.

[55] Kachanov, M. (1987). Elastic solids with many cracks: a simple method of analysis. *International Journal of Solids and Structures*, 23(1):23–43 0020–7683.

[56] Kachanov, M. (2003). On the problems of crack interactions and crack coalescence. *International journal of fracture*, 120(3):537–543 0376–9429.

[57] Kashcheyevs, V. (2011). Exact non-hookean scaling of cylindrically bent elastic sheets and the large-amplitude pendulum. *American Journal of Physics*, 79(6):657–661

[58] Katz, O. and Reches, Z. (2004). Microfracturing, damage, and failure of brittle granites. *Journal of Geophysical Research: Solid Earth (1978–2012)*, 109(B1

[59] Kloster, M., Hansen, A., and Hemmer, P. C. (1997). Burst avalanches in solvable models of fibrous materials. *Physical Review E*, 56(3):2615.

[60] Krajcinovic, D. (1989). Damage mechanics. *Mechanics of materials*, 8(2):117–197

[61] Krajcinovic, D. and Van Mier, J. (2000). *Introduction to damage mechanics*. Springer.

[62] Kun, F., Raischel, F., Hidalgo, R., and Herrmann, H. (2006). *Extensions of fibre bundle models*, pages 57–92 Springer.

[63] Kupfer, H., Hilsdorf, H. K., and Rusch, H. (1969). *Behavior of concrete under biaxial stresses*, volume 66. ACI.

[64] Lawn, B. R. and Marshall, D. B. (1998). Nonlinear stress-strain curves for solids containing closed cracks with friction. *Journal of the Mechanics and Physics of Solids*, 46(1):85–113

[65] Lei, X., Nishizawa, O., Kusunose, K., and Satoh, T. (1992). Fractal structure of the hypocenter distributions and focal mechanism solutions of acoustic emission in two granites of different grain sizes. *Journal of Physics of the Earth*, 40(6):617–634

[66] Lemaitre, J. (2012). *A course on damage mechanics*. Springer Science & Business Media.

[67] Lemaitre, J. and Dufailly, J. (1987). Damage measurements. *Engineering Fracture Mechanics*, 28(5):643–661

[68] Leschhorn, H., Nattermann, T., Stepanow, S., and Tang, L. (1997). Driven interface depinning in a disordered medium. *Annalen der Physik*, 509(1):1–34

[69] Lin, J., Lerner, E., Rosso, A., and Wyart, M. (2014). Scaling description of the yielding transition in soft amorphous solids at zero temperature. *Proceedings of the National Academy of Sciences*, 111(40):14382–14387

[70] Lockner, D. (1993). *The role of acoustic emission in the study of rock fracture*, volume 30. Elsevier.

[71] Lockner, D., Byerlee, J., Kuksenko, V., Ponomarev, A., and Sidorin, A. (1991). Quasi-static fault growth and shear fracture energy in granite. *Nature*, 350(6313):39–42

[72] Locknet, D. and Byerlee, J. D. (1995). Precursory ae patterns leading to rock fracture. *Series on rock and soil mechanics*, 19:45–58

[73] Lorentz, E. and Andrieux, S. (2003). Analysis of non-local models through energetic formulations. *International Journal of Solids and Structures*, 40(12):2905–2936

[74] Maes, C., Van Moffaert, A., Frederix, H., and Strauven, H. (1998). Criticality in creep experiments on cellular glass. *Physical review b*, 57(9):4987.

[75] Maire, E. and Withers, P. (2014). Quantitative x-ray tomography. *International materials reviews*, 59(1):1–43

[76] Mazars, J., Boerman, D., and Piatti, G. (2013). *Mechanical damage and fracture of concrete structures*.

[77] Nukala, P. K. V., Zapperi, S., and Šimunović, S. (2005). Statistical properties of fracture in a random spring model. *Physical Review E*, 71(6):066106.

[78] Obert, L. (1941). *Use of subaudible noises for prediction of rock bursts*, volume 3555. US Dept. of the Interior, Bureau of Mines.

[79] Papka, S. and Kyriakides, S. (1999). Biaxial crushing of honeycombs:—part 1: Experiments. *International Journal of Solids and Structures*, 36(29):4367–4396

[80] Papka, S. D. and Kyriakides, S. (1998). In-plane crushing of a polycarbonate honeycomb. *International Journal of Solids and Structures*, 35(3):239–267

[81] Peerlings, R. H. J., de Borst, R., Brekelmans, W. A. M., and de Vree, J. H. P. (1996). Gradient enhanced damage for quasi-brittle materials. *International Journal for numerical methods in engineering*, 39:3391–3403.

[82] Petri, A., Paparo, G., Vespignani, A., Alippi, A., and Costantini, M. (1994). Experimental evidence for critical dynamics in microfracturing processes. *Physical Review Letters*, 73(25):3423.

[83] Pham, K., Amor, H., Marigo, J.-J., and Maurini, C. (2011a). Gradient damage models and their use to approximate brittle fracture. *International Journal of Damage Mechanics*, 20(4):618–652 1056–7895.

[84] Pham, K., Marigo, J.-J., and Maurini, C. (2011b). The issues of the uniqueness and the stability of the homogeneous response in uniaxial tests with gradient damage models. *Journal of the Mechanics and Physics of Solids*, 59(6):1163–1190

[85] Picallo, C. B. and López, J. M. (2008). Energy dissipation statistics in the random fuse model. *Physical Review E*, 77(4):046114.

[86] Picard, G., Ajdari, A., Lequeux, F., and Bocquet, L. (2004). Elastic consequences of a single plastic event: A step towards the microscopic modeling of the flow of yield stress fluids. *The European Physical Journal E*, 15(4):371–381

[87] Pijaudier-Cabot, G. and Bažant, Z. P. (1987). Nonlocal damage theory. *Journal of engineering mechanics*, 113(10):1512–1533 0733–9399.

[88] Pijaudier-Cabot, G. and Berthaud, Y. (1990). Effets des interactions dans l'endommagement d'un milieu fragile. formulation non locale. *Comptes rendus de l'Académie des sciences. Série 2, Mécanique, Physique, Chimie, Sciences de l'univers, Sciences de la Terre*, 310(12):1577–1582

[89] Pijaudier-Cabot, G., Haidar, K., and Dubé, J. (2004). Nonlocal damage model with evolving internal length. *International journal for numerical and analytical methods in geomechanics*, 28(78):633–652

[90] Poirier, C., Ammi, M., Bideau, D., and Troadec, J. (1992). Experimental study of the geometrical effects in the localization of deformation. *Physical review letters*, 68(2):216.

[91] Poon, B., Ponson, L., Zhao, J., and Ravichandran, G. (2011). Damage accumulation and hysteretic behavior of max phase materials. *Journal of the Mechanics and Physics of Solids*, 59(10):2238–2257

[92] Pradhan, S., Bhattacharyya, P., and Chakrabarti, B. (2002). Dynamic critical behavior of failure and plastic deformation in the random fiber bundle model. *Physical Review E*, 66(1):016116.

[93] Pradhan, S., Hansen, A., and Chakrabarti, B. K. (2010). Failure processes in elastic fiber bundles. *Reviews of modern physics*, 82(1):499.

[94] Pradhan, S., Hansen, A., and Hemmer, P. C. (2006). Crossover behavior in failure avalanches. *Physical Review E*, 74(1):016122.

[95] Pratt, H., Black, A., Brown, W., and Brace, W. (1972). *The effect of speciment size on the mechanical properties of unjointed diorite*, volume 9. Elsevier.

[96] Puglisi, G. and Truskinovsky, L. (2005). Thermodynamics of rate-independent plasticity. *Journal of the Mechanics and Physics of Solids*, 53(3):655–679

[97] Raischel, F., Kun, F., and Herrmann, H. J. (2008). Continuous damage fiber bundle model for strongly disordered materials. *Physical Review E*, 77(4):046102.

[98] Ravichandran, G. and Subhash, G. (1995). A micromechanical model for high strain rate behavior of ceramics. *International Journal of Solids and structures*, 32(17):2627–2646

[99] Rojas-Solano, L. B., Grégoire, D., and Pijaudier-Cabot, G. (2013). Interaction-based non-local damage model for failure in quasi-brittle materials. *Mechanics Research Communications*, 54:56–62

[100] Salminen, L., Alava, M., and Niskanen, K. (2003). Analysis of long crack lines in paper webs. *The European Physical Journal B-Condensed Matter and Complex Systems*, 32(3):369–374

[101] Salminen, L., Tolvanen, A., and Alava, M. (2002). Acoustic emission from paper fracture. *Physical Review Letters*, 89(18):185503.

[102] Schall, P., Weitz, D. A., and Spaepen, F. (2007). Structural rearrangements that govern flow in colloidal glasses. *Science*, 318(5858):1895–1899

[103] Schmittbuhl, J., Roux, S., Vilotte, J.-P., and Måløy, K. J. (1995). Interfacial crack pinning: effect of nonlocal interactions. *Physical Review Letters*, 74(10):1787.

[104] Schneebeli, G. (1956). Une analogie mécanique pour les terres sans cohésion. *Comptes rendus hebdomadaires des séances de l'académie des sciences*, 243(2):125–126.

[105] Sethna, J. P., Dahmen, K. A., and Myers, C. R. (2001). Crackling noise. *Nature*, 410(6825):242–250

[106] Sornette, D. and Andersen, J. V. (1998). Scaling with respect to disorder in time-to-failure. *The European Physical Journal B-Condensed Matter and Complex Systems*, 1(3):353–357

[107] Stojanova, M., Santucci, S., Vanel, L., and Ramos, O. (2014). High frequency monitoring reveals aftershocks in subcritical crack growth. *Phys. Rev. Lett.*, 112:115502.

[108] Travers, T., Ammi, M., Bideau, D., Gervois, A., Messager, J., and Troadec, J. (1987). Uniaxial compression of 2d packings of cylinders. effects of weak disorder. *EPL (Europhysics Letters)*, 4(3):329

[109] Travers, T., Bideau, D., Gervois, A., Troadec, J., and Messager, J. (1986). Uniaxial compression effects on 2d mixtures of'hard'and'soft'cylinders. *Journal of physics A: mathematical and general*, 19(16):L1033 0305–4470.

[110] van Vliet, M. R. and van Mier, J. G. (2000). Experimental investigation of size effect in concrete and sandstone under uniaxial tension. *Engineering Fracture Mechanics*, 65(2):165–188

[111] Vandembroucq, D. and Roux, S. (2011). Mechanical noise dependent aging and shear banding behavior of a mesoscopic model of amorphous plasticity. *Physical Review B*, 84(13):134210.

[112] Weibull, W. (1939). *A statistical theory of the strength of materials*. Number 151. Generalstabens litografiska anstalts förlag.

[113] Weiss, J., Girard, L., Gimbert, F., Amitrano, D., and Vandembroucq, D. (2014). (finite) statistical size effects on compressive strength. *Proceedings of the National Academy of Sciences*, 111(17):6231–6236

[114] Weiss, J., Rhouma, W. B., Richeton, T., Dechanel, S., Louchet, F., and Truskinovsky, L. (2015). From mild to wild fluctuations in crystal plasticity. *Physical review letters*, 114(10):105504.

[115] Wu, L., Liu, S., Wu, Y., and Wang, C. (2006). Precursors for rock fracturing and failure—part i: Irr image abnormalities. *International journal of rock mechanics and mining sciences*, 43(3):473–482

[116] Xia, S., Ponson, L., Ravichandran, G., and Bhattacharya, K. (2012). Toughening and asymmetry in peeling of heterogeneous adhesives. *Physical review letters*, 108(19):196101.

[117] Xia, S., Ponson, L., Ravichandran, G., and Bhattacharya, K. (under review). Adhesion of heterogeneous thin films: Ii. adhesive heterogeneity. *J. Mech. Phys. Solids*.

[118] Zang, A., Wagner, F. C., Stanchits, S., Dresen, G., Andresen, R., and Haidekker, M. A. (1998). Source analysis of acoustic emissions in aue granite cores under symmetric and asymmetric compressive loads. *Geophysical Journal International*, 135(3):1113–1130 0956–540X.

[119] Zapperi, S., Cizeau, P., Durin, G., and Stanley, H. E. (1998). Dynamics of a ferromagnetic domain wall: Avalanches, depinning transition, and the barkhausen effect. *Physical Review B*, 58(10):6353.

[120] Zapperi, S., Nukala, P. K. V., and Šimunović, S. (2005). Crack roughness and avalanche precursors in the random fuse model. *Physical Review E*, 71(2):026106.

[121] Zapperi, S., Vespignani, A., and Stanley, H. E. (1997). Plasticity and avalanche behaviour in microfracturing phenomena. *Nature*, 388(6643):658–660

APPENDIX A

DERIVATION OF THE EVOLUTION LAW OF THE DAMAGE FIELD

In this Appendix we detail the calculations used for the determination of the damage equilibrium of Eq. (2.8). We first show the calculations when we write energy conservation with respect to loading variation:

$$\frac{\partial E}{\partial \Delta} = 0 \tag{A.1}$$

Then, we show that the same result is obtained when considering the conservation with respect to damage variation at constant applied displacement

$$\frac{\delta E}{\delta d} = 0 \tag{A.2}$$

where a fonctional derivative is used for the computations. We start with the derivation with respect to displacement. In Eq. (A.1) we replace E by the expression of the total energy of the system, given by Eq. (2.4):

$$\frac{\partial}{\partial \Delta}\left[\int_\Sigma \frac{1}{2}\Delta^2 k[\overline{d}(\vec{x},\Delta)]d\vec{x} + \int_0^\Delta \int_\Sigma \left.\frac{\partial d}{\partial \Delta}\right|_{\vec{x},\tilde{\Delta}} Y_c(\vec{x},d)d\vec{x}d\tilde{\Delta} - \int_0^\Delta F(\tilde{\Delta})d\tilde{\Delta}\right] = 0 \tag{A.3}$$

$$\Rightarrow \int_\Sigma \Delta k[\overline{d}(\vec{x},\Delta)]d\vec{x} + \int_\Sigma \frac{1}{2}\Delta^2 \frac{\partial k[\overline{d}(\vec{x},\Delta)]}{\partial \Delta}d\vec{x} + \int_\Sigma \left.\frac{\partial d}{\partial \Delta}\right|_{\vec{x},\tilde{\Delta}} Y_c(\vec{x},d)d\vec{x} - F(\Delta) = 0 \tag{A.4}$$

$$\Rightarrow \int_\Sigma \frac{1}{2}\Delta^2 \frac{\partial k[\overline{d}(\vec{x},\Delta)]}{\partial \overline{d}} \left.\frac{\partial \overline{d}}{\partial \Delta}\right|_{\vec{x},\tilde{\Delta}} d\vec{x} + \int_\Sigma \left.\frac{\partial d}{\partial \Delta}\right|_{\vec{x},\tilde{\Delta}} Y_c(\vec{x},d)d\vec{x} = 0 \tag{A.5}$$

$$\Rightarrow \int_\Sigma \frac{1}{2}\Delta^2 k'[\overline{d}(\vec{x},\Delta)] \left.\frac{\partial \overline{d}}{\partial \Delta}\right|_{\vec{x},\tilde{\Delta}} d\vec{x} + \int_\Sigma \left.\frac{\partial d}{\partial \Delta}\right|_{\vec{x},\tilde{\Delta}} Y_c(\vec{x},d)d\vec{x} = 0 \tag{A.6}$$

$$\Rightarrow -\int_\Sigma Y(\vec{x},\Delta)\frac{\partial}{\partial \Delta}\int_\Sigma \alpha(\vec{x}-\vec{\xi})d(\vec{\xi})d\vec{\xi}d\vec{x} + \int_\Sigma \left.\frac{\partial d}{\partial \Delta}\right|_{\vec{x},\tilde{\Delta}} Y_c(\vec{x},d)d\vec{x} = 0 \tag{A.7}$$

$$\Rightarrow -\int_\Sigma \left.\frac{\partial d}{\partial \Delta}\right|_{\vec{\xi},\tilde{\Delta}} \int_\Sigma \alpha(\vec{x}-\vec{\xi})Y(\vec{x},\Delta)d\vec{x}d\vec{\xi} + \int_\Sigma \left.\frac{\partial d}{\partial \Delta}\right|_{\vec{x},\tilde{\Delta}} Y_c(\vec{x},d)d\vec{x} = 0 \tag{A.8}$$

$$\Rightarrow -\int_\Sigma \left.\frac{\partial d}{\partial \Delta}\right|_{\vec{\xi},\tilde{\Delta}} \overline{Y}(\vec{\xi},\Delta)d\vec{\xi} + \int_\Sigma \left.\frac{\partial d}{\partial \Delta}\right|_{\vec{x},\tilde{\Delta}} Y_c(\vec{x},d)d\vec{x} = 0 \tag{A.9}$$

$$\Rightarrow \int_\Sigma \left.\frac{\partial d}{\partial \Delta}\right|_{\vec{x},\tilde{\Delta}} \left(\overline{Y}(\vec{x},\Delta) - Y_c(\vec{x},d)\right) d\vec{x} = 0 \tag{A.10}$$

Therefore, the equilibrium condition writes as

$$\overline{Y}(\vec{x},\Delta) = Y_c(\vec{x},d) \tag{A.11}$$

We now perform the same calculations using a functional derivative of the total energy with respect to damage. Let $d_0(\vec{x})$ be the damage field at a given Δ. We consider a small fluctuation $\delta d_0 \delta(\vec{x} - \vec{x_0})$ applied at some point $\vec{x_0}$ in the system and such that δd_0 is very small. The damage field hence writes as

$$d(\vec{x}) = d_0(\vec{x}) + \delta d_0 \delta(\vec{x} - \vec{x_0}) \tag{A.12}$$

Which results in a non-local damage field of the form

$$\overline{d}(\vec{x}) = \overline{d}_0(\vec{x}) + \alpha(\vec{x} - \vec{x_0})\delta d_0 \tag{A.13}$$

Using that δd_0 tends to zero, we express both the stiffness and fracture energy fields as a first order expansion:

$$k[\overline{d}(\vec{x}] = k[\overline{d}_0(\vec{x})] + k'[\overline{d}_0(\vec{x})]\delta d_0 \alpha(\vec{x} - \vec{x_0}) \tag{A.14}$$

$$\Rightarrow Y_c[\vec{x},d] = Y_c[\vec{x},d_0] + Y_c'[\vec{x},d_0]\delta d_0 \delta(\vec{x} - \vec{x_0}) \tag{A.15}$$

We define the functional derivative of the elastic energy as

$$\begin{aligned}
&\lim_{\delta d_0 \to 0} \frac{E^{el}[\Delta, d_0(\vec{x}) + \delta d_0 \delta(\vec{x} - \vec{x_0})] - E^{el}[\Delta, d_0(\vec{x})]}{\delta d_0} \\
&= \int_\Sigma \frac{1}{2}\Delta^2 k'[d_0(\vec{x})]\alpha(\vec{x} - \vec{x_0})d\vec{x} = -\int_\Sigma Y(\vec{x},\Delta)\alpha(\vec{x} - \vec{x_0})d\vec{x} \\
&= -\ell^n \overline{Y}(\vec{x_0},\Delta)
\end{aligned} \tag{A.16}$$

Similarly, we obtain the rate of dissipated energy by damage as

$$\begin{aligned}
&\lim_{\delta d_0 \to 0} \frac{E^d[\Delta, d_0(\vec{x}) + \delta d_0 \delta(\vec{x} - \vec{x_0})] - E^d[\Delta, d_0(\vec{x})]}{\delta d_0} \\
&= \lim_{\delta d_0 \to 0} \frac{1}{\delta d_0} \left[\int_\Sigma \int_0^\Delta \left.\frac{\partial d}{\partial \Delta}\right|_{\vec{x},\tilde{\Delta}} \left(Y_c[\vec{x},d_0] + Y_c'[\vec{x},d_0]\delta d_0 \delta(\vec{x} - \vec{x_0})\right) d\vec{x} - \int_\Sigma \int_0^\Delta \left.\frac{\partial d}{\partial \Delta}\right|_{\vec{x},\tilde{\Delta}} Y_c[\vec{x},d_0]d\vec{x} \right] \\
&= \lim_{\delta d_0 \to 0} \frac{1}{\delta d_0} \left(\ell^n \delta d_0 \left(Y_c[\vec{x_0},d_0] + \delta d_0 Y_c'[\vec{x_0},d_0]\right)\right) \\
&= \ell^n Y_c(\vec{x_0},d_0)
\end{aligned} \tag{A.17}$$

We finally obtain the equilibrium equation that writes as

$$\frac{\delta E^t}{\delta d} = 0 \Rightarrow \overline{Y}(\vec{x}_0, \Delta) = Y_c(\vec{x}_0, d_0) \tag{A.18}$$

APPENDIX B

NON-HARDENING BRITTLE DISORDERED MATERIAL

We have seen that with the introduction of hardening and a continuous damage evolution, a behavior close to that of a mean field system is obtained whatever the internal length ℓ_0. If we remove the hardening property of the material, as the heterogeneities have a brittle behavior (the parameter a of the stiffness expression Eq. (2.11) is negative) their damage parameter is either 0 (intact element) or 1 (broken). We show in this section that in that case we have a continuous transition from two classes of models. For large internal lengths, the response does not differ from that obtained when material has a hardening behavior and corresponds to a mean field system response. On the other hand, for low internal lengths, the behavior strongly differs as a different damage mechanism dominates, resulting in the apparition of bounded fluctuations that scale with ℓ_0.

We first study the macroscopic response of the system as a function of the ℓ_0 values and characterize the dependency of the critical loading at failure with this parameter. It appears that a continuous scaling with ℓ_0 is obtained for small internal lengths while for large ones the failure loading is that of global load sharing model, as emphasized by an analytical prediction of Δ_c in that case. The study of the fluctuations highlights this transition. The system has bounded fluctuations that scale with ℓ_0 for small redistribution ranges, while they diverge as the internal length ℓ_0 becomes much larger than the heterogeneities.

For the numerical simulations, a large system size of $N = 100000$ elements is used, the internal length is varied from 1 to infinity and the disorder intensity σ_g is set to 0.2.

B.1 Macroscopic behavior

The normalized macroscopic response of the non-hardening system is shown for various internal lengths on Fig. B.1a. Two behaviors are obtained: (i) for low internal lengths, $\ell_0 \leq 5$, the response is continuous until failure, which occurs at a critical displacement that is lowered as ℓ_0 is increased; (ii) for large ℓ_0 values, the response becomes independent of the value of the parameter

and a catastrophic failure is observed.

To characterize the critical loading dependency with the internal length, we show on Fig. B.1b the evolution of the normalized critical loading at failure as a function of the internal length value. As expected from the observation of the force-displacement response, failure occurs earlier as the range of interaction is increased, up to a threshold value: for $\ell_0 \geq 100$ the critical displacement becomes independent of the value of the internal length. On the other hand, for $\ell_0 < 100$, a continuous evolution is observed.

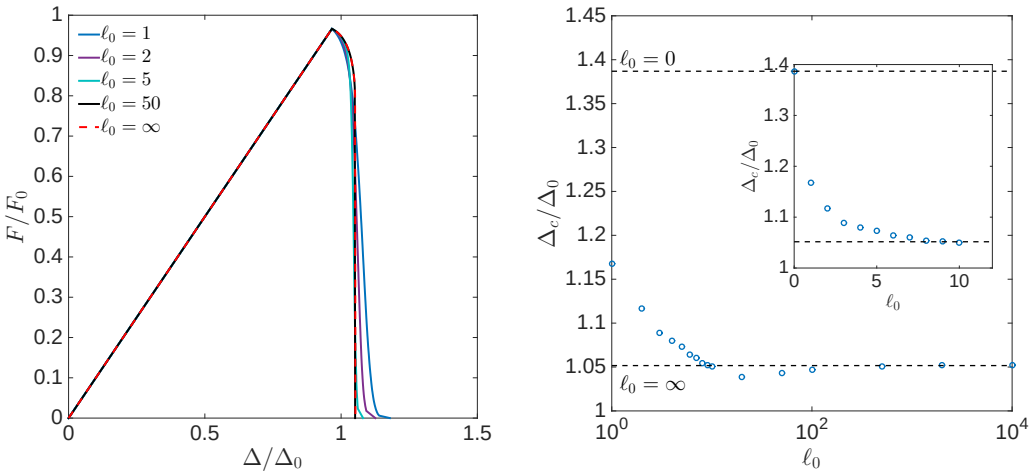

(a) (b)

Figure B.1: (a) Normalized macroscopic reponse obtained for different internal lengths. Two behaviors emerge: for small internal length ($\ell_0 \leq 5$) a continuous response is obtained up to failure, the critical loading of which varies with ℓ_0, the response becomes independent of the ℓ_0 value for large internal length and exhibits a catastrophic failure; (b) Evolution of the normalized critical loading at failure as a function of the internal length, the analytical prediction for a global load sharing ($\ell_0 = \infty$) and percolation model ($\ell_0 = 0$) are indicated and emphasizes the two regimes: continuous decrease for low ℓ_0 values while for $\ell_0 \geq 100$ the critical loading is that of a mean field system.

To understand both the upper and lower limits, we first determine the critical loading at failure in the two extreme limits of independent heterogeneities ($\ell_0 = 0$) and mean field redistributions ($\ell_0 = \infty$). The lower limit value renders the system response particularly simple to predict and analyze: setting ℓ_0 to zero corresponds to a Dirac redistribution function, which leads to each element behaving independently from the others. It is equivalent to treating the system as interaction-free: the system is solely characterized by its fracture energies and the model becomes local. Due to the brittle behavior of the heterogeneities, the evolution equation concerns only intact elements and is given by Eq. (2.25) where the fracture energy is damage independent:

$$Y(\vec{x}, \Delta) = Y_c(\vec{x}) \tag{B.1}$$

As intact heterogeneities are not affected by a failure event taking place elsewhere, the system fails by breaking each element one by one, from the weakest to the strongest, respecting the ascending order of fracture energies values that we denote by $Y_{c1} < Y_{c2} < ... < Y_{cN}$. To break the $k-$th element of fracture energy Y_{ck}, we shall apply a loading Δ calculated as

$$\Delta = \sqrt{-\frac{2Y_{ck}}{k'[0]}} \tag{B.2}$$

At this loading, the corresponding statistical number of intact elements is $N(1-P(Y_{ck}))$, where $P(Y_{ck})$ is the cumulative distribution function of the uniform probability density expressed in equation (2.10):

$$P(Y_c) = \begin{cases} 0 & \text{for } Y_c < Y_c^{\min} \\ \dfrac{Y_c - Y_c^{\min}}{Y_c^{\max} - Y_c^{\min}} & \text{for } Y_c^{\min} \leq Y_c \leq Y_c^{\max} \\ 1 & \text{for } Y_c \geq Y_c^{\max} \end{cases} \tag{B.3}$$

Using that the local stiffness is either 0 ($d=1$) or k_0 ($d=0$), we obtain the corresponding macroscopic force to break the element the element of fracture energy Y_{ck}:

$$F(Y_{ck}) = Lk_0(1-P(Y_{ck}))\Delta = Lk_0\frac{Y_c^{\max} - Y_{ck}}{Y_c^{\max} - Y_c^{\min}}\sqrt{-\frac{2Y_{ck}}{k'[0]}} \tag{B.4}$$

where we have replaced Δ using Eq. (B.2). Hence, knowing the fracture energy distribution, e.g. uniform, we can predict the full statistical macroscopic response of the system. To obtain the critical displacement at failure, we must consider the strength $Y_c^{\max}$ of the strongest element. Using that $Y_c^{\max} = Y_{c0} + \sqrt{3}\sigma_g$ (see Sec. 2.1.2), we obtain the dependency of Δ_c with the disorder intensity:

$$\Delta_c = \sqrt{\frac{-2(Y_{c0} + \sqrt{3}\sigma_g)}{k'[0]}} \tag{B.5}$$

We now treat the case of an infinite internal length $\ell_0 = \infty$, which corresponds to an equal redistribution of the driving force among the heterogeneities, independently of their state (broken or intact) and distance to the damage point. It corresponds to a non-local damage parameter expressed as

$$\overline{d}(x,\Delta) = < d(\Delta) > = 1 - \frac{N_s(\Delta)}{N} = 1 - U(\Delta) \tag{B.6}$$

where N_s and U are respectively the number and density of surviving elements. As the non-local field is spatially independent, it leads to a local damage driving force:

$$\overline{Y}(x,\Delta) = Y(\Delta) = -\frac{1}{2}\Delta^2 k'[U(\Delta)] \tag{B.7}$$

To predict the system response, we follow the approach of Pradhan et al.[92]: assume that we start with an intact material ($U_0 = 1$) and apply a load Δ to break a first element, *i.e.* the weakest one.

The corresponding damage driving force writes as

$$Y_1(\Delta) = -\frac{1}{2}\Delta^2 k_0(3a(1-U_0)^2 - (a+1)) \tag{B.8}$$

From the evolution equation $Y(\Delta) = Y_c(\vec{x})$, where Y_c is drawn from a given distribution, we have a density of surviving elements which can be expressed as

$$U_1(\Delta) = (1 - P(Y_1)) \tag{B.9}$$

As the first element is broken, we have a redistribution of the driving force. At the same fixed applied loading, it leads to a resulting Y field that writes as

$$Y_2(\Delta) = -\frac{1}{2}\Delta^2 k_0(3a(1-U_1)^2 - (a+1)) \tag{B.10}$$

We assume that it is high enough to trigger the failure of the second weakest element, of fracture energy Y_{c2}. After this damage event, the surviving density is

$$U_2(\Delta) = (1 - P(Y_2)) \tag{B.11}$$

The failure event again leads to a damage driving force redistribution, which can itself lead to the failure of one more element. The system goes on until equilibrium is reached. From this process, we can establish the recurrence relation:

$$U_{t+1}(\Delta) = (1 - P(Y_t)) = 1 - \frac{-1/2\Delta^2 k_0(3a(1-U_t)^2 - (a+1)) - Y_c^{\min}}{Y_c^{\max} - Y_c^{\min}} \tag{B.12}$$

At a given applied loading Δ, this recurrence relation is of the form $U_{t+1} = \mathcal{H}(U_t)$ from which a fixed point U^* can be obtained using its definition $U^* = \mathcal{H}(U^*)$. Considering the Equation (B.12) one gets

$$U^*(\Delta) = 1 + \frac{Y_c^{\max} - Y_c^{\min}}{3ak_0\Delta^2} - \frac{\sqrt{6a\Delta^2 k_0(\Delta^2 * k_0 - Y_c^{\min}) + (Y_c^{\max} - Y_c^{\min})^2}}{3a\Delta^2 k_0} \tag{B.13}$$

At a given loading, the system will eventually reach an equilibrium state, corresponding to a density U^* of intact elements, or $N - N_s$ broken heterogeneities. To break the next $k-$th fiber, the loading is increased, the fiber is broken which in turns trigger more failure until a new equilibrium position is reached. For each applied loading, the system is damaged until a density $U^*(\Delta)$ is obtained. This quantity U^* represents the density of surviving elements and should hence be real. Its existence is thus controlled by the sign of the term under the square-root. This leads to the critical loading Δ_c upon which no fixed point is obtained. If we apply this critical displacement, the iterative failure process of the elements will not stop until all intact elements are broken: the system evolves unstably up to complete failure. The loading threshold writes as

$$\Delta_c = \sqrt{\frac{3Y_0 + (a+1)k_0\sqrt{\frac{3(2a-1)Y_0^2 + 6(a+1)Y_0Y_r - 3(a+1)Y_r^2}{a(a+1)^2k_0^2}}}{3(a+1)k_0}} \tag{B.14}$$

Also note that the full macroscopic response can be obtained, writing the macroscopic force

$$F(\Delta) = k[(1 - U^*(\Delta))]\Delta \tag{B.15}$$

where U^* is given as a function of the applied displacement Δ by Eq. (B.13). Therefore, for both limit cases the response of the system is purely statistical. The macroscopic response and critical loading are solely dependent on the distribution of fracture energy threshold. It should be emphasized that unlike when hardening is introduced, here in the limit of zero disorder the system fails as soon as the first damage event takes place. The failure is delayed by the introduction of randomness that save the system from instantaneous early failure at the first damage event. This is well shown by the expressions of critical loadings of Eqs. (B.14) and (B.5) which both scale with the distribution parameters $Y_c^{\max} = Y_{c0} + \sqrt{3}\sigma_g$ where σ_g is the disorder intensity.

Now that the limit cases critical loadings are determined, we compare them to that obtained for finite, positive internal lengths. From Fig. B.1b, we see that the constant critical displacement obtained for large ℓ_0 values corresponds indeed to the mean field limit. On the other hand, the continuous evolution towards the upper limit (case of independent heterogeneities) as ℓ_0 tends to zero is well shown in the inset of the figure. Therefore, it seems that we have a continuous transition between two classes of behavior: (i) for large internal lengths a mean field macroscopic response is obtained with a characteristic catastrophic avalanche responsible for the failure of the system, (ii) for low internal lengths the system is continuously damaged until full failure of the system, which occurs at a critical loading that scales with ℓ_0 and is upper bounded by that of an interaction-free system. Moreover, from the macroscopic response obtained for $\ell_0 \leq 5$ it seems that there is a slow-down of the damage process close to failure, as indicated by the small inflection of the curve before failure. To study this effect, we characterize the temporal behavior of the precursors to failure in the next section.

B.2 Temporal evolution of the damage events

The avalanche sizes are shown as a function of δ on Fig. B.2a for $\ell_0 = 5$ (top) and $\ell_0 = \infty$ (bottom). The latter one exhibits the characteristic behavior observed from our numerical model with hardening and from experiments. The former has a peculiar response: the intermittency and amplitude go through a maximum. It increases from $\delta = 1$ to $\delta \simeq 0.2$, and then a slow down of the damage process occurs until failure. To emphasize this effect, we study the evolution of average avalanche size with the distance to failure, as shown on Fig. B.2b where $\langle S \rangle$ is normalized by the internal length value considered. For small internal length, $\ell_0 \in [1, 5]$, the average size of the bursts sharply increases before reaching a maximum value of about $10\ell_0$. The plateau regime occurs earlier as the interaction length is decreased. Moreover, the response is obtained for $\delta \in [10^{-2}, 1]$ only: two few avalanches take place closer to failure, and hence the lack of statistics does not allow to obtain the characteristic avalanche size. Therefore, the fluctuations appear bounded to a size that scales with ℓ_0 and a saturation occurs, leading to a decrease in the damage density variation close to failure. On the contrary, if

ℓ_0 is large, the average avalanche size follows a power law behavior of exponent $\simeq 0.5 \pm 0.1$, corresponding to the analytically determined exponent $1/2$ in the mean-field limit, as shown in the inset.

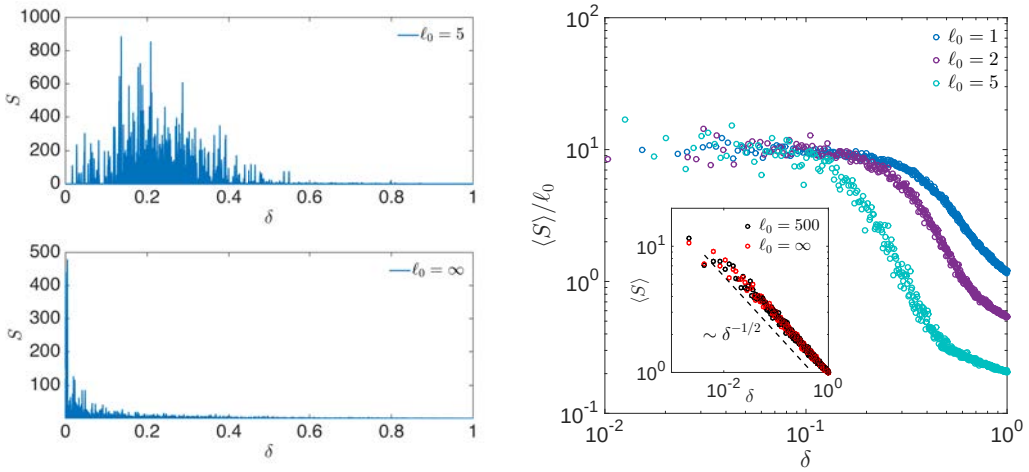

(a) (b)

Figure B.2: (a) Avalanche size S vs the distance to failure δ for (top) $\ell_0 = 5$ and (bottom) $\ell_0 = \infty$: for low internal length the intermittency and amplitude of avalanches decrease close to failure while they are amplified close to failure for the latter (note that in that case the last, much larger, avalanche was removed); (b) Evolution of the average avalanche sizes normalized by the internal length as a function of δ for low internal lengths showing a saturation that scales with ℓ_0 and occurs earlier as the parameter is lowered, in the inset is shown $\langle S \rangle$ vs δ for large internal lengths, showing the expected mean field behavior with a power law of exponent close to $1/2$.

The normalized probability densities are shown for $\ell_0 = 5$ and $\ell_0 = \infty$ on Figs. B.3a and B.3b, respectively. For the lower value, the functions are dominated by an exponential tail from which is extracted an avalanche size S^*. This characteristic burst size follows the behavior of $\langle S \rangle$ with δ. For $\ell_0 = \infty$, the distributions follow the characteristic gamma law, with an exponent of the power law $\simeq 1.5 \pm 0.1$. Since we also have $\langle S \rangle \sim \delta^{-1/2}$ we deduce that in that case $S^* \sim \delta^{-1}$, see Sec.4.1.2. The change of behavior of the probability densities when considering a local or global redistributions has been well observed in the context of fiber bundle [44, 59].

To emphasize the transition from one type of model to the other, the evolution of the maximum value of the cutoff S^* is shown on Fig. B.4a as a function of ℓ_0. If the system shows a catastrophic behavior we instead indicate the average size of the last avalanche. We once again observe a clear change of behavior: for $\ell_0 \leq 5$ the maximum cutoff value is linear with ℓ_0, it then sharply increases for $\ell_0 \leq 10$, value above which the average catastrophic avalanche has a rather constant value. This is in agreement with the analysis of the macroscopic response analysis as we obtain roughly the same critical internal length ($\ell_0 \simeq 100$) above which a mean field behavior takes place.

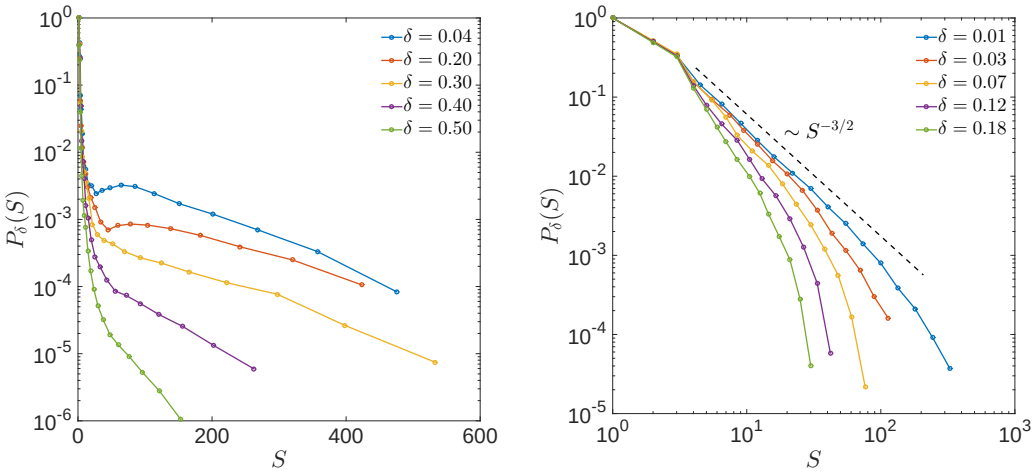

(a) (b)

Figure B.3: Avalanche size distribution densities for (a) $\ell_0 = 5$ showing that an exponential behavior dominates even close to failure; (b) $\ell_0 = \infty$ for which we retrieve the gamma law of exponent $3/2$ predicted for a global load sharing model.

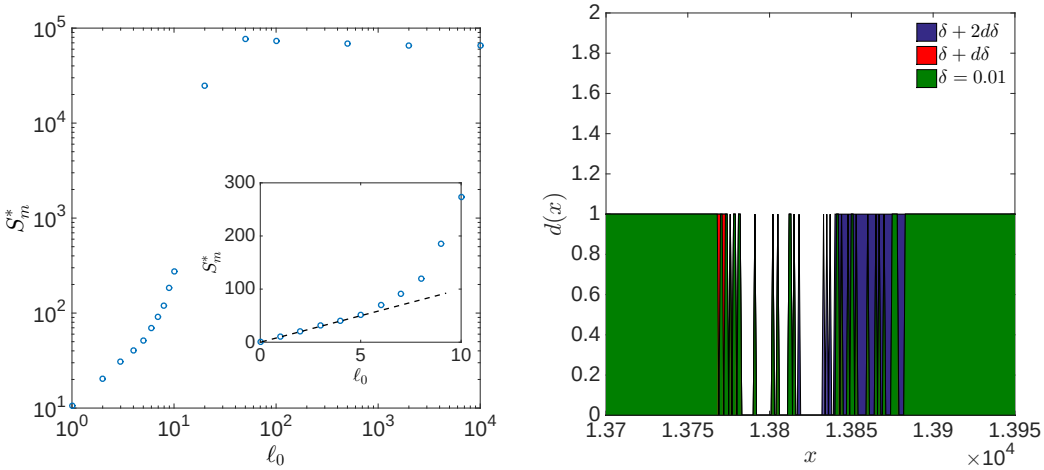

(a) (b)

Figure B.4: (a) Evolution of the maximum cutoff value S^* as a function of ℓ_0, for large ℓ_0 values the S^* corresponds to the average size of the last catastrophic avalanche. This figure highlights the transition from a loca to global load sharing behavior; (b) Damage field close to failure for $\delta \simeq 0.01$, after a first avalanche $(\delta + d\delta)$ and a second one $(\delta + 2d\delta)$ showing the locking mechanism that takes place when only the strongest heterogeneities remain intact and local redistributions take place.

We think that the change of response for local and mean-field behaviors results from different damage mechanisms. For large internal lengths, smooth, almost constant, interactions take place over large scales. As depicted from the analytical prediction of the system macroscopic response in the mean field limit, in that case avalanches are only dependent on the fracture energies distribution and spatial repartition of these thresholds. For small redistribution lengths, we think that there exists

three different stages in the system response, each of which having a different damage mechanism. For low loadings, the failure is mainly controlled by the disorder spatial distribution: the weakest points, which are randomly located, break due to the applied loading. Since few points are damaged, the influence of the interactions remain of low amplitude. Once damage is spread all over the system, the interactions begin to dominate the failure process: as small clusters of broken elements are formed, the redistributions induce further localized breaking events. Close to failure, we use the damage field shown on Fig. B.4b to describe the damage mechanism. The damage field consists in large cracks (regions were all elements are broken) separated by small ligaments of intact elements (see the green field at $\delta \simeq 0.01$). The weakest heterogeneities are already broken due to the applied loading (disorder dominancy) as also the moderately strong heterogeneities (coaction of loading and interactions) and only the strongest points remain intact, blocking the diffusion of damage through interactions. Since the interactions are short ranged, only a few elements see the effect of already damaged points. Hence, it is most likely that upon the application of a higher loading it is the point at the extremity of a crack that will break. This can trigger other events but since the fracture energy of the neighboring elements is high, the diffusion of damage is most likely to be blocked. Therefore, only small avalanches take place. This mechanism is well observable on Fig. B.4b: two main microcracks are formed at $\delta \simeq 0.01$ and small localized broken elements are located between them. As the loading is increased, corresponding to an increase $d\delta$, the elements close to the left crack break but damage does not diffuse to link the two cracks. The same occurs from the right crack as the loading is further increased ($\delta + 2d\delta$), see the blue profile.

B.3 Conclusions

Therefore, it arises that without hardening a continuous transition is observed with the internal length ℓ_0. For small internal length, the macroscopic response is continuous until failure, which occurs at a critical loading that scale with ℓ_0. The distributions of avalanche sizes are dominated by an exponential behavior, from which a characteristic burst size is extracted and its maximum value is shown to be set by ℓ_0. On the other hand, for sufficiently large internal length values, the system falls into the mean field limit. In that case, we recover the behavior obtained for hardening, continuously damaging system. Indeed, the system exhibit a catastrophic failure event, at a critical loading independent of ℓ_0 and predicted in the mean field limit. In addition to that, the distributions are shown to follow power law behavior up to a cutoff that also follows a power law behavior with the distance to failure, the exponent of which corresponds to the mean field prediction.

Therefore, since for local redistributions of the damage driving force the precursors fluctuations are bounded whereas the adequate intermittency is obtained only for large internal lengths, corresponding to a mean field limit where no spatial organization of damage is obtained, it appears that the introduction of hardening in the material response seem relevant for an adequate description of the failure of quasi-brittle materials.